The Dissertation Committee for Kevin Carl Gullikson certifies that this is the approved version of the following dissertation:

Spectroscopic Detection and Characterization of Extreme Flux-Ratio Binary Systems

Committee:

Adam Kraus, Supervisor

Sarah Dodson-Robinson

Daniel T. Jaffe

Edward L. Robinson

Michael Meyer

Spectroscopic Detection and Characterization of Extreme Flux-Ratio Binary Systems

by

Kevin Carl Gullikson, B.S; M.A.

Dissertation

Presented to the Faculty of the Graduate School of
The University of Texas at Austin
in Partial Fulfillment
of the Requirements
for the degree of
Doctor of Philosophy

The University of Texas at Austin
May, 2016

Dedicated to my loving parents, who encouraged my exploration of science from an early age.

Acknowledgements

I would like to start by thanking everyone who served as a supervisor during part of my thesis. Mike Endl served as my co-supervisor for two years, taught me how to observe on the 2.7m telescope at McDonald observatory, and involved me in the planet search program for the last 5 years. That experience provided many interesting nights, a fun "side project", and gave me the confidence to do much of the observing for my main survey program. Sally Dodson-Robinson served as my thesis supervisor for my first two years. She gave me a great deal of independence in my project, while providing valuable feedback. I would like to thank both her and my current supervisor, Adam Kraus, for nominating me for several UT fellowships and funding me as a research assistant during much of my graduate career. The freedom to work exclusively on research has been invaluable, and facilitated much of the progress that I made. Adam, thank you for being a great advisor. Despite being brand new at this, you provide a great mix of a hands-on style when I need it and hands-off when I don't, and have been nothing but supportive in every way.

I would also like to thank Rob Robinson, my committee member, for numerous discussions on statistical methods both while planning and analyzing the results of my survey program. Discussions with you, not to mention your excellent data analysis class, have really helped me to think of statistical methods in a way that makes sense.

Finally, I would like to thank all of my friends and colleagues at UT for making these last years so much fun. From the usual crowd at Crown to cookouts at Paul's to boat parties and volleyball with Tom Montemayor, I have rarely lacked for a way to blow off some steam and relax in between the stressful moments. And of course, I would like to thank my girlfriend Cori Norman. You have made the last three years absolutely wonderful.

Spectroscopic Detection and Characterization of Extreme Flux-Ratio Binary Systems

Kevin Carl Gullikson, Ph.D.
The University of Texas at Austin, 2016

Supervisor: Adam Kraus

Binary stars and higher-order multiple systems are a ubiquitous outcome of star formation, especially as the system mass increases. The companion mass-ratio distribution is a unique probe into the conditions of the collapsing cloud core and circumstellar disk(s) of the binary fragments. Inside $a \sim 1000$ AU the disks from the two forming stars can interact, and additionally companions can form directly through disk fragmentation. We might therefore expect the mass-ratio distribution of close companions to differ from that of wide companions. This prediction is difficult to test with intermediate-mass primary stars using traditional methods because the contrast ratios that would be required to detect low-mass companions at narrow working angles are not yet achievable. In this thesis, we present a spectroscopic method to detect and characterize close companions to a variety of stars. We demonstrate applications of the method to detection of stars and even planets around sun-like stars, and present the results of a survey searching for companions to A- and B-type stars. As part of the survey, we estimate the temperatures and surface gravity of most of the 341 sample stars, and derive their masses and ages. We additionally estimate the temperatures and masses of the 64 companions we find, 23 of which are new detections. We find that the mass-ratio distribution for our sample has a turnover near $q \approx 0.3$, in contrast to the scale-free power law that describes the widely separated binary systems. We take this characteristic scale as evidence that companions are accreting a significant of material through disk interactions as they form, and that the scale is largely set by the disk lifetime and the time at which the fragments form.

Contents

List of Figures

Chapter One: Introduction

Stellar multiplicity is an inevitable and common outcome of star formation, with roughly half of all solar-type field stars in binary or multiple systems (Raghavan et al., 2010) and an even higher fraction as the stellar mass increases (Zinnecker & Yorke, 2007). Young stellar associations and clusters tend to have even higher multiplicity (Duchêne & Kraus, 2013), indicating that stars often form in multiple systems that are subsequently destroyed by dynamical interactions as the cluster dissociates.

1.1 Binary Star Formation

The overall multiplicity rate and the distributions of mass ratio, period, and eccentricity of a binary star population place important constraints on the mode of binary star formation. While the period and eccentricity are altered by dynamical processing in the birth cluster, the present-day mass ratio of a binary system is a direct result of its formation (Parker & Reggiani, 2013). There are several mechanisms by which binary stars may form: fission (Lyttleton, 1953; Lebovitz, 1974, 1984), in which a molecular core begins spinning fast enough as it collapses that it splits into two stars; various capture scenarios (e.g. Fabian et al., 1975), in which two stars pass close enough to each other to dissipate kinetic energy and become bound; core fragmentation (see e.g. Boss & Bodenheimer, 1979; Boss, 1986; Bate et al., 1995), in which a collapsing core develops two or more overdensities which then begin collapsing separately; and disk fragmentation (see e.g. Kratter & Matzner, 2006; Stamatellos & Whitworth, 2011), in which the circumstellar disk surrounding the primary star becomes gravitationally unstable and creates a secondary star. While the fission scenario was once thought to be important, it has since fallen out of favor because the viscous dissipation timescale, which would drive a spinning body towards fission, is much longer than the core collapse timescale (Tohline, 2002) and because hydrodynamic simulations fail to cause the rotating core to actually split rather than just deform (Tohline & Durisen, 2001). Likewise, the capture mechanism may function through star-disk interactions in which one star passes close enough to another star to perturb its disk and dissipate kinetic energy, but is unlikely to generate a significant fraction of the

observed binary systems (Tohline, 2002).

Most binary stars are thought to form via core fragmentation. The number and initial masses of the fragments are set by the total core mass, as well as its rotation, turbulence, and its temperature and density structure. Machida et al. (2008) performed a parameter study by simulating several collapsing clouds with different levels of thermal, rotational, and magnetic energies. They found that the initial fragments occur on wide separations ($a \gtrsim 3AU$) if the rotational energy dominates that of the magnetic field. If the magnetic energy dominates, however, then the fragmentation occurs much later and generates very close binary systems ($a \lesssim 1AU$).

Machida et al. (2008) do not follow the accretion or migration evolution of the fragments, but we can estimate that evolution from the relevant physics: If the fragments are well separated ($a \gtrsim 1000$ AU), they will evolve independently of each other, accreting mass from the core material onto their own protostellar disks and then onto the protostars themselves. However, close fragments ($a \sim 100$ AU) will interact with each other; the protostellar disk may be truncated, destabilized, or form into a circumbinary disk if the separation is small enough (Bate & Bonnell, 1997). In addition, an unstable disk can fragment to form low-mass close companions (Kratter & Matzner, 2006; Stamatellos & Whitworth, 2011) directly. The mass ratios of close companions formed via either mechanism should be affected by preferential accretion. Most work has suggested that the disk material and high angular momentum infalling core material will preferentially accrete onto the lower mass companion as it migrates inward (Bate & Bonnell, 1997; Bate et al., 2002), although some recent work has suggested the preferential accretion may go in the opposite direction as a result of magnetic disk braking (Zhao & Li, 2013).

1.2 Other Implications of Binarity

Beyond informing star formation models, intermediate-mass stars have recently seen a revival of interest as potential young planet hosts, spurred largely by the detection of planets orbiting nearby $\sim 2M_{\odot}$ stars on both wide (e.g. Lagrange et al., 2010; Marois et al., 2008) and close (Johnson et al., 2011) orbits. Since the main sequence lifetime of an A- or B-type star is tens to hundreds of Myrs, a planetary companion would still be bright and easier to detect with direct imaging techniques than the

same companion orbiting an old, solar-type star (Marley et al., 2007). Robust age estimates for nearby intermediate-mass stars are therefore very important to provide a vetted sample of young systems to search, and to convert the companion brightness into a mass estimate.

In the context of planetary companions, stellar-mass binary companions are contaminants; companions complicate radial velocity planet searches because they necessitate simultaneous modeling of both stellar motions (e.g. Bergmann et al., 2015). Likewise, companions complicate direct imaging planet searches by requiring either extremely high-contrast instrumentation (Thalmann et al., 2014) or specialized coronagraphs (Crepp et al., 2010).

However, known binary stars are typically avoided in planet search programs for a more fundamental reason: the binary companion depletes or destroys the planet-forming disk. By combining a binary census of the $\sim$ 2 Myr Taurus-Auriga star-forming region with a disk census of the same, Kraus et al. (2012) showed that close ($\lesssim$ 40 AU) binaries are about 2-3 times less likely to host a protoplanetary disk, and so hasten disk dispersal. Even if a disk survives, it tends to be depleted in mass by a factor of $\sim$ 25 for binary separations $\lesssim$ 30 AU (Harris et al., 2012). A full binary census focusing on companions within $\sim$ 100 AU is therefore necessary in order to generate a direct-imaging planet search sample.

Since intermediate-mass stars have main-sequence lifetimes of tens to hundreds of Myr, dynamical mass estimates for late-type companions provide a direct test of stellar evolutionary models. Therefore a binarity survey for close companions to intermediate-mass stars, which measures the companion temperature, surface gravity, metallicity, and mass, is necessary. The survey we describe in this thesis does not directly measure the companion mass; in fact, we use stellar evolutionary models to estimate the mass. However, follow-up observations of the systems we detect to fit the full double-lined spectroscopic orbit would provide just such a survey.

1.3 Detection Methods

There are three methods traditionally used to search for companions to stars, whether they be stellar or planetary companions. The first is direct imaging, in which we take an image of the star and look for nearby point sources in the image. This can be either

seeing-limited, in which case it is difficult to find companions inside $1''$ of the primary, or with adaptive optics systems on large-aperture telescopes, in which case the inner working angle is near the diffraction limit of the telescope. We can detect companions outside of a few hundred mas from the primary with adaptive optics imaging methods (see De Rosa et al., 2014, for typical sensitivity curves of a binary survey), and even closer with more time-consuming and complicated observational techniques such as angular differential imaging (Marois et al., 2006) and locally optimized combination of images (LOCI, Lafrenière et al., 2007).

The second detection method is interferometry, in which multiple beams of light from the source are allowed to constructively or destructively interfere with each other before recording the light. In some cases, interferometry is done with multiple telescopes separated by several tens of meters, producing an effective aperture much larger than can be produced as a single mirror. In other cases, a mask is introduced in front of a single telescope to only allow light from certain beams through (aperture masking, Tuthill et al., 2000; Ireland et al., 2008). Interferometry can usually achieve smaller working angles than imaging, but cannot achieve as high contrast (see e.g. Aldoretta et al., 2015) because the atmosphere changes on short timescales, necessitating even shorter exposure times.

The final traditional method useful in searching for stellar companions is radial velocity monitoring, in which the radial velocity of the star is measured many times over periods of years to decades. An unseen companion will cause the radial velocity of the primary star to oscillate. Unlike the previous two methods, the radial velocity method has no inner working angle; in fact, it works best at finding very close companions. The sensitivity falls off as the companion orbital separation increases, because the signal induced on the primary star decreases. The sensitivity also falls off as the number of spectral lines in the primary star spectrum falls, and as it rotation speed ($v \sin i$) increases. Careful radial velocity monitoring surveys are capable of detecting motion as small as $\sim 1\text{m s}^{-1}$ when observing slowly rotating solar-type stars (e.g. Wittenmyer et al., 2006; Fischer et al., 2009; Pepe et al., 2011), but have difficulty achieving better than $\sim 1\text{km s}^{-1}$ when observing rapidly rotating hot stars (Becker et al., 2015).

Both imaging and interferometry can usually characterize the companion in a single image, provided the primary star parameters are sufficiently well-known. However, radial velocity monitoring is typically only capable of measuring the mass function

of the binary system:

$$f(M_1, M_2) = \frac{(M_2 \sin i)^3}{(M_1 + M_2)^3} \tag{1.1}$$

and only after monitoring the system for 1−2 orbital periods. For companions on long-period ($\sim$ 10 years) orbits, it is an extremely time-consuming method. The exception is for double-lined binary systems (SB2s), for which the lines of both components are visible in the spectrum and vary enough that they can be resolved. In this case, spectroscopic companions can be fully characterized, and even provide model-independent masses, but still take $1-2$ orbital periods to measure. In Chapter 2, we introduce a spectroscopic method that is capable of both detecting and characterizing close companions in single observations, with no dependence on separation or inner working angle.

1.4 Previous Observational Results

The mass ratio, period, and eccentricity distributions are well-known for solar type stars and cooler stars. M dwarf binary systems tend to have roughly equal-mass components at separations of a few AU (Fischer & Marcy, 1992), while binaries with a solar-type primary have a flat mass-ratio distribution and are found at separations of a few tens to hundreds of AU (Raghavan et al., 2010). Interestingly, the mass-ratio distribution appears to be invariant to separation for binaries at these masses (Reggiani & Meyer, 2011, 2013).

All of the distributions are much less certain for more massive stars. The reason for this is two-fold: first, more massive stars tend to be more rare and farther away, meaning many of the companions are angularly close to the very bright primaries and difficult to detect with imaging techniques. Second, the primary stars tend to be rapid rotators with few intrinsic spectral lines, which limits radial velocity precision to $\sim$ 1km s^{-1}. Additionally, detecting the companion spectrum suffers from the same flux-ratio difficulties as imaging methods, and is the only way to characterize the detected companion.

Binary systems with O-type primaries are mostly known through radial velocity monitoring surveys because they are so rare that only very few are amenable to imaging methods. Sana et al. (2013) measured the mass-ratio distribution of O-type binary systems in the Tarantula Nebula, finding it is well-fit by a power-law

$f(q) \sim q^{-\gamma}$ with $\gamma = 1.00 \pm 0.40$, indicating a preference for companions much smaller than the primary. Other surveys with typically smaller sample sizes tend towards a more uniform mass-ratio distribution, albeit with large uncertainty (Sana et al., 2012; Kiminki & Kobulnicky, 2012). Imaging surveys, while incomplete, also find that the mass-ratio distribution is consistent with flat (Peter et al., 2012) at wide separations.

Intermediate-mass binary systems (primary spectral type A or B), while still rarer than solar-type binaries, are common enough that less biased surveys are possible. Building on the work in Shatsky & Tokovinin (2002), Kouwenhoven et al. (2007) combine imaging and radial velocity measurements of intermediate-mass stars in the young Scorpius OB2 association, and find that the mass-ratio distribution favors low-mass companions ($\gamma \approx 0.4$). More recently, De Rosa et al. (2014) performed an adaptive optics imaging survey of a large sample of nearby field A-type stars, and found that the mass-ratio distribution is well-described by a power law with large slope, indicating a very strong preference for low-mass companions. They also found initial evidence that the mass-ratio distribution for companions inside 125 AU has a much shallower power law slope than that of wide companions, and is consistent with flat. Their close companion subsample contained only 18 binary systems, and the result is complicated by the inherent difficulty of detecting close companions with low mass ratios in an imaging survey.

There are few systematic radial velocity surveys around normal intermediate-mass stars, which would provide a more complete picture of the close companion mass-ratio distribution. Chemically peculiar Am stars are typically slow rotators, a fact typically attributed to tidal braking from binary companions; they thus form a highly biased sample of intermediate-mass stars that contains almost exclusively close binary systems. Nonetheless, it is interesting to note that they have a mass-ratio distribution which peaks near $q \sim 0.5$ (Vuissoz & Debernardi, 2004), an entirely different form than the power law distribution found around chemically normal stars at wide separations.

The bulk of this thesis is devoted to a spectroscopic survey of field intermediate-mass stars. We introduce the general method in great detail in Chapter 2. We then detour to discuss TelFit, a tool we created to fit and remove the contamination from Earth's atmosphere in Chapter 3. We apply a variant of the direct spectral detection method to two side projects in Chapters 4 and 5. We then describe the pilot and

main survey program in Chapters 6 and 7 (respectively), and provide overall survey conclusions in Chapter 8.

Chapter Two: Direct Spectral Detection: An Efficient Method to Detect and Characterize Binary Systems[1]

2.1 Background

It is difficult to detect low-mass companions very near an intrinsically bright primary star and even more difficult to characterize the companion. There are three commonly used techniques for binary star searches: direct imaging with adaptive optics systems, interferometry, and radial velocity monitoring. Imaging can easily detect low-mass companions at wide apparent separations, but loses sensitivity as the on-sky distance from the primary star decreases (see De Rosa et al., 2014, for typical sensitivity curves). Interferometry can usually achieve smaller working angles than imaging, but cannot achieve as high contrast (see e.g. Aldoretta et al., 2015).

Radial velocity monitoring can find companions on very short-period orbits, but its sensitivity to low-mass companions drops as the physical separation increases. This is especially true for A- and B-type stars, where radial velocity precision is typically limited to $\sim$ 1km s^{-1} by their rotationally broadened lines. Additionally, radial velocity monitoring techniques cannot *characterize* the companion unless the inclination is known or if the companion spectral lines are also visible. All three techniques have separation-dependent sensitivity, which introduces observational bias in any search for a parameter that changes with physical separation.

One technique that is separation independent is to search directly for the composite spectrum of two stars. Burgasser (2007) used single-epoch low-resolution spectroscopy to identify and characterize a brown dwarf binary system by fitting both spectra simultaneously. This method only works if the stars have a similar brightness but very different spectra, such that the spectral features from both components

[1]This chapter was previously published (Gullikson et al., 2016). Adam Kraus and Sarah Dodson-Robinson were both my advisors for part of the time that I spent developing the method outlined below. Daniel Jaffe is the principal investigator for one of the instruments used in this work, the IGRINS spectrograph. The rest of the authors provided data that I used to calibrate the method.

are visible and distinguishable. If, as in the case of binary systems with very large flux ratios, the companion spectrum is buried within the noise of the primary star, a different method is needed.

The direct spectral detection method (hereafter referred to as the DSD method), and variations thereof, has been used to search for binary companions to early B-stars (Gullikson & Endl, 2013), main sequence FGK-stars (Kolbl et al., 2015), young K-M stars (Prato et al., 2002), and even 'Hot Jupiter' type planets (Snellen et al., 2010; Brogi et al., 2012; de Kok et al., 2013) orbiting FGK-stars. The method relies on the cross-correlation function (CCF) of a high-spectral-resolution spectrum of the primary star with a model spectrum for the expected companion. The CCF uses every pixel in the spectrum, and more importantly every spectral line in the secondary spectrum. A simple experiment with synthetic spectra containing increasing numbers of spectral lines (N) in noisy data shows that the CCF peak significance increases as $\sim \sqrt{N}$. For high-resolution cross-dispersed échelle spectra, this amplification can reach several factors of 10, allowing the detection *and characterization* of a secondary spectrum where the individual lines are completely buried in noise. Since the DSD method uses a seeing-limited spectrum of the primary star, its sensitivity is independent of separation inside $\sim 1''$ and can make use of small telescopes to detect high-contrast companions.

In this chapter, we describe the DSD method in detail, and use it to detect the secondary star in nine known binary systems. We describe the method in Section 2.2. We describe the observations and data reduction in Section 2.3, then use the observations to estimate the accuracy with which we can measure the companion temperature in Section 2.4 and the sensitivity of the method in Section 2.5. In Section 2.6 we use the DSD method to search for known companions, and discuss the results in Section 2.7.

2.2 Direct Spectral Detection Method

All implementations of the DSD method use high-spectral-resolution and high signal-to-noise spectra, and search for companions with extreme flux ratios by cross-correlating the observed spectra with models for the expected companion. The main differences between the various implementations are the primary star and telluric line removal

processes. The 'Hot Jupiter' searches (e.g. Snellen et al., 2010) use known orbital phase information and a high degree of phase coverage to simultaneously estimate an empirical stellar and telluric spectrum with minimal contamination from the planet. We discuss similar techniques in Chapters 4 and 5 of this thesis. Kolbl et al. (2015) use optical data, and remove the primary star spectrum with a best-fit model spectrum; they do not attempt any telluric correction. Note that the approach of Kolbl et al. (2015) is conceptually similar to the todcor code (Mazeh & Zucker, 1994), which is widely used to search for double-lined spectroscopic binary systems.

Unlike most previous work, we focus on not only detecting but accurately characterizing the companion. We additionally optimize our technique for detecting cool companions to rapidly rotating early-type stars, for which it is very difficult to detect the reflex motion of the primary star. We fit and remove the telluric absorption using the TelFit code (Gullikson et al., 2014, and Chapter 3), and estimate an empirical primary star spectrum with a Gaussian smoothing filter applied to the telluric-corrected data. We chose to use a smoothing filter over subtracting model spectra for two reasons: first, the model spectra are a poor representation of the data, especially at the high signal-to-noise ratios that we use, and so leave very large-scale features in the residual spectrum. Second, the smoothing filter removes any large-scale instrumental systematics in the spectrum, aiding in companion detection. We use a smoothing filter with a window size (w) set by

$$w = \frac{v \sin i \cdot f}{c} \cdot \frac{\lambda_0}{\Delta\lambda} \tag{2.1}$$

where $v \sin i$ is the literature rotational velocity of the star, λ_0 is the central wavelength of the échelle order, $\Delta\lambda$ is the wavelength spacing per pixel of the order, c is the speed of light, and $f = 0.25$ is an empirically determined parameter to give a visually adequate fit. Typical window sizes ranged from 50 - 100 pixels.

We use the following subset of the Phoenix library of model spectra prepared by Husser et al. (2013) throughout this work:

- $T_{\rm eff} = 3000 - 7000$ K[2], in steps of 100 K
- [Fe/H] = -0.5, 0.0, +0.5

[2]We extend the grid to higher temperatures if the measured temperature (see Section 2.4) is near 7000 K

- $v \sin i = 1, 5, 10, 20, 30$ km s^{-1}

Here, the $v \sin i$ is the rotational velocity of the secondary star. We account for the small influence that the smoothing kernel has on the companion spectrum by convolving the model with the same smoothing kernel used for the data, and subtracting the convolved model from the original. Treating the model spectrum in this way is more commonly known as unsharp masking. Finally, we cross-correlate every échelle order that does not have strong telluric residuals against the corresponding model spectrum, and combine the CCFs for each order using a simple average. The method is summarized below:

1. Smooth the observed spectrum with a Gaussian smoothing kernel with width given by Equation 2.1, and subtract the smoothed spectrum from the original
2. Rotationally broaden the Phoenix model spectrum to the requested companion $v \sin i$
3. Smooth the broadened spectrum to the instrumental resolution by convolving it with a gaussian kernel of appropriate width.
4. Unsharp mask the broadened model spectrum
5. Resample the processed model spectrum to the same wavelength spacing per pixel as the observed spectrum.
6. Cross-correlate each échelle order against the corresponding processed model spectrum, and combine using a simple average.

2.3 Observations and Data Reduction

We use three separate samples in this work. The first set, given in Table 2.1, contains A- and B-type stars with the following published properties:

- Spectral type B0V - A9V (only main sequence)
- $V < 6$
- $v \sin i > 80$km s^{-1}

- No known companions within $3''$, and no sign of a companion in our data.

The lower limit on $v \sin i$ in our sample ensures that the empirical primary star template is accurate and only minimally affects any companions.

The second dataset (Table 2.2) contains F-M type stars which have a high-quality temperature estimate in the literature. We use the first two samples in Sections 2.4 and 2.5 to assess the accuracy of the temperature estimation using the DSD method and the sensitivity to companions of various temperatures.

Finally, we use the third dataset (Table 2.3) to search for the spectral lines of the companion in several known binary systems. The third dataset has the same properties as the first, except that they have one *and only one* known companion within $1''$. We further require that the literature data either puts no constraints on the companion temperature (as in the case of single-lined spectroscopic binaries) or that the companion has $T_{\rm eff} < 7500$ K.

We estimate the expected companion temperature depending on whether it is part of a spectroscopic (Table 2.4) or visual (Table 2.5) binary system. In the case of double-lined spectroscopic binaries, we use the ratio of the semi-amplitudes given in the 9th catalog of spectroscopic binary orbits (SB9, Pourbaix et al., 2009) to estimate the mass ratio of the system. We convert the primary star spectral type from the Simbad database (Wenger et al., 2000) to mass by interpolating Table 5 of Pecaut & Mamajek (2013). The mass ratio and primary mass gives an estimate of the companion mass, which we convert to temperature by interpolating the same table. Most of the directly-imaged binary systems do not have orbital information, so we use the magnitude difference published in the Washington Double Star catalog (WDS, Mason et al., 2014). We use the Simbad spectral type of the primary star and Table 5 of Pecaut & Mamajek (2013) to estimate the primary star temperature (T_1) and radius (R_1). We then find the companion temperature that minimizes the following function for the companion temperature (T_2), given the observed magnitude difference (Δm_{obs})

$$Q = (m(T_2, R_2) - m(T_1, R_1) - \Delta m_{obs})^2 \tag{2.2}$$

where $m(T, R)$ is the Vega magnitude of a star with temperature T and radius R. We use the pysynphot package[3] and a Kurucz model grid (Castelli & Kurucz, 2003) to

[3]pysynphot is a python code package to perform synthetic photometry, and is available at this url: `https://pypi.python.org/pypi/pysynphot`

calculate $m(T, R)$, and assume the companion is on the main sequence to estimate its radius (R_2). For both spectroscopic and visual binary systems, we assume spectral type uncertainties of ± 1 subtype on the primary stars, and propagate the uncertainties into uncertainty in the companion temperature. We include the binary system in the sample if the expected companion temperature is < 7500 K.

We use the same set of instruments and settings for all observations throughout the three datasets. We use the CHIRON spectrograph (Tokovinin et al., 2013) on the 1.5m telescope at Cerro Tololo Inter-American Observatory for most southern targets. This spectrograph is an $R \equiv \lambda/\Delta\lambda = 80000$ cross-dispersed échelle spectrograph with wavelength coverage from 450 - 850 nm, and is fed by a $2.7''$ optical fiber. The data are automatically reduced with a standard CHIRON data reduction pipeline, but the pipeline leaves residuals of strong lines in adjacent orders. We therefore bias-correct, flat-field and extract the spectra with the optimum extraction technique (Horne, 1986) using standard IRAF[4] tasks, and use the wavelength calibration from the pipeline reduced spectra.

For the northern targets, we use a combination of the High Resolution Spectrograph (HRS, Tull, 1998) on the Hobby Eberly Telescope, and the Tull coudé (TS23, Tull et al., 1995) and IGRINS (Park et al., 2014) spectrographs, both on the 2.7m Harlan J. Smith Telescope. All three northern instruments are at McDonald Observatory. For the HRS, we use the $R = 60000$ setting with a $2''$ fiber, and with wavelength coverage from 410-780 nm. We bias-correct, flat-field, and extract the spectra using an IRAF pipeline. The HRS spectra are wavelength-calibrated using a Th-Ar lamp observed immediately before or after the science observations.

For the TS23, we use a $1.2''$ slit in combination with the E2 échelle grating (53 grooves/mm, blaze angle 65°), yielding a resolving power of $R = 60000$ and a wavelength coverage from 375-1020 nm. We reduce the data using an IRAF pipeline very similar to the one we use for the HRS, and wavelength calibrate using a Th-Ar lamp observed immediately before the science observations.

IGRINS only has one setting with $R = 40000$. It has complete wavelength coverage from 1475-2480 nm, except for where telluric absorption is almost 100% from 1810 - 1930 nm. Each star is observed in an ABBA nodding mode, and reduced using

[4]IRAF is distributed by the National Optical Astronomy Observatories, which are operated by the Association of Universities for Research in Astronomy, Inc., under cooperative agreement with the National Science Foundation.

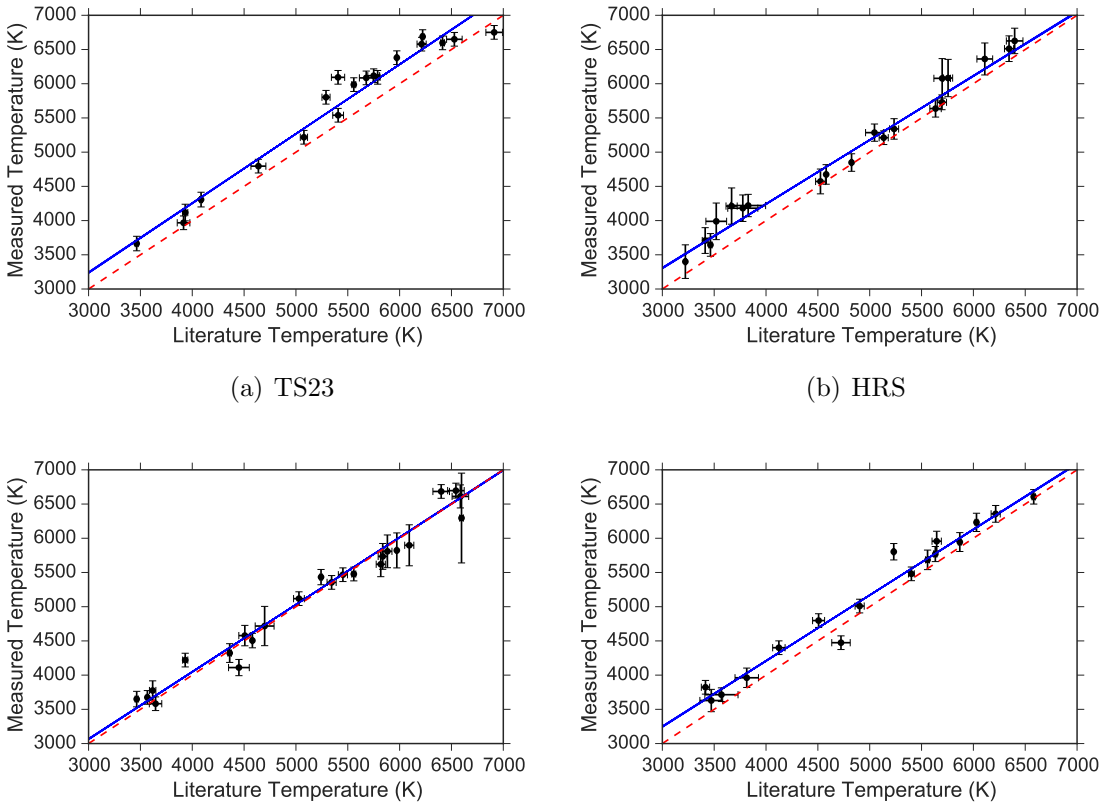

(a) TS23

(b) HRS

(c) IGRINS

(d) CHIRON

Figure 2.1: Correspondence between the companion temperature measured with the direct spectral detection method, and the actual (literature) values. In all figures, the red dashed line has unity slope, the values with uncertainties are the measurements from the synthetic binary observations (see Section 2.4), and the blue lines are the line of best-fit through the data. There is significant bias in all of the measurements except for those using the near-infrared IGRINS instrument.

the standard IGRINS pipeline (Lee, 2015). The standard pipeline uses atmospheric OH emission lines as well as a Th-Ar calibration frame to calibrate the wavelengths; we further refine the wavelength solution using telluric absorption lines and the TelFit code.

2.4 Parameter Determination

In the absence of noise, the CCF of an observed spectrum with a perfect model will have a value of 1 at the radial velocity of the star. As the model becomes a worse representation of the data, the peak height of the resulting CCF will decrease. Thus the CCFs act in a similar way as a χ^2 map of the parameter space, allowing us to measure the effective temperature, metallicity, and rotational broadening of the secondary star. However, the presence of noise and the imperfections in the model spectra cause the measured values to deviate from the true parameters of the secondary star.

To measure the impact of both random and systematic noise on the parameter estimation, we created several hundred synthetic binary systems for each instrument used in our program. We made the synthetic binary systems by combining the early-type star spectra from Table 2.1 with those of the late-type stars in Table 2.2 in every possible combination, provided both observations came from the same instrument. By combining actual observations of early-type and late-type stars, our synthetic binary observations retain any instrument-specific effects that may impact the temperature estimation. We scaled the flux of the late-type star such that the flux ratio ($F_{\rm secondary}/F_{\rm primary}$) is ten times larger than the expected flux ratio for main sequence components. The artificial brightening relative to a real binary system is to ensure that the temperature estimation uncertainties are separate from the overall sensitivity of the method, which we discuss in Section 2.5. We estimate the main sequence flux ratio from the published temperature of the late type star (given in Table 2.2) and the published spectral types of the primaries available on Simbad (Wenger et al., 2000), and convert to temperature and luminosity by using Table 5 of Pecaut & Mamajek (2013).

We analyzed each synthetic binary star system using the method described above, and measured the temperature (T_m) and variance (σ_T^2) as a weighted sum near the grid point with the highest CCF peak value, weighting by the peak CCF height at each temperature (C_i):

$$T_m = \sum_i C_i T_i / \sum_i C_i \tag{2.3}$$

$$\sigma_T^2 = \frac{\sum_i C_i (T_i - T_m)^2}{\sum_i C_i - \sum_i C_i^2 / \sum_i C_i} \tag{2.4}$$

Each synthetic binary observation contributes a pair of measured and actual (literature) companion temperatures, and so each late-type star in Table 2.2 has many independent temperature measurements made with the DSD method. To determine the correspondence between measured and actual temperature, we perform a Markov Chain Monte Carlo (MCMC) fit to a straight line using the emcee code (Foreman-Mackey et al., 2013). We plot the mean and standard deviation of the measured temperatures in Figure 2.1, along with 300 MCMC samples for the linear fit and the line of unity slope. The MCMC samples give posterior probability distributions for the parameters a and b relating the actual temperature (T_a) to the measured temperature (T_m) through

$$T_m = a + bT_a \tag{2.5}$$

In Section 2.6 we invert this relation to determine the actual companion temperature, given the measured temperature from Equation 2.3.

The typical temperature uncertainty with the DSD method is $\sim 150 - 200$ K, but the optical instruments systematically overestimate the companion temperature. *The error analysis is therefore not just important to measure the parameter uncertainties, but also to get the correct answer.* We suspect the systematic biases come from a mismatch between the Phoenix model spectrum template and the real spectrum of a late-type star. The biases are different for each instrument because the instruments have different wavelength ranges, and so the spectral lines that contribute most to the cross-correlation function are different.

2.5 Detection Sensitivity

The detectability of a companion decreases primarily as the contrast between it and the primary star increases. Rotation plays an important role in the detection rate as well, since the cross-correlation function derives most of its power from narrow

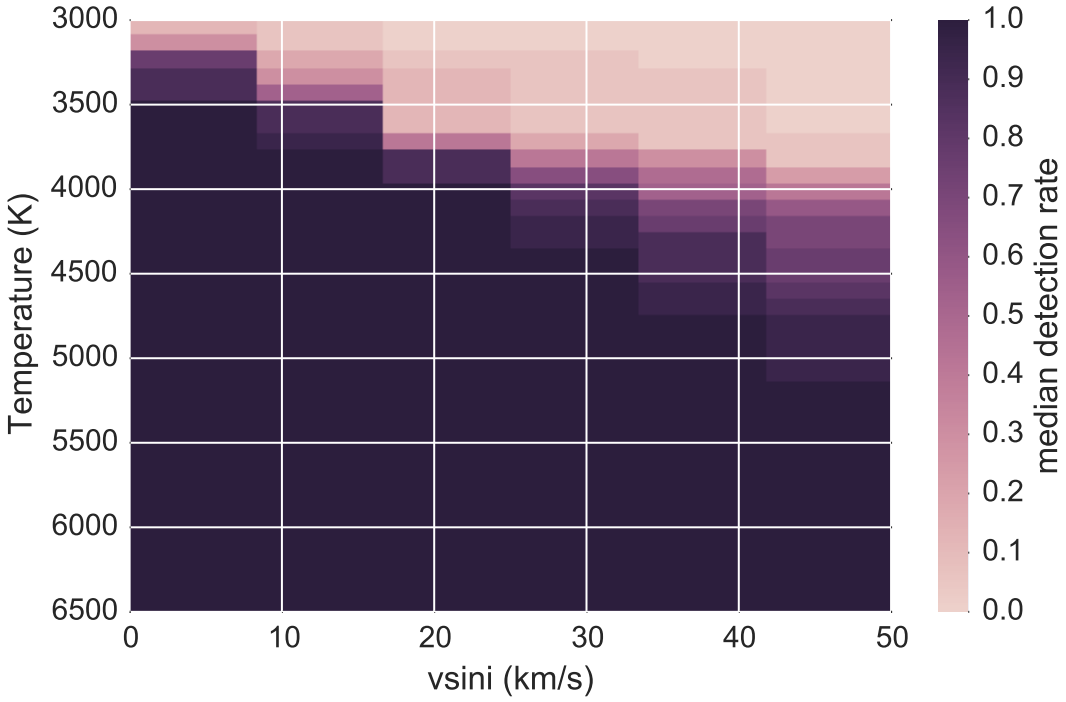

Figure 2.2: Median detection rate as a function of companion temperature and rotation speed. Each cell represents the median detection rate for targets with no detection in Table 2.3. Companions represented by dark cells are detectable. See Section 2.5 for details of the analysis.

spectral features. We follow a similar strategy as above to estimate the detection rate as a function of temperature and rotational velocity for each star, with the key differences that we scale the model spectra to replicate a binary star observation with main sequence observations (rather than scaling the companion to ten times main sequence), and that we add *Phoenix model spectra* for late-type stars to the data instead of real spectra. We use synthetic spectra so that we can use a finer grid of temperatures and rotational broadening and not be limited by the temperatures or the temperature estimation uncertainties of real late-type stars. However, since we are comparing models to models any mismatch between the model spectrum and the real spectrum of a star of that temperature will tend to make the sensitivity calculations somewhat optimistic. This will have the largest impact for very cool stars, where the difficult to model molecular absorption is more important.

For each observed early-type star, we generate several synthetic binary star observations by adding model spectra for stars with $T_{\rm eff} = 3000 - 7000$ K in steps of 100 K and rotational velocities $v \sin i = 0 - 50$ km s^{-1} in steps of 10 km s^{-1}. For each temperature and $v \sin i$ combination, we make 17 independent synthetic observations by adding the model to the data with a radial velocity shift between -400 to 400 km s^{-1} in steps of 50 km s^{-1}. We label a companion as detected if the highest peak in the CCF of the synthetic data with the model spectrum of the same temperature is within 5 km s^{-1} (the approximate instrumental broadening) of the correct velocity.

The median detection rate for targets in Table 2.3 is shown in Figure 2.2[5]. We can usually detect very cool stars if they are slowly rotating, but the sensitivity quickly degrades as the companion $v \sin i$ increases. Cool stars spin down as they age (Barnes, 2003) so the rotation speed dependence is equivalent to an age dependence. We estimate the impact of rotation on our detection method by using the gyrochronology relation given in Barnes (2010):

$$\frac{k_C t}{\tau} = \ln\left(\frac{P}{P_0}\right) \frac{k_I k_C}{2\tau^2}(P^2 - P_0^2) \tag{2.6}$$

In Equation 2.6, k_C and k_I are constants fit to data with known ages and rotation periods, P and P_0 are respectively the current and zero-age main sequence (ZAMS) rotation periods, τ is the convective turnover time scale and t is the current age of the star. We use the same values that Barnes (2010) use for the constants:

- $k_C = 0.646$ day/Myr
- $k_I = 452$ Myr/day

We use Equation 2.6 to estimate the expected rotation period for a companion star of given temperature and age as follows: First, we convert from temperature to convective timescale (τ) by interpolating Table 1 in Barnes & Kim (2010). Next we sample an appropriate probability density function (PDF) for the age of the binary system; if the primary star was analyzed in David & Hillenbrand (2015), we use their posterior age PDFs. Otherwise, we use a uniform PDF from the Zero Age Main Sequence (ZAMS) age of the primary star to its main sequence lifetime (typically

[5]A file with the results of the sensitivity analysis, as well as sensitivity figures similar to Figure 2.2 for each individual target, are available at this url: `https://github.com/kgullikson88/DSD-Paper`

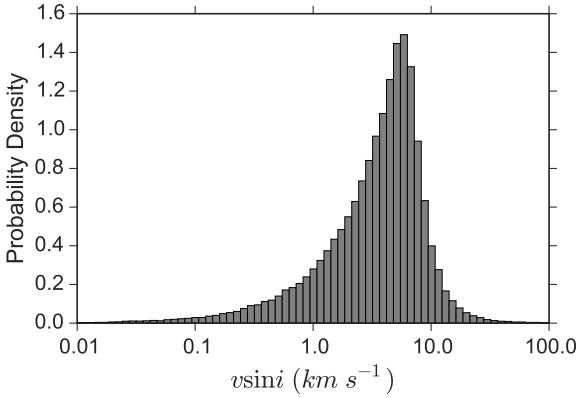

Figure 2.3: Typical probability density function for companion rotational velocity $v \sin i$. The distribution peaks near $\sim 5 - 10$ km s^{-1} and extends to very high velocities. Note that the x-axis is log-spaced to more clearly show the tails of the distribution.

10-200 Myr for our sample). Following the discussion in Barnes (2010), we uniformly sample initial rotation periods from 0.2 - 5 days for all stars. We estimate the current rotation period for each pair of age and initial rotation period samples using Equation 2.6 to build up a PDF of current rotation periods. We transform the period distribution into a PDF for $v \sin i$ using the main sequence radius of a star of the given temperature, obtained by interpolating Table 1 of Barnes & Kim (2010), and a uniform sampling of inclinations ($\sin i$). Figure 2.3 shows a typical $v \sin i$ distribution, which peaks near $\sim 5 - 10$ km s^{-1} and has a long tail extending to $\sim 40 - 50$ km s^{-1}.

By combining the sensitivity calculations described above with the $v \sin i$ samples, we marginalize over the expected rotation periods of the secondary stars to get simpler curves of detection rate as a function of companion star temperature. We show the median and approximate range of the marginalized detection rate in Figure 2.4. The DSD method can reliably detect companions as cool as 3700 K in most cases, although the primary star spectral type plays a dominant role in setting the coolest detectable companion.

Companions with $T \gtrsim 6250$ K, the canonical limit at which the convective zone is too small to transfer angular momentum to the stellar wind and spin down the star (Pinsonneault et al., 2001), may have rotational velocities comparable to that of the primary star. In that case, estimating the primary star spectrum with a gaussian filter may remove much or all of the companion spectrum. Since these are the types

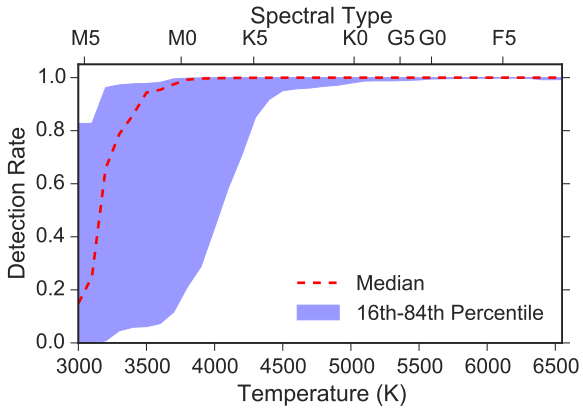

Figure 2.4: Summary of the detection rate as a function of temperature for the sample stars (Table 2.3) in which we do not detect a companion. The red dashed line gives the median detection rate, and the blue filled area illustrates the range across different primary stars. The direct spectral detection method can detect companions as late as M0 for most of our targets.

of stars with less extreme flux- and mass-ratios, they are easier to detect with more conventional methods. However, this shortcoming could be overcome by using model spectra for the primary star as in Kolbl et al. (2015). In this work, we have optimized the method for finding cool companions.

2.6 Application to Known Binary Systems

We now use the DSD method to measure the temperatures of several known binary systems (Table 2.3). We cross-correlate the spectra against the full grid of model spectra enumerated in Section 2.2, and find the temperature of the companion using Equation 2.3. We then convert the measured temperature to PDFs of the true companion temperature using the MCMC chains developed in Section 2.4 (see also Figure 2.1). For stars with multiple observations, we multiply the PDFs from each detection. Finally, we calculate the companion temperature and confidence interval from the integral of the PDF:

$$f = \int_{-\infty}^{x} pdf(T)dT \tag{2.7}$$

We use as the central value the value of x such that $f = 0.5$ (the median). Likewise, we calculate the 1σ lower and upper bounds such that $f = 0.16$ and $f = 0.84$, respectively. The CCFs for the companions that we detect are shown in Figures 2.5 and 2.6. For each star, we show the CCF which has the maximum peak value and annotate the figures with the parameters. Most of the CCFs have very strong peaks. The exception is HIP 22958; however, the detection is strengthened by the fact that we observed this star twice and measured a similar temperature both times. The CCFs for HIP 22958 and HIP 24902 demonstrate the adverse effect a large companion rotational velocity has on the detection significance.

2.6.1 Comparison to Literature Data

We use the literature data to predict an expected temperature for each companion in order to directly compare our measurements to previous results. The procedure outlined in Section 2.3 using the magnitude difference or orbital information alone produces reasonable estimates, but in many cases there is additional information in the literature to refine the estimates. The refined estimates are described below.

HIP 76267 and HIP 84606 are found in the David & Hillenbrand (2015) sample; we use the mass and temperature estimates provided there rather than going through the Simbad spectral type and assuming main-sequence relationships.

Shatsky & Tokovinin (2002) provide a color estimate of the companion star to HIP 79199 ($J - K = 0.57 \pm 0.12$). We convert this directly into a temperature estimate through Table 5 of Pecaut & Mamajek (2013).

Zorec & Royer (2012) find fundamental parameters for HIP 22958, and determine a temperature slightly cooler and luminosity much greater than the spectral type (B6V) would suggest. Because of this the usual analysis, which uses main sequence relationships, results in a biased answer. We estimate the companion temperature by assuming that the companion *does* follow the main sequence relationships as described in Section 2.3, but sample the uncertainty distributions given in Zorec & Royer (2012) for the temperature and radius of the primary star.

We compare our companion temperature measurements from the DSD method to the estimates described above in Figure 2.7. There is overall excellent agreement between the temperatures, with 5/6 falling within 1σ of equality. We test for a bias (Δ) between the measured temperatures (T_m) and expected temperatures (T_a) with

the equations

$$\Delta = \sum_i (T_{m,i} - T_{a,i}) \tag{2.8}$$

$$\sigma_\Delta^2 = \sum_i (\sigma_{T_{m,i}}^2 + \sigma_{T_{a,i}}^2) \tag{2.9}$$

which results in $\Delta = -580 \pm 770$ K. Our temperature measurements are consistent with the expected temperatures.

We list our measurements as well as the expected temperatures described above in Table 2.6. The expected $v \sin i$ values come from application of Equation 2.6 as described in Section 2.5. While we do give the measured $v \sin i$ and metallicity for our detections, the accuracy of these parameters is not calibrated and is determined with a coarse grid; the values should only be taken as rough estimates. We do note that most of the measurements have $[Fe/H] = -0.5$. This is likely a measurement bias since we do not expect the binary systems to have significantly sub-solar metallicity. As metallicity increases, so do the line depths of most of the lines in the spectrum. Any lines that are poorly modeled will then have a larger negative impact on the resulting CCF; thus the bias towards low metallicity is likely a result of imperfect model atmosphere templates. We do not attempt to identify the poorly modeled lines in this work.

2.6.2 Non-detections

There are many companions in Table 2.3 that we do not detect. Most of these are single-lined spectroscopic binaries (Table 2.4), and are likely too cool to detect with our data; very high signal-to-noise spectra with a near-infrared instrument such as IGRINS may uncover them. Several of the remaining un-detected companions have expected temperatures $T > 6250$ K, and so are likely to be rapid rotators. Since the cross-correlation function gets most of its power from sharp spectral features, these rapidly rotating companions are difficult to detect (see Figure 2.2).

Finally, HIP 88290 is hot enough and expected to be rotating slowly enough that we should be able to easily detect it. In fact, we would expect to be able to directly see the companion in the spectra (the green lines in Figure 2.8). The fact that we do not see the composite spectrum or see a peak in the cross-correlation function implies that the companion must be rotating with $v \sin i > 50$km s^{-1}, much more

quickly than Equation 2.6 predicts, that the primary is a giant and therefore much brighter than main-sequence relationships suggest, or that the companion fell outside the spectrograph slit. This star is in the David & Hillenbrand (2015) sample and has an effective temperature and mass consistent with main sequence, so we can rule out the giant primary possibility. Additionally, the binary separation is $0.47''$ (Tokovinin et al., 2015) and the CHIRON spectrograph has a $\sim 2.7''$ diameter fiber; light from the companion is guaranteed to fall on the slit.

2.7 Discussion and Conclusions

We have presented and extensively characterized the direct spectral detection method for finding companions to intermediate-mass stars using high-resolution cross-dispersed échelle spectroscopy. Using a very large number of synthetic but realistic binary star observations, we constrained the uncertainty and systematic errors present in determining the companion temperature with the direct spectral detection method. The typical uncertainties are of the order of 200 K across all instruments used in this study, with a systematic offset of similar magnitude (for the optical instruments). We used the synthetic binary star analysis to calibrate the direct spectral detection method for the four instruments used in this study between the temperatures $3500\ K < T < 6500\ K$.

We also estimated the sensitivity to detection of companions with a range of temperature and $v \sin i$ by creating a second set of synthetic companions. The method can detect companions as late as M0 in most cases, although the lower limit depends on the primary star spectral type, the signal-to-noise ratio achieved, and the instrument used. The median detection limit corresponds to average flux ratios as small as $F_{\rm sec}/F_{\rm prim} \sim 10^{-3}$ and binary mass-ratios $M_{\rm sec}/M_{\rm prim} \sim 0.2$, or a main-sequence M0 star orbiting an A0V primary.

The lowest detectable mass ratio is even more striking for young stars. At 1 Myr, both the A0 star and its companion are still contracting onto the main sequence (Bressan et al., 2012). The flux ratio limit corresponds to a $\sim$ M1 companion, similar to the main sequence case. However the mass ratio in this young system is $M_{\rm sec}/M_{\rm prim} \sim 0.1$, half that of main-sequence components with similar spectral types. The direct spectral detection method is therefore well suited for finding close,

low-mass companions to massive young stars.

There is also an upper detection limit near 6500 K set by rotation. Our method of removing the primary star spectrum can also remove the companion spectrum if it has a similar rotational velocity, which hot companions are likely to have. Subtracting a model atmosphere for the primary star would remove the upper limit, but would reduce the detection rate for cool companions that are most difficult to detect with any other means. We alleviate the problem somewhat in Chapter 7 by extending the CCF search grid (see Section 2.2) to higher temperatures and rotational velocities.

Finally, we applied the direct spectral detection method to a set of known binary systems with close, late-type companions. We detected the companion spectrum in 9 of 34 known binary systems, 3 of which we characterized for the first time. Most of the companions we failed to detect are likely very cool, falling below the sensitivity limit of our data.

The direct spectral detection method is able to detect close binary companions with comparable or better sensitivity than imaging techniques, and does not require large telescopes with extremely competitive time allocation requests. This method is an excellent way to identify and perform initial characterization on new binary systems using smaller telescopes, but care must be taken to calibrate the parameter estimation.

Acknowledgements

This research has made use of the SIMBAD database, operated at CDS, Strasbourg, France, and of Astropy, a community-developed core Python package for Astronomy (Astropy Collaboration, 2013). It was supported by a start-up grant to Adam Kraus as well as a University of Texas Continuing Fellowship to Kevin Gullikson. J.-E. Lee was supported by the Basic Science Research Program through the National Research Foundation of Korea (NRF) (grant No. NRF-2015R1A2A2A01004769) and the Korea Astronomy and Space Science Institute under the R&D program (Project No. 2015-1-320-18) supervised by the Ministry of Science, ICT and Future Planning.

This work used the Immersion Grating Infrared Spectrograph (IGRINS) that was developed under a collaboration between the University of Texas at Austin and the Korea Astronomy and Space Science Institute (KASI) with the financial support of

the US National Science Foundation under grant AST-1229522, of the University of Texas at Austin, and of the Korean GMT Project of KASI.

The Hobby-Eberly Telescope (HET) is a joint project of the University of Texas at Austin, the Pennsylvania State University, Stanford University, Ludwig-Maximilians-Universität München, and Georg-August-Universität Göttingen. The HET is named in honor of its principal benefactors, William P. Hobby and Robert E. Eberly.

Based on observations at Cerro Tololo Inter-American Observatory, National Optical Astronomy Observatory (NOAO Prop. IDs: 13A-0139, 13B-0112, 2014A-0260, 14A-0260, 15A-0245; PI: Kevin Gullikson), which is operated by the Association of Universities for Research in Astronomy (AURA) under a cooperative agreement with the National Science Foundation.

We would like to thank Bill Cochran and Mike Endl for observing some of the spectra used in this project. Finally, we would like to thank the anonymous referee for numerous comments that improved the paper.

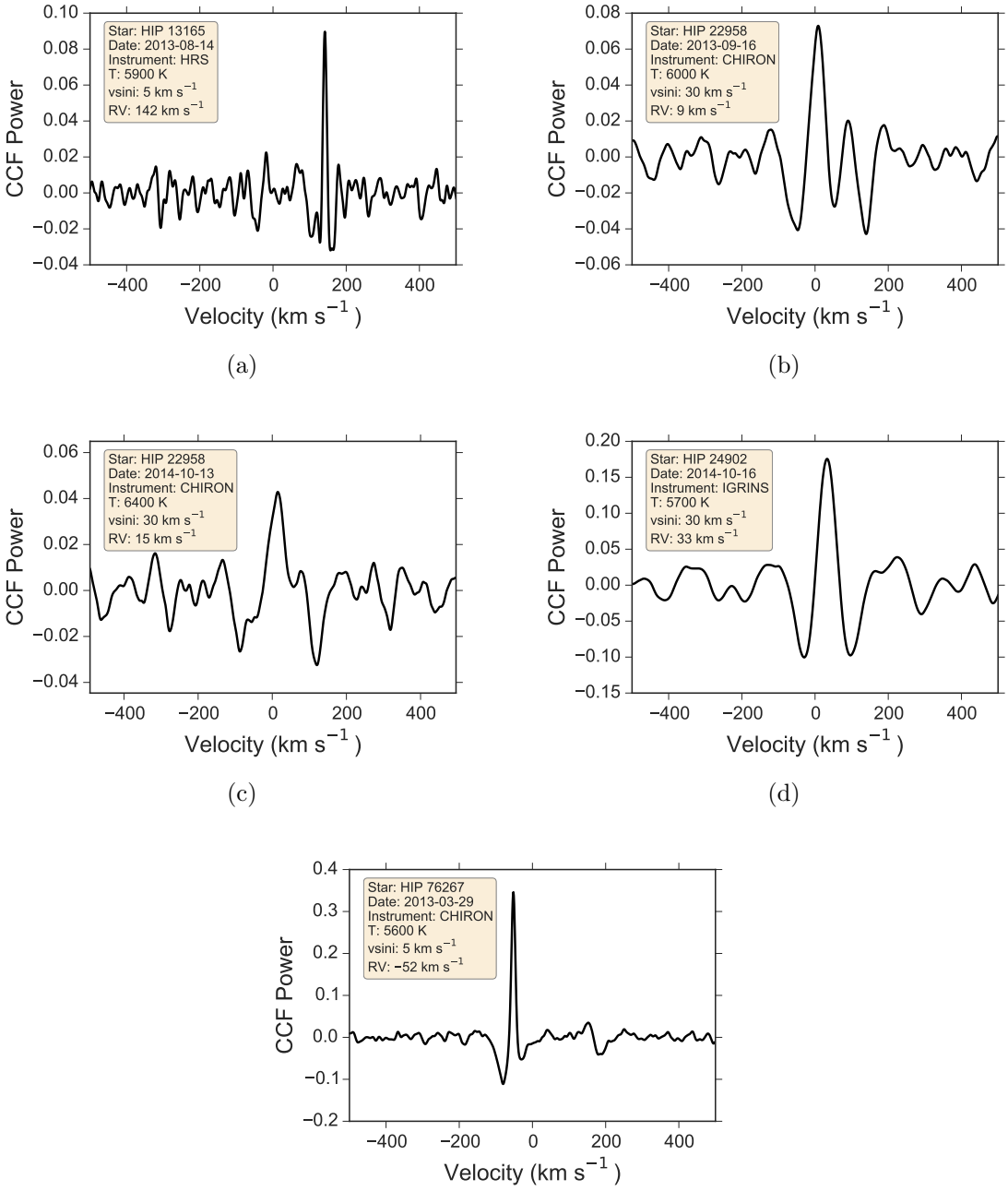

Figure 2.5: Cross-correlation functions for detected companions

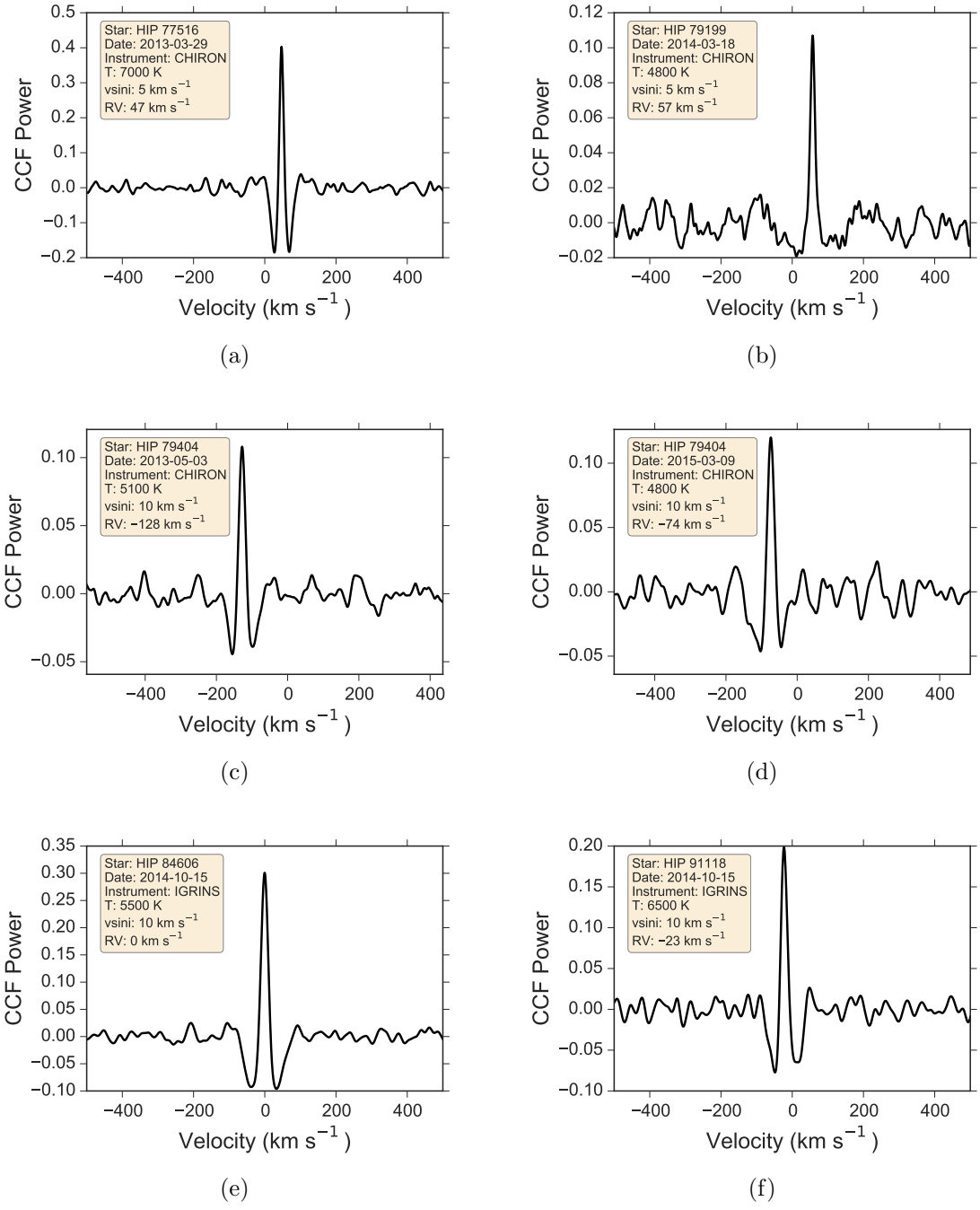

Figure 2.6: Cross-correlation functions for detected companions

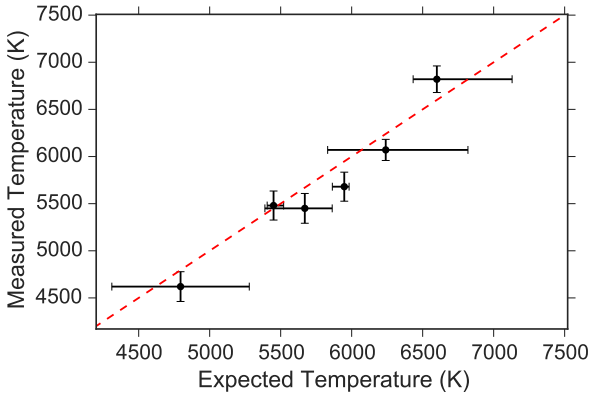

Figure 2.7: Temperature comparison for binaries with known secondary spectral types. The x-axis shows the companion temperature expected from the literature data (see Section 2.6.1).

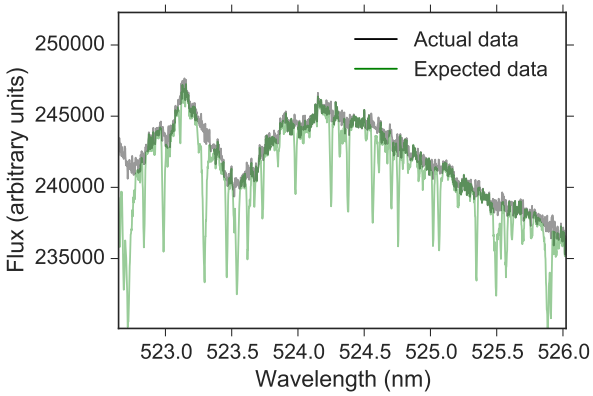

Figure 2.8: Observed (black) and expected (green) spectra for the known binary system HIP 88290. At the expected flux ratio, the spectral lines from the companion should be easily visible.

Table 2.1: Early type star sample.
The spectral types are adopted from the Simbad database (Wenger et al., 2000).

Star	RA	DEC	SpT	V	K	Instrument	Date	Exp. Time (min)
HIP 1191	00:14:54.5	-09:34:10.4	B8.5V	5.76	5.94	CHIRON	2013-09-17	180.00
HIP 2381	00:30:22.6	-23:47:15.6	A3V	5.19	4.83	CHIRON	2014-08-05	58.18
HIP 10320	02:12:54.4	-30:43:25.7	B9V	5.26	5.21	CHIRON	2013-08-28	119.00
HIP 13717	02:56:37.4	-03:42:44.3	A3V	5.16	4.86	CHIRON	2014-11-09	74.99
HIP 14293	03:04:16.5	-07:36:03.0	A5V	5.30	4.74	CHIRON	2014-09-19	53.33
HIP 16285	03:29:55.1	-42:38:03.3	A5V	5.77	5.18	CHIRON	2014-10-03	76.29
HIP 17457	03:44:30.5	-01:09:47.1	B7IV	5.25	5.43	CHIRON	2013-08-27	107.13
HIP 18788	04:01:32.0	-01:32:58.7	B5V	5.28	5.66	CHIRON	2013-08-31	121.22
HIP 20264	04:20:39.0	-20:38:22.6	A0V	5.38	5.33	CHIRON	2014-03-02	100.33
HIP 20507	04:23:40.8	-03:44:43.6	A2V	5.17	4.93	CHIRON	2014-03-02	11.92
HIP 20507	04:23:40.8	-03:44:43.6	A2V	5.17	4.93	CHIRON	2014-03-03	52.30
HIP 22913	04:55:50.1	+15:02:25.0	B9V	5.78	5.97	CHIRON	2013-10-20	200.00
HIP 23362	05:01:25.5	-20:03:06.9	B9V	4.89	4.97	CHIRON	2013-09-13	84.58
HIP 25280	05:24:28.4	-16:58:32.8	A0V	5.64	5.65	CHIRON	2014-10-20	67.52
HIP 25608	05:28:15.3	-37:13:50.7	A1V	5.56	5.50	CHIRON	2014-03-02	103.00
HIP 27321	05:47:17.0	-51:03:59.4	A6V	3.86	3.48	CHIRON	2014-02-08	23.23
HIP 28910	06:06:09.3	-14:56:06.9	A0V	4.67	4.52	CHIRON	2014-02-05	33.31
HIP 29735	06:15:44.8	-13:43:06.2	B9V	5.00	5.10	CHIRON	2013-09-24	93.68
HIP 30069	06:19:40.9	-34:23:47.7	B9V	5.75	5.93	CHIRON	2013-10-08	180.00
HIP 30788	06:28:10.2	-32:34:48.2	B4V	4.48	4.91	CHIRON	2013-10-09	56.93
HIP 31362	06:34:35.3	-32:42:58.5	B8V	5.61	5.73	CHIRON	2013-11-02	160.00
HIP 32474	06:46:39.0	-10:06:26.4	B9.5V	5.65	5.66	CHIRON	2013-10-27	160.00
HIP 33575	06:58:35.8	-25:24:50.9	B2V	5.58	6.05	CHIRON	2013-11-03	140.00
HIP 35180	07:16:14.5	-15:35:08.4	A1V	5.45	5.27	CHIRON	2014-02-08	90.55
HR 2948	07:38:49.3	-26:48:06.4	B6V	4.50	4.96	CHIRON	2013-10-19	67.20
HIP 37450	07:41:15.8	-38:32:00.7	B5V	5.41	5.78	CHIRON	2013-11-04	136.62
HIP 40429	08:15:15.9	-62:54:56.3	A2V	5.16	···	CHIRON	2014-02-03	82.83
HIP 40706	08:18:33.3	-36:39:33.4	A8V	4.40	4.00	CHIRON	2013-02-04	32.32
HIP 42334	08:37:52.1	-26:15:18.0	A0V	5.27	5.32	CHIRON	2014-02-24	48.60
HIP 45344	09:14:24.4	-43:13:38.9	B4V	5.25	5.59	CHIRON	2013-11-16	116.78
HR 4259	10:55:36.8	+24:44:59.0	A1V	4.50	···	CHIRON	2013-02-12	35.47
HIP 56633	11:36:40.9	-09:48:08.0	B9.5Vn	4.68	4.78	CHIRON	2013-02-12	41.77
HIP 57328	11:45:17.0	+08:15:29.2	A4V	4.84	4.41	CHIRON	2013-02-15	48.88
HIP 57328	11:45:17.0	+08:15:29.2	A4V	4.84	4.41	CHIRON	2013-03-19	48.88
HIP 61622	12:37:42.1	-48:32:28.6	A1IVnn	3.86	3.70	CHIRON	2013-03-27	19.48
HIP 66249	13:34:41.7	-00:35:45.3	A2Van	3.38	3.07	CHIRON	2013-03-27	12.83
HIP 66821	13:41:44.7	-54:33:33.9	B8.5Vn	5.01	···	CHIRON	2014-03-02	71.17
HIP 68520	14:01:38.7	+01:32:40.3	A3V	4.24	4.09	CHIRON	2013-04-21	27.88
HIP 70327	14:23:22.6	+08:26:47.8	A0V	5.12	5.07	CHIRON	2014-03-03	42.15
HIP 72104	14:44:59.2	-35:11:30.5	A0V	4.92	4.78	CHIRON	2014-03-04	58.09
HIP 73049	14:55:44.7	-33:51:20.8	A0V	5.32	5.13	CHIRON	2014-02-27	69.75
HIP 75304	15:23:09.3	-36:51:30.5	B4V	4.54	4.94	CHIRON	2013-05-15	36.05

Table 2.1: - (Continued)

Star	RA	DEC	SpT	V	K	Instrument	Date	Exp. Time (min)
HIP 77233	15:46:11.2	+15:25:18.5	A3V	3.67	3.42	CHIRON	2013-05-14	16.33
HIP 77635	15:50:58.7	-25:45:04.6	B1.5Vn	4.64	4.78	CHIRON	2014-03-09	30.80
HIP 78105	15:56:53.4	-33:57:58.0	A3V	5.08	4.85	CHIRON	2014-07-31	21.30
HIP 78105	15:56:53.4	-33:57:58.0	A3V	5.08	4.85	CHIRON	2014-08-01	48.91
HIP 78106	15:56:54.1	-33:57:51.3	B9V	5.55	5.42	CHIRON	2014-03-20	70.48
HIP 78554	16:02:17.6	+22:48:16.0	A3V	4.82	4.62	CHIRON	2013-05-15	47.60
HIP 79007	16:07:37.5	+09:53:30.2	A7V	5.64	5.09	CHIRON	2014-08-04	58.79
HIP 79007	16:07:37.5	+09:53:30.2	A7V	5.64	5.09	CHIRON	2014-08-05	21.23
HIP 79387	16:12:07.3	-08:32:51.2	A4V	5.43	5.05	CHIRON	2014-03-30	70.72
HIP 79653	16:15:15.3	-47:22:19.2	B8V	5.12	5.42	CHIRON	2014-03-24	47.12
HIP 80815	16:30:12.4	-25:06:54.8	B3V	4.79	5.10	CHIRON	2013-03-27	45.85
HIP 85537	17:28:49.6	+00:19:50.2	A7V	5.42	4.80	CHIRON	2014-05-15	60.83
HIP 85922	17:33:29.8	-05:44:41.2	A5V	5.62	5.14	CHIRON	2014-08-17	95.90
HIP 86019	17:34:46.3	-11:14:31.1	B8Vn	5.54	5.36	CHIRON	2014-03-31	69.76
HIP 87108	17:47:53.5	+02:42:26.2	A1Vnk	3.75	3.65	CHIRON	2013-06-02	17.73
HIP 90887	18:32:21.3	-39:42:14.4	A3Vn	5.16	4.93	CHIRON	2014-04-01	73.61
HIP 91875	18:43:46.9	-38:19:24.3	A2Vn	5.12	4.86	CHIRON	2014-03-29	46.61
HIP 92946	18:56:13.1	+04:12:12.9	A5V	4.62	4.09	CHIRON	2013-07-02	39.55
HIP 93805	19:06:14.9	-04:52:57.2	B9Vn	3.43	3.65	CHIRON	2014-04-28	10.92
HIP 101589	20:35:18.5	+14:40:27.1	A3V	4.66	4.36	CHIRON	2013-06-05	41.07
HIP 104139	21:05:56.8	-17:13:58.3	A1V	4.07	4.10	CHIRON	2013-06-05	23.80
HIP 105140	21:17:56.2	-32:10:21.1	A1V	4.72	4.49	CHIRON	2013-07-12	43.40
HIP 107517	21:46:32.0	-11:21:57.4	A1V	5.57	5.57	CHIRON	2014-08-04	118.70
HIP 107608	21:47:44.1	-30:53:53.9	A2V	5.02	4.85	CHIRON	2014-05-11	52.76
HIP 108294	21:56:22.7	-37:15:13.1	A2Vn	5.46	5.17	CHIRON	2014-05-13	57.20
HIP 110935	22:28:37.6	-67:29:20.6	A4V	5.57	5.05	CHIRON	2014-08-27	74.48
HIP 117089	23:44:12.0	-18:16:36.9	B9V	5.24	5.38	CHIRON	2013-08-09	102.52
HIP 5361	01:08:33.4	+58:15:48.4	B8V	5.77	5.75	HRS	2013-08-19	50.00
HIP 8016	01:42:55.8	+70:37:21.0	B9V	5.18	5.22	HRS	2013-08-18	16.40
HIP 14043	03:00:52.2	+52:21:06.2	B7V	5.25	5.43	HRS	2013-08-19	20.00
HIP 14143	03:02:22.5	+04:21:10.3	B7V	5.61	5.90	HRS	2013-08-14	23.10
HIP 15404	03:18:37.7	+50:13:19.8	B3V	5.16	5.33	HRS	2013-08-13	10.25
HIP 18396	03:55:58.1	+47:52:17.1	B6V	5.38	5.58	HRS	2013-08-12	12.95
HIP 20430	04:22:34.9	+25:37:45.5	B9Vnn	5.38	5.45	HRS	2013-08-16	18.00
HIP 20579	04:24:29.1	+34:07:50.7	B8V	5.72	5.81	HRS	2013-08-13	24.50
HIP 66798	13:41:29.8	+64:49:20.6	A2V	5.85	5.65	HRS	2013-03-26	18.10
HIP 67194	13:46:13.5	+41:05:19.4	A5V	5.89	5.34	HRS	2013-04-07	18.40
HIP 67782	13:53:10.2	+28:38:53.2	A7V	5.91	5.47	HRS	2013-04-12	17.95
HIP 70384	14:24:00.8	+08:14:38.2	A3V	5.93	5.72	HRS	2013-04-21	21.00
HIP 72154	14:45:30.2	+00:43:02.1	B9.5V	5.67	5.60	HRS	2013-04-21	15.00
HIP 80991	16:32:25.6	+60:49:23.9	A2V	5.91	5.78	HRS	2013-04-07	20.20
HIP 82350	16:49:34.6	+13:15:40.1	A1V	5.91	5.86	HRS	2013-04-09	20.20
HIP 83635	17:05:32.2	-00:53:31.4	B1V	5.61	5.29	HRS	2013-04-25	15.80
HIP 85379	17:26:44.2	+48:15:36.2	A4V	5.83	5.38	HRS	2013-04-16	16.50
HIP 86782	17:43:59.1	+53:48:06.1	A2V	5.76	5.59	HRS	2013-04-22	15.50

Table 2.1: - (Continued)

Star	RA	DEC	SpT	V	K	Instrument	Date	Exp. Time (min)
HIP 88817	18:07:49.5	+26:05:50.4	A3V	5.90	5.51	HRS	2013-04-23	20.00
HIP 90052	18:22:35.3	+12:01:46.8	A2V	5.98	5.77	HRS	2013-04-23	25.00
HIP 92312	18:48:53.3	+19:19:43.3	A1V	5.89	5.82	HRS	2013-04-26	19.50
HIP 93393	19:01:17.3	+26:17:29.0	B5V	5.68	5.84	HRS	2013-04-22	16.00
HIP 96840	19:41:05.5	+13:48:56.4	B5V	5.99	6.21	HRS	2013-04-26	27.60
HIP 100069	20:18:06.9	+40:43:55.5	O9V	5.84	5.72	HRS	2013-04-27	22.55
HIP 105282	21:19:28.7	+49:30:37.0	B6V	5.74	6.08	HRS	2013-08-18	36.77
HIP 105942	21:27:21.3	+37:07:00.4	B3V	5.29	5.64	HRS	2013-08-19	24.00
HIP 105972	21:27:46.1	+66:48:32.7	B7V	5.41	5.60	HRS	2013-08-03	13.35
HIP 5132	01:05:41.7	+21:27:55.5	A0Vn	5.53	5.61	IGRINS	2014-07-09	6.67
HIP 5518	01:10:39.3	+68:46:43.0	A0Vnn	5.32	5.31	IGRINS	2014-10-15	3.73
HIP 5626	01:12:16.8	+79:40:26.2	A3V	5.60	5.49	IGRINS	2014-10-15	3.73
HIP 9564	02:02:52.4	+64:54:05.2	A1Vn	6.00	5.92	IGRINS	2014-10-15	3.73
HIP 12803	02:44:32.9	+15:18:42.7	B9Vn	5.78	5.79	IGRINS	2014-10-17	3.73
HIP 13879	02:58:45.6	+39:39:45.8	A2Vn	4.70	4.42	IGRINS	2014-10-15	3.73
HIP 14862	03:11:56.2	+74:23:37.1	A2Vnn	4.84	4.71	IGRINS	2014-10-15	3.73
HIP 15110	03:14:54.0	+21:02:40.0	A1V	4.88	4.82	IGRINS	2014-10-16	4.20
HIP 16599	03:33:39.0	+54:58:29.4	A3V	5.98	5.68	IGRINS	2014-10-15	3.73
HIP 17527	03:45:09.7	+24:50:21.3	B8V	5.64	5.81	IGRINS	2014-10-17	3.73
HIP 20789	04:27:17.4	+22:59:46.8	B7V	5.51	5.74	IGRINS	2014-10-16	3.73
HIP 21683	04:39:16.5	+15:55:04.7	A5Vn	4.68	4.23	IGRINS	2014-10-18	3.83
HIP 22028	04:44:07.9	-18:39:59.7	A1V	5.53	5.44	IGRINS	2014-10-17	4.00
HIP 23362	05:01:25.5	-20:03:06.9	B9V	4.89	4.97	IGRINS	2014-10-16	4.00
ADS 3962 AB	05:22:50.3	+03 32 52	B1Vn	4.99	···	IGRINS	2014-10-16	4.67
HIP 25143	05:22:50.3	+41:01:45.3	A3V	5.55	5.11	IGRINS	2014-10-16	3.73
HIP 25280	05:24:28.4	-16:58:32.8	A0V	5.64	5.65	IGRINS	2014-10-17	4.00
HIP 25790	05:30:26.1	+15:21:37.6	A3Vn	5.94	5.55	IGRINS	2014-10-16	3.73
HIP 26093	05:33:54.2	+14:18:20.0	B3V	5.59	5.96	IGRINS	2014-10-16	4.67
HIP 27713	05:52:07.7	-09:02:30.8	A2Vn	5.96	5.65	IGRINS	2014-10-16	4.00
HIP 29151	06:08:57.9	+02:29:58.8	A3Vn	5.73	5.35	IGRINS	2014-10-16	4.40
HIP 29735	06:15:44.8	-13:43:06.2	B9V	5.00	5.10	IGRINS	2014-10-16	4.00
HIP 30666	06:26:39.5	-01:30:26.4	A3Vn	5.87	5.64	IGRINS	2014-10-16	4.67
HIP 31278	06:33:37.9	-01:13:12.5	B5Vn	5.08	5.46	IGRINS	2014-10-16	4.00
HIP 36812	07:34:15.8	+03:22:18.1	A0Vnn	5.83	5.74	IGRINS	2014-10-17	4.00
HIP 40881	08:20:32.1	+24:01:20.3	B9.5V	5.93	5.91	IGRINS	2014-10-17	4.00
HIP 85290	17:25:41.3	+60:02:54.2	A1Vn	5.64	5.50	IGRINS	2014-10-16	3.73
HIP 85385	17:26:49.1	+20:04:51.5	B5V	5.51	5.84	IGRINS	2014-07-10	8.00
HIP 93713	19:04:55.1	+53:23:47.9	A0Vn	5.38	5.41	IGRINS	2014-07-10	8.00
HIP 94620	19:15:17.3	+21:13:55.6	A4V	5.65	5.30	IGRINS	2014-07-10	10.00
HIP 97376	19:47:27.7	+38:24:27.4	B8Vn	5.83	6.01	IGRINS	2014-07-10	8.00
HIP 99742	20:14:16.6	+15:11:51.3	A2V	4.95	4.77	IGRINS	2014-10-15	8.00
HIP 101123	20:29:53.9	-18:34:59.4	A1V	5.91	5.72	IGRINS	2014-10-15	4.00
HIP 101909	20:39:04.9	+15:50:17.5	B3V	5.98	···	IGRINS	2014-10-15	6.00
HIP 102487	20:46:09.9	-21:30:50.5	A1V	5.91	5.77	IGRINS	2014-07-09	8.00
HIP 104365	21:08:33.6	-21:11:37.2	A0V	5.28	5.30	IGRINS	2014-07-09	8.00

Table 2.1: - (Continued)

Star	RA	DEC	SpT	V	K	Instrument	Date	Exp. Time (min)
HIP 105891	21:26:44.9	+52:53:54.7	B7III	5.99	6.34	IGRINS	2014-10-16	3.73
HIP 108339	21:56:56.3	+12:04:35.3	A2Vnn	5.54	5.36	IGRINS	2014-10-15	3.73
HIP 109831	22:14:44.3	+42:57:14.0	A2Vnn	5.72	5.66	IGRINS	2014-10-15	3.73
HIP 111056	22:29:52.9	+78:49:27.4	A3V	5.46	5.23	IGRINS	2014-10-15	4.67
HIP 1366	00:17:05.4	+38:40:53.8	A2V	4.61	4.42	TS23	2013-10-20	32.17
HIP 4436	00:56:45.2	+38:29:57.6	A5V	3.87	3.49	TS23	2013-10-20	18.14
HIP 9312	01:59:38.0	+64:37:17.7	A0Vn	5.28	5.22	TS23	2013-10-21	59.25
HIP 13327	02:51:29.5	+15:04:55.4	B7V	5.51	5.78	TS23	2014-01-13	120.70
HIP 15444	03:19:07.6	+50:05:41.8	B5V	5.04	5.20	TS23	2013-10-17	49.84
HIP 16340	03:30:36.9	+48:06:12.9	B8V	5.82	5.90	TS23	2014-01-21	71.58
HIP 18141	03:52:41.6	-05:21:40.5	B8V	5.48	5.71	TS23	2014-01-21	58.26
HIP 21819	04:41:19.7	+28:36:53.9	A2V	5.73	5.70	TS23	2014-01-22	74.02
HIP 21928	04:42:54.3	+43:21:54.5	A1Vn	5.30	5.20	TS23	2014-01-20	73.64
HIP 25555	05:27:45.6	+15:52:26.5	B9.5Vn	5.51	5.33	TS23	2014-01-13	95.73
HIP 29997	06:18:50.7	+69:19:11.2	A0Vn	4.76	4.67	TS23	2014-01-22	35.16
HIP 31434	06:35:12.0	+28:01:20.3	A0Vnn	5.27	5.15	TS23	2014-01-19	58.71
HIP 34769	07:11:51.8	-00:29:33.9	A2V	4.15	3.90	TS23	2014-01-20	27.36
HIP 35341	07:18:02.2	+40:53:00.2	A5Vn	5.87	5.33	TS23	2014-01-23	83.54
HIP 36393	07:29:20.4	+28:07:05.7	A4V	5.07	4.74	TS23	2014-01-19	51.08
HIP 38538	07:53:29.8	+26:45:56.8	A3V	4.98	4.66	TS23	2014-01-12	56.54
HIP 39236	08:01:30.2	+16:27:19.1	B9.5Vn	5.99	5.94	TS23	2014-01-22	128.84
HIP 41307	08:25:39.6	-03:54:23.1	A0V	3.90	3.93	TS23	2014-01-10	43.84
HIP 42313	08:37:39.3	+05:42:13.6	A1Vnn	4.14	4.03	TS23	2014-01-24	58.27
HIP 43142	08:47:14.9	-01:53:49.3	A3V	5.28	5.04	TS23	2014-01-13	83.95
HIP 44127	08:59:12.4	+48:02:30.5	A7V(n)	3.14	2.66	TS23	2014-01-20	18.24
HIP 47006	09:34:49.4	+52:03:05.3	A0Vn	4.48	4.34	TS23	2014-01-19	27.62
HIP 50303	10:16:14.4	+29:18:37.8	A0Vn	5.49	5.39	TS23	2014-01-20	116.86
HIP 50860	10:23:06.3	+33:54:29.3	A6V	5.90	5.51	TS23	2014-01-21	138.85
HIP 51685	10:33:30.9	+34:59:19.2	A2Vn	5.58	5.35	TS23	2014-01-20	92.78
HIP 52422	10:43:01.8	+26:19:32.0	A4Vn	5.52	5.05	TS23	2014-01-19	52.89
HIP 52457	10:43:24.9	+23:11:18.2	A3Vn	5.07	4.92	TS23	2014-01-19	44.36
HIP 52638	10:45:51.8	+30:40:56.3	A1Vn	5.35	5.40	TS23	2014-01-12	94.63
HIP 52911	10:49:15.4	+10:32:42.7	A2V	5.31	5.07	TS23	2014-01-13	99.47
HIP 54849	11:13:45.5	-00:04:10.2	A0V	5.40	5.33	TS23	2014-01-13	150.85
HIP 56034	11:29:04.1	+39:20:13.1	A2V	5.35	5.31	TS23	2014-01-19	39.60
HIP 59819	12:16:00.1	+14:53:56.6	A3V	5.09	4.89	TS23	2014-01-12	67.54
HIP 60595	12:25:11.7	-11:36:38.1	A1V	5.95	5.83	TS23	2014-01-19	114.15
HIP 60957	12:29:43.2	+20:53:45.9	A3V	5.68	5.43	TS23	2014-01-21	92.45
HIP 65728	13:28:27.0	+59:56:44.8	A1Vn	5.40	5.43	TS23	2014-01-20	106.14
HIP 75178	15:21:48.5	+32:56:01.3	B9Vn	5.38	5.49	TS23	2014-01-21	84.18
HIP 93747	19:05:24.6	+13:51:48.5	A0Vnn	2.99	2.88	TS23	2013-10-22	10.90
HIP 95853	19:29:42.3	+51:43:47.2	A5V	3.77	3.60	TS23	2013-10-20	18.37
HIP 96288	19:34:41.2	+42:24:45.0	A2V	5.35	5.05	TS23	2013-10-20	67.76
HIP 99080	20:06:53.4	+23:36:51.9	B3V	5.06	5.57	TS23	2013-10-18	55.24
HIP 101716	20:37:04.6	+26:27:43.0	B8V	5.59	5.71	TS23	2013-10-17	49.96

Table 2.1: - (Continued)

Star	RA	DEC	SpT	V	K	Instrument	Date	Exp. Time (min)
HIP 105966	21:27:40.0	+27:36:30.9	A1V	5.39	5.29	TS23	2013-10-20	72.23
HIP 111169	22:31:17.5	+50:16:56.9	A1V	3.77	3.75	TS23	2013-10-20	17.03
HIP 111841	22:39:15.6	+39:03:00.9	O9V	4.88	5.50	TS23	2013-10-18	35.70
HIP 113788	23:02:36.3	+42:45:28.0	A3Vn	5.10	4.69	TS23	2013-10-21	47.51
HIP 114520	23:11:44.1	+08:43:12.3	A5Vn	5.16	4.74	TS23	2013-10-22	72.27
HIP 117371	23:47:54.7	+67:48:24.5	A1Vn	5.05	4.97	TS23	2013-10-21	44.52

Table 2.2: Late type star sample.
The temperatures come from the following sources, and are labeled as superscripts after the temperature. [1]: Woolf & Wallerstein (2005); [2]: Sousa et al. (2008); [3]: Boyajian et al. (2013); [4]: Alonso et al. (1996); [5]: Valenti & Fischer (2005); [6]: Neves et al. (2014); [7]: Mann et al. (2015); [8]: Casagrande et al. (2011); [9]: Ramírez & Meléndez (2005); [10]: Casagrande et al. (2008); [11]: Mishenina et al. (2012); [12]: Casagrande et al. (2010); [13]: Boyajian et al. (2012); [14]: Pecaut & Mamajek (2013); [15]: Zboril & Byrne (1998)

Star	RA	DEC	V	K	$T_{\rm eff}$ (K)	Instrument	Date	Exp. Time (min)
HD 33793	05:11:40.5	-45:01:06.2	8.85	5.05	3570 ± 160^{1}	CHIRON	2015-01-13	60.00
HD 36379	05:30:59.9	-10:04:51.9	6.91	5.56	6030 ± 14^{2}	CHIRON	2015-01-14	9.58
HD 38858	05:48:34.9	-04:05:40.7	5.97	4.41	5646 ± 45^{3}	CHIRON	2015-01-14	5.31
HD 42581	06:10:34.6	-21:51:52.7	8.12	4.17	3814 ± 113^{4}	CHIRON	2015-01-14	30.62
HD 45184	06:24:43.8	-28:46:48.4	6.39	4.87	5869 ± 14^{2}	CHIRON	2015-01-14	5.30
HD 50806	06:53:33.9	-28:32:23.2	6.04	4.33	5633 ± 15^{2}	CHIRON	2015-01-14	3.99
HD 61421	07:39:18.1	+05:13:29.9	0.37	-0.65	6582 ± 16^{3}	CHIRON	2015-01-16	0.05
HD 69830	08:18:23.9	-12:37:55.8	5.95	4.16	5402 ± 28^{2}	CHIRON	2015-01-14	5.03
HD 102634	11:49:01.2	-00:19:07.2	6.15	4.92	6215 ± 44^{5}	CHIRON	2015-01-17	5.18
GJ 465	12:24:52.5	-18:14:32.2	11.27	6.95	3472 ± 110^{6}	CHIRON	2015-01-17	65.00
HD 115617	13:18:24.3	-18:18:40.3	4.74	2.96	5558 ± 19^{2}	CHIRON	2015-01-17	1.32
HD 125072	14:19:04.8	-59:22:44.5	6.66	4.33	4903 ± 44^{5}	CHIRON	2015-02-11	9.14
HD 128621	14:39:35.0	-60:50:15.0	1.33	-0.60	5232 ± 8^{3}	CHIRON	2015-02-06	0.03
HD 154363	17:05:03.3	-05:03:59.4	7.71	4.73	4723 ± 89^{2}	CHIRON	2015-03-12	26.27
HD 157881	17:25:45.2	+02:06:41.1	7.56	4.14	4124 ± 60^{7}	CHIRON	2015-03-13	25.86
HD 165222	18:05:07.5	-03:01:52.7	9.36	5.31	3416 ± 40^{7}	CHIRON	2015-02-11	3.83
HD 225239	00:04:53.7	+34:39:35.2	6.11	4.44	5699 ± 80^{8}	HRS	2002-09-18	8.00
HD 3651	00:39:21.8	+21:15:01.7	5.88	4.00	5046 ± 86^{3}	HRS	2005-07-30	3.00
HD 16895	02:44:11.9	+49:13:42.4	4.11	2.78	6344 ± 44^{5}	HRS	2006-12-02	0.11
HD 38529	05:46:34.9	+01:10:05.4	5.94	4.21	5697 ± 44^{5}	HRS	2004-12-02	0.55
GJ 270	07:19:31.2	+32:49:48.3	10.05	6.38	3668 ± 54^{9}	HRS	2002-12-11	20.00
HD 58855	07:29:55.9	+49:40:20.8	5.36	4.18	6398 ± 80^{8}	HRS	2006-03-12	0.50
GJ 281	07:39:23.0	+02:11:01.1	9.59	5.87	3776 ± 145^{10}	HRS	2003-01-19	20.00
HD 69056	08:15:33.2	+11:25:51.4	7.70	6.06	5635 ± 55^{8}	HRS	2003-12-02	13.00
HD 73732	08:52:35.8	+28:19:50.9	5.95	4.01	5235 ± 44^{5}	HRS	2003-10-15	3.33
GJ 328	08:55:07.5	+01:32:56.4	9.98	6.35	3828 ± 168^{10}	HRS	2003-01-14	20.00
HD 79969	09:17:53.4	+28:33:37.8	7.21	4.77	4825 ± 8^{11}	HRS	2003-12-02	10.00
HIP 53070	10:51:28.1	+20:16:38.9	8.22	6.83	6110 ± 76^{8}	HRS	2009-02-14	20.00
HIP 53169	10:52:36.4	-02:06:33.5	9.82	7.05	4525 ± 47^{12}	HRS	2009-01-09	15.00
GJ 411	11:03:20.1	+35:58:11.5	7.52	3.34	3464 ± 15^{13}	HRS	2001-12-27	5.00
HD 114783	13:12:43.7	-02:15:54.1	7.55	5.47	5135 ± 44^{5}	HRS	2005-01-08	7.08
GJ 525	13:45:05.0	+17:47:07.5	9.75	6.22	3680 ± 150^{14}	HRS	2008-04-21	15.00
GJ 535	13:59:19.4	+22:52:11.1	9.04	6.24	4580 ± 7^{11}	HRS	2002-04-29	12.16
HD 142267	15:53:12.0	+13:11:47.8	6.12	4.53	5756 ± 44^{5}	HRS	2002-08-11	2.08
GJ 687	17:36:25.8	+68:20:20.9	9.15	4.55	3413 ± 28^{13}	HRS	2002-04-30	12.50
GJ 699	17:57:48.4	+04:41:36.2	9.51	4.52	3222 ± 10^{13}	HRS	2002-05-25	15.00

Table 2.2: - (Continued)

Star	RA	DEC	V	K	$T_{\rm eff}$ (K)	Instrument	Date	Exp. Time (min)
GJ 699	17:57:48.4	+04:41:36.2	9.51	4.52	3222 ± 10^{13}	HRS	2002-05-25	35.00
GL 15A	00:18:22.8	+44:01:22.6	8.13	4.02	3567 ± 11^{13}	IGRINS	2014-11-23	4.00
GL 15B	00:18:25.4	+44:01:37.6	11.04	5.95	3218 ± 60^{7}	IGRINS	2014-11-23	8.00
HD 1835	00:22:51.7	-12:12:33.9	6.39	4.86	5837 ± 44^{5}	IGRINS	2014-12-07	8.00
HD 4614	00:49:06.2	+57:48:54.6	3.44	1.99	5973 ± 8^{3}	IGRINS	2014-12-06	0.67
HD 10476	01:42:29.7	+20:16:06.6	5.24	3.25	5242 ± 12^{3}	IGRINS	2014-11-18	2.67
GL 1094	07:02:42.9	-06:47:57.2	8.35	5.76	4698 ± 91^{2}	IGRINS	2014-11-24	6.00
HD 58946	07:29:06.7	+31:47:04.3	4.18	2.98	6597 ± 18^{3}	IGRINS	2015-01-20	0.83
HD 67767	08:10:27.1	+25:30:26.4	5.73	3.84	5344 ± 44^{5}	IGRINS	2015-01-20	1.50
HD 71148	08:27:36.7	+45:39:10.7	6.30	4.83	5818 ± 44^{5}	IGRINS	2015-01-20	4.67
HD 76151	08:54:17.9	-05:26:04.0	6.00	4.46	5788 ± 23^{2}	IGRINS	2014-11-23	8.00
HD 87141	10:04:36.3	+53:53:30.1	5.72	4.50	6401 ± 80^{8}	IGRINS	2015-01-23	4.67
HD 87822	10:08:15.8	+31:36:14.5	6.24	5.13	6586 ± 80^{8}	IGRINS	2015-01-23	26.67
HD 91752	10:36:21.4	+36:19:36.9	6.30	5.20	6543 ± 80^{8}	IGRINS	2015-01-20	24.00
HD 95128	10:59:27.9	+40:25:48.9	5.04	3.75	5882 ± 44^{5}	IGRINS	2015-01-23	4.00
HD 95735	11:03:20.1	+35:58:11.5	7.52	3.34	3464 ± 15^{13}	IGRINS	2015-01-23	2.00
BS 5019	13:18:24.3	-18:18:40.3	4.74	2.96	5558 ± 19^{2}	IGRINS	2015-01-06	6.00
HD 119850	13:45:43.7	+14:53:29.4	8.50	4.41	3618 ± 31^{13}	IGRINS	2015-01-27	2.00
HD 122120	13:59:19.4	+22:52:11.1	9.04	6.24	4580 ± 7^{11}	IGRINS	2015-01-27	6.00
HD 122652	14:02:31.6	+31:39:39.0	7.15	5.88	6093 ± 44^{5}	IGRINS	2015-01-27	4.00
GJ 570A	14:57:28.0	-21:24:55.7	5.72	3.10	4507 ± 58^{13}	IGRINS	2014-05-27	1.33
GJ 576	15:04:53.5	+05:38:17.1	9.81	6.47	4450 ± 100^{15}	IGRINS	2015-01-27	6.00
GJ 758	19:23:34.0	+33:13:19.0	6.36	4.49	5453 ± 44^{5}	IGRINS	2014-10-10	3.00
GJ 820 A	21:06:53.9	+38:44:57.9	5.21	2.68	4361 ± 17^{13}	IGRINS	2014-12-05	0.67
GJ 820 B	21:06:55.2	+38:44:31.4	6.03	2.32	3932 ± 25^{13}	IGRINS	2014-12-05	0.67
HD 220339	23:23:04.8	-10:45:51.2	7.80	5.59	5029 ± 52^{2}	IGRINS	2014-12-07	13.00
HIP 117473	23:49:12.5	+02:24:04.4	8.99	5.04	3646 ± 60^{7}	IGRINS	2014-11-24	4.00
HD 4614	00:49:06.2	+57:48:54.6	3.44	1.99	5973 ± 8^{3}	TS23	1998-07-16	2.50
HD 10700	01:44:04.0	-15:56:14.9	3.50	1.68	5290 ± 39^{3}	TS23	1998-07-16	3.00
GJ 74	01:46:38.7	+12:24:42.3	8.89	6.32	4638 ± 72^{12}	TS23	2008-04-12	20.00
HD 22049	03:32:55.8	-09:27:29.7	3.73	1.67	5077 ± 35^{13}	TS23	2000-09-22	1.67
HR 1287	04:10:49.8	+26:28:51.4	5.40	4.48	6912 ± 80^{8}	TS23	2008-03-30	5.00
HD 30652	04:49:50.4	+06:57:40.5	3.19	2.05	6414 ± 19^{3}	TS23	1998-11-03	1.00
HD 40590	05:59:51.5	+00:03:21.4	8.07	6.91	6528 ± 75^{8}	TS23	2004-02-03	21.67
HR 3538	08:54:17.9	-05:26:04.0	6.00	4.46	5788 ± 23^{2}	TS23	2000-01-15	15.00
GJ 380	10:11:22.1	+49:27:15.2	6.61	3.26	4085 ± 14^{13}	TS23	2012-10-02	13.33
GJ 411	11:03:20.1	+35:58:11.5	7.52	3.34	3464 ± 15^{13}	TS23	2008-03-27	10.00
61 Vir	13:18:24.3	-18:18:40.3	4.74	2.96	5558 ± 19^{2}	TS23	2000-01-12	12.00
70 Vir	13:28:25.8	+13:46:43.6	4.97	3.24	5406 ± 64^{3}	TS23	1998-07-14	8.00
HD 142860	15:56:27.1	+15:39:41.8	3.84	2.62	6222 ± 13^{3}	TS23	1998-07-14	2.50
GJ 699	17:57:48.4	+04:41:36.2	9.51	4.52	3222 ± 10^{13}	TS23	2000-05-24	35.00
70 Oph A	18:05:27.3	+02:29:59.3	4.20	1.79	5407 ± 52^{13}	TS23	1998-07-14	3.00
16 Cyg A	19:41:48.9	+50:31:30.2	5.95	4.43	5750 ± 57^{3}	TS23	2005-10-12	6.67
16 Cyg B	19:41:51.9	+50:31:03.0	6.20	4.65	5678 ± 66^{3}	TS23	2002-09-21	13.33
61 Cyg B	21:06:55.2	+38:44:31.4	6.03	2.32	3932 ± 25^{13}	TS23	1998-07-14	10.00

Table 2.2: - (Continued)

Star	RA	DEC	V	K	$T_{\rm eff}$ (K)	Instrument	Date	Exp. Time (min)
GJ 864	22:36:09.6	-00:50:30.0	9.92	6.16	3916 ± 61^{7}	TS23	2002-11-22	25.00
HD 216625	22:54:07.4	+19:53:31.3	7.02	5.73	6212 ± 44^{5}	TS23	2001-07-25	20.00

Table 2.3: Known Binary Stars.
The spectral types are from the Simbad database (Wenger et al., 2000).

Star	RA	DEC	V	K	(K)	Instrument	Date	Exp. Time (min)
HIP 1366	00:17:5.50	+38:40:53.89	A2V	4.62	4.42	TS23	2013-10-20	32.17
HIP 3300	00:42:3.90	+50:30:45.09	B2V	4.80	5.08	TS23	2013-01-07	41.49
HIP 12719	02:43:27.11	+27:42:25.72	B3V	4.64	4.97	TS23	2013-10-18	36.43
HIP 13165	02:49:17.56	+17:27:51.52	B6V	5.31	5.41	HRS	2013-08-14	13.75
HIP 15338	03:17:47.35	+44:01:30.08	B8V	5.48	5.59	HRS	2013-08-19	28.50
HIP 17563	03:45:40.44	+06:02:59.98	B3V	5.33	5.59	CHIRON	2013-09-03	126.93
HIP 22840	04:54:50.71	+00:28:1.81	B5V	5.97	6.25	TS23	2014-01-21	96.21
HIP 22958	04:56:24.19	-05:10:16.87	B6V	5.49	5.79	CHIRON	2013-09-16	140.00
HIP 22958	04:56:24.19	-05:10:16.87	B6V	5.49	5.79	CHIRON	2014-10-13	32.50
HIP 24902	05:20:14.67	+41:05:10.35	A3V	5.47	5.02	IGRINS	2014-10-16	3.73
HIP 26063	05:33:31.45	-01:09:21.87	B1V	5.38	5.86	CHIRON	2013-10-17	132.88
HIP 26563	05:38:53.08	-07:12:46.18	A4V	4.80	4.42	TS23	2014-01-20	69.49
HIP 28691	06:03:27.37	+19:41:26.02	B8V	5.13	5.36	TS23	2013-01-06	66.53
HIP 33372	06:56:25.83	+09:57:23.67	B8Vn	5.91	6.08	TS23	2014-01-21	110.74
HIP 33372	06:56:25.83	+09:57:23.67	B8Vn	5.91	6.08	IGRINS	2014-10-17	5.33
HIP 44127	08:59:12.45	+48:02:30.57	A7V	3.10	2.66	TS23	2014-01-20	18.24
HIP 58590	12:00:52.39	+06:36:51.56	A5V	4.66	4.25	CHIRON	2013-02-15	41.07
HIP 65477	13:25:13.54	+54:59:16.65	A5V	4.01	···	TS23	2014-01-12	37.12
HIP 76267	15:34:41.27	+26:42:52.89	A1IV	2.21	2.21	CHIRON	2013-03-29	4.20
HIP 77516	15:49:37.21	-03:25:48.74	A0V	3.55	3.70	CHIRON	2013-03-29	14.70
HIP 77858	15:53:53.92	-24:31:59.37	B5V	5.38	5.36	CHIRON	2014-03-17	76.07
HIP 79199	16:09:52.59	-33:32:44.90	B8V	5.50	5.65	CHIRON	2014-03-18	49.49
HIP 79404	16:12:18.20	-27:55:34.95	B2V	4.57	4.98	CHIRON	2013-05-03	37.80
HIP 79404	16:12:18.20	-27:55:34.95	B2V	4.57	4.98	CHIRON	2015-02-23	21.78
HIP 79404	16:12:18.20	-27:55:34.95	B2V	4.57	4.98	CHIRON	2015-03-09	18.92
HIP 81641	16:40:38.69	+04:13:11.23	A1V	5.77	5.74	HRS	2013-04-22	16.00
HIP 84606	17:17:40.25	+37:17:29.40	A2V	4.62	4.44	IGRINS	2014-10-15	7.47
HIP 85385	17:26:49.13	+20:04:51.52	B5V	5.51	5.84	IGRINS	2014-07-10	8.00
HIP 88290	18:01:45.20	+01:18:18.28	A2Vn	4.44	4.23	CHIRON	2014-08-04	39.32
HIP 91118	18:35:12.60	+18:12:12.28	A0Vn	5.79	5.67	IGRINS	2014-10-15	6.00
HIP 92027	18:45:28.36	+05:30:0.44	A1V	5.83	5.66	HRS	2013-04-23	18.00
HIP 92728	18:53:43.56	+36:58:18.19	B2.5V	5.57	5.99	HRS	2013-04-23	14.00
HIP 98055	19:55:37.79	+52:26:20.21	A4Vn	4.92	4.49	TS23	2013-10-21	42.82
HIP 100221	20:19:36.72	+62:15:26.90	B9V	5.71	5.71	HRS	2013-08-19	43.70
HIP 106786	21:37:45.11	-07:51:15.13	A7V	4.69	4.25	CHIRON	2014-05-17	23.75
HIP 106786	21:37:45.11	-07:51:15.13	A7V	4.69	4.25	IGRINS	2014-10-15	3.73
HIP 106786	21:37:45.11	-07:51:15.13	A7V	4.69	4.25	TS23	2014-11-01	19.99
HIP 113788	23:02:36.38	+42:45:28.06	A3Vn	5.10	4.69	TS23	2013-10-21	47.51
HIP 116247	23:33:16.62	-20:54:52.22	A0V	4.71	4.52	CHIRON	2013-06-20	42.93
HIP 116611	23:37:56.80	+18:24:2.40	A1Vn	5.48	5.42	IGRINS	2014-10-16	4.20

Table 2.4: Literature Spectroscopic Data.
Known binary stars with spectroscopic orbit solutions. The orbital data is from the SB9 database (Pourbaix et al., 2004), and the original references are provided as superscripts after the star names: [1]: Hill et al. (1971); [2]: Lloyd (1981); [3]: Rucinski et al. (2005); [4]: Abt & Levy (1978) [5]: Pourbaix et al. (2004); [6]: Morrell & Abt (1992); [7]: Abt et al. (1990); [8]: Fekel & Tomkin (1982); [9]: Lucy & Sweeney (1971); [10]: Pogo (1928); [11]: Duerbeck (1975); [12]: Abt (1965); [13]: Scarfe et al. (2000); [14]: Tomkin & Popper (1986); [15]: Levato et al. (1987); [16]: Richardson & McKellar (1957); [17]: Leone & Catanzaro (1999); [18]: Hube (1973); [19]: Pearce (1936)

Star	K_1 (km s^{-1})	K_2 (km s^{-1})	Period (days)
HIP 3300[4]	11.90	···	940.20
HIP 12719[4]	8.80	···	490.00
HIP 13165[5]	24.80	···	3.85
HIP 15338[6]	20.00	···	36.50
HIP 17563[7]	26.80	···	1.69
HIP 22840[7]	24.50	···	24.10
HIP 26063[11]	13.50	···	119.09
HIP 26563[12]	28.60	···	445.74
HIP 28691[13]	12.22	···	4741.10
HIP 44127[12]	6.00	···	4028.00
HIP 58590[12]	26.20	···	282.69
HIP 76267[14]	35.40	99.00	17.36
HIP 77858[15]	32.90	···	1.92
HIP 79404[15]	31.50	···	5.78
HIP 85385[7]	17.10	···	8.96
HIP 92728[16]	39.70	···	88.35
HIP 100221[18]	49.70	···	5.30
HIP 106786[12]	11.30	···	8016.00
HIP 116611[3]	25.19	···	0.50

Table 2.5: Literature Image Data.
Known binary stars detected through either high-contrast imaging or interferometry. The imaging data comes from the Washington Double Star Catalog (Mason et al., 2014), and the most recent measurements are given as superscripts to the star name: [1]: McAlister et al. (1989); [2]: Roberts et al. (2007); [3]: ESA (1997); [4]: Mamajek et al. (2010); [5]: Drummond (2014); [6]: Shatsky & Tokovinin (2002); [7]: Tokovinin et al. (2010); [8]: McAlister et al. (1987); [9]: Horch et al. (2010); [10]: Horch et al. (2008); [11]: Horch et al. (2001); [12]: De Rosa et al. (2012)

	Separation		Wavelength
Star	($''$)	(Δm)	(nm)
HIP 1366[1]	0.06	···	549
HIP 22958[3]	0.65	4.15 ± 0.14	511
HIP 24902[3]	0.38	2.97 ± 0.06	511
HIP 33372[3]	0.75	3.27 ± 0.04	511
HIP 65477[4]	1.11	5.18 ± 0.07	4770
HIP 77516[5]	0.20	1.70 ± 0.05	780
HIP 79199[6]	1.12	4.62 ± 0.12	1250
HIP 81641[7]	0.04	1.90 ± 0.00	551
HIP 84606[3]	0.84	4.02 ± 0.08	511
HIP 88290[3]	0.58	2.95 ± 0.04	511
HIP 91118[8]	0.16	···	549
HIP 92027[9]	0.17	1.53 ± 0.00	550
HIP 98055[10]	0.10	0.51 ± 0.00	550
HIP 113788[3]	0.39	2.17 ± 0.02	511
HIP 116247[11]	0.84	2.43 ± 0.15	541
HIP 116611[12]	0.95	5.93 ± 0.09	2169

Table 2.6: Companion Data.

	Measured Values			Expected Values	
Primary Star	$T_{\rm eff}$ (K)	[Fe/H] (dex)	vsini (km s^{-1})	$T_{\rm eff}$ (K)	$v \sin i$ (km s^{-1})
HIP 13165	5770 ± 162	-0.5	5	···	···
HIP 22958	6070 ± 112	-0.5	30	6240^{+579}_{-409}	11^{+16}_{-8}
HIP 24902	5680 ± 154	0.0	30	5950^{+34}_{-84}	4^{+3}_{-3}
HIP 33372	···	···	···	6955^{+238}_{-550}	12^{+16}_{-8}
HIP 65477	···	···	···	3861^{+34}_{-11}	2^{+3}_{-1}
HIP 76267	5450 ± 158	-0.5	5	5670^{+193}_{-281}	3^{+4}_{-2}
HIP 77516	6820 ± 141	0.5	5	6600^{+530}_{-167}	12^{+17}_{-8}
HIP 79199	4620 ± 158	-0.5	5	4800^{+484}_{-484}	6^{+7}_{-4}
HIP 79404	4770 ± 112	-0.5	10	···	···
HIP 81641	···	···	···	6475^{+126}_{-96}	10^{+12}_{-7}
HIP 84606	5480 ± 154	0.0	10	5450^{+71}_{-45}	3^{+3}_{-2}
HIP 88290	···	···	···	5847^{+41}_{-24}	4^{+4}_{-3}
HIP 91118	6490 ± 154	-0.5	10	···	···
HIP 92027	···	···	···	6752^{+315}_{-96}	12^{+16}_{-8}
HIP 98055	···	···	···	7366^{+391}_{-113}	13^{+18}_{-9}
HIP 113788	···	···	···	6276^{+34}_{-92}	7^{+6}_{-4}
HIP 116247	···	···	···	6351^{+482}_{-218}	8^{+10}_{-6}
HIP 116611	···	···	···	3842^{+103}_{-50}	2^{+4}_{-1}

Chapter Three: Correcting for Telluric Absorption: Methods, Case Studies, and the TelFit Code[1]

3.1 Introduction

All ground-based astronomical spectra suffer from contamination by the Earth's atmosphere, which introduces so-called telluric lines into the spectrum. The wavelength of the telluric lines change very slightly with wind along the line of sight and pressure shifts in water lines, and the relative line strength can vary a great deal with the observatory location, weather and the airmass of the observation. The telluric lines must be removed from the spectrum to retrieve many stellar features redward of about 500 nm, which is a nontrivial task.

Often, telluric lines are removed by observing a rapidly rotating hot star (spectral type A or late B) near the same time and airmass as the target star and using it as a template for the telluric spectrum. This approach has several disadvantages: (1) it can be difficult to find a suitable standard star near the same time and airmass as the observation, so approximate corrections are made to the line strengths using Beer's law (Beer, 1852); (2) The water vapor content changes much more rapidly than the other absorbing species in the atmosphere, so scaling the whole empirical telluric spectrum is incorrect (3) the standard star has strong hydrogen and helium lines and weak metal lines that can further contaminate the science spectrum; (4) observing a standard star can take a significant amount of precious telescope time, especially for high signal-to-noise work.

A better solution is often to generate a theoretical telluric absorption spectrum from a line list and the observing conditions. Recently, several groups (Seifahrt et al., 2010; Bertaux et al., 2014; Husser & Ulbrich, 2013; Cotton et al., 2014; Gullikson & Endl, 2013) have used the LBLRTM code[2] (Clough et al., 2005, Line By Line

[1]This chapter was previously published (Gullikson et al., 2014). Both co-authors were my advisor at some point while I was developing this code. They helped guide the code requirements and provided a science case study for the work. Adam Kraus provided observational data for the case study.

[2]`http://www.rtweb.aer.com/lblrtm_description.html`

Radiative Transfer Model) for this purpose. However, the interface for the LBLRTM code can be difficult to learn, and can not directly fit an observed spectrum.

Telluric correction is vital to the work described in this thesis. In the optical, it allows us to use more of the spectrum to search for faint companions. Importantly, the red parts of the optical spectrum that are most affected by telluric contamination are where the primary-to-secondary flux ratio is smallest, and so where much of the companion-detecting power lies. Telluric correction is even more important in near-infrared spectra, where the contamination dominates at almost all wavelengths.

In this chapter we describe Telfit[3], a code that acts as a wrapper to LBLRTM and allows for easy fitting of the telluric spectrum in astronomical data. We compare the results to those obtained from empiricial telluric correction in optical echelle spectra, and find that model-fitting produces similar telluric line residuals and is in fact better for dim targets or high signal-to-noise ratio work. We only demonstrate the use of TelFit in optical spectra in this work, but note that we use it to accurately remove the telluric contamination in near-infrared spectra in Chapters 2 and 7, and use an earlier version of TelFit for near-infrared spectra in Chapter 6.

We describe the observations and data reduction used in this chapter in Section 3.2. We then describe the TelFit code and give a brief description of the telluric fitting procedure in Section 3.3. Finally, we demonstrate the use of the TelFit code to correct several optical telluric bands in Section 3.4.

3.2 Observations and Reduction

We observed representative spectra for the early and late-type stars listed in Table 3.1. The A-stars HIP 20264 and HIP 25608 were observed with the CHIRON spectrograph on the 1.5m telescope at Cerro Tololo Interamerican Observatory (CTIO). This spectrograph has a spectral resolution of $R = 80000$ from $\lambda = 460 - 860$ nm, and uses 3x1 binning along the spatial direction. The data were bias-subtracted, flat-fielded, and extracted using standard IRAF tasks. The reduced spectra were wavelength-calibrated using a ThAr lamp exposure from immediately before the observation of the star. In order to reach high a signal-to-noise ratio and avoid detector saturation, we co-added 7 spectra after reduction and telluric correction (see Section 3.3).

[3]The TelFit code documentation and installation directions can be found at `http://telfit.readthedocs.org/en/latest/`

In addition, several M-type stars were observed with the Magellan Inamori Kyocera Echelle (MIKE) optical echelle spectrograph on the Clay telescope at Magellan Observatory as spectral type standards for a study of young stars (Kraus et al., 2014). We used the $0.7''$ slit, which yields a spectral resolution of $R = 35000$ from $\lambda = 335 - 950$ nm. The pixel scale oversamples the resolution with the $0.7''$ slit, so we used 2x binning in the spatial and spectral directions. The spectra were reduced using the CarPy pipeline (Kelson, 2003)[4]. The reduced spectra were wavelength calibrated using a combination of a ThAr lamp exposure and the 760 nm telluric A band (see Kraus et al., 2014, for details).

TelFit can handle rapidly rotating early-type stars without preprocessing the spectra by fitting a Savitzky-Golay smoothing filter (Savitzky & Golay, 1964) as a pseudo-continuum for the telluric lines. For more feature-rich late-type stars, we remove an approximation to the stellar spectrum using the procedure below before fitting the telluric lines.

1. Make an initial guess telluric spectrum with TelFit. The guess spectrum intentionally has slightly higher molecular mixing ratios than the correct values so that it over-corrects the telluric lines.

2. Divide the observed spectrum by the guess telluric spectrum. This leaves a spectrum with stellar lines in absorption and telluric residuals appearing like emission lines.

3. Find the best-fit stellar model to the absorption lines using a grid of PHOENIX model spectra (Hauschildt et al., 1999) with effective temperature and log(g) near the expected values for the star.

4. Divide the original data (before the telluric over-correction in step 1) by the best-fit normalized stellar spectrum. This leaves a spectrum that is mostly telluric lines, but which may have strong stellar line residuals.

5. Enumerate the wavelength ranges that are strongly affected by stellar line residuals, and tell TelFit to ignore them. We ignored all wavelengths from 817.5 - 820 nm in our M-star spectra, which have strong residuals from the sodium lines.

[4] `http://code.obs.carnegiescience.edu/mike`

The fit to the primary star does not need to be perfect. Indeed, if we could perfectly model stellar spectra there would be little reason to observe them! The purpose of the preprocessing described above is to ensure that telluric lines dominate the spectrum before fitting. Any strong residuals from that process can and should be ignored in the telluric fit. While a physically better solution would be to fit the stellar and telluric spectra simultaneously, the method described above will often work well enough for most purposes and is much faster than a simultaneous fit.

3.3 Telluric Fitting Method

The TelFit code performs a least-squares fit using a constrained Levenberg-Marquardt algorithm (Marquardt, 1963). It is extremely flexible; the user can decide which atmospheric parameters to fit, which spectral regions to use in the fit, how the detector point spread function (PSF) is modeled, the order of the continuum fit used in each iteration, and whether the data wavelengths are calibrated to fit the model or vice versa. The algorithm will optimize the fitting variables, as well as the detector resolution and the wavelength solution. LBLRTM requires an atmosphere profile giving the temperature, pressure, and the abundance of several molecules as a function of height. We provide a default atmosphere profile[5] with the TelFit code that is acceptable for mid-latitude observatories, but provide the ability to easily give an alternate atmosphere profile for more accurate results.

While TelFit explicitly fits the temperature, pressure, and abundances at the observatory altitude, it scales the quantities at *all* atmosphere layers. For the pressure and temperature, it finds the difference between the requested pressure (temperature) at the requested altitude, and the pressure (temperature) in the atmosphere profile. If P_r is the requested pressure at altitude z, and the atmosphere profile pressure is P_0 at that altitude, then the pressure P_i at each atmosphere layer z_i is scaled as

$$P_i \rightarrow P_i - (P_r - P_0)e^{\frac{-(z_i - z)^2}{2\cdot(10\text{km})^2}}$$

The temperature is scaled in the same way as the pressure above, and is done in this way so that the quantities more than about 10 km above the observatory are

[5]The default atmosphere profile was developed for the Michelson Interferometer for Passive Atmospheric Sounding (MIPAS) spacecraft, are is available from `http://www-atm.physics.ox.ac.uk/RFM/atm/`

Table 3.1: Observations used in this paper.

Star	R (mag)	K_s (mag)	SpT	UT date yyyymmdd	Spectrograph	SNR @820 nm
GJ 83.1	10.94	6.65	M4.6	20120902	MIKE	200
GJ 109	9.49	5.961	M3.0	20120902	MIKE	219
GJ 173	9.33	6.09	M1.6	20130203	MIKE	166
GJ 273	8.70	4.86	M3.6	20130204	MIKE	215
GJ 447	9.86	5.65	M4.0	20130203	MIKE	324
GJ 581	9.46	5.84	M2.6	20130202	MIKE	336
GJ 628	8.92	5.08	M3.0	20120716	MIKE	346
GJ 908	8.03	5.04	M1.0	20120717	MIKE	328
HD 33793	7.90	5.05	M1.0	20130203	MIKE	315
HIP 20264	5.38	5.33	A0.0	20140301	CHIRON	167
HIP 25608	5.54	5.50	A1.0	20140301	CHIRON	214

effectively unchanged. The mixing ratio of all molecules is scaled in a much simpler way: if A_r is the requested mixing ratio at the telescope altitude, and A_0 is the mixing ratio in the atmosphere profile, the mixing ratio at each layer A_i is given by

$$A_i \rightarrow A_i \frac{A_r}{A_0}$$

Because of the way TelFit scales the temperature, pressure, and molecular mixing ratios in every atmosphere layer, the optimized values should not be taken as a measurement of the actual surface mixing ratios.

In each iteration for the main variables (temperature, pressure, telescope zenith angle, and molecular abundances), TelFit refines the wavelength solution and detector resolution. The wavelength fitter performs a third-order polynomial fit to adjust the wavelengths of the model such that the telluric lines match the data. Alternatively, the data wavelengths can be adjusted to fit the model. The wavelength solution of the data should be very close, as TelFit will not shift any wavelengths by more than 0.1 nm. By default, TelFit fits the spectrograph PSF as a gaussian, and fits the detector resolution by finding the best gaussian width to convolve the model against. Alternatively, TelFit can do a nonparametric fit to the spectrograph PSF using the singular value decomposition described in detail in Rucinski (1999)

3.4 Results

We fit the spectra for the rapidly-rotating A0V star HIP 20264 with a two-step approach. In the first step, we fit the observatory temperature and humidity in the echelle orders dominated by the water bands at 590 nm, 650 nm, 700 nm, and 730 nm. For the rest of the fit, the humidity and temperature were fixed at the χ^2-weighted average of the fits for each band. Next, we fit the O_2 abundance with the γ and B bands near 630 nm and 690 nm, respectively. Because the blue end of the B band is extremely strong and absorbs nearly all the light, we only use the red half in the fit. The O_2 abundance was fixed at the χ^2-weighted average of the individual fitted values for the two echelle orders. We then applied the best-fit parameters to every echelle order, allowing the fitter to adjust the model wavelengths and detector resolution separately for each order. For all telluric fits in this paper, we adjusted the temperature, pressure, and water vapor atmosphere profile with sounding data from the Global Data Assimilation System (GDAS) meteorological archive[6]. As stated in Section 3.2, we fit each frame of HIP 20264 separately, and co-added the telluric-corrected spectra. The fitted value of the relative humidity varied from 18.7% to 22.1%, and the airmass of the star increased from 1.15 to 1.52 (a change of 19° in zenith angle) over the course of the 7 frames, making the individual fits crucial.

We show the telluric correction for the observation of the A0V star HIP 20264 in four water bands and two O_2 bands in Figures 3.1 and 3.2, respectively. The telluric model shown is the average telluric model of the 7 individual exposures, since we corrected each one separately to better account for the changing water vapor content and telescope zenith angle. We apply a Savitzky-Golay smoothing filter to the corrected data to remove any broad features in the stellar spectrum. The water features are corrected to near the noise level of the spectrum, with the exception of the very strong telluric water band near 730 nm. The poor correction may be due to a slightly incorrect temperature and water-vapor atmospheric profile, which causes the line profile to change appreciably for strong lines. In addition, small errors in the line strength parameters are more noticable for strong telluric lines. The correction in the O_2 B and γ bands (Figure 3.2) is somewhat worse. The same O_2 mixing ratio undercorrects the γ band and slightly overcorrects the B band. This systematic error

[6]The GDAS archive is available starting in December 2004 at `http://ready.arl.noaa.gov/READYamet.php`. Instructions for its use are included in the code documentation.

may be from incorrect line strengths in the HITRAN database for the two bands.

We observed the A1V star HIP 25608 30 minutes after HIP 20264 and at similar airmass, and so use it as a telluric standard star to directly compare our method to the empirical telluric correction method. To have comparable S/N ratios as in Figures 3.1 and 3.2, we co-added all 7 frames of both the the target star (HIP 20264) and the standard star (HIP 25608). We account for the different column density of absorbers in the target and standard star observations using Beer's law (Beer, 1852) as follows. For each order, we scaled the normalized flux of the standard star (f_s) with

$$f_s \rightarrow f_s^{\gamma} \tag{3.1}$$

where γ is determined using the normalized flux of the standard star and target star (f_t) and is defined as

$$\gamma = \text{median}\left(\frac{\log f_t}{\log f_s}\right) \tag{3.2}$$

In Equation 3.2, we only use the points with $f_t < 0.95$ in the median computation, so that the noise does not dominate in the orders with few telluric lines. These empirical telluric corrections are shown in the top row of Figure 3.3. The corrections are quite poor in this case, mostly because the airmass of the target (standard) star changes from 1.15-1.52 (1.31-1.86) from the first to last frame, and co-adding the spectra amounts to a flux-weighted average over airmass that the correction in Equation 3.1 cannot capture.

We also test an empirical telluric correction using only the last frame of the target star and the first frame of the standard star, and show the result in the bottom row of Figure 3.3. In this case, the airmass can be treated as approximately constant and Equation 3.1 does a much better job in accounting for the small airmass difference between the target and standard star spectra, with the exception of the nearly saturated oxygen lines (bottom left panel). The water line correction results in similar line residual amplitudes to the telluric modeling method (see Figure 3.1 for comparison).

We now turn to a more typical-use case for the TelFit code: correcting the telluric lines in late-type stars near a feature of interest. For this, we use a series of M-type stars (see Table 3.1) with observations near the 819 nm sodium doublet, which is

used as a gravity-sensitive age indicator for late-type stars (Slesnick et al., 2006). As the stellar age and therefore surface gravity increases, the line strength increases. Amongst main sequence M-stars, later spectral types have higher surface gravity and so we expect the equivalent width of the sodium lines to increase as we go towards later spectral types.

Figure 3.4 shows the telluric correction for the M1V star GJ 908. For this and all M-star spectra in this work, we fit the water vapor, temperature, and O_2 mixing ratio at the same time for the spectral order covering 819 nm. The bottom panel of Figure 3.4 shows that each of the spectral lines after telluric correction come from the star itself, and that the telluric contamination is reduced to near the noise level of the spectrum. Importantly, the telluric lines that fall within the sodium doublet line profile no longer affect the profile shape. We can now directly compare the line profile of the sodium doublet lines as a function of spectral type, without the influence of telluric lines. Figure 3.5 shows the evolution of the doublet lines. The central depth stays about the same throughout the sequence, but the later spectral type stars show significantly broader line wings, leading to the known sequence in equivalent width (Slesnick et al., 2006). The robust recovery of the sodium line strengths and profiles demonstrate that TelFit can accurately remove telluric lines, even in feature-rich spectra.

3.5 Conclusions

We presented the TelFit code, an object-oriented Python code capable of accurately fitting the telluric spectrum in ground-based spectra. We use a high signal-to-noise ratio echelle spectrum of the A0V star HIP 20264 to demonstrate the fit quality in Figures 3.1 and 3.2. Contrary to expectation, the water lines are typically fit to much higher precision than the O_2 telluric lines. This is likely coming from a systematic error in the HITRAN line strength database, since the same O_2 mixing ratio overfits the B band and underfits the γ band. We compare our code to an empirical telluric correction of HIP 20264, and find that the model is at least as accurate. In fact, TelFit is significantly more accurate than the empirical method when several frames of both the target and standard star are co-added.

We also demonstrated the use of TelFit for in-depth analysis of spectral features in

late-type stars with a series of M-star observations near the 819 nm sodium doublet. The telluric lines were removed to near the noise level of the observations, allowing for analysis of the sodium line profiles and recovery of the known sequence of increasing equivalent width with later spectral types. Regions contaminated by telluric lines are often ignored in optical spectral analysis; accurate correction of telluric features could help open these regions up for further analysis.

This code was mostly developed and tested for correction of optical spectra. However, an early version of this code was used in Gullikson & Endl (2013) to correct for telluric methane absorption in B-star spectra, with similar line residuals to those that Seifahrt et al. (2010) found in the same spectral region. We encourage the use of TelFit for correcting telluric absorption in near-infrared as well as optical data.

We would like to thank Andreas Seifahrt for his help in the early stages of code development. This project was funded by a UT Austin Hutchinson fellowship to Kevin Gullikson and start-up funding to Sarah Dodson-Robinson from the University of Texas. This work makes use of Astropy, a community-developed core Python package for Astronomy (Astropy Collaboration et al., 2013), as well as SciPy, NumPy (Oliphant, 2007), and of course LBLRTM. We would like to thank the developers of all of those packages.

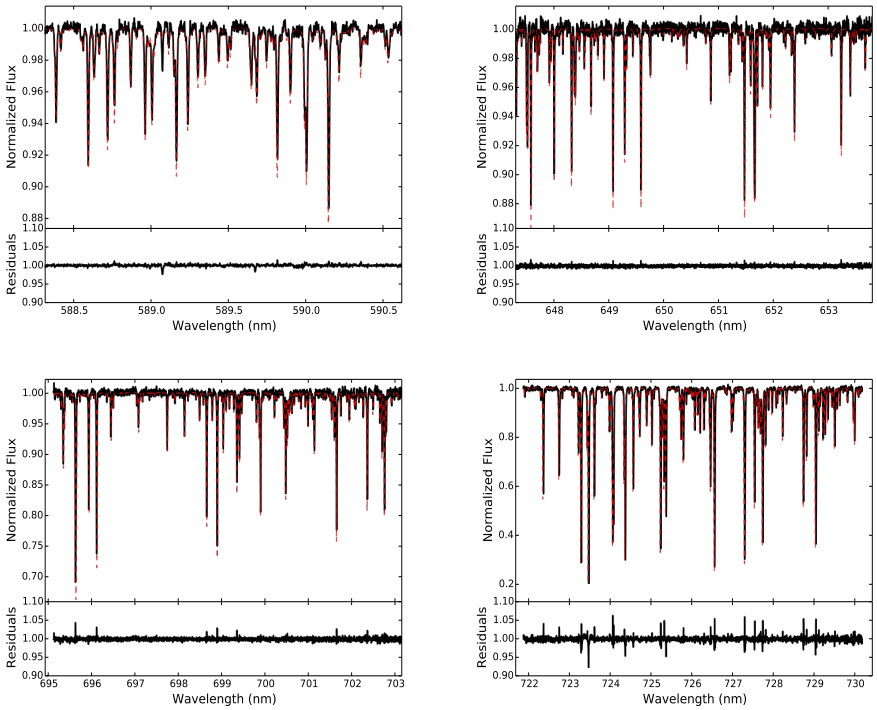

Figure 3.1: Correction of the water bands in optical spectra. All spectra are of the A0V star HIP 20264, and are smoothed with a Savitzky-Golay filter after telluric correction to remove any broad features in the stellar spectrum. The top panel of each figure shows the observed spectrum (black solid line) and the best-fit telluric model (red dashed line), and the bottom panel shows the residuals after division by the telluric model. The telluric water lines are corrected to very near the noise level of the spectrum in the top row, revealing weak interstellar Na D lines (top left). The telluric correction leaves residuals on the order of 5% of the continuum for strong telluric lines (bottom right), possibly due to an incorrect atmosphere profile for water vapor.

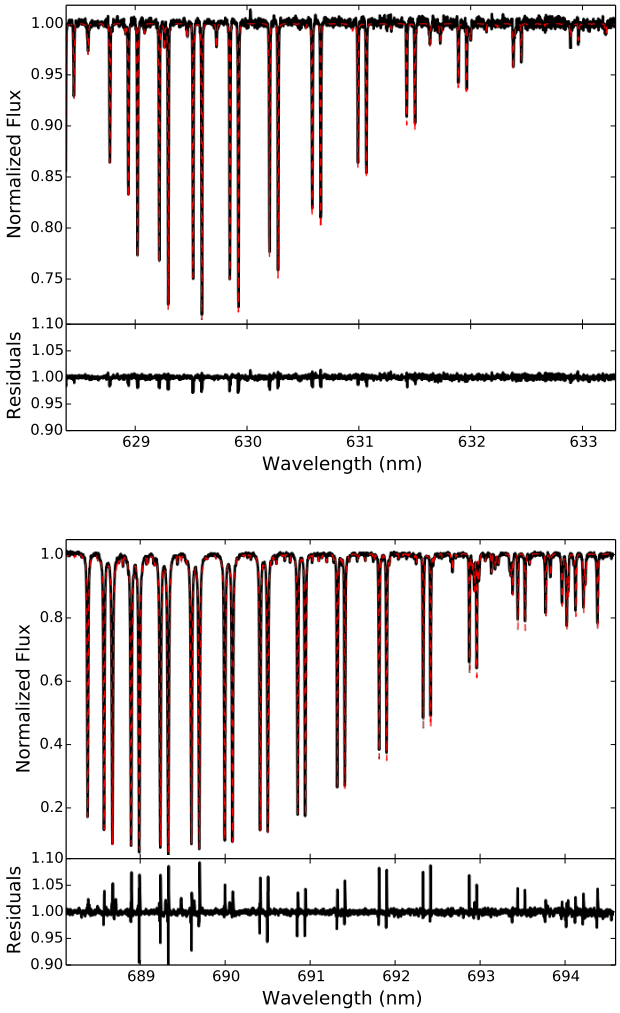

Figure 3.2: Correction of the O_2 bands in optical spectra. All spectra are of the A0V star HIP 20264, and are smoothed with a Savitzky-Golay filter after telluric correction to remove any broad features in the stellar spectrum. The top panel of each figure shows the observed spectrum (black solid line) and the best-fit telluric model (red dashed line), and the bottom panel shows the residuals after division by the telluric model.

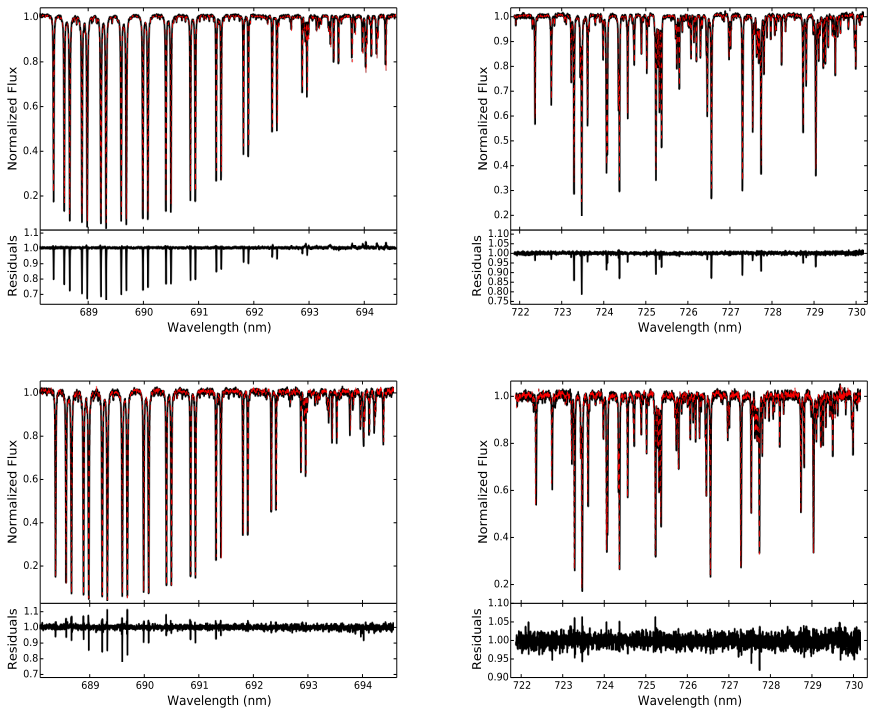

Figure 3.3: Empirical telluric corrections. *Top Row*: Correction at high S/N ratio, where all 7 frames of both the target star (HIP 20264, A0V) and the telluric standard star (HIP 25608, A1V) were co-added before the telluric correction. In this case, both the humidity and the airmass are changing throughout both exposures and the empirical telluric correction is very poor. *Bottom Row*: Correction between the last frame taken of the target star and the first frame of the standard star, a more common mode of empirical correction. In this case, the empirical telluric correction is comparable to the model fitting method presented in this paper. The left column should be compared to the bottom panel in Figure 3.2, and the right column should be compared to the bottom right subfigure in Figure 3.1. The poor correction in the oxygen band (lower left panel) is the result of the slight airmass difference between the science and standard stars. The correction in equation 3.1 is only valid for weak or moderate lines, and does not work as well for the nearly saturated lines shown here. The empirical correction under-corrects the line core while over-correcting the wings.

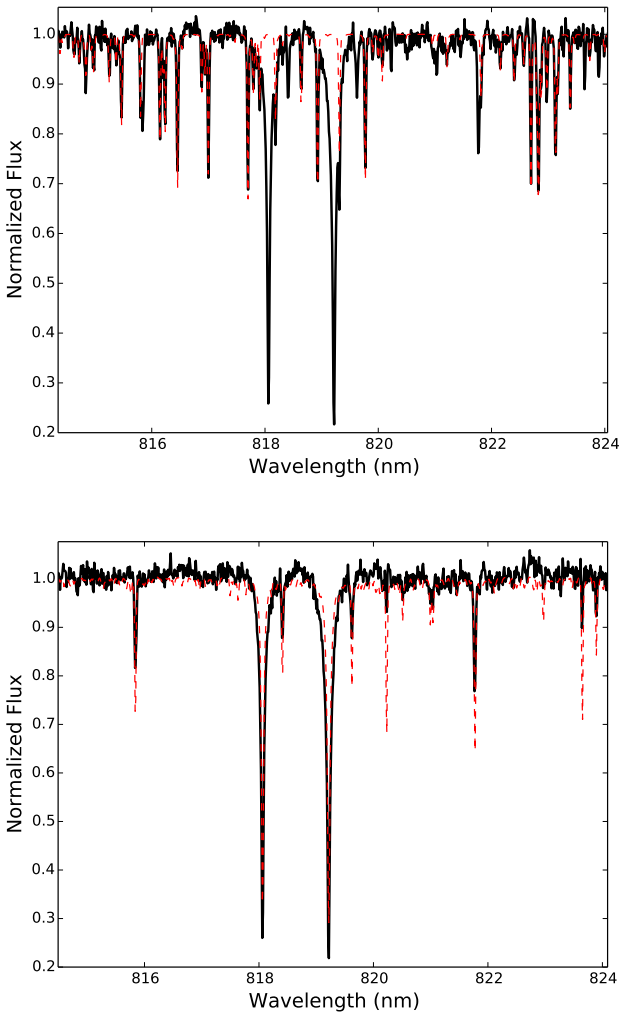

Figure 3.4: *Top*: The observed spectrum of GJ 908 (black solid line) with the best-fit telluric spectrum (red dashed line) overplotted. There are telluric lines within the sodium doublet line profiles which affect any line shape measurements if they are not corrected. *Bottom*: The telluric-corrected spectrum of GJ 908 (black solid line) with a PHOENIX model spectrum (red dashed line) overplotted to guide the eye. The model spectrum has the following parameters: $T_{\rm eff} = 3700K$, $\log g = 4.0$, and [Fe/H] $= -0.5$, and has been convolved with a gaussian to match the detector resolution. All of the remaining absorption lines in the spectrum come from the star.

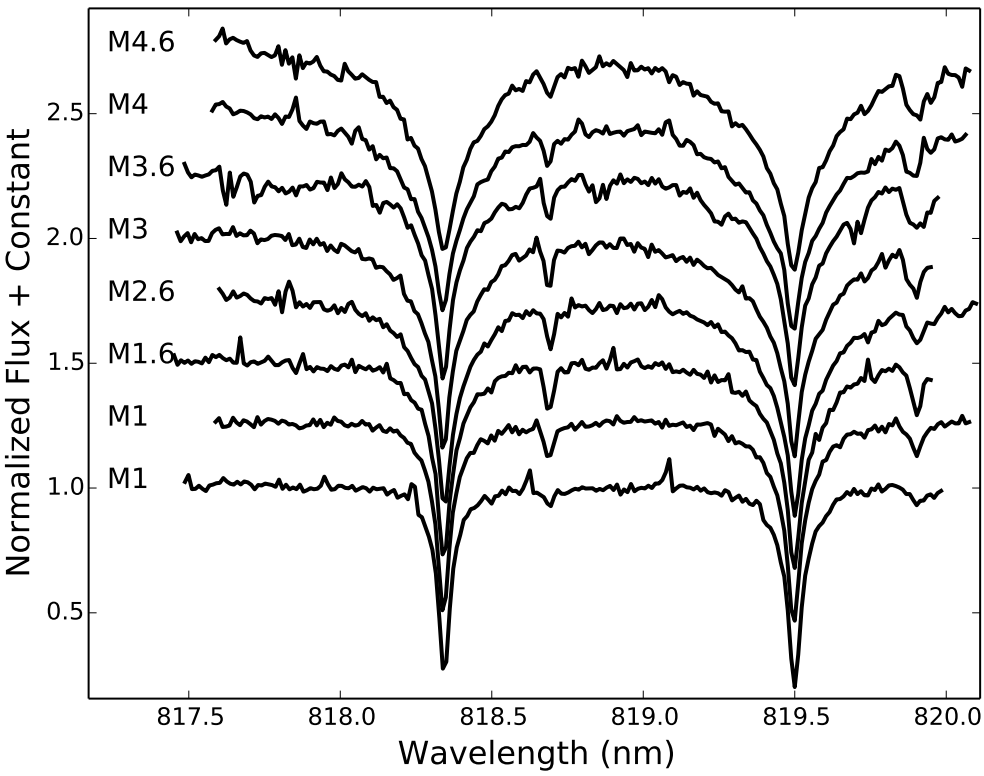

Figure 3.5: The evolution of the sodium doublet line profile with spectral type for a series of main-sequence M-type stars. The later spectral types show significantly broader line wings.

Chapter Four: Mining Planet Search Data for Binary Stars: The ψ^1 Draconis system[1]

We now turn to our first case study in using the direct spectral detection method to find a faint companion to the bright star ψ^1 Draconis. in this chapter, we use archival data originally obtained in order to search for planetary companions.

4.1 Introduction

Several groups (e.g. Wittenmyer et al., 2006; Fischer et al., 2009; Pepe et al., 2011) have used the radial velocity method to search for planets around nearby stars for well over a decade, and have collectively uncovered several hundred planets to date. Close binary stars are usually cut from the star sample because they complicate the detection method (e.g. Bergmann et al., 2015), and because they have long been suspected to inhibit planet formation by quickly destroying (Kraus et al., 2012) or depleting (Harris et al., 2012) the planet-forming disk.

Previously unknown stellar binary companions are nonetheless still uncovered in planet–search data through large–amplitude linear trends or even full long-period orbits, but may be ignored since the goal is to find planet–mass companions. Since binary stars are usually excluded in the star sample, companions that are found tend to have extreme flux- and mass-ratios. Binary stars with extreme mass-ratios on orbits with $\sim$ 10 year timescales are precisely the ones that are most difficult to detect and characterize with imaging techniques, and so they should not be ignored.

Several groups have recently worked towards using high-resolution spectroscopy to search for very faint companions to nearby stars, both in the context of detecting emission (Snellen et al., 2010; Gullikson & Endl, 2013) or reflection (Martins et al., 2013) from "Hot Jupiter" planets, and in the context of detecting stellar binary systems with high contrast ratios (e.g. Gullikson & Dodson-Robinson, 2013; Kolbl et al., 2015). Those groups all use a cross-correlation analysis to search directly for

[1]This chapter was previously published (Gullikson et al., 2015). The co-authors noticed a trend in the data, and suggested I look into it with the direct spectral detection methodology. They obtained the majority of the data used in the work.

the spectral lines of the faint companion and mainly differ in their treatment of the primary star and telluric lines. We describe one method of removing the primary star spectrum in Chapter 2; in this chapter, we describe a second method that uses orbital information to estimate an empirical primary star spectrum.

In this chapter we use data from the McDonald Observatory Planet Search team to examine the ψ^1 Draconis system, which consists of an F5IV–V star (ψ^1 Dra A) orbited by a G0V star (ψ^1 Dra B) with angular separation 30″ (Mason et al., 2014) (680 AU). Tokovinin & Smekhov (2002) searched for signs of a spectroscopic companion to ψ^1 Dra A from 1991–1995, but found no radial velocity variation. More recently Toyota et al. (2009) noted a linear trend in their radial velocity measurements, and predicted a companion with $M > 50 M_J$. Our data have a much longer time baseline than either of the previous studies, and show a significant fraction of the orbit which has recently reached quadrature. Furthermore, Endl et al. (2016) use adaptive-optics imaging to detect a $\sim 4500\ K$ companion 155 mas from ψ^1 Dra A, which they hypothesize is the source of the orbital motion seen in the primary-star radial-velocity measurements.

Here, we use all of our spectra of ψ^1 Dra A to search directly for the spectral lines of the companion and measure the system mass ratio. We describe the observations and data reduction in Section 4.2, and the method we use to search for the companion in Section 4.3. Finally, we estimate the mass-ratio of the system and give the parameters for the companion in Section 4.4.

4.2 Observations and Data Reduction

All data were taken at the 2.7 m Harlan J. Smith Telescope at McDonald observatory using the 2dcoudé échelle spectrograph (Tull et al., 1995) at a resolving power $R \equiv \frac{\lambda}{\Delta\lambda} = 60000$. The starlight was filtered through a temperature-stabilized I_2 cell to imprint many sharp absorption lines on each spectrum to use for both a precise velocity metric (Butler et al., 1996) and to model the instrument profile (Endl et al., 2000). The raw CCD data were reduced with standard IRAF[2] tasks, and include steps for overscan trimming, bad–pixel processing, bias–frame subtraction, scattered–light removal, flat–field division, order extraction, and wavelength solution fitting using a

[2]IRAF is distributed by the National Optical Astronomy Observatories, which are operated by the Association of Universities for Research in Astronomy, Inc., under cooperative agreement with the National Science Foundation.

Th–Ar calibration lamp spectrum. Particularly strong cosmic–ray hits were removed manually by interpolating across nearby pixels.

We used the *Austral* code (Endl et al., 2000) to measure the differential radial velocity of ψ^1 Dra A at each observation by comparing each spectrum to a high signal-to-noise ratio template spectrum of the same star. We provide the raw velocity measurements in Table 4.1, as well as the velocities shifted into the system velocity rest frame. The velocity shift necessary to convert from the differential radial velocities to that frame is found in Section 4.4. Table 4.1 also gives the measurements of the companion radial velocity (described in the next section).

4.3 Companion Search

We use a cross-correlation analysis inspired by recent work attempting to detect light from planetary companions around late-type stars (Gullikson & Endl, 2013; Martins et al., 2013) to search for the companion (ψ^1 Dra C). We start by dividing all spectra by the blaze function of the spectrograph, and further divide them by an empirical I_2 cell absorption spectrum in the spectral orders with $500 < \lambda < 640$ nm. The blaze function is derived by fitting a high-order polynomial to the extracted spectrum of an incandescent light source (a flat lamp), and the empirical I_2 spectrum is the spectrum of a flat lamp with the I_2 cell inserted in the light path. Both the flat lamp and I_2 spectra are observed each day of each observing run. We use the Telfit code (Gullikson et al., 2014, and Chapter 3) to fit and remove the unsaturated telluric absorption lines in the spectrum, and cross-correlate each residual spectrum against a Phoenix model spectrum (Husser & Ulbrich, 2013) with parameters

- $T_{\rm eff} = 4400$ K
- $\log g = 4.5$ (cgs units)
- [Fe/H] = 0.0

The model temperature was chosen on the basis of high–contrast imaging in Endl et al. (2016), which finds a companion with approximately that temperature. We shift each CCF so that the dominant peak, which signifies the match of the M-star model template with the F-type primary star, falls at $v = 0$. That effectively puts

Table 4.1: The velocities in the 'raw' columns are our actual measurements. Those in the 'shifted' columns are shifted into the system velocity rest frame using the results of the orbital fit described in Section 4.4.

Julian Date	Primary RV (km/s)			Secondary RV (km/s)		
	raw	shifted	σ	raw	shifted	σ
2451809.66	1.927	-2.174	0.013	···	···	···
2451809.67	1.929	-2.172	0.014	···	···	···
2452142.68	1.841	-2.259	0.012	···	···	···
2453319.64	2.433	-1.668	0.011	···	···	···
2453585.85	2.559	-1.542	0.010	···	···	···
2453585.88	2.550	-1.551	0.011	···	···	···
2453634.64	2.654	-1.446	0.011	···	···	···
2453635.62	2.554	-1.547	0.009	···	···	···
2453655.64	2.711	-1.390	0.009	···	···	···
2453655.64	2.780	-1.321	0.027	···	···	···
2453689.54	2.665	-1.436	0.008	···	···	···
2453907.85	2.960	-1.141	0.011	···	···	···
2453928.80	2.858	-1.243	0.012	···	···	···
2454019.60	2.930	-1.171	0.012	···	···	···
2454279.75	3.068	-1.033	0.011	···	···	···
2454279.76	3.056	-1.044	0.010	···	···	···
2454309.79	3.021	-1.080	0.013	···	···	···
2454345.63	3.270	-0.830	0.010	···	···	···
2454401.56	3.155	-0.945	0.009	···	···	···
2454662.93	3.349	-0.752	0.015	-4.34	0.36	0.37
2454665.77	3.486	-0.615	0.014	-3.95	0.75	0.35
2454665.77	3.492	-0.609	0.015	-4.06	0.64	0.36
2454730.71	3.457	-0.644	0.014	-4.09	0.68	0.36
2455100.57	3.875	-0.226	0.016	-5.14	0.04	0.44
2455100.58	3.891	-0.210	0.014	-5.02	0.16	0.44
2455398.75	4.209	0.108	0.015	-6.49	-0.89	0.51
2455790.72	4.977	0.876	0.021	-8.65	-2.34	0.67
2455869.58	5.211	1.111	0.017	-8.14	-1.66	0.60

Table 4.1: - (Continued)

Julian Date	Primary RV (km/s)			Secondary RV (km/s)		
	raw	shifted	σ	raw	shifted	σ
2455910.57	5.321	1.221	0.018	-8.40	-1.82	0.63
2455992.02	5.538	1.437	0.012	-9.01	-2.22	0.65
2456016.93	5.659	1.558	0.014	-9.23	-2.37	0.62
2456106.78	5.784	1.683	0.015	-10.36	-3.24	0.67
2456138.84	5.944	1.844	0.020	-10.73	-3.51	0.73
2456145.65	5.947	1.846	0.025	-11.38	-4.14	0.80
2456145.66	5.929	1.828	0.018	-11.43	-4.19	0.79
2456145.66	5.965	1.864	0.018	-11.15	-3.91	0.79
2456173.73	5.955	1.854	0.018	-10.82	-3.48	0.75
2456401.97	6.964	2.864	0.014	-14.11	-5.87	0.69
2456401.97	6.941	2.841	0.012	-14.39	-6.15	0.68
2456433.74	7.238	3.138	0.013	-14.54	-6.14	0.62
2456433.74	7.209	3.108	0.012	-14.61	-6.21	0.65
2456435.87	7.208	3.108	0.015	-14.73	-6.33	0.64
2456435.87	7.205	3.104	0.015	-15.08	-6.68	0.64
2456461.87	7.358	3.257	0.012	-14.96	-6.42	0.63
2456461.88	7.351	3.250	0.015	-14.65	-6.11	0.65
2456461.88	7.326	3.225	0.016	-14.60	-6.06	0.61
2456465.80	7.297	3.196	0.014	-14.74	-6.18	0.53
2456497.86	7.574	3.473	0.019	-15.86	-7.13	0.73
2456519.62	7.765	3.664	0.015	-16.78	-7.93	0.59
2456525.66	7.725	3.624	0.017	-16.27	-7.38	0.64
2456560.58	7.812	3.711	0.013	-16.32	-7.22	0.90
2456564.59	7.781	3.680	0.015	-16.18	-7.05	0.86
2456613.55	8.089	3.988	0.016	-15.96	-6.51	0.91
2456614.58	8.139	4.038	0.012	-16.52	-7.06	0.85
2456755.98	9.308	5.208	0.014	-21.44	-10.84	0.74
2456759.97	9.366	5.265	0.015	-21.91	-11.28	0.76
2456784.84	9.603	5.502	0.017	-22.56	-11.69	0.81
2456816.67	9.895	5.794	0.014	-23.36	-12.17	0.74
2456816.67	9.907	5.806	0.015	-23.68	-12.49	0.72
2456860.73	10.402	6.301	0.016	-25.64	-13.97	0.88

Table 4.1: - (Continued)

Julian Date	Primary RV (km/s)			Secondary RV (km/s)		
	raw	shifted	σ	raw	shifted	σ
2456860.73	10.421	6.321	0.015	-25.77	-14.11	0.83
2456885.62	10.607	6.507	0.015	-27.23	-15.29	0.84
2456938.63	11.189	7.089	0.016	-29.30	-16.77	1.03
2456938.64	11.173	7.072	0.015	-28.99	-16.45	0.96
2457092.02	12.114	8.013	0.015	-31.57	-18.09	1.00
2457109.85	12.077	7.976	0.015	-32.79	-19.40	1.10
2457118.96	11.987	7.886	0.016	-31.14	-17.82	0.90
2457150.92	11.685	7.584	0.017	...	...	...
2457174.96	11.267	7.167	0.017	-28.58	-16.13	0.81
2457214.83	10.240	6.139	0.017	-24.68	-13.16	0.82
2457214.84	10.253	6.152	0.016	-25.36	-13.85	0.90
2457216.73	10.220	6.119	0.016	-25.13	-13.66	0.86
2457216.73	10.228	6.128	0.015	-25.15	-13.69	0.80
2457245.60	9.302	5.201	0.016	-22.21	-11.52	0.77
2457245.61	9.299	5.199	0.016	-21.85	-11.16	0.72
2457248.61	9.338	5.237	0.017	-21.66	-11.05	0.70

the cross-correlation functions in the rest frame of the primary star, although there is a constant velocity offset caused by small errors in the vacuum to air wavelength conversion and spectrograph wavelength drift throughout the night. We denote this shift as Δv_2 in later sections of this paper.

We normalize each CCF by subtracting a quadratic function that we fit well away from the peak, and then dividing by the height of the CCF at $v = 0$ (the peak). The average of the shifted CCFs is a close estimate for the cross-correlation function of the M-star template with the F5 primary star, since the contribution from the companion is diluted by shifting the CCFs to the primary star rest frame. We remove the contribution from the primary star by subtracting the average from each CCF. The result is a series of residual cross-correlation functions that are estimates for the CCF of the companion spectrum against the 4400 K model spectrum template, with significant noise. We show the residual CCFs in Figure 4.1; the trace of the companion star is easily visible as the dark curve near the top middle. We are unable

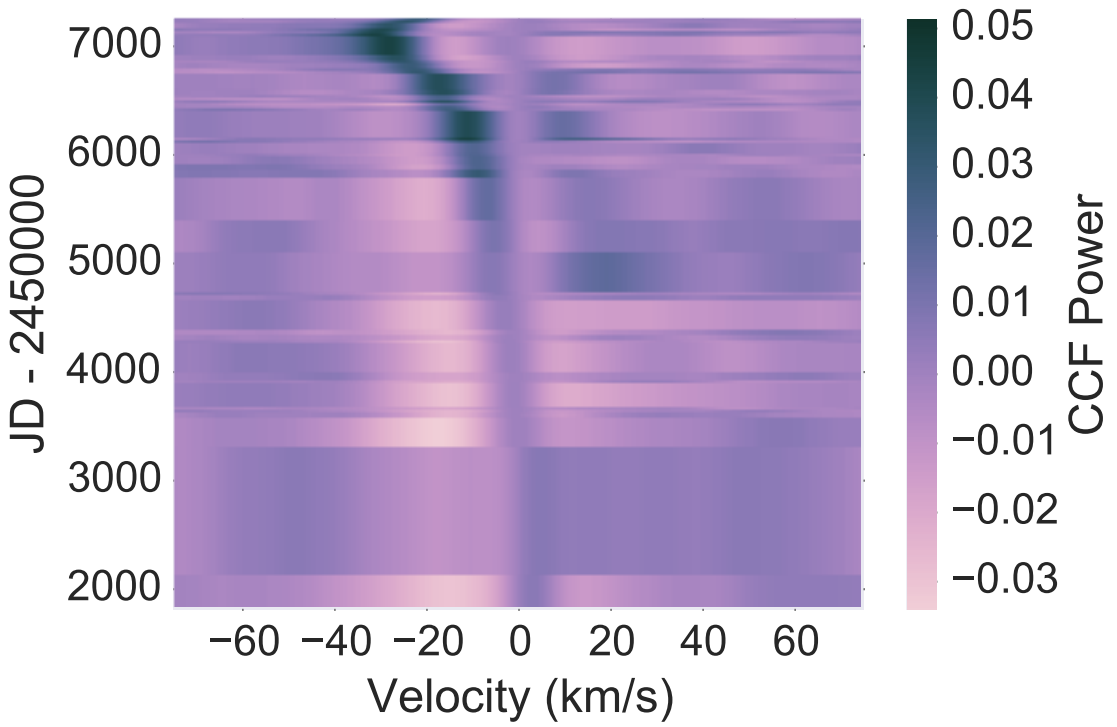

Figure 4.1: Cross-correlation functions of a 4400 K model spectrum template with the data, after subtraction of the average CCF. The dark curve in the top middle is the signal of the companion star.

to recover the companion signal at early dates when the two stars were close to one another in velocity space.

We measure the radial velocity of the companion at each epoch by finding the maximum and full-width-half-maximum (FWHM) of the residual CCF. On the basis of Figure 4.1, we use only the portion of the CCFs with $-50 < v < 10$ km s^{-1}; we show a typical residual CCF in Figure 4.2. Since the CCFs were shifted to subtract the contribution from the primary star, the measured velocities ($v_{m,2}$) are related to the true barycentric velocities (v_1 and v_2 for the primary and secondary, respectively) and the constant shift described above (Δv_2) through

$$v_{m,2}(t) = v_2(t) - v_1(t) + \Delta v_2 \tag{4.1}$$

We give the measured companion velocities in Table 4.1 (column 5). We additionally provide the velocities in the system velocity rest–frame (v_2) by using Equation 4.1

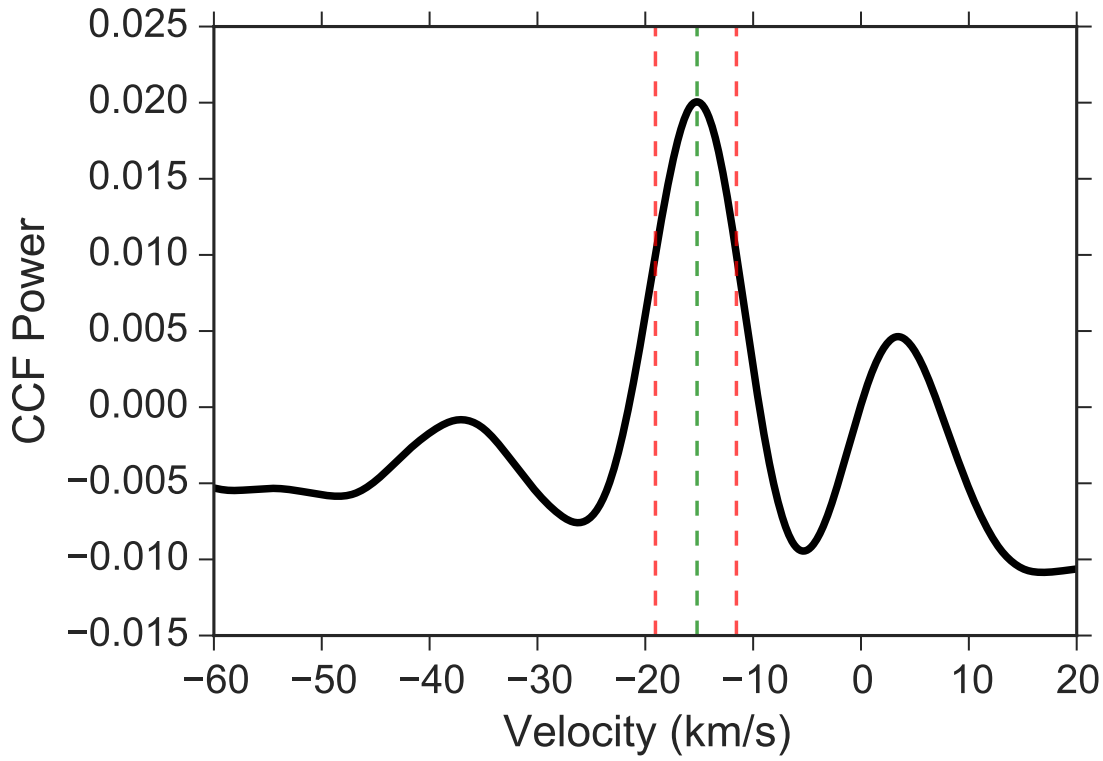

Figure 4.2: An example of a typical residual cross-correlation function. The dominant peak denotes the template match of the 4400 K template with the companion to ψ^1 Draconis A. The velocities are in the approximate rest frame of the primary star (see text for details), and the centroid and FWHM are given as vertical dotted lines.

and the results of the analysis described below. The uncertainties given in Table 4.1 are determined from the CCF peak width and the scaling factor (f) derived below. The shifted primary and secondary velocities given in Table 4.1 are for the reader's convenience since they are in the same reference frame; we use the raw measurements in the orbital fit.

4.4 Orbital Fit

We now use the radial–velocity measurements to find the best orbital parameters to describe the orbit, as well as some data scaling and shifting factors. The orbit is described by the semi-amplitudes for both the primary and secondary stars (K_1 and K_2, respectively), the longitude of pericenter (ω), the eccentricity (e), the period

(P), and the periastron–passage epoch (T_0). We cannot measure the system radial velocity, which is usually the final orbital element, because the measured primary–star velocities are differential and the secondary–star velocities are measured relative to the primary star.

Since the primary–star radial velocity measurements are differential measurements, we must also fit a constant shift (Δv_1) to account for the absolute radial velocity of the primary at the time at which our template spectrum was observed. We include an rv–jitter term (σ_J) to the fit to account for radial–velocity variations not encompassed by the orbital solution, and add the value in quadrature with the formal uncertainties on the primary star–velocity measurements.

The companion radial velocities are measured relative to the primary star plus a small velocity shift (Δv_2) caused by slight inaccuracies in the vacuum–to–air wavelength conversion in the model spectrum and spectrograph wavelength drift throughout the night. Finally, the CCF peak full-width at half maximum vastly overestimates the velocity uncertainty and so we fit a scale factor (f) to apply to the companion velocity uncertainties. The uncertainties given in Table 4.1 are already scaled by that factor. The full log-likelihood function ($\mathcal{L}$) is then given by:

$$
\begin{aligned}
s_1 &= \sum_{t_m} \frac{(v_{1,m} - v_1(t_m) - \Delta v_1)^2}{\sigma_{v_1}^2 + \sigma_J^2} + \ln 2\pi(\sigma_{v_1}^2 + \sigma_J^2) \\
s_2 &= \sum_{t_m} \frac{(v_{2,m} - v_2(t_m)(1 + \frac{K_1}{K_2}) - \Delta v_2)^2}{f\sigma_{v_2}^2} + \ln 2\pi(f\sigma_{v_2}^2) \\
\mathcal{L} &= -0.5(s_1 + s_2)
\end{aligned}
$$

where $v_{1,2}(t) = v(T_0, P, e, K_{1,2}, \omega, t)$ is the velocity at time t given by the orbital elements T_0, P, e, K, and ω.

We use the affine invariant sampler provided in the emcee code (Foreman-Mackey et al., 2013) to perform a Markov Chain Monte Carlo (MCMC) fit to all of the parameters described above. We use flat priors in all variables except for the rv–jitter and companion rv uncertainty scale factors (σ_J and f, respectively), for which we use log-uniform priors to allow for a large range of values. We give the median value and uncertainty for each parameter in Table 4.2., and display samples from the marginal posterior distributions of the orbital parameters in Figure 4.3 The uncertainties are

estimated from the posterior probability distribution samples such that the lower and upper bounds give the 16th and 84th percentile (i.e. they are 1σ credibility intervals). We plot the best-fit orbit with the data in Figure 4.4, with the uncertainties on the companion velocities scaled and the velocities shifted by Δv_1 and Δv_2.

Next, we calculate a series of derived quantities to characterize the companion and report them in Table 4.2. The mass ratio of the system is the ratio $K_1/K_2 = 0.47$. We estimate the primary star mass by interpolating Dartmouth isochrones (Dotter et al., 2008) with the 'isochrones' code (described in Montet et al., 2015), and using spectroscopic parameters derived in Endl et al. (2016). The secondary mass is $M_2 = qM_1 \sim 0.70\ M_\odot$; assuming the same age and metallicity as the primary, the Dartmouth isochrones give an expected temperature of ∼4400 K. That temperature is in excellent agreement with the high–contrast–imaging data, which support a companion of ∼4400 K with large uncertainty. With both the primary and secondary star mass, we calculate the orbital inclination and semimajor axis and report them in Table 4.2.

4.5 Discussion and Conclusions

We use nearly 15 years of time-series spectra of the star ψ^1 Draconis A to search for the spectral lines of a companion identified by a large–amplitude trend in the primary–star radial velocities and later by direct imaging. We cross-correlate each spectrum against a Phoenix model spectrum of a 4400 K star and subtract the average CCF. The residual CCFs clearly show the template match with the companion (Figure 4.1), and we are able to measure the companion radial velocities for most dates.

We use the radial–velocity measurements for both the primary and secondary stars to find an orbital solution for the now double-lined spectroscopic binary. The summary values of the fitted parameters are given in Table 4.2. Finally, we report the mass and expected temperature of the companion as well as the orbital inclination and semi–major axis. The temperature agrees well with high–contrast imaging, validating our method.

The ψ^1 Draconis system is therefore a hierarchical multiple system with the component parameters given in Table 4.2. ψ^1 Dra A and B are separated by ∼680 AU and have a mass-ratio $q = 0.82$, while A and C (the new companion) have a much

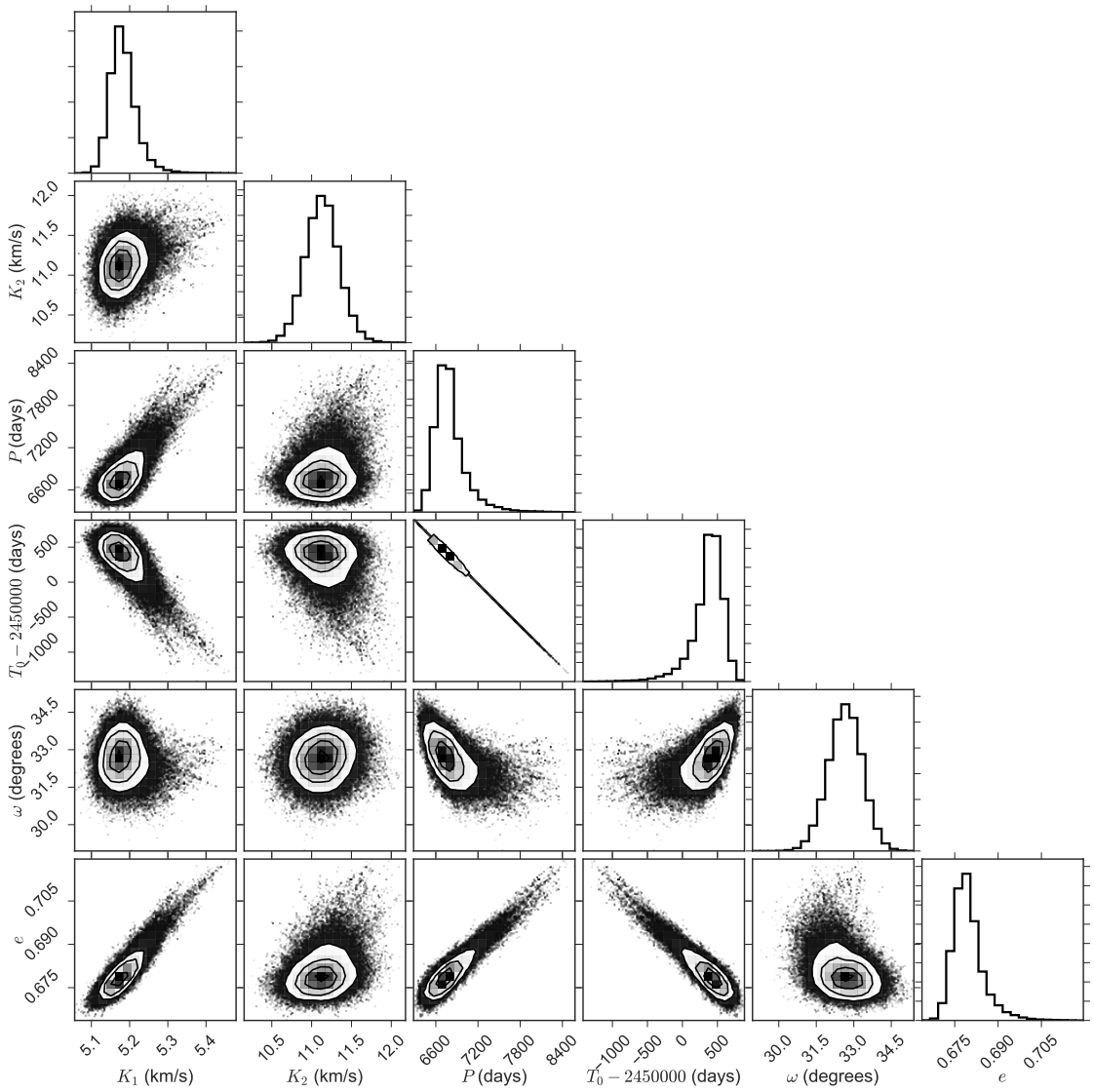

Figure 4.3: Marginalized posterior probability distribution estimates for the orbital parameters we fit. There is a strong degeneracy between the period and epoch of periastron (T_0) because we have not yet observed a full orbit.

closer orbit with with $a = 9.1$ AU and $q = 0.47$.

This method could be used to search for the spectral lines of stellar companions to other stars observed with high–precision radial–velocity surveys. To that end, and in the goal of open science, we make the source code used for the analysis and generating the plots for this paper available at `https://github.com/kgullikson88/`

Table 4.2: The primary mass is derived using the spectroscopic $T_{\rm eff}$, $\log g$, and [Fe/H] and interpolating Dartmouth isochrones. The companion temperature is likewise derived from the companion mass using Dartmouth isochrones of the same metallicity.

Parameters from Endl et al. (2016)	
$T_{\rm eff,1}$ (K)	6544 ± 42
$\log g$	3.90 ± 0.11
[Fe/H]	-0.10 ± 0.05
Parameters measured in this work	
K_1 (km s^{-1})	$5.18^{+0.04}_{-0.03}$
K_2 (km s^{-1})	11.1 ± 0.2
Period (days)	6774^{+271}_{-167}
Periastron passage time (JD)	2450388^{+169}_{-273}
ω (degrees)	32.6 ± 0.7
e	$0.679^{+0.006}_{-0.004}$
Δv_1 (km s^{-1})	$4.10^{+0.06}_{-0.09}$
Δv_2 (km s^{-1})	$-5.4^{+0.3}_{-0.2}$
Companion uncertainty scale factor (f)	0.17 ± 0.02
rv jitter (m s^{-1})	72^{+7}_{-5}
reduced χ^2	0.41
Derived Values	
q	0.466 ± 0.008
M_1 ($M_\odot$)	$1.38^{+0.15}_{-0.08}$
M_2 ($M_\odot$)	0.70 ± 0.07
$T_{\rm eff,2}$ (K)	4400 ± 300
i (degrees)	31 ± 1
a (AU)	$9.1^{+0.4}_{-0.3}$

`Companion-Finder`. The raw radial–velocity measurements for both the primary and secondary star, as well as the MCMC chains, are available at the same url.

This research has made use of the SIMBAD database, operated at CDS, Strasbourg, France, and of Astropy, a community-developed core Python package for Astronomy (Astropy Collaboration, 2013). It was supported by a start-up grant to Adam Kraus from the University of Texas. The McDonald Observatory planet search is supported by the National Science Foundation under grant AST-1313075. We would like to thank the referee for various suggestions that improved this paper.

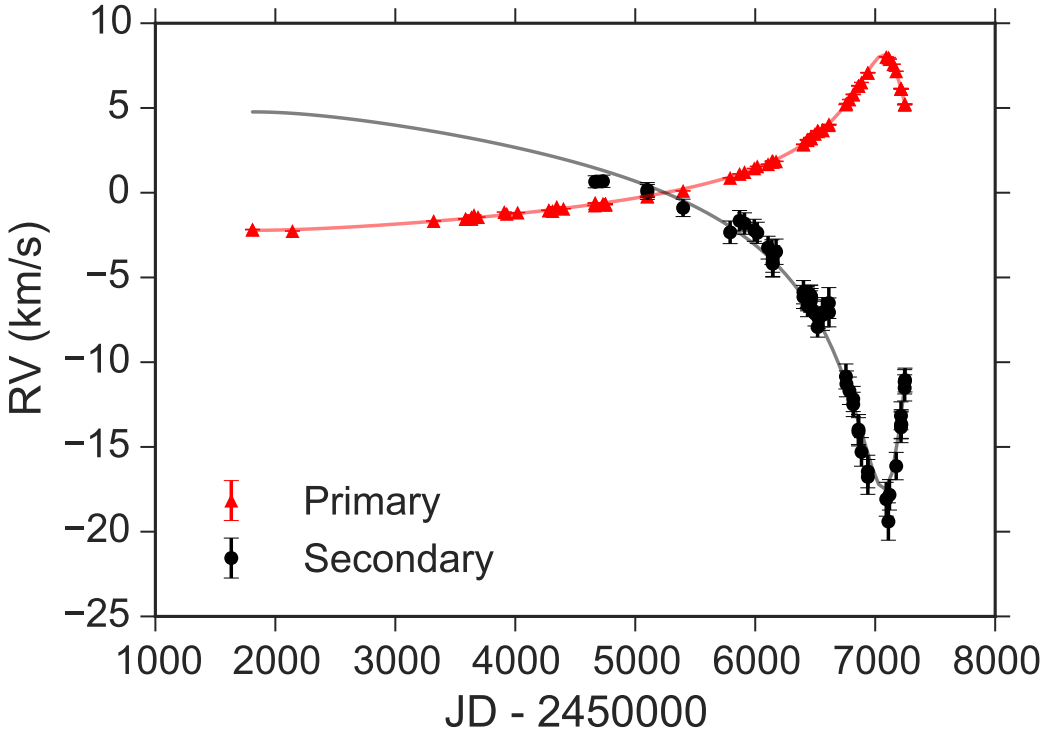

Figure 4.4: Best-fit double-lined orbit for the ψ^1 Draconis AC subsystem. There are no measurements of the companion at early dates because they could not be reliably measured in the residual cross-correlation functions.

Chapter Five: Future Direct Spectroscopic Detection of Hot Jupiters with IGRINS[1]

Several authors have used a variant of the method we described in Chapter 4 to search for emission from "Hot Jupiter" planets orbiting a sun-like star. In this case the flux ratio is much more extreme, but still possible with enough high signal-to-noise ratio spectra. In this chapter, we generate simulations of the IGRINS instrument to assess whether it can detect Hot Jupiter emission. While the instrument was being built at the time of publication, it is now functioning on the 2.7m telescope at McDonald Observatory and a pilot survey based on this work is in progress.

5.1 Introduction

With about 1600 confirmed extrasolar planets (from exoplanets.org: Wright et al., 2011), the time for characterization of these planets is here. A first step towards characterization is a determination of the planet mass. Most of the exoplanets so far discovered around nearby stars were found using the radial velocity technique, which measures the periodic Doppler shift of the parent star. Unfortunately, the inclination of the orbit cannot be determined without another complementary method. This means that planet masses from radial-velocity surveys are only *minimum* masses. In principle, precise astrometry could provide the complementary measurement that is needed to determine the true planet mass. However, the astrometric motion is very difficult to detect with current technology. The amplitude of the motion of a sun-like star with a Jupiter-mass planet orbiting at 0.1 AU and a distance from Earth of 10 pc is roughly 20μas, an order of magnitude below the precision of the Hubble Space Telescope Fine Guidance Sensors (Benedict et al., 2006) and will be very near the precision of GAIA (Sozzetti et al., 2001).

We can measure the true mass and inclination of a planet only if the radial velocity of the planet was known as well as that of its parent star. There are two ways that the

[1]This chapter was previously published (Gullikson & Endl, 2013). The co-author, Mike Endl, was my co-supervisor at the time and provided much of the inspiration for the work as well as a great deal of technical assistance.

radial velocity of an orbiting planet could be measured: light reflected from the parent star or the characteristic spectrum of the planet itself. Both methods require high resolution spectroscopy in order to detect the doppler motion of the spectral lines. Several groups have attempted to detect the reflected light from orbiting planets, but at the time of this writing none have been successful (Collier Cameron et al., 2002; Rodler et al., 2008, 2010; Langford et al., 2011) and have only been able to set upper limits on the planet albedo ($A_B \sim 0.1$).

While searches for reflected light are best done in the optical, the thermal emission from a $\sim$ 1000K planet will peak in the near-infrared. The thermal emission from a small group of planets has been detected, including HD209458b (e.g. Knutson et al., 2007a; Swain et al., 2008; Cubillos et al., 2010), HD189733b (e.g. Grillmair et al., 2007; Knutson et al., 2007b; Charbonneau et al., 2008; Agol et al., 2010), Wasp-3b (Zhao et al., 2012), and even the Super-Earth 55 Cnc b (Demory et al., 2012). These detections were mostly made using either Spitzer photometry or low-resolution spectroscopy, and they are all transiting planets. Recently, the emission spectrum from Tau Boo b (Brogi et al., 2012; Rodler et al., 2012), HD 189733b (de Kok et al., 2013), and possibly 51 Peg b (Brogi et al., 2013) has been detected in high resolution using VLT/CRIRES. In this paper, we describe a similar technique using the IGRINS instrument, which offers a much larger spectral range in a single observation than CRIRES, and is expected to see first light on the 2.7m Harlan J. Smith Telescope at McDonald Observatory in late 2013.

There are several challenges to detecting the planet's near-infrared spectrum, especially in high resolution. The very low flux ratio between the planet and the star ($F_p/F_s \sim 10^{-4}$ in the K-band) requires a very sensitive instrument and a high signal-to-noise ratio (S/N), which is very challenging on current near-infrared spectrographs. Second, the near-infrared spectrum is highly contaminated by absorption from the Earth's atmosphere (telluric absorption). In order to detect a planetary spectrum, the telluric lines must be removed very well. Finally, the stellar spectrum must be removed to detect the planetary spectrum. This is extremely challenging for non-transiting planets, for which the planet is never blocked by the star.

In this chapter, we investigate a technique to detect the spectrum from an approximately Jupiter mass object on a very close orbit (a Hot Jupiter) using the near-infrared spectrograph IGRINS. We briefly describe the IGRINS instrument and the simulated observations in Section 5.2. In Section 5.3, we test the sensitivity of

our detection method to the S/N of the observations, the efficiency of heat redistribution from dayside to nightside in the planet's atmosphere, and the model atmosphere dependence of the method. We summarize our results and compare our sensitivity to the recent detections of Hot Jupiters in Section 5.4.

5.2 Instrument and Methodology

The IGRINS instrument is explained in detail in Park et al. (2014). IGRINS is an immersion grating echelle spectrograph, and is capable of observing the entire H (1.4-1.8 μm) and K (2.0-2.4 μm) spectral windows at once, with a resolution of $R = \lambda/\Delta\lambda \sim 40000$. IGRINS was commissioned on the 2.7-meter Harlan J Smith telescope at McDonald Observatory in the spring of 2014, about 1 year after this chapter was originally published.

We make several assumptions and simplifications in this work. We ignore any *instrumental* effects that may introduce systematic noise, although we do introduce systematic noise in the form of telluric contamination. We also ignore any light reflected from the star, since it contributes little to the total planet brightness in the H and K bands. Finally, we assume the IGRINS detector has equal sensitivity to all wavelengths of light, so the signal-to-noise ratio is set only by the light from the target.

There are three main steps in our simulated observing program: generating a series of synthetic observations, removing the signature of Earth's atmosphere as well as the parent star's spectrum, and searching for the planet signal in the residuals. Each of these steps is detailed below.

5.2.1 Synthetic Observation Generation

An observed spectrum of a star and planet system can be divided into three parts: the star, the planet, and the Earth's atmosphere (telluric contamination). We use two test cases for this work: HD 189733 and HD 209458. The basic parameters of the systems are given in Table 5.1. We choose these planets as test cases becase they are very well-studied, with detections of the atmosphere both in transmission and emission. As a result of this, they are one of the very few planets with constrained atmospheric temperature-pressure profiles and chemical abundances. These planets are also useful

as test cases since HD 209458b is thought to have a thermal inversion layer in its atmosphere (Knutson et al., 2008), while HD 189733b does not (Charbonneau et al., 2008).

We simulate the stellar and planetary spectra using a code based on the Phoenix-ACES stellar atmosphere code (described in Barman et al., 2011), modified to self-consistently treat a planet with intense incoming stellar radiation by using the stellar radiation field as a boundary condition on F_ν. (Barman et al., 2001). For this work, we used one dimensional spherical geometry, with no clouds and solar abundance ratios (Asplund et al., 2005). The temperature-pressure profiles are described in Barman (2008) and Barman et al. (2002) for HD 189733b and HD 209458b (respectively). The chemical abundances are solved at each layer by assuming complete chemical equilibrium.

The absorption due to earth's atmosphere was modeled using the Line-By-Line Radiative Transfer Model (LBLRTM) code (Clough et al., 2005). This code takes the pressure, temperature, and abundance of several molecular species at a series of heights in the atmosphere, and outputs a transmission spectrum. The code also requires a line list containing the molecular line strengths and positions which, along with the molecular abundance and the airmass of the observation, determines the amount of absorption at a given wavelength. We use the HITRAN database (Rothman et al., 2009) for the line list.

The synthetic observations were made by first adding the star and planet model spectra at the appropriate flux ratio and Doppler shifts. The flux ratio was determined by the model spectra themselves, multiplied by the radius of the body. We determined the Doppler shift by fixing the orbital parameters and masses of both the star and planet (which we will ultimately recover). Synthetic observations were made at several phases in the planet's orbit as well as different phases of the *Earth's* orbit around the Sun, resulting in a variety of relative radial velocities between the star, planet, and telluric spectral lines.

Hot Jupiters are expected to be tidally locked with their parent stars (Fabrycky, 2010), meaning there are permanent day and night sides. The extent of heat redistribution from the dayside to the nightside is uncertain, but appears to vary throughout the Hot Jupiter planetary class. Knutson et al. (2007b) find that HD189733 b is consistent with a high degree of heat redistribution between its day and night side. Conversely, Harrington et al. (2006) find that ν And b is consistent with no heat

redistribution.

For planets with little heat redistribution, the planetary spectrum will change throughout the orbit, as different amounts of the cold nightside are exposed. Without a full suite of planetary atmospheres calculated with a self-consistent phase curve, we cannot treat the issue of heat redistribution in a fully realistic way. We approximate a planet with inefficient heat redistribution by scaling the dayside planet spectrum with a phase-dependent factor before adding it to the stellar spectrum. In this work, we consider only two cases: one with complete heat redistribution where the temperature of the planet is invariant to the orbital phase, and a second where the effective temperature seen on the nightside is some fraction ($f_{\rm red}$) of the dayside temperature, resulting in a minimum scaling factor of $f_{\rm red}^4$. WASP-12b, a very extreme case, has $f_{\rm red} = 1/3$ (Cowan et al., 2012); we simulate observations with $f_{\rm red} = 1/2$ as a reasonable value, and adopt a sinusoidal phase curve. For this case, the nightside planet spectrum is $2^4 = 16$ times dimmer than the dayside spectrum.

After adding the star and planet spectra as above, we multiply the sum by a model of the telluric absorption spectrum. We then convolve the spectrum with a gaussian instrumental profile and rebin the data according to the predicted resolution and spectral format of IGRINS (Figures 2 and 3 of Park et al., 2014). Finally, we set the average signal-to-noise ratio by adding gaussian random noise to each pixel.

5.2.2 Telluric and Stellar Line Removal

We now begin attempting to recover the planet spectrum from the synthetic observations. To remove the telluric contamination, we use a method similar to that described by Rodler et al. (2012). With this method, a "telluric standard" star, which is usually an A- or B-star, is observed immediately after the science target at a similar airmass. The telluric contamination is modeled independently for both stars, and then the residuals of the science star fit are divided by the residuals of the standard star fit. Using a telluric model accounts for changes in airmass, water vapor column density, and the instrumental profile between the science and standard stars, but can leave systematic errors if certain lines have incorrect oscillator strengths. Dividing the residuals after the telluric model fit removes most of these systematic errors. We simulate observations of the science target as described above, and simulate the observation of a B-type telluric standard star with a 20000 K blackbody. The generation

of this synthetic observation was identical to that used for the science star, except we used a telluric model with a different telescope altitude (airmass) and we did not add the planet model spectrum.

Since we are using a telluric model to make the observations, performing a model fit as described above will perfectly remove the telluric spectrum. In order to simulate systematic errors in the model fit, we divided both the science star and the standard star by telluric models that had $\pm 1\%$ water column density from the "actual" value used to make the observation. This process left large telluric residuals on the order of $5-10\%$ of the continuum, but the residuals were quite similar in both the science star and the standard star observations. Thus, division of the science star residuals by the standard star residuals adequately (but not completely) removes the telluric contamination. Telluric residuals in the water bands at the edges of the H and K spectral windows were on the order of $1-2\%$ of the continuum. Figure 5.1 illustrates the telluric removal process for a region with particularly severe telluric contamination.

With the telluric contamination removed, the simulated observations consist of just the star, the planet, and noise. To generate a stellar spectrum with minimal contamination from either telluric lines or planet lines, we simulate observations of the the star at various phases in the planet's orbit as well as the Earth's orbit. After correcting for the Doppler shift from both the Earth's motion and the star's reflex motion, both of which are assumed known, we co-add the spectra from several observations. This process will reduce the strength of the planet's spectral lines and any residual telluric lines, as well as reduce the random noise in the spectrum by a factor of $\sqrt{N}$, where N is the number of observations of the planet. The result is a very high S/N stellar template spectrum, which we subtract from each observation. While the planetary lines are reduced in intensity in the stellar template, they are still present at several radial velocities for any finite number of observations. Thus, subtracting the stellar spectrum will also subtract some of the signal we are interested in. For observations of the system at N distinct phases, this stellar subtraction algorithm will subtract 1/N of the planet signal. Thus, for non-transiting systems we expect the sensitivity to scale approximately linearly with the number of observations at distinct orbital phases. For systems with inefficient heat redistribution, where the different orbital phases contribute different amounts of planet flux, the scaling relation is more complicated and will depend on the phases observed. However, the general result that more observations increase the overall sensitivity is robust.

We note that our method of correcting for the telluric and stellar lines is quite different from that used in most previous work by Brogi et al. (2012, 2013), and de Kok et al. (2013), although the telluric correction is very similar to that described by Rodler et al. (2012). In most previous work, the contamination was removed by placing all observations of the star in a matrix and removing features that are stationary in time. This works because the planet will be orbiting, and so its spectrum will shift several pixels throughout the course of the observation while the telluric and stellar lines will remain (approximately) constant. In contrast to this, we perform a physical fit to the telluric spectrum for each individual observation, and we account for the small stellar radial velocity when generating a stellar spectrum template. The method used here is more physical than that of previous work, but can be more expensive in both observational and computational time since it requires the observation of a standard star and the computation of a large number of telluric models over a wide wavelength range.

5.2.3 Recovery of Planet Radial Velocity

After removing the telluric and stellar lines, each observation has been reduced to a very noisy planet spectrum. The low planet to star flux ratio of $F_p/F_s \sim 10^{-4}$ means the random noise generally has an amplitude greater than the variation in the planet spectrum itself (i.e. the S/N < 1). The situation is even more difficult in spectral regions with severe telluric absorption, where small errors in the telluric correction complicate the stellar spectrum removal and effectively add systematic noise. Nonetheless, we can still detect the planet signature by cross-correlating the residuals against a planet model spectrum. The cross-correlation will show a peak at the velocity corresponding to the radial velocity of the planet.

Except for observations with extremely high S/N ratios, the cross-correlation function (CCF) for a single observation will show several peaks: one for the true planet signal, and several more coming from chance alignments with either random noise or telluric and stellar residuals. Here, we use a method similar to the one described by Brogi et al. (2012, 2013) by using our knowledge of the planet's orbit. For planets found with the radial velocity technique, the *stellar* radial velocity (v_s) is known for each observation (or orbital phase ϕ), and the planet radial velocity (v_p) is simply

$$v_p(\phi) = v_s(\phi)\frac{M_s}{M_p} \tag{5.1}$$

To find the true mass of the planet, we test several guess values for the ratio of stellar mass to planet mass (M_s/M_p). For each value, we co-add all of the CCFs after correcting for the planet radial velocity and barycentric motion. When the mass-ratio guess is correct, chance alignments with residual noise will tend to cancel out while the CCF peaks coming from the true alignment of the planet model with the planetary spectrum add together. Thus, the total CCF shows a strong peak at 0 km s^{-1}, indicating the detection of the planetary spectrum. Figure 5.2 demonstrates the advantage of adding the cross-correlation functions from all observed orbital phases; even though the planet is only weakly detected in a few of the individual observations, the total CCF has a very strong ($\sim 6\sigma$) peak. We determine the correct mass-ratio by comparing the height of the CCF at 0 km s^{-1} for all of the mass-ratio guesses; the correct mass-ratio will have the highest CCF peak.

5.3 Results

We simulated a series of IGRINS observations of non-transiting Hot Jupiter systems by using model spectra for the well studied systems HD189733 and HD209458. For both systems, we calculate the minimum S/N ratio necessary to detect the planet. In this work we consider a planet detected if the total (summed) CCF has a peak at 0 km s^{-1} with at least 4σ significance, and that the planet mass is recovered correctly and unambiguously. We consider the effect of heat redistribution by taking two extreme cases as described in Section 5.2.1, and we estimate the model dependence of our method by cross-correlating our synthetic observations against the wrong planet model spectrum. Our method of testing the model dependence is most likely pessimistic; in a real observing campaign and indeed in current searches (Brogi et al., 2012, 2013; Rodler et al., 2012; de Kok et al., 2013) a library of planetary atmosphere grids with different temperature, pressure, and molecular abundance profiles would be tested. We consider it likely that one model in such a model library would be closer to the true planet spectrum than our two test cases are to each other (see Figure 5.3 for a visual comparison of the planet model spectra).

In general, the critical S/N ratio necessary to detect any non-transiting planet with our method depends on the ratio of the signal coming from the planet to that of the star. This ratio is not simply the flux ratio, since our cross-correlation technique requires several deep spectral lines in the planetary spectrum. If the planetary atmosphere is nearly isothermal as in WASP-12b (Crossfield et al., 2012), or has a thick haze layer in the near-infrared as HD 187333b may (Gibson et al., 2012), then the spectrum will be relatively featureless and it will be very difficult to detect in high resolution. The critical S/N ratio can be calculated from the continuum surface flux of the planet and star ($F_{\rm p,cont}$ and $F_{\rm s,cont}$, respectively), the ratio of the flux in an average spectral line to the flux in the continuum for the planet (r), the radii of the planet and the star (R_p and R_s, respectively), and unknown constants A and S_0:

$$S/N_{\rm crit} = A\frac{F_{\rm s,cont}}{F_{\rm p,cont}(1-r)}\left(\frac{R_s}{R_p}\right)^2 + S_0 \tag{5.2}$$

To first order, the continuum fluxes can be calculated from the blackbody fluxes and the effective temperatures of the planet and star. The planet temperature can be approximated from the stellar temperature, the semimajor axis of the planet's orbit (a), and the bond albedo of the planet (A_B) by radiative equilibrium with

$$T_p^4 = \frac{1-A_B}{4}\left(\frac{R_s}{a}\right)^2 T_s^4 \tag{5.3}$$

To test the dependence on S/N, we generated a series of synthetic observations at 25 approximately evenly spaced orbital phases for average S/N ratios ranging from 100 - 1500, with both efficient and inefficient heat redistribution (see the discussion of heat redistribution in section 5.2.1). We did not attempt to optimize the observing schedule for the planets with inefficient heat redistribution, and so the minimum S/N ratios we find for that case may be somewhat pessimistic. We determined the minimum S/N ratio necessary to detect the planet, and report the results in Table 5.2. In general, HD 209458b requires higher S/N to detect than HD 189733b. HD 209458 is a hotter star while the planets are roughly the same temperature, and so the flux ratio is more extreme. In addition, HD 189733b has much deeper lines throughout its spectrum, largely from a higher water abundance (Madhusudhan & Seager, 2009), making the detection easier. A second trend evident in Table 5.2 is that planets with inefficient heat redistribution require a larger increase in S/N ratio

to detect if the wrong planet model is used, and so are more model dependent than those with efficient heat redistribution.

We now determine A and S_0 from Equation 5.2 from the known flux ratios and line strengths in HD 189733b and HD 209458b, along with the minimum S/N ratio values in Table 5.2. For efficient heat redistribution, $A = 0.1$ and $S_0 = 46$. Likewise, $A = 0.1$ and $S_0 = 107$ for inefficient heat redistribution. With these values, we can estimate the S/N ratio necessary to detect other Hot Jupiters. The planet radius is not known for non-transiting planets, but we approximate this from mass-radius relationships for hydrogen-dominated planets given in Swift et al. (2012). Lacking any information on the line strength for non-transiting planets, we take a typical value to be the average of our two test cases: $r = 0.83$. We use $A = 0.1$ and $S_0 = 75$ in Equation 5.2 to consider some level of heat redistribution. Table 5.3 estimates the flux ratio for each of the non-transiting Hot Jupiter planets in the exoplanets.org database (Wright et al., 2011), assuming $A_B = 0.2$. The minimum S/N ratios were found with Equation 5.2. We calculate the exposure time for each target from the net atmospheric transmission in the K band, the expected 7% net throughput of IGRINS (Dan Jaffe, priv. comm.), and simple Poisson statistics since these observations will be well within the source noise limit.

To estimate the uncertainty in the planet to star mass-ratio, and therefore the uncertainty in the true planet mass, we compare the significance of the $v = 0$ km s^{-1} point of the total CCFs for various mass-ratio guesses. As the guess begins getting closer to correct, the correct peaks in the individual CCFs will begin to align and the significance of the total peak will increase (See Figure 5.4). We can estimate the mass-ratio uncertainty from the points where the significance of the total CCF peak drops $\sim 1\sigma$ from the most significant mass-ratio. Smaller mass-ratio systems will have faster moving planets, so the individual CCF peaks only line up for a more narrow range of mass-ratio guesses than they would for more massive planets. Therefore, the the planet mass uncertainty with this method *decreases* as the mass-ratio decreases, as long as the planet remains detectable. The width of the peak in Figure 5.4, which is for a detection of HD 189733b, is $\sigma_{M_p/M_s} = 1.6 \times 10^{-4}$. Combining this with the stellar mass uncertainty gives a planet mass uncertainty of $\sigma_{M_p} = 0.15 M_{\rm Jup}$. The width of the corresponding peak for a detection of HD 209458b is $\sigma_{M_p/M_s} = 2 \times 10^{-5}$ giving $\sigma_{M_p} = 0.03 M_{\rm Jup}$. The planet mass uncertainty could be improved by focusing on phases near quadrature, rather than evenly sampling the orbit as we do in this

chapter.

5.4 Summary and Conclusions

We have described a technique for directly detecting the near-infrared spectrum from a non-transiting Hot Jupiter using high resolution, high signal-to-noise ratio spectra. We have applied this technique to simulated observations with the IGRINS near-infrared instrument, which is sensitive to the entire H and K bands and will begin operating on the 2.7m Harlan J. Smith Telescope at McDonald Observatory in late 2013. Using models of the well-studied Hot Jupiters HD189733b and HD209458b, we make synthetic observations at various phases of the planet's orbit and at several different barycentric radial velocities to simulate observations taken at different times of the (Earth's) year. We then remove the telluric absorption and parent star spectra, and search for the planet spectra by cross-correlating the residuals against models of the planet spectrum.

We have shown that the true mass and inclination of a Hot Jupiter planet can be recovered, and have determined the effect of S/N ratio as well as heat redistribution, and have estimated the model dependence of our method. Table 5.2 summarizes the results for our two test case planets, and Table 5.3 estimates the S/N ratios and exposure times necessary to detect several known, non-transiting Hot Jupiters.

Our simulated observations are similar to the recent detections of Tau Boo b (Rodler et al., 2012; Brogi et al., 2012), HD 189733 b (de Kok et al., 2013), and 51 Peg b (Brogi et al., 2013), all of which used the CRIRES high resolution spectrograph. The IGRINS instrument covers the entire H and K bands at once, rather than the ~ 40 nm range observed by CRIRES. Since the cross-correlation signal roughly scales as the square root of the number of deep spectral lines, we expect IGRINS to be more sensitive to detecting planets than CRIRES despite being on a smaller telescope. As well as simulating a different instrument, we simulate a different observing strategy; whereas previous work has used several hundred observations of a star over the course of a few closely-spaced nights, we have simulated an observing strategy where the star is observed ~ 25 times at various points in its phase *as well as various times of the year*. This strategy is more compatible with a campaign to monitor several Hot Jupiters rather than using one observing run for each planet. It also allows for the

easy addition of more data when it is received.

This research has made use of the Exoplanet Orbit Database and the Exoplanet Data Explorer at exoplanets.org. We would like to thank the anonymous referee for several very helpful comments, Travis Barman for generating the high-resolution model spectra for the stars and planets used in this work, and Dan Jaffe for his help with estimating the performance of the IGRINS instrument.

Table 5.1: Physical properties of the HD 189733 and HD 209458 planetary systems. The effective temperatures, masses, and radii are from Torres et al. (2008), and r (the ratio of the flux in an average spectral line to the flux in the continuum for the planet) are from the model spectra used in this work (See Figure 5.3 and the discussion before Equation 5.2).

Star	$T_{\rm eff,star}$ (K)	$T_{\rm eff,planet}$ (K)	M_p (M_{Jup})	R_p (R_{Jup})	r
HD 189733	5040	1200	1.14	1.138	0.77
HD 209458	6065	1450	0.69	1.359	0.90

Table 5.2: Summary of minimum S/N ratios needed to detect planets for our test cases. Efficient heat redistribution refers to observations where the dayside and nightside temperatures are the same, while inefficient heat redistribution is when the nightside temperature is half that of the dayside temperature. The model dependence is estimated by using different planet models to cross-correlate against the same observation (see section 5.3). We do not attempt to simulate observations with S/N > 1500 because such a high value would be very difficult to achieve in the near-infrared.

Star	Planet Model for CCF	Heat Redistribution	Critical S/N Ratio
HD 189733	HD 189733b	efficient	200
HD 189733	HD 189733b	inefficient	450
HD 189733	HD 209458b	efficient	300
HD 189733	HD 209458b	inefficient	800
HD 209458	HD 209458b	efficient	900
HD 209458	HD 209458b	inefficient	1200
HD 209458	HD 189733b	efficient	1200
HD 209458	HD 189733b	inefficient	>1500

Table 5.3: Estimated exposure times required for correctly retrieving the true masses of Hot Jupiters. The times are for a single observation; roughly 20-25 observations of the system at different phases are necessary to detect the planet. See Section 5.3 for the calculation of the flux ratio and critical S/N.

Star Name	K_s Magnitude	K-band flux ratio	S/N required	Time Required (Minutes)
τ Boo	3.36	1.26×10^{-03}	541	1.0
HD 189733	5.54	3.08×10^{-03}	200	1.0
υ And	2.86	8.22×10^{-04}	791	1.4
HD 41004 B	6.43	8.95×10^{-03}	141	1.7
HD 179949	4.93	1.22×10^{-03}	559	4.7
HD 162020	6.54	2.99×10^{-03}	272	4.8
HD 217107	4.53	7.22×10^{-04}	890	8.2
HD 73256	6.26	1.53×10^{-03}	461	10.8
HD 187123	6.34	1.28×10^{-03}	534	15.5
HD 86081	7.3	1.64×10^{-03}	434	25.0
HD 68988	6.74	1.17×10^{-03}	576	26.3
HIP 14810	6.83	1.05×10^{-03}	637	34.8
HD 330075	7.17	1.23×10^{-03}	553	35.9
HD 149143	6.43	7.71×10^{-04}	838	41.9
HD 209458	6.31	1.21×10^{-03}	900	43.0
HD 185269	5.26	3.05×10^{-04}	2002	81.0
HD 118203	6.54	4.77×10^{-04}	1309	112.9
HD 102956	5.66	2.06×10^{-04}	2935	253.0

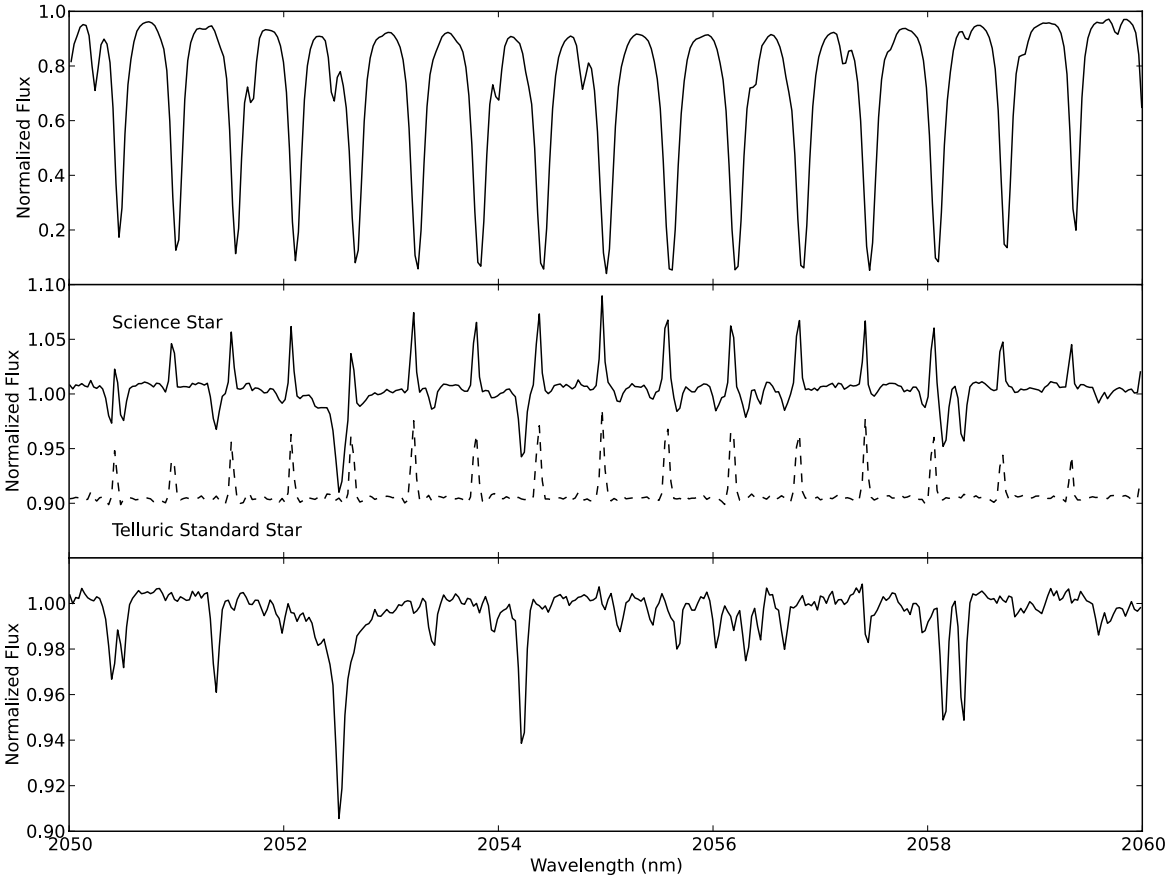

Figure 5.1: Telluric Correction process. *Top Panel*: Original science star spectrum for a segment in the water band on the blue side of the K band. *Middle Panel*: Telluric residuals after the model fit. The science star residuals are in the upper (solid) line, and the standard star residuals are in the lower (dashed) line. The systematic errors we introduced appear like emission lines in both spectra. *Bottom Panel*: Result after division of the science star residuals by the standard star residuals. The telluric contamination has largely been removed.

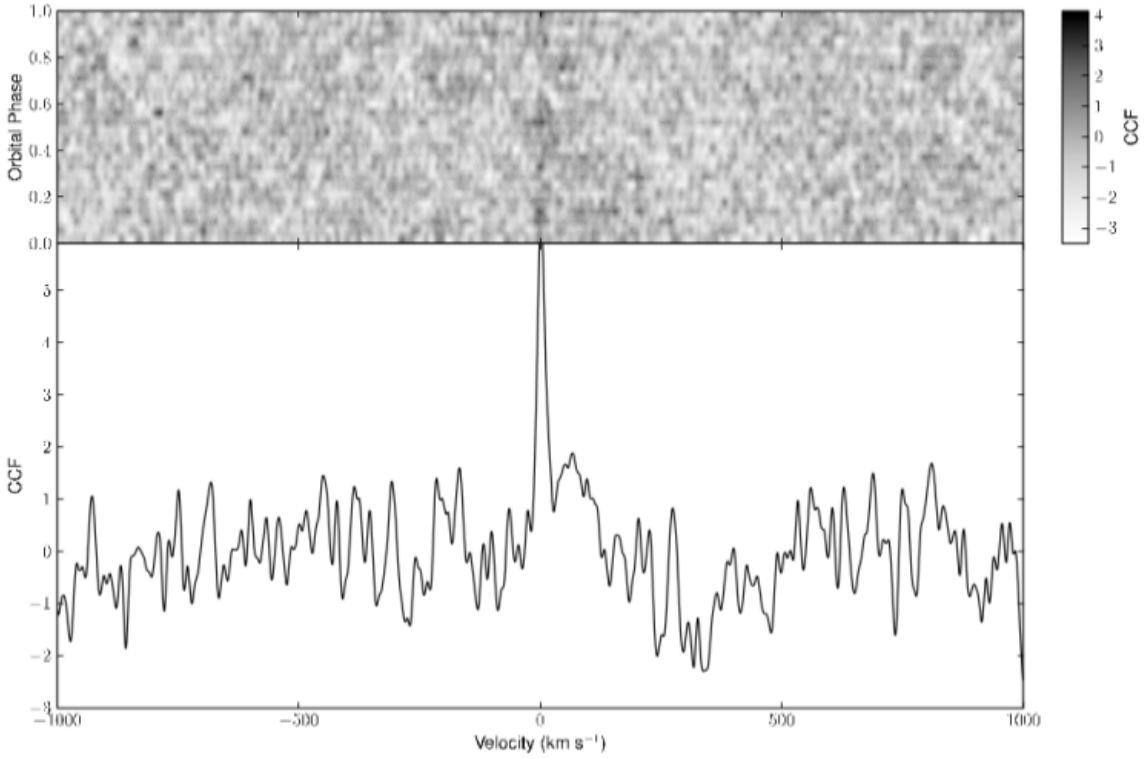

Figure 5.2: *Top Panel*: Individual cross-correlation functions for simulations of HD 189733 with an average S/N = 500, and with complete heat redistribution. The velocities are shifted at each orbital phase such that the cross-correlation function should have a peak at 0 km s^{-1}; the planet is only detected in a few of the observations. *Bottom panel*: The total cross-correlation function, after adding the cross-correlation functions for each individual observation. Here the planet is very clearly detected with 6.29σ significance.

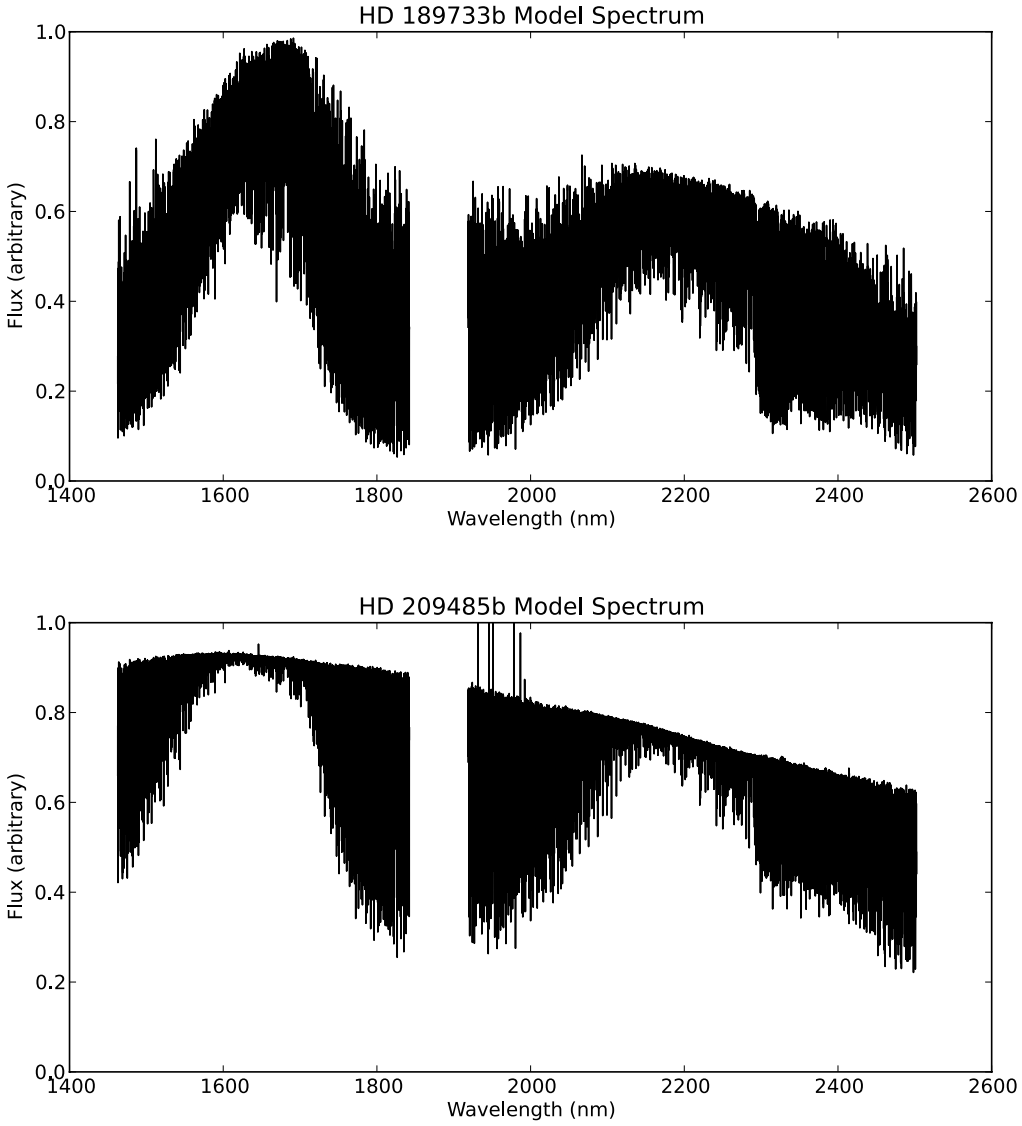

Figure 5.3: A comparison of the HD189733 planet model with the HD209458 planet model. The gap in the middle is is in between the H and K spectral windows, where water absorption in the Earth's atmosphere blocks most of the incoming light. HD209458b has a thermal inversion in its atmosphere, which generates the emission lines near 1950 nm. HD189733 b is somewhat cooler and has more water, giving its spectrum stronger spectral lines.

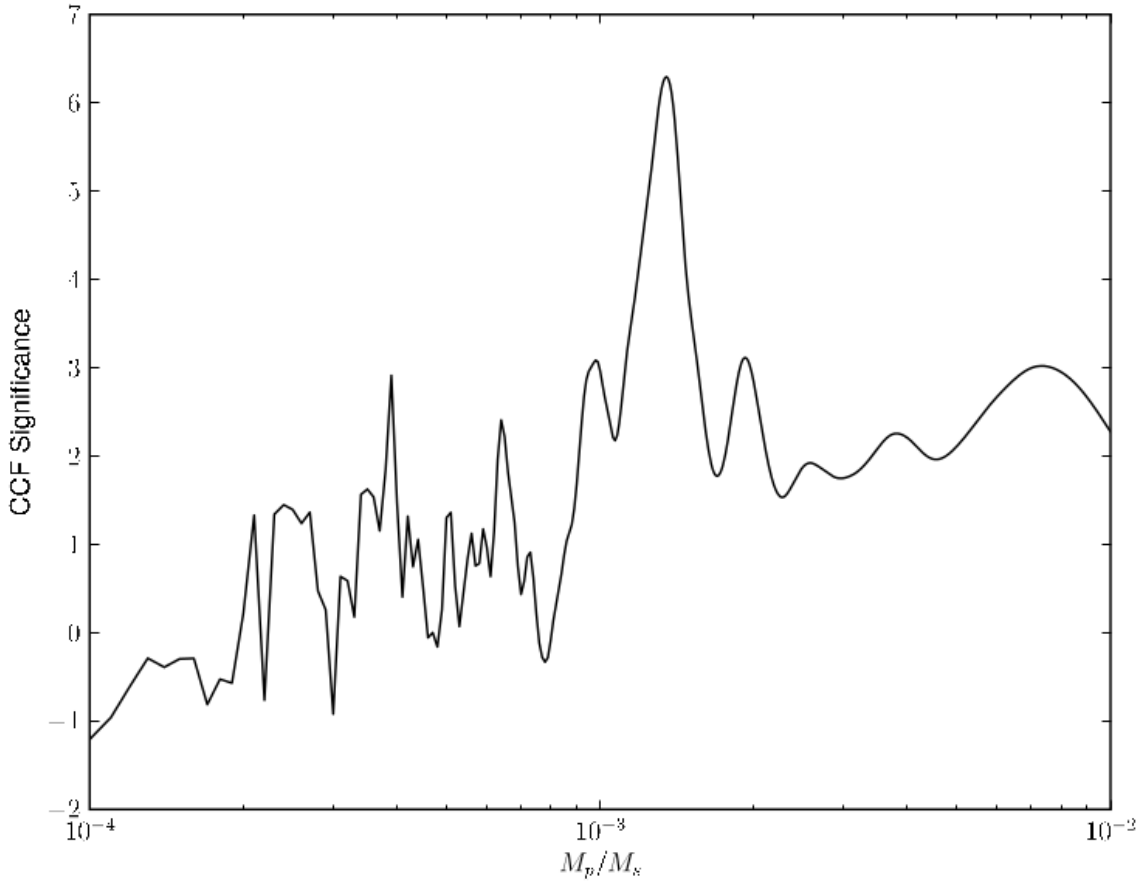

Figure 5.4: A summary of the significance of the point at 0 km s^{-1} in the total cross-correlation functions for each of the mass-ratio guesses, for a series of observations of HD 189733 with an average S/N = 500 and complete heat redistribution (the same as in Figure 5.2). The peak in this figure determines the planet to star mass-ratio, and therefore the true planet mass. The width of the peak 1σ below its maximum determines the uncertainty in the planet mass.

Chapter Six: Detection of Low-Mass-ratio Stellar Binary Systems[1]

We now turn back to the variant of the direct spectral detection method originally discussed in Chapter 2, in which the targets are very early-type, rapidly-rotating stars.

6.1 Introduction

O- and B-type stars are often found in binary or multiple systems: Mason et al. (2009) estimate that at least 57% of O-stars are in spectroscopic multiple systems, and at least 75% are in any type of binary or multiple system. Yet the multiplicity fraction of high-mass stars may be underestimated due to the difficulty of detecting low-mass secondary stars (Sana & Evans, 2011). While the mass-ratio distribution is reasonably well known for high-mass binaries with mass-ratio $q \equiv M_s/M_p > 0.2$, there are almost no constraints for low mass-ratio binaries. However, binaries of low mass-ratio are important probes of star formation since they may have formed in a different way than approximately equal-mass binaries. Here we define low mass-ratios to be those with $q < 0.2$, where M_s is the mass of the secondary (lower mass binary component), and M_p is the mass of the primary (higher mass binary component). We also use the term "low-mass" to describe star with $M < 1M_\odot$, and "high-mass" to describe stars with $M > 5M_\odot$

6.1.1 Binary Formation in High-Mass Stars

With such a high fraction of high-mass stars found in binary or multiple systems, any theory of high-mass star formation should be able to explain the high binary formation rate. There are several mechanisms by which binary stars may form: fission (Lyttleton, 1953; Lebovitz, 1974, 1984), in which a molecular core begins spinning fast enough as it collapses that it splits into two stars; core fragmentation (see e.g.

[1]This chapter was previously published (Gullikson & Dodson-Robinson, 2013). The co-author, Sarah Dodson-Robinson, was my advisor at the time and provided much of the idea for the project.

Boss & Bodenheimer, 1979; Boss, 1986; Bate et al., 1995), in which a collapsing core develops two or more overdensities which then begin collapsing separately; and disk fragmentation (see e.g. Kratter & Matzner, 2006; Stamatellos & Whitworth, 2011), in which the circumstellar disk surrounding the primary star becomes gravitationally unstable and creates a secondary star. While the fission scenario was once thought to be important, it has since fallen out of favor because the viscous dissipation timescale, which would drive a spinning body towards fission, is much longer than the core collapse timescale (Tohline, 2002) and because hydrodynamic simulations fail to cause the rotating core to actually split rather than just deform (Tohline & Durisen, 2001). Both core and disk fragmentation are still thought to be viable binary formation mechanisms. It is likely that both mechanisms play a role in shaping the binary mass-ratio and separation distributions. In the formation of higher-order multiples, it is very possible that both mechanisms operate.

The primary method of forming binary systems is thought to be core fragmentation. As a molecular cloud begins isothermally collapsing, its density increases, causing the Jeans mass to decrease. Thus, an initially Jeans-mass collapsing core can fragment into smaller objects. Core fragmentation will initially yield binaries with separations $10AU < a < 1000AU$, which may move closer by interacting with the surrounding gas, a circumbinary disk, or through dynamical interactions with other nearby stars (Bate et al., 2002). Assuming independent component masses chosen from the initial mass function (IMF), a binary with a $10M_{\odot}$ primary would most often have a $0.1M_{\odot}$ secondary, giving an initial mass ratio near $q = 0.01$. The unmodified mass-ratio distribution of high-mass binaries would therefore strongly favor low mass ratios. However, accretion of high specific angular-momentum gas from either the collapsing molecular core or the circumbinary disk will preferentially be captured by the lower-mass companion, driving the binary mass-ratio toward unity and decreasing the orbital separation (Bate, 2000; Bonnell & Bate, 2005). Additionally, dynamical interactions tend to replace low-mass binary companions with higher-mass ones, or to kick the lower-mass component out to a wide orbit and create a hierarchical triple system. Over time, these processes tend to create high-mass binary systems with nearly equal masses and small separations (Bate et al., 2002). Dynamical interactions are most important in dense environments where the probability of stellar encounters is high. Therefore, they are probably more important in dense OB star clusters than in the much looser OB associations, where many B stars are found.

Another potentially important way to form binary systems is disk instability (see e.g. Kratter & Matzner, 2006; Stamatellos & Whitworth, 2011). In this scenario, the fragment forms in an unstable circumstellar disk with an initial separation of $\sim 100AU$ and initial mass-ratios near $q \sim 0.03$, similar to the core fragmentation case (Kratter & Matzner, 2006). The final mass-ratio is expected to rise due to accretion, but the amount of mass the companion accretes depends on when it forms. Companions that form very early can accrete a significant amount of mass, driving the mass ratio towards unity. In contrast, a companion that forms late will not have as much time to accrete mass from the disk before it dissipates, and so the final mass ratio will be smaller. The more specific theoretical predictions of disk fragmentation companion evolution is far from resolved. A semi-analytical treatment of embedded protostellar disks by Kratter et al. (2008) finds that massive stars with $M > 2M_{\odot}$ maintain $0.01-0.1M_{\odot}$ in orbiting fragments after about 2 Myr. Krumholz et al. (2007) simulate a $100M_{\odot}$ collapsing core for a much shorter time (20 kyr), but also find that the disk fragments and that the final fragment mass ratio is $q \approx 0.1$. However, Krumholz et al. (2009) simulate the same mass core but start it with a slow solid body rotation instead of a turbulent velocity field and run the model for about twice as long (57 kyr), and find that it leads to a very massive binary ($M_1 + M_2 = 70\mathrm{M}_{\odot}$) with a mass-ratio $q = 0.7$. Work by Clarke (2009) indicates that as mass is transported inwards onto the star, the outer disk can become unstable at late times. This instability can lead to a delayed disk fragmentation, with a fragment mass-ratio in the range $0.1 < q < 0.5$. The simulations by Clarke (2009) were done for a $\sim 1M_{\odot}$ primary star, and the delayed fragmentation occured after about 10^5 years. Delayed fragmentation may not be possible in disks surrounding high-mass stars, as the time at which fragmentation occurs is comparable to the disk dispersal timescale (Klahr & Brandner, 2006). However, if it does occur, the similar fragmentation and dispersal timescales suggest that the fragment would not undergo significant accretion or migration and would leave a wide binary ($a \approx 100AU$) with mass-ratio in the range $0.1 < q < 0.5$.

Unfortunately, there are no true binary population synthesis simulations for high-mass binary systems formed by either mechanism discussed above. The lack of population synthesis models is driven by computational issues; a collapsing cloud that reproduces the stellar IMF *and* generates enough high-mass stars to meaningfully analyze the binary statistics would have to be very massive and therefore difficult to

simulate. Disk fragmentation simulations often either stop the simulation once a fragment forms rather than follow its mass accretion history (e.g. Boss, 2011; Krumholz et al., 2007), or lack high enough resolution to follow the secondary very near the star (e.g. Bonnell & Bate, 2005). Fortunately, such models may be in the near future. Realistic simulations of massive collapsing molecular clouds have begun appearing that can meaningfully discuss the multiplicity of low-mass binary systems (Bate, 2012; Krumholz et al., 2012). These simulations reproduce the observed increase in multiplicity fraction with primary star mass, but do not yet generate enough high-mass binary system to compare the parameter distributions to observations. Despite the current lack of models, we can draw the general conclusion that disk fragmentation tends to produce lower-mass companions than core fragmentation. For this reason, probing the low mass-ratio regime can provide information on the relative importance of both scenarios in forming high-mass binary systems, and may help constrain models once computational power increases.

In addition to binary star formation, disk instability is often invoked as a way to form planets of a few Jupiter masses orbiting $\sim 1 M_{\odot}$ stars. While the massive star formation process as a whole may not simply be a scaled up version of low-mass star formation (Zinnecker & Yorke, 2007), the process of disk fragmentation may be. One expects that disks around high-mass stars, with correspondingly higher accretion rates and more mass, fragment more often than disks around low-mass stars (Boss, 2011, 2006; Dodson-Robinson et al., 2009; Kratter & Matzner, 2006). Thus, if disk fragmentation plays an important role in high-mass star formation, it may also play a role in low-mass star formation by creating $\sim 10 M_{Jup}$ planets and substellar companions.

6.1.2 Observing low mass-ratio binaries

Detection of OB-star binaries with mass-ratio $q \approx 0.1$ or lower is very difficult, since the ratio of the secondary flux F_s to the primary flux F_p is $F_s/F_p \sim 10^{-3}$ or lower in the V-band. Imaging surveys can detect such contrast ratios for wide orbits, but lose sensitivity as the separation decreases below about $1''$ (e.g. Maíz Apellániz, 2010). Spectroscopic binary surveys do well for short-period systems where a full orbit can be mapped in a reasonable amount of time, but lose sensitivity for periods greater than about one year (e.g. Sana et al., 2009; Evans et al., 2010). However, low-mass

companions ($q \lesssim 0.2$), which induce a small reflex motion on the primary, are very difficult to find with traditional spectroscopic surveys.

One method to find low-mass companions to late B-type primaries is to search for high x-ray emission. Stars later than about B3 are not expected to have strong enough winds to emit X-rays (Gagne et al., 1997), and stars of earlier type than about A7 do not have a radiative-convective boundary that can drive a magnetic dynamo and create an X-ray generating corona (Schmitt, 1997). Stars in between spectral types B4 and A7 with strong X-ray emission are thought to have young low-mass companions, because the luminosity and X-ray spectral energy distribution is similar to observed T-Tauri stars (Huélamo et al., 2000). Evans et al. (2011) use this fact to search fo low-mass companions to late B-stars in the open cluster Trumpler 16. They find a significant number of companions, and set the multiplicity fraction at 39%. This value is a lower limit, but the authors believe that the true value is not much above 39%. Unfortunately, X-ray imaging is not effective for primary star spectral types earlier than B3, which are also strong x-ray emitters (Gagne et al., 1997) and will drown out any companions.

In this paper, we introduce a technique that is sensitive to young binary systems with secondary temperatures 4000 K $\lesssim T_{\rm eff} \lesssim$ 6000K. For early B-type primaries with ages $\sim$ 15 Myr, these temperatures correspond to mass-ratios $q \approx 0.05 - 0.3$, right where we expect to see binaries formed by disk instability (see section 6.1.1). Rather than attempting to detect the reflex motion of the parent star as in exoplanet searches and SB1 binaries, we attempt to directly detect the spectrum of the young low-mass companion using high signal-to-noise, high-resolution data. There is a multitude of archived B-star observations in the near-infrared, where they are used as telluric standard stars to remove the absorption spectrum of the Earth's atmosphere (telluric lines). This method is equally sensitive to all separations within the point spread function, which is dominated by the seeing since the adaptive optics are not used in telluric standard star observations. A typical seeing of $\sim 0.8''$ corresponds to up to $\sim$ 900 AU for targets within a few kpc. In this paper, we describe a search for young F5-K9 type companions in archived VLT/CRIRES spectra of 34 early B-type stars.

In section 6.2 we describe our detection method in more detail. Section 6.3 describes the B-star sample we use in this work. Section 6.4 contains the data reduction and telluric correction methods. We summarize our results in section 6.5. We examine the completeness of our sample in section 6.6 and put limits on the multiplicity

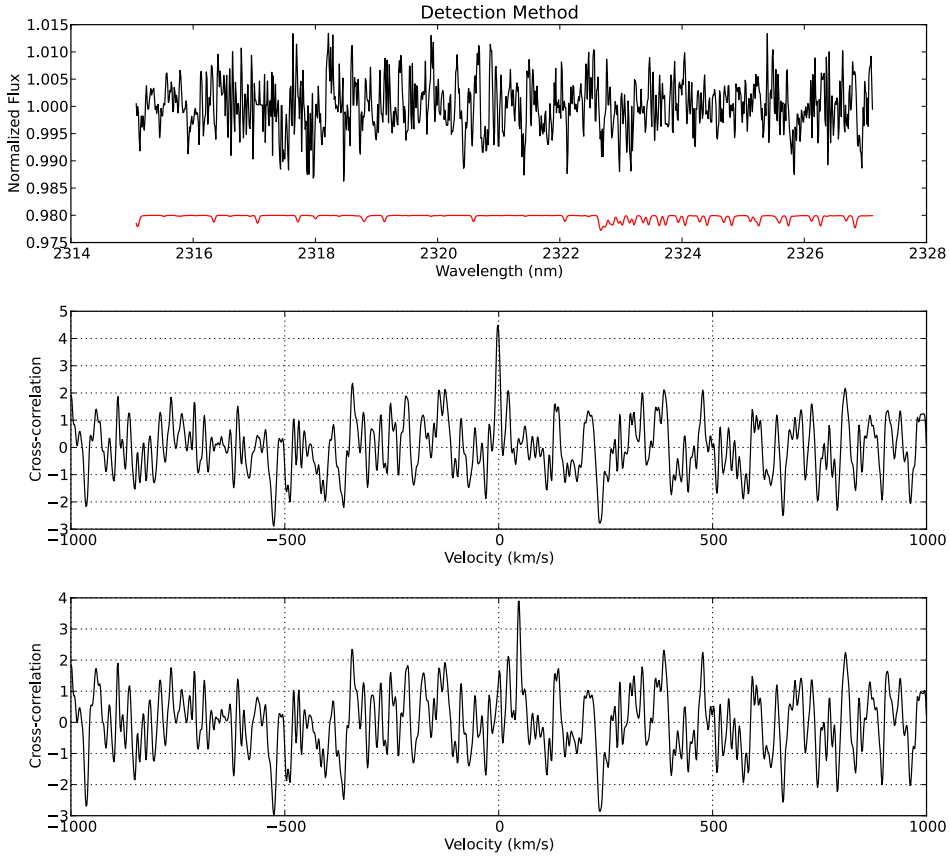

Figure 6.1: This figure illustrates the approximate flux ratio limit to the detection method outlined in section 6.2. *Top panel*: Residuals after telluric correction (see section 6.4) for chip 2 of HIP 80582 are in black, with an atmosphere model for an $0.9M_{\odot}$ star at 50.1 Myr below it in red. The flux ratio at this age is $F_s/F_p = 0.0092$. *Middle panel*: The scaled model spectrum was added to the telluric residuals, and then the sum was cross-correlated with the model. Despite the signal being significantly below the noise level, the star was detected at a high significance. The y axis, in units of the standard deviation of the cross-correlation function, shows that the significance of the peak is over 4σ. *Bottom panel*: Same as the middle panel, but the model spectrum was added to the residuals with a 50 km s^{-1} velocity offset.

fraction as a function of mass-ratio in section 6.7. Finally, we present our conclusions about the prevalence of low mass-ratio companions to early B-type stars and discuss how our results constrain star formation mechanisms in Section 6.8.

6.2 Direct Spectral Detection Method

We describe here our method to detect the emission from an approximately solar-mass star orbiting an early B-type star, which we will hereafter call the direct spectral detection method. The basis of this method is to cross-correlate a high signal-to-noise ratio B-star spectrum with a synthetic F,G, or K star spectrum. If a low-mass star with such a spectrum is orbiting the B-star, we expect to find a peak in the cross-correlation function at the radial velocity corresponding to the low-mass star's motion. A peak in the cross-correlation function should appear even if the flux from the low-mass star is comparable to or even slightly less than the noise level in the spectrum. Figure 6.1 illustrates the approximately limiting case for the flux ratio. The top panel shows a fully reduced CRIRES spectrum of HIP 108975 (see section 6.4) with a model spectrum for an $0.9 M_{\odot}$ star at a realistic flux ratio below it. We used evolutionary tracks published by Landin et al. (2008) to evolve the secondary star to 50.1 Myr, the age of the system (Tetzlaff et al., 2010), in order to determine the flux ratio between the primary and secondary. The secondary star model was then added to the telluric-corrected B-star spectrum at two different velocities. It is clear that the model spectrum has an amplitude much smaller than the noise. Nonetheless, the bottom two panels show that a cross-correlation will have a peak with high significance at the velocity of the secondary star.

A careful choice of the wavelength region is critical for the direct spectral detection method. First, we want a wavelength region where the B-star spectrum is mostly continuum (i.e. very few spectral lines). Since B-stars have few spectral lines, it is easy to find a such a spectral region. Secondly, we want a region where the low-mass star would have many closely spaced, strong lines. The more lines there are in the low-mass star, the stronger the peak will be in the cross-correlation function. Finally, we want a spectral region where the flux ratio between the low-mass and the high-mass star is maximized. It is not helpful to go much redder than a few microns for companions with $T > 4000$K, because both the high-mass and the low-mass star are firmly in the Rayleigh-Jeans limit by this point, where the flux ratio is approximately constant. For this project, we choose wavelengths from $2300 - 2400$ nm, which is the CO $\Delta\nu = 0 - 2$ bandhead in the low-mass star.

There is both a lower and upper mass detection limit. Secondary stars that are too cool will be too faint, and any signal will be lost in the noise. Additionally, a more

massive (and hotter) primary star will decrease the flux ratio, and push the lower mass limit up. On the other end, secondary stars that are too hot will dissociate CO, destroying the bandhead that we are looking for. The temperature and size of the secondary star will depend on its age as well as its mass since it will still be evolving towards the Main Sequence during the lifetime of the B-star. The exact mass sensitivity will thus depend on the age, primary star mass, and signal-to-noise ratio of the system being observed.

The detector resolution is also important for the direct spectral detection method. Deeper lines, providing more contrast from the continuum, are easier to detect than broad, shallow lines. In addition, narrow spectral lines will result in a stronger, narrower peak in the cross-correlation function, which is most sensitive to the steep line edges. Therefore, we want the spectral lines in the low-mass companion to be as deep and narrow as possible. The intrinsic width of CO bandhead lines is roughly 5-7 km s^{-1}. In order for the observed line width to be this small, we need the resolution of the instrument to be $R = \lambda/\Delta\lambda \gtrsim 50000$.

There are two main difficulties with the direct spectral detection method: telluric line removal and the low flux ratio between the primary and secondary star. Figure 6.2 shows the transmittance through the Earth's atmosphere (the telluric spectrum) in the wavelength range we are interested in. Most of the spectral lines are from methane, with a few deep water lines towards the red end of the range shown (See section 6.4 for details on the telluric line removal). The low flux ratio makes the telluric contamination especially troublesome, since the telluric lines are stronger than the lines in the companion star spectrum. The flux ratio of $F_s/F_p \sim 10^{-2}$ effectively sets a lower limit on the signal-to-noise ratio for which the direct spectral detection method is possible. Any flux coming from a low-mass star will be completely buried in the Poisson noise for spectra with SNR $\ll 100$. Removal of the telluric contamination will add more noise to the spectrum, so a spectrum should have SNR of a few hundred *before telluric line removal* to have a good chance of detecting a companion.

6.3 Star Sample

B-type stars are commonly used in the near-IR as telluric standard stars. Astronomers will observe their science targets, and then move to a B-type star. Since B-type stars

have few spectral lines relative to cooler stars, most of the observed spectral lines will be from the absorption of Earth's atmosphere (telluric absorption). Therefore, these stars provide an empirical estimate of the telluric spectrum; division of the science spectrum by the normalized standard star spectrum will mostly remove the telluric lines.

Since B-type stars are commonly used as above, there are many high signal-to-noise ratio (S/N $\gtrsim$ 100) observations of such stars in archived data. We used the VLT/CRIRES archive in this project. CRIRES is a high resolution ($R = \lambda/\Delta\lambda \approx$ 100000) infrared spectrograph on the VLT at Paranal Observatory. The detector consists of four 1024x512 ccd chips that are mosaiced end-to-end, and the spectrum falls across them. There are several wavelength settings available, which determine what parts of the spectrum fall on each chip. For wavelength settings in the CO bandhead near 2300 nm, each chip will hold rougly 10 nm of spectrum with roughly 1-2 nm gaps between the chips.

To generate the sample, we started with all single, main sequence B0-B5 stars with CRIRES observations from 2300-2400 nm. We then excluded any shell stars, which have circumstellar disks (Porter & Rivinius, 2003) that may create false positives. Table 6.1 shows the complete sample used in this project. The spectral types and ages were obtained from a catalog of nearby young stars (Tetzlaff et al., 2010). The one exception is HIP 97611, which was not in Tetzlaff et al. (2010). For this star, the age was taken from Westin (1985) and the spectral type from the Simbad database[2] . The distances to all stars were determined from parallaxes given in the Simbad database. The maximum separation column estimates the approximate maximum separation of the binary orbit we are sensitive to, assuming a seeing of 0.8" which is typical of Paranal Observatory. The median of the maximum separations to which we are sensitive is 124 AU. The final column gives the number of distinct observations of the star. We count all nodding positions taken on a given night with the same detector wavelength setting as one observation.

[2] `http://simbad.u-strasbg.fr/simbad/`

6.4 Data Reduction and Telluric Correction

The data reduction was done using standard methods in IRAF[3]. All observations were taken in an AB or ABBA nodding pattern. For each set of AB nods, A-B and B-A frames were made to remove any atmospheric emission lines and dark current. The resulting difference images were then treated to a quadratic nonlinearity correction, using coefficients made available by the CRIRES teamThe corrected frames were then divided by a normalized flat-field. Due to the slit curvature, the spectrum can shift by up to a pixel in the dispersion direction between the A and B nod positions. Therefore, combining the 2D frames before extraction can reduce the spectral resolution and affect the line shapes. For this reason, we combined the nodding positions only after the wavelength calibration and telluric correction. Each nod position was extracted using the optimal algorithm in the apall task in IRAF. The spectra were wavelength calibrated using a model telluric spectrum generated with the atmospheric modeling code LBLRTM(Clough et al., 2005).

For telluric correction, we used a similar procedure to the one outlined by Seifahrt et al. (2010). The atmosphere modeling code LBLRTM was used to generate a synthetic telluric absorption spectrum. The abundances of water, methane, and carbon monoxide were fit using a Python implementation of a Levenberg-Marquardt nonlinear least squares fitting algorithm. The Levenberg-Marquardt fit also refined the wavelength solution to the telluric model, fit the continuum, and fit the resolution of the spectrograph with a Gaussian profile. The FWHM of the profile was the only free parameter in the resolution fit.

The LBLRTM code expects a model atmosphere, which contains the temperature, pressure, and abundance of 30 molecules as a function of atmospheric height. For the majority of molecular species, we used a mid-latitude nighttime MIPAS[4] profile, which provides the temperature, pressure, and abundances of various molecules in 1 km intervals from sea level to 120 km. The low-altitude ($z \lesssim 30$ km) temperature, pressure (Kerber et al., 2010), and humidity (Chacón et al., 2010) profiles were obtained from radiosonde data taken from Paranal Observatory.

The LBLRTM atmospheric modeling code comes with a molecular line list based

[3]IRAF is distributed by the National Optical Astronomy Observatories, which are operated by the Association of Universities for Research in Astronomy, Inc., under cooperative agreement with the National Science Foundation.

[4]`http://www-atm.physics.ox.ac.uk/RFM/atm/`

on the HITRAN 2008 database (Rothman et al., 2009), with a few molecules individually updated. Since none of these updates were relevant for the wavelength range from $2300-2400$ nm, we in essence used the stock HITRAN 2008 database. However, in the process of modeling, we found several water and methane lines that were consistently under- or over-fit. For these cases, we manually adjusted the line strengths in the database. The line strengths were fit visually and should not be considered rigourous new line strengths. Table 6.2 summarizes these changes.

In some of the 2007 data, the first chip was not well illuminated by the flatfield lamp. This introduced an unphysical continuum shape in the data and made the resulting model fit very poor. For these cases, we ignored the first chip in further analysis. In addition, the fourth chip has several bad pixels on the left edge and a streak down the middle. None of the telluric model fits were very good on this chip, and so we have ignored it completely in our analysis.

After the observed spectrum was fit, we found that the residuals still contained large spikes, even on the good detector chips. These spikes can come from a variety of sources. For the deepest lines, simple Poisson noise can create large residuals when dividing by the telluric model. In addition, a poorly fit continuum may cause the model to over- or under-estimate the abundance of a given molecule. This can be especially troublesome for water lines, for which only a few exist in the wavelength region we are investigating. If a strong water line is near the edge of the chip, where the continuum is usually least certain, the best-fit water abundance may be skewed and cause none of the water lines to be well fit. We do know that large residuals are *not* coming from the spectrum of a low-mass star, due to the expected flux ratio between the primary and secondary, $F_s/F_p \sim 10^{-2}$. Any residuals with amplitude greater than 1% of the continuum level come from uncorrected telluric lines, cosmic rays, or bad pixels.

In order to minimize these spikes, we performed a second fit to any residuals significantly above the continuum noise level. To make sure we were not fitting away any low-mass star lines, we only corrected spikes whose amplitude was greater than 5% of the continuum level. In this second fit, we first attempted to fit a Gaussian to each spike. If the spike was well fit by a Gaussian, we divided the residuals by the fit. If not, we simply masked out the line core, so that it would not affect the cross-correlation in later analysis (see section 6.2). Figure 6.3 shows the steps involved in the telluric correction. Notice that the secondary correction removes the large

residuals, while leaving the rest of the spectrum unaffected.

The telluric correction described above usually reduced any telluric lines to near the Poisson noise level in the spectrum, which is the best a fitting routine can do. To search for any systematic errors in the telluric correction, we added all spectra of each wavelength setting together to make a series of master telluric residual spectra. These master spectra had less random noise than any individual observation, and therefore we were immediately able to see whether some telluric lines are systematically under- or over-fit. We found that for wavelength settings with at least ten spectra in our sample, dividing the corrected spectra by this systematic telluric residual template increased the sensitivity to companions. We did not make this final correction for wavelength settings with fewer than ten individual spectra in our sample.

6.5 Results

Each telluric residual spectrum was cross-correlated against a suite of model atmospheres generated by the Phoenix stellar atmosphere code (Hauschildt et al., 1999). All model spectra had solar metallicity. The effective temperatures ranged from $3000 - 7200$ K, in 100K intervals. We used several surface gravities based on the stellar temperature. For the model secondary stars with $3000 < T_{\rm eff} < 3600$, which would have to be very young (and large) to be detectable, we used a $\log(g) = 3.5$. For the secondaries with $3600 < T_{\rm eff} < 6500$, we used $\log(g) = 4.0$. Finally, we used $\log(g) = 4.5$ for $T_{\rm eff} > 6500$, which can be detected closer to the Main Sequence. We found that the surface gravity has only a very small effect on the cross-correlation, which is more sensitive to the line position than its precise width or depth. We compiled a list of all cross-correlations that show a single peak with at least 3σ significance. For a given telluric-corrected residual spectrum, several model atmospheres may generate a significant peak at the same velocity. This is because the model spectra of two stars differing by only a few hundred kelvin are not very different. To keep from counting peaks twice, we only counted the cross-correlation that resulted in the most significant peak at a given velocity. We then attempted to reject spurious peaks caused by the noise or incomplete telluric line removal in a multi-stage process.

The first rejection stage was done by identifying peaks in the cross-correlation caused by telluric residuals. To do this, we cross-correlated a spectrum uncorrected

for telluric absorption with the same suite of model atmospheres as we used for the corrected spectra (see above). We did these cross-correlations for one observation of each wavelength setting. The cross-correlation of uncorrected spectra with model-atmosphere spectra generated a series of cross-correlations with peaks arising exclusively from telluric lines. We visually compared all of the binary candidate signals with these telluric cross-correlations. If the dominant cross-correlation peak was at the same velocity and had a similar width as a peak in the telluric cross-correlation function corresponding to the same wavelength setting and secondary model temperature, we assumed that the peak was caused by incomplete telluric removal and rejected the candidate. There were several cross-correlations with peaks at the same location as a telluric peak, but with a different width. In these cases, we marked the candidate as probably coming from incomplete telluric correction, but did not reject the candidate.

Next, we determined whether the signal-to-noise ratio and telluric line removal in a given observation would allow us to detect the candidate companion star. To do this, we added a model atmosphere with the same temperature as the candidate to the telluric-corrected spectrum at 17 different radial velocities ranging from -400 to 400 km s^{-1}. We do not expect to see any peaks from real companions with $|v| > 400$ km s^{-1}, the approximate radial velocity of a $1M_{\odot}$ star orbiting a $10M_{\odot}$ star such that the stellar surfaces are in contact. The flux ratio of the model atmosphere to the primary was obtained by interpolating pre-main-sequence evolutionary tracks from Landin et al. (2008) at the age of the system, as well at age$\pm\sigma_{age}$. The primary star ages for our sample are given in Table 6.1. We cross-correlated each of these semi-synthetic spectra against the model spectrum; if the largest peak was at the correct velocity, we counted the star as detected. If the star was not detected in the sensitivity analysis at least 50% of the time, we rejected the candidate. The significance of the correct peak in the cross-correlation function can vary greatly, depending on where the stellar spectrum falls in relation to the telluric line residuals. Therefore, we cannot usually reject a peak based solely on its significance.

We then visually inspected the remaining candidate cross-correlations, picking out those with a single dominant peak with $|v_r| < v_{\rm max}$ where $v_{\rm max}$ is the maximum possible radial velocity for a star of temperature $T_{\rm sec}$ to be orbiting a hotter star of temperature $T_{\rm prim}$ with a semimajor axis a. Assuming a circular orbit, $v_{\rm max}$ is given by

$$v_{\max} = \sqrt{\frac{2G(M_{\rm prim} + M_{\rm sec})}{R_{\rm prim}}} \cdot \frac{T_{\rm sec}}{T_{\rm prim}} \tag{6.1}$$

where $M_{\rm prim}$ and $M_{\rm sec}$ are the masses of the primary and secondary stars, respectively, and $R_{\rm prim}$ is the radius of the primary star. The primary masses are given in Tetzlaff et al. (2010), while the radii and primary star temperatures were estimated from spectral type relations given in Carroll & Ostlie (2006). An eccentric orbit could have a larger maximum velocity than that estimated by equation 6.1, if the orbit was oriented such that the the secondary star was moving directly towards or away from earth at or near periastron. A star in an eccentric orbit cannot get so close to the primary that they touch, and its *average* distance must still be far enough to allow for the observed secondary star temperature. These conditions lead to a maximum eccentricity, given by

$$e_{\max} = 1 - \frac{v_{\max}^2 (R_{\rm prim} + R_{\rm sec})}{G(M_{\rm prim} + M_{\rm sec})} \tag{6.2}$$

where $R_{\rm prim}$ and $R_{\rm sec}$ are the radii of the primary and secondary stars, respectively, and $v_{\max}$ is the maximum circular velocity given by equation 6.1. Typical values give $e_{\max} \approx 0.6$. Eccentricities near this value could allow for velocities significantly greater than $v_{\max}$ given by equation 6.1.

The above analysis is summarized in Table 6.3. There are two binary candidate systems that we have not been able to reject. For both of these, we checked what other observations the candidate star had within the CO bandhead spectral region ($2300 - 2400$ nm). The analysis of each of these stars is done separately below.

6.5.1 HIP 26713

The cross-correlation for this candidate is shown in figure 6.4. The strong peak at -220 km s^{-1} has a significance just over 4σ, and corresponds to a 5600 K star model. A sensitivity analysis (Table 6.3, step 2) gives a median peak significance of $\sim 6\sigma$ with a large ($\sim 2\sigma$) spread. Due to the large spread, we cannot reject the peak based on the observed significance.

The candidate radial velocity amplitude of 220 km s^{-1} is very near the upper limit given by equation 6.1 of 256 km s^{-1}. If this candidate is a real binary companion, it

must have been observed very near its radial velocity maximum and the orbital inclination must be very near edge-on. Assuming a circular orbit and equal probabilities of observing any given phase or inclination, the probability of this occuring for this system is ~ 0.01. However, the probability for one system in our entire sample to be caught with this chance alignment rises to 0.14. In addition, we cannot discount the possibility of an eccentric orbit leading to a higher value of $v_{\max}$ than estimated by equation 6.1. Without more data, we can neither confirm nor disprove the existence of a companion star orbiting HIP 26713.

If HIP 26713 is a true binary system, evolutionary tracks by Landin et al. (2008) give a secondary star mass of $1.6 \pm 0.2 M_{\odot}$. The mass of the primary star is $9.4 \pm 0.2 M_{\odot}$ (Tetzlaff et al., 2010), giving a mass-ratio of $q = 0.17 \pm 0.02$. For a circular orbit, the corresponds to an orbital period of 10.0 days. If the companion star is on an eccentric orbit, its true period would be longer than this.

6.5.2 HIP 92855

There were seven observations of HIP 92855 on different dates, all with the 2336 nm wavelength setting. The cross-correlations for four of the observation dates show a single strong peak when using a 6100K model star as template. Figure 6.5 shows the cross-correlations of the telluric-corrected spectra with a 6100K model for all of the observations. Table 6.4 summarizes the sensitivity and cross-correlation significance. The detection rate is the fraction of the 17 radial velocities between -400 and 400 km s^{-1} that were correctly detected in the sensitivity analysis (Table 6.3, step 2). The variation in detection rate is due to the different signal-to-noise levels and telluric line corrections in the observations at different dates. The expected significance is the median significance of the radial velocities which were detected in the sensitivity analysis, in units of the standard deviation of the cross-correlation function. The observed significance and velocity are for the observed peaks. The velocities in Table 6.4 are corrected for the barycentric motion and the known systematic radial velocity of HIP 92855, while those in Figure 6.5 are not.

As Table 6.4 shows, a 6100K star orbiting HIP 92855 is at the limit of detectability with the direct spectral detection method. With the exception of the observation on 2007 September 16, the cross-correlations for the dates with the highest detection rates have a single large peak. We consider this an excellent candidate for follow-up

observations.

If HIP 92855 is a true binary system, evolutionary tracks by Landin et al. (2008) give a secondary star mass of $1.2\pm0.2M_{\odot}$. The mass of the primary star is $7.8\pm0.2M_{\odot}$ (Tetzlaff et al., 2010), giving a mass ratio of $q = 0.15 \pm 0.04$. The maximum radial velocity, observed on 2007 August 2, was 234 km s^{-1}. If this is the radial velocity semi-amplitude and if the companion is on a circular orbit, the binary orbit would have a period of 6.8 days. If the true velocity semi-amplitude is larger either because no observation was taken when the companion star was at quadrature or because the orbit is inclined, the period would be shorter than this. If the companion star is on an eccentric orbit, the period could be longer than 6.8 days if the large velocity observed was near periastron.

6.6 Completeness

We now estimate the completeness of the direct spectral detection method applied to this data set. For each telluric-corrected observation, we created a series of synthetic binary-star spectra by adding stellar models to the data at various flux ratios, temperatures, and radial velocities. We used evolutionary tracks from Landin et al. (2008) to find the luminosity of model companion stars with temperatures ranging from 3000K to 7000K in steps of 500 K. To find the model flux ratio F_s/F_p, we used the best-fit age for each star quoted in Table 6.1, as well as the best-fit age$\pm\sigma_{age}$. Model secondary spectra generated with the Phoenix code (Hauschildt et al., 1999) were added to the telluric-corrected observations at 17 different radial velocities ranging from -400 to +400 km s^{-1}. Changing the radial velocity of the model spectrum changes where the companion spectral lines fall with respect to the telluric lines. Finally, we cross-correlated each synthetic spectrum with its corresponding model secondary star spectrum, and examined the cross correlation function.

If the highest peak in the cross-correlation function was at the correct velocity, the companion was considered detected. We then tabulated how many times the companion star was detected in the 17 radial velocity trials. Figure 6.6 shows the fraction of trials that detected the companion for all of the model radial velocities, as a function of primary (B-star) mass and the binary mass-ratio. The points correspond to individual spectra, with their sizes indicating the signal-to-noise ratio in the

spectrum, and the contours are drawn by interpolating between the points. The four panels are for different companion star temperatures. Companion stars with effective temperatures from $4600 - 5400$ K have large regions with a very high detection rate. Stars cooler than about 4600 K are too dim to detect without much higher signal-to-noise ratios than present in our dataset, and stars hotter than about 5400 K do not have a strong CO bandhead and so the cross-correlation function is not as sensitive.

Figure 6.6 shows that the direct spectral detection method is able to find companion stars with a mass-ratio of $q \approx 0.1 - 0.2$, for a range of effective temperatures. The regions with a detection rate near 1 are completely sampled, and a companion star in that region would be detected. For primary stars with $M < 10 M_{\odot}$, we are sensitive to almost all companions with $4600 < T_{\rm eff} < 5400$ K.

6.7 Multiplicity Fraction

We have not found any unambiguous low mass-ratio companions in our sample, though we do have two candidates that require follow-up observations (HIP 92855 amd HIP 26713). From the work described in section 6.6, we define a range of mass-ratios for which the direct spectral detection method is sensitive for each primary (B-) star. We can then rule out any companions with mass-ratios in that range, for that primary star.

In order to convert these star-by-star limits on the presence of a companion into upper limits on the multiplicity fraction of the parent population, we first count the number of stars that rule out companions in a particular range of mass-ratios. We then apply binomial statistics, where the probability P of finding k companions from n samples of a parent population with a true binary fraction p is given by

$$P(k|p,n) = \frac{n!}{k!(n-k)!} p^k (1-p)^{n-k} \tag{6.3}$$

For no detected binary companions (k=0), the corresponding likelihood function for the binary fraction is

$$P(p|k=0,n) = (n+1) \cdot (1-p)^n \tag{6.4}$$

A 90% upper limit is given by

$$0.9 = \int_0^p (n+1) \cdot (1-p')^n dp' \tag{6.5}$$

with solution

$$p_{90} = 1 - 0.1^{\frac{1}{n+1}} \tag{6.6}$$

A similar derivation gives 90% upper limits for one detection (k=1). Figure 6.7 shows the 90% upper limits to the binary fraction as a function of mass-ratio. To find n in equation 6.6, we counted the number of stars that ruled out a companion at the given mass-ratio. We only counted companions that were found in all 17 radial velocity trials (see section 6.6), and were always found with at least 4σ significance. We also included upper limits assuming that HIP 92855, the more likely of our two candidates, is a true binary system. Figure 6.7 also shows the lower multiplicity limit set by Evans et al. (2011) (blue dotted line) and the *intrinsic* O star mass-ratio distribution derived by Sana et al. (2012). Evans et al. (2011) do not split their multiplicity by mass-ratio, and so the line shown in figure 6.7 is an average value. While we include them for comparison with our results, neither of these studies are directly comparable to our sample. Sana et al. (2012) have only O stars in their sample and are only able to measure mass-ratios $q \approx 0.2 - 1$, although they consider mass-ratios down to $q = 0.1$ when deriving the intrinsic distribution. Evans et al. (2011) are sensitive to similar mass-ratios as our sample, but they sample late B-stars (B4-B9) while we sample early B stars (B0-B5). Our results are almost perfectly complementary to those of Evans et al. (2011). It is encouraging that our upper limits for $0.1 < q < 0.2$, where our sample is most complete, lie in between the results of Sana et al. (2012) who measure the binary fraction of more massive primaries, and Evans et al. (2011) who measure the binary fraction of less massive primaries than we do.

The above analysis assumes that the sample of B-stars given in Table 6.1 is representative of the B-star population as a whole. Most of the sample stars are field B-stars, which have a lower overall multiplicity than cluster or association B-stars (Mason et al., 2009). However, the close binaries this method is sensitive to would be difficult to disrupt with dynamical interactions in a cluster environment, and we therefore expect this sample to be representative of both populations. A potential complication is that telluric standard stars are often chosen specifically because they

are *not* known binary systems. While this may introduce a bias for large mass-ratios, the direct spectral detection method is sensitive to low mass-ratio companions that may not have been found with other methods such as classical spectroscopy or imaging and so companions with $q \lesssim 0.2$ may be less effected. The amount of bias introduced into the above measurement depends on how carefully the individual observers chose the telluric standard stars, and so is very difficult to assess.

6.8 Conclusion

We have described a new technique for finding binary systems with a flux ratio of $F_p/F_s \approx 100$, where F_p and F_s are the fluxes from the primary and secondary star, respectively. In this technique, which we call the direct spectral detection technique, we use high signal-to-noise, high resolution spectra of a binary candidate. We remove the contamination from the Earth's atmosphere with the telluric modeling code LBLRTM, and cross-correlate the residuals with a library of stellar models for late type stars (F2-M5). A binary detection would appear as a strong peak in the cross-correlation function.

We prove the feasibility of the direct spectral detection method by adding a synthetic signal to real data, and successfully recovering it. We further investigate the completeness of the method in section 6.6. This method is sensitive to detecting a range of companion stars, set by the spectral type and age of the primary and the signal-to-noise ratio of the observation. Our sample is sensitive to almost all companion stars with $4600 < T < 5400$, corresponding to binary mass-ratios of $0.1 \lesssim q \lesssim 0.2$.

We have applied this technique to a sample of 34 archived main sequence early B-stars (B0-B5) with spectra taken with the CRIRES near-infrared spectrograph. We found no unambiguous companions in our sample, but identify two targets as candidate binary systems: HIP 92855 and HIP 26713. HIP 92855 is B2.5V type star, with a candidate companion star with effective temperature $T = 6100$ K and mass $1.2 \pm 0.2 M_\odot$. Such a companion star is very near the detection limit of the direct spectral detection technique and deserves further follow-up observations. HIP 26713 is a B1.5V type star, with a candidate companion star with $T = 5600$ K and $M = 1.6 \pm 0.2 M_\odot$. This star was only observed once in our sample, and so may be a series of incompletely removed telluric absorption lines masquerading as a companion

star.

We set upper limits on the binary fraction of early B stars as a function of binary mass-ratio (see Figure 6.7). As well as showing the upper limit for no detections in our sample, we also show the binary fraction upper limit assuming the HIP 92855 is a true binary system. Our upper limits are strongest for mass-ratios $q \approx 0.1 - 0.15$, and are about 20%. We compare our limits to the intrinsic binary mass-ratio distribution for O-type primaries derived by Sana et al. (2012), as well as the lower limit *average* binary fraction seen by Evans et al. (2011) for late B-stars (B4-B9). Our strongest upper limits ($0.1 \leq q \leq 0.15$) fall in between these two previous studies.

Companion stars formed by circumstellar disk instability are expected to have typical mass-ratios near $q = 0.1$ (Kratter & Matzner, 2006; Stamatellos & Whitworth, 2011), near where our upper limits are strongest. If there was a large population of low mass-ratio companions formed by disk fragmentation, we would expect to see a peak in the mass-ratio distribution near $q \approx 0.1$. Since our results agree well with the nearly flat mass-ratio distribution derived by Sana et al. (2012), it is unlikely that such a peak exists. There are several possible interpretations of this result, three of which we give below.

1. Stellar companions formed by disk instability have a much lower characteristic mass-ratio than $q = 0.1$ which remain invisible to observations.

2. The mass-ratio distribution of companions formed by disk instability is very broad, and so we would not expect a strong peak in the observed mass-ratio distribution. This interpretation may be supported by the flatness of the mass-ratio distribution as well as disk instability simulations that end with massive companions (e.g. Krumholz et al., 2009; Clarke, 2009).

3. Disk instability is not a dominant formation mechanism for low mass-ratio binary systems, and molecular core fragmentation alone can generate the nearly flat mass-ratio distribution down to low mass-ratios.

It is difficult to distinguish between these interpretations at this time. More observational work, as well as computational work, is required to explain the binary properties of high-mass stars.

We would like to acknowledge Andreas Seifahrt, Rob Robinson, and Daniel Jaffe for their generous help with the telluric modeling procedure and some of the statistical

aspects of this work. We would also like to thank the referee for a quick review and many helpful comments. This research has made use of the following online resources: the SIMBAD database and the VizieR catalogue access tool at CDS, Strasbourg, France, and the ESO Science Archive Facility. Funding for this work was provided by a National Science Foundation CAREER award to Sarah Dodson-Robinson (AST-1055910) and by start-up funding from the University of Texas College of Natural Sciences.

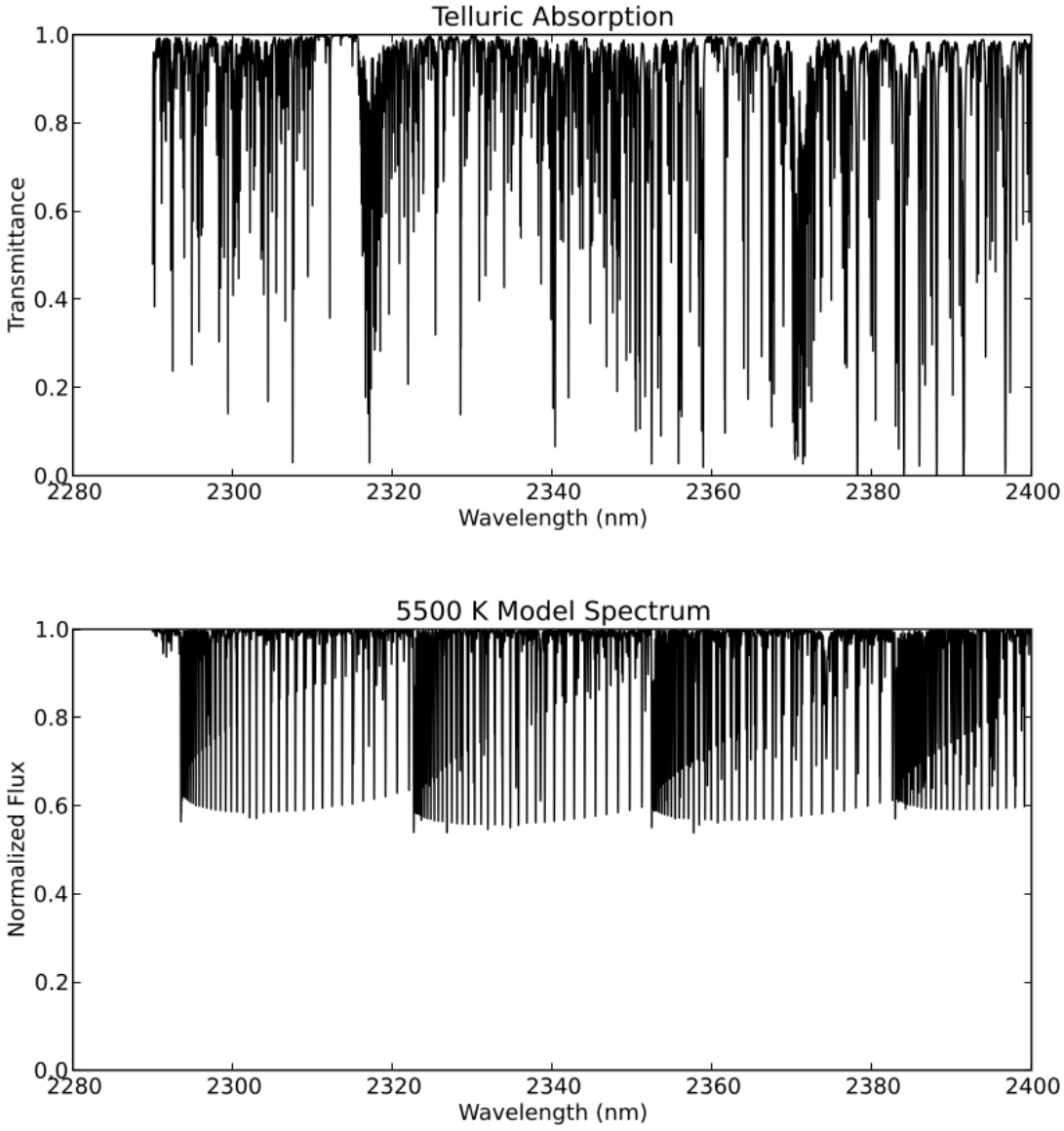

Figure 6.2: *Top panel*: The telluric spectrum (absorption due to Earth's atmosphere) in the wavelength range from $2290 - 2400$ nm. Most of the lines are from CH_4, with a few H_2O lines appearing in the right half. *Bottom panel*: The model spectrum of a 5500 K star with $\log(g) = 4.0$ and solar metallicity. Note that the line density of telluric lines is comparable to or greater than that of the star model, and many of the telluric lines are stronger than the stellar lines.

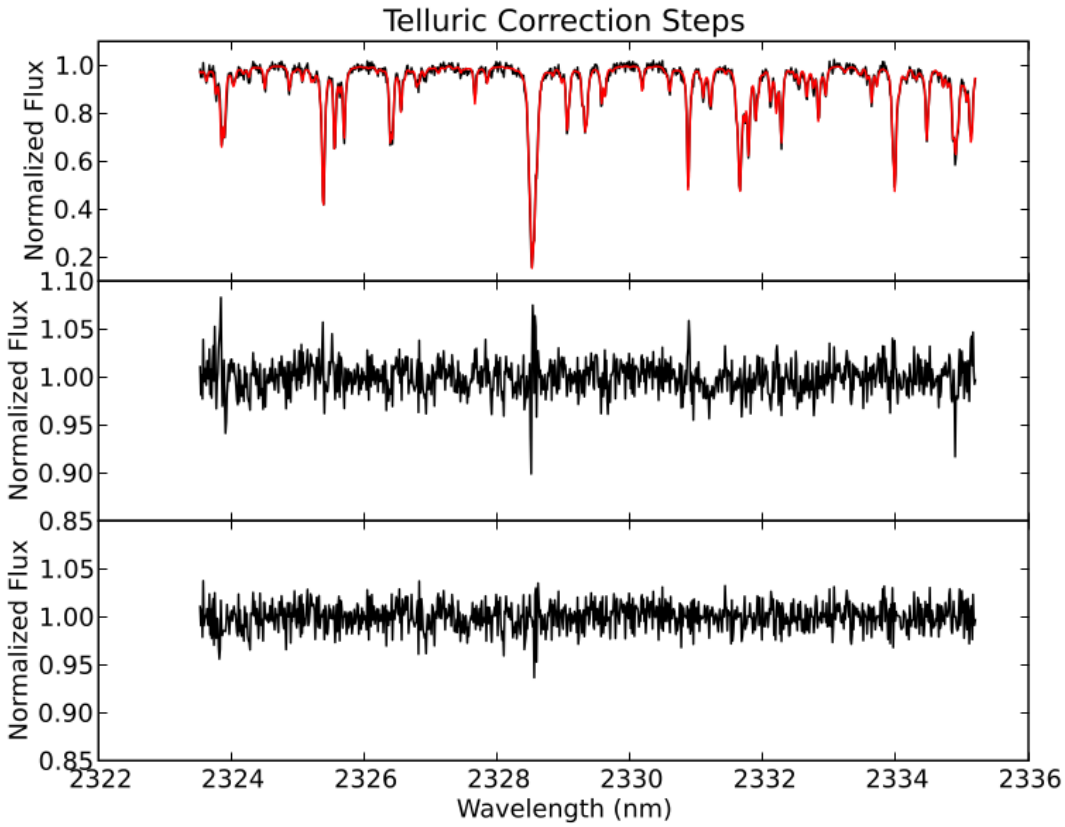

Figure 6.3: The telluric correction steps for chip three of CRIRES wavelength setting $\lambda_{ref} = 2329.3$ nm. *Top panel:* Normalized spectrum (black), with the best-fit telluric model (red). *Middle panel:* Residuals after dividing the observed spectrum by the telluric model. Note the large spikes near 2328.5, 2331, and 2335 nm. *Bottom panel:* Correction after fitting the large residuals to Gaussians.

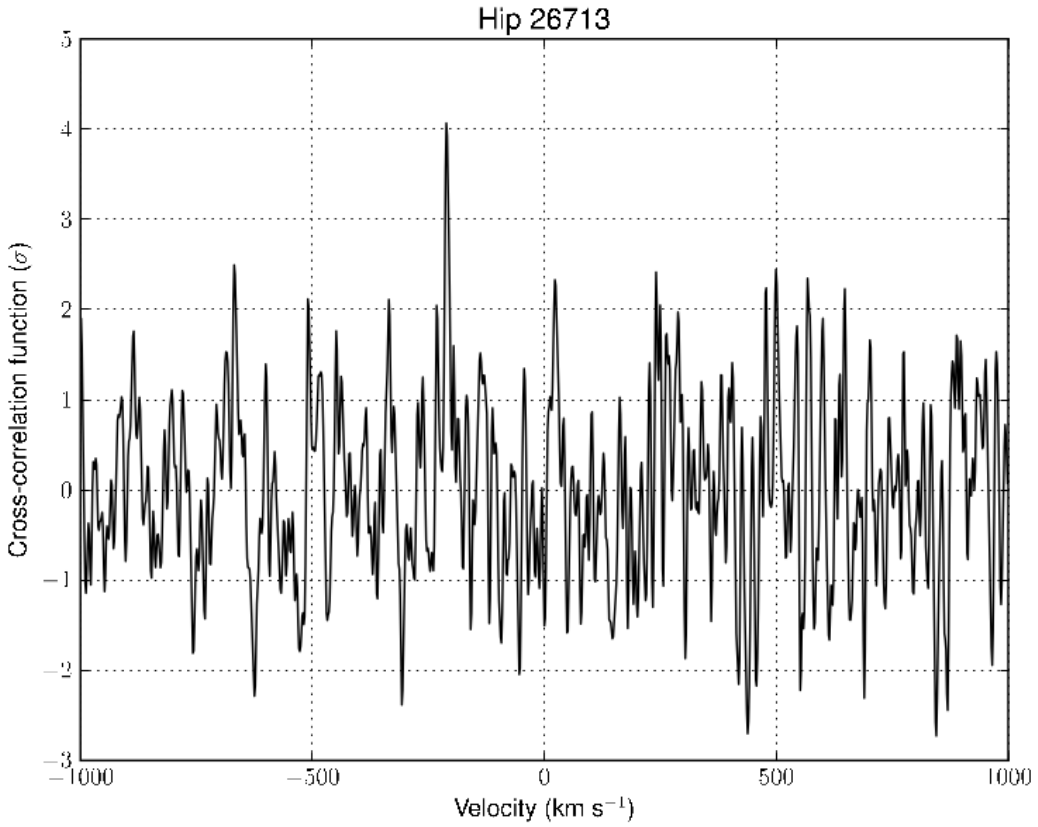

Figure 6.4: Cross-correlation for HIP 26713, using a 5600 K star model spectrum as template. The y-axis is in units of the standard deviation of the cross-correlation function. The peak is very near the maximum velocity of $|v_{\max}| = 256$ km s^{-1}, assuming a circular orbit (see equation 6.1). The likelihood of observing the system nearly edge on and at a quadrature point, so that $|v| \sim |v_{\max}|$, is $p \approx 0.01$. However, it is possible that the system has an eccentric orbit, effectively increasing $|v_{\max}|$.

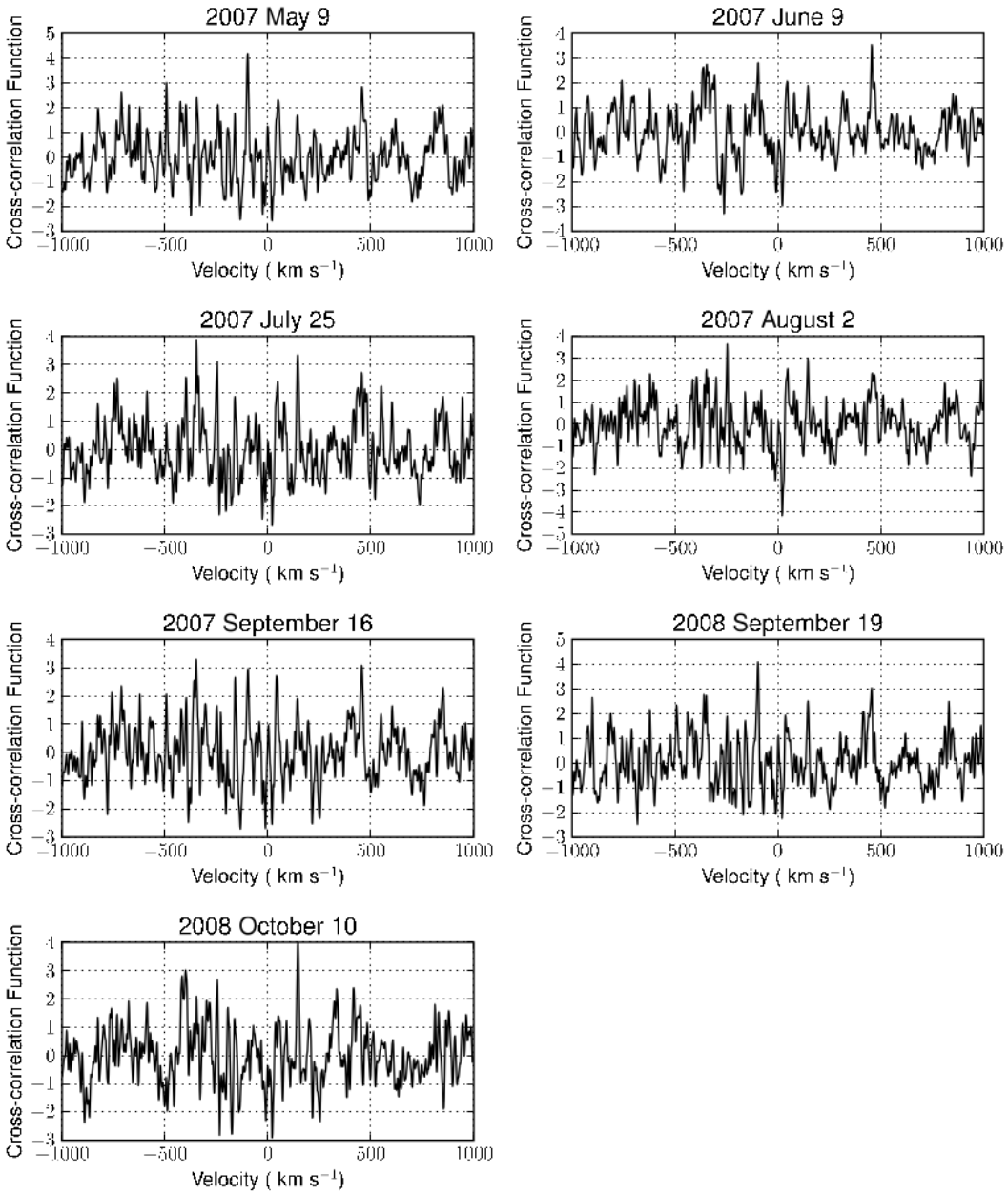

Figure 6.5: Cross-correlations for HIP 92855, for all dates observed. A 6100 K star model spectrum is used as the template for each cross-correlation. The y-axis is in units of the standard deviation of the cross-correlation function. A single strong peak is seen in the cross-correlations from 2007 May 9, 2007 August 2, 2008 September 19, and 2008 October 10. The reasonably strong peak on 2007 June 9 is identified as probably arising from imperfect telluric line removal or random noise, since it has $v > v_{\rm max}$ given by equation 6.1.

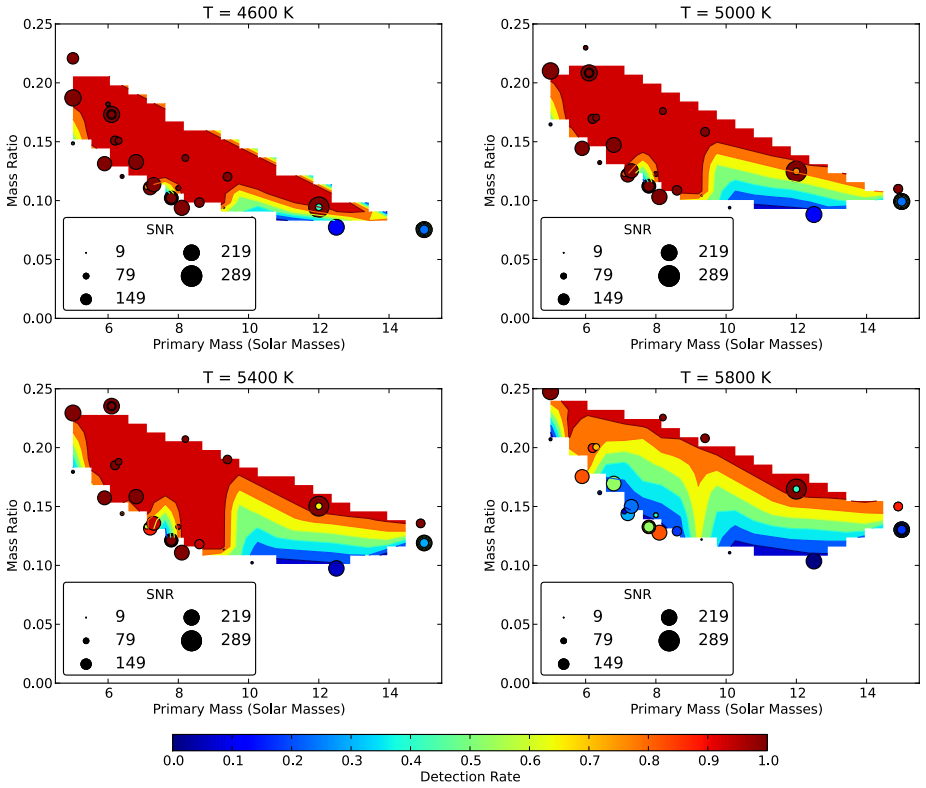

Figure 6.6: Completeness diagram for the full sample of main-sequence B stars, split up by the effective temperature of the secondary star. The points correspond to the individual stars in the sample, and their sizes reflect the signal-to-noise ratio in the spectrum. Note that the signal-to-noise is calculated after the telluric line removal, and counts any telluric residuals as noise. The figures are also color-coded by the fraction of trials that detected the companion (see section 6.6). Contours are drawn to guide the eye. The red areas in each plot indicate the regions for which our sample is complete.

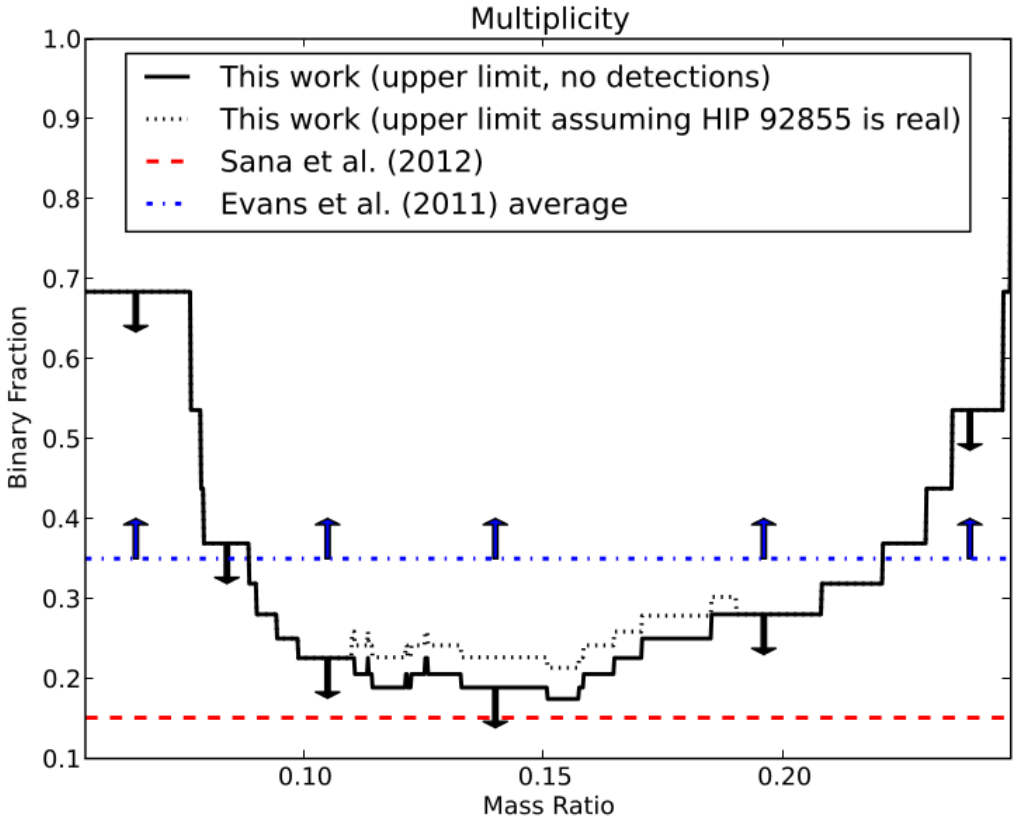

Figure 6.7: Estimates of the binary fraction of B0-B5 stars, as a function of binary mass-ratio. This work found no unambiguous companions, and so we give 90% upper limits (solid black line). 90% upper limits are also given assuming that HIP 92855 is a real binary system (dotted black line). The upper limits are only different within the 1σ error bars on the mass-ratio for HIP 92855. The nearly flat distribution found by Sana et al. (2012) is shown as the dashed red line. The average binary fraction found by Evans et al. (2011) is also shown (dash-dot blue line). The Evans et al. (2011) value is a *lower* limit and an average over all mass-ratios from $0.1 < q < 0.3$, but they estimate that their sample is very complete, and so the true multiplicity fraction is quite close to their value.

Table 6.1: Full star sample

Star	Spectral Type	Age (Myr)	Distance (pc)	Maximum Separation (AU)	Number of Observations
HIP 23364	B3V	31.6 ± 0.6	31.65	25.32	1
HIP 26713	B1.5V	7.2 ± 2.5	138.89	111.11	1
HIP 27204	B1IV/V	12.6 ± 4.6	408.2	326.5	1
HIP 30122	B2.5V	32 ± 0.4	111.1	88.9	4
HIP 32292	B2V	8.2 ± 0.1	1111.1	888.9	1
HIP 39866	B3V	25.1 ± 2.6	840.3	672.3	1
HIP 48782	B3V	32.3 ± 0.6	370.4	296.3	1
HIP 52370	B3V	17.2 ± 1.3	58.14	46.51	2
HIP 52419	B0Vp	4 ± 0.7	250	200	2
HIP 54327	B2V	11.7 ± 6.2	252.5	202.0	3
HIP 55667	B2IV-V	22.5 ± 2.6	847.5	678.0	1
HIP 60823	B3V	25.3 ± 6.3	39.53	31.62	5
HIP 62327	B3V	8.2 ± 1.8	121.95	97.56	4
HIP 63945	B5V	27.3 ± 11.4	36.63	29.3	1
HIP 61585	B2IV-V	18.3 ± 3.2	96.7	77.4	8
HIP 62327	B3V	8.2 ± 1.8	117.9	94.3	4
HIP 63007	B4Vne	53.3 ± 8.1	117.6	94.1	2
HIP 63945	B5V	27.3 ± 11.4	119.6	95.7	1
HIP 67796	B2V	15.4 ± 0.4	970.9	776.7	1
HIP 68282	B2IV-V	13 ± 2	76.92	61.54	2
HIP 68862	B2V	9.1 ± 3.8	109.89	87.91	1
HIP 71352	B1Vn + A	5.6 ± 1	178.57	142.86	2
HIP 73129	B4Vnpe	27.1 ± 6.1	36.9	29.52	1
HIP 74110	B3V	33.2 ± 7.3	30.12	24.1	1
HIP 76126	B3V	15.9 ± 1.3	62.89	50.31	1
HIP 78820	B0.5V	13.8 ± 0.4	123.9	99.1	1
HIP 80582	B4V	50.1 ± 14	19.96	15.97	2
HIP 80815	B3V	10.5 ± 2.1	95.24	76.19	4
HIP 81266	B0.2V	5.7 ± 1	175.44	140.35	12
HIP 82514	B1.5Vp+	20 ± 2	50	40	1
HIP 87314	B2/B3Vnn	23.2 ± 2.9	43.1	34.48	7
HIP 92855	B2.5V	31.4 ± 0.4	31.85	25.48	7

Table 6.1 – Continued

Star	Spectral Type	Age (Myr)	Distance (pc)	Maximum Separation (AU)	Number of Observations
HIP 92989	B3V	7.9 ± 2.1	126.58	101.27	1
HIP 97611	B5V	45 ± 10	66.67	53.33	1

Table 6.2: Summary of adjusted line strengths. The units of line strength are $cm^{-1}/(molecule \times cm^{-2})$

Wavelength (nm)	Molecule	Old Strength	New Strength
2317.12	CH_4	5.445×10^{-21}	5.034×10^{-21}
2318.24	H_2O	1.400×10^{-24}	2.256×10^{-24}
2328.51	CH_4	2.521×10^{-21}	2.371×10^{-21}
2328.56	CH_4	1.270×10^{-21}	1.358×10^{-21}
2340.12	CH_4	3.085×10^{-21}	2.963×10^{-21}
2340.36	CH_4	3.343×10^{-21}	3.211×10^{-21}
2351.64	H_2O	1.670×10^{-23}	1.393×10^{-23}
2351.69	H_2O	1.085×10^{-23}	7.985×10^{-24}
2352.43	CH_4	3.144×10^{-23}	4.031×10^{-24}
2352.45	H_2O	4.639×10^{-23}	4.939×10^{-23}
2353.62	CH_4	2.708×10^{-21}	2.654×10^{-21}
2355.82	CH_4	5.101×10^{-21}	4.949×10^{-21}
2358.9	CH_4	5.160×10^{-21}	4.710×10^{-21}
2364.03	H_2O	1.408×10^{-23}	1.217×10^{-23}
2367.23	H_2O	2.078×10^{-23}	2.182×10^{-23}
2370.35	CH_4	4.028×10^{-21}	3.625×10^{-21}
2370.41	CH_4	2.437×10^{-21}	2.021×10^{-21}
2370.75	CH_4	1.466×10^{-21}	9.138×10^{-22}
2371.39	H_2O	3.905×10^{-23}	3.171×10^{-23}
236.62	H_2O	1.146×10^{-23}	9.186×10^{-24}
2376.63	H_2O	3.824×10^{-24}	3.820×10^{-24}
2378.2	H_2O	1.134×10^{-22}	1.021×10^{-22}
2379.67	H_2O	6.334×10^{-24}	8.408×10^{-24}
2385.98	H_2O	6.051×10^{-23}	5.407×10^{-23}

Table 6.3: Summary of Cross-Correlation Function Peak Rejection Steps. See Section 6.5 for more information

Step	Description	Method
1	Telluric Residual Peak Identification	Compare cross-correlation function of telluric-corrected spectrum with that of an uncorrected spectrum.
2	Sensitivity Analysis	Check that signal-to-noise ratio is high enough to detect secondary candidate at a range of velocities
3	Velocity Analysis	Check that a blackbody with the candidate temperature can exist as close to the primary B-star as the velocity indicates (assumes circular orbit)

Table 6.4: Summary of HIP 92855 observations. Significance is in units of the standard deviation of the cross-correlation function. The detection rate and expected significances are from the sensitivity analysis (Table 6.3, step 2).

Date	Detection Rate	Expected Significance	Observed Significance	Velocity (km s^{-1})
2007 May 9	0.35	3.3 σ	4.1 σ	-74
2007 June 9	0.18	3.6 σ	N/A	N/A
2007 July 25	0.35	3.7 σ	N/A	N/A
2007 August 2	0.47	3.6 σ	3.5 σ	-234
2007 September 16	0.82	4.2 σ	N/A	N/A
2008 September 19	0.71	3.4 σ	4.1 σ	-126
2008 September 10	0.59	3.3 σ	4.0 σ	116

Chapter Seven: The Inner Mass-Ratio Distribution of Intermediate-Mass Stars[1]

7.1 Background

Stellar multiplicity is an inevitable and common outcome of star formation, with roughly half of all solar-type field stars in binary or multiple systems (Raghavan et al., 2010) and an even higher fraction as the stellar mass increases (Zinnecker & Yorke, 2007). Young stellar associations and clusters tend to have even higher multiplicity (Duchêne & Kraus, 2013), indicating that stars often form in multiple systems that are subsequently destroyed by dynamical interactions as the cluster dissociates.

The overall multiplicity rate and the distributions of mass ratio, period, and eccentricity of a binary star population place important constraints on the mode of binary star formation. While the period and eccentricity are altered by dynamical processing in the birth cluster, the present-day mass ratio of a binary system is a direct result of its formation (Parker & Reggiani, 2013). Most binary stars are thought to form via core fragmentation (Boss & Bodenheimer, 1979; Boss, 1986; Bate et al., 1995), in which a collapsing core fragments into two or more individual protostars. The number and initial masses of the fragments are set by the total core mass, as well as its rotation, turbulence, and its temperature and density structure. If the fragments are well separated ($a \gtrsim 1000$ AU), they will evolve independently of each other, accreting mass from the core material onto their own protostellar disks and then onto the protostars themselves. However close fragments ($a \sim 100$ AU) will interact with each other; the protostellar disk may be truncated, destabilized, or form into a circumbinary disk if the separation is small enough (Bate & Bonnell, 1997). In addition, an unstable disk can fragment to form low-mass companions (Kratter & Matzner, 2006; Stamatellos & Whitworth, 2011). The mass ratios of close companions formed via either mechanism should be affected by preferential accretion. Most work has suggested that the disk material will preferentially accrete onto the

[1]This chapter has been accepted for publication to the Astronomical Journal, but is not yet published.

lower mass companion (Bate & Bonnell, 1997; Bate et al., 2002); however, recent work has indicated that magnetic disk braking may result in preferential accretion onto the more massive component (Zhao & Li, 2013) instead. In either case, we would expect to find a mass-ratio distribution for companions inside a few 100 AU that differs from that of companions on wider orbits.

The mass ratio, period, and eccentricity distributions are well-known for solar type stars (Duquennoy & Mayor, 1991; Raghavan et al., 2010) and cooler stars (Fischer & Marcy, 1992; Delfosse et al., 2004). Interestingly, Reggiani & Meyer (2011), and later Reggiani & Meyer (2013), found that the mass-ratio distribution of field solar-type and M-dwarf stars is invariant to separation. The field M-dwarf semimajor axis distribution peaks near ~ 5 AU (Duchêne & Kraus, 2013), with very few companions at separation $\gtrsim 100$ AU; the 27 stars used in the analysis by Reggiani & Meyer (2011) is unsufficient to compare the mass-ratio distribution inside ~ 100 AU with that outside it. However, the solar-type period distribution peaks near 45 AU (Raghavan et al., 2010), with roughly 40% of binary systems on orbits wider than 100 AU. The nondetection of a difference in mass-ratio distribution is significant, although with only 30 stars in the field sample it is difficult to completely rule out that such a difference exists.

All of the orbital distributions are much less certain for more massive stars. The reason for this is two-fold: first, more massive stars tend to be more distant than sunlike or low-mass stars, meaning many of the companions are angularly close to the primaries and difficult to detect with imaging techniques. Second, the primary stars tend to be rapid rotators, which limits radial velocity precision to ~ 1km s^{-1} and causes the spectral lines of double-lined systems to blend. Radial velocity monitoring can only measure a mass ratio if spectral lines from both components are visible and separable; this typically suffers from the same flux ratio difficulty as imaging techniques.

Nonetheless, De Rosa et al. (2014) performed an adaptive optics imaging survey of nearby A-type stars, and found that the mass-ratio distribution is well-described by a power law with large slope, indicating a very strong preference for low-mass companions. They also found initial evidence that the mass-ratio distribution for companions inside 125 AU has a much shallower power law slope than that of wide companions, and is consistent with flat. Their close companion subsample contained only 18 binary systems, and the result is complicated by the inherent difficulty of

detecting close companions with low mass ratios in an imaging survey.

Radial velocity monitoring surveys can detect much closer companions than imaging surveys, but are typically only complete to low-mass companions if the primary is a slow rotator. Chemically peculiar Am stars are typically associated with binary companions, and are slow rotators due to tidal braking; they thus form a highly biased sample of intermediate-mass stars. Nonetheless, it is interesting to note that they have a mass-ratio distribution which peaks near $q \sim 0.5$ (Vuissoz & Debernardi, 2004), an entirely different form than the distribution found around chemically normal stars at wide separations.

In this paper, we describe a spectroscopic survey of nearby chemically normal, main sequence intermediate-mass stars ($M \approx 1.5-15 M_{\odot}$). We search for companions using the direct spectral detection technique (Gullikson et al., 2016), which has a separation-invariant detection rate for all separations inside $\sim 1''$. We describe the stellar sample and data used for the survey in Section 7.2, as well as the data reduction steps in the same section. Next, we describe the direct spectral detection method and tabulate the companion detections in Section 7.3. We estimate the mass and age of the sample stars in Section 7.4, and discuss the survey completeness in Section 7.5. Finally, we end with a derivation of the mass-ratio distribution from our sample in Section 7.6 and discuss its implications for binary formation in Section 7.7.

7.2 Observations and Data Reduction

The stellar sample for this survey is defined by the following criteria:

- $V < 6$ mag
- $v \sin i > 80$km s^{-1}
- Spectral Type A or B with the following additional constraints
  - Main Sequence
  - No spectral peculiarities except for 'n', which denotes broad lines.

The magnitude limit ensures that a sufficiently high signal-to-noise ratio can be achieved in a short period of time. It does introduce a Malmquist bias in the derived

mass ratio, which we discuss and correct for in Section 7.6. Likewise, the $v \sin i$ limit makes accounting for the primary star spectrum in the companion search trivial; since most A- or B-type stars are rapid rotators, the cutoff removes less than half of the stars from the potential sample. We exclude pre-main sequence stars because both the primary and the companion mass would depend very strongly on young and uncertain ($\lesssim 1$ Myr) evolutionary models. Finally, we exclude post-main sequence stars from our sample because the binary flux ratio would be even less favorable to companion detection in an evolved star. Most of the spectral peculiarities denote narrow lines, which are already removed from the sample by the $v \sin i$ cut. The sample is given in Table 7.1. The spectral type, coordinates, V magnitude, and parallax are all adopted from the Simbad Database (Wenger et al., 2000), while the stellar effective temperature, surface gravity, masses, and ages are discussed in Section 7.4.

The sample, being comprised of early-type stars, is heavily biased towards young stars. The estimated ages range from about 10 Myr to 1 Gyr, with most falling in the range of a few tens or hundreds of Myrs. The sample also mostly contains nearby stars, although the magnitude limit provides a greater extent than a volume-limited survey would have. The parallactic distances in our sample range from $\sim 15 - 2000$ pc. The maximum detectable separation, which we define as the point at which the companion is no longer guaranteed to fall on the spectrograph slit (see Section 7.2.1 for a description of the spectrographs we use), is $\sim 20 - 4000$ AU. The median parallactic distance in our sample is 95 pc, corresponding to a projected separation of $\sim$ 200 AU. Most of the companions we are able to detect are close enough to have been impacted by the circumprimary disk, with 85% of the sample sensitive to companions inside 100 AU.

7.2.1 Spectroscopic Data

We use several high spectral resolution, cross-dispersed échelle spectrographs for this survey. We use the CHIRON spectrograph (Tokovinin et al., 2013) on the 1.5m telescope at Cerro Tololo Inter-American Observatory for most southern targets. This spectrograph is an $R \equiv \lambda/\Delta\lambda = 80000$ spectrograph with wavelength coverage from 450 - 850 nm, and is fed by a $2.7''$ optical fiber. The data are automatically reduced with a standard CHIRON data reduction pipeline, but the pipeline leaves residuals of strong lines in adjacent orders. We therefore bias-correct, flat-field and extract the

spectra with the optimum extraction technique (Horne, 1986) using standard IRAF[2] tasks, and use the wavelength calibration from the pipeline reduced spectra.

For the northern targets, we use a combination of the High Resolution Spectrograph (HRS, Tull, 1998) on the Hobby Eberly Telescope, and the Tull coudé (TS23, Tull et al., 1995) and IGRINS (Park et al., 2014) spectrographs, both on the 2.7m Harlan J. Smith Telescope. All three northern instruments are at McDonald Observatory. For the HRS, we use the $R = 60000$ setting with a $2''$ fiber, and with wavelength coverage from 410-780 nm. We bias-correct, flat-field, and extract the spectra using an IRAF pipeline very similar to the one we use for the CHIRON data. The HRS spectra are wavelength-calibrated using a Th-Ar lamp observed immediately before or after the science observations.

For the TS23 spectrograph, we use a $1.2''$ slit in combination with the E2 échelle grating (53 grooves/mm, blaze angle 65°), yielding a resolving power of $R = 60000$ and a wavelength coverage from 375-1020 nm. We reduce the data using an IRAF pipeline very similar to the ones we use for CHIRON and HRS, and wavelength calibrate using a Th-Ar lamp observed immediately before the science observations.

IGRINS has a single setting with $R = 40000$. It has complete wavelength coverage from $1475 - 2480$ nm, except in the telluric water band from $1810 - 1930$ nm. Each star is observed in an ABBA nodding mode, and reduced using the standard IGRINS pipeline (Lee, 2015). The standard pipeline uses atmospheric OH emission lines as well as a Th-Ar calibration frame to calibrate the wavelengths; we further refine the wavelength solution using telluric absorption lines in the science spectrum.

After reducing the data, we fit and remove the telluric spectrum using the TelFit code (Gullikson et al., 2014). We fit each échelle order affected by telluric absorption independently from each other to get the best removal. The telluric correction is critical for IGRINS spectra, where every order is dominated by telluric absorption lines. For the optical spectra, it is less critical but allows us to use some of the redder orders than we otherwise would be able to. For unsaturated lines, the best-fit telluric model reproduces the data to within $\sim 1 - 5\%$ of the continuum level.

We give the spectroscopic observation log in Table 7.2. We calculate the signal-to-noise ratio (the "snr" column) for the optical instruments (CHIRON, TS23, and

[2]IRAF is distributed by the National Optical Astronomy Observatories, which are operated by the Association of Universities for Research in Astronomy, Inc., under cooperative agreement with the National Science Foundation.

HRS) as the median of the extracted flux divided by it's uncertainty for each pixel from the échelle order nearest 675 nm. For the IGRINS instrument, we calculate the signal-to-noise ratio from the order nearest 2200 nm.

7.2.2 Imaging Data

As part of the follow-up effort, we used the NIRI instrument behind the Altair adaptive optics system on the Gemini North Telescope. For each star listed in Table 7.3, we obtained 25 images in 5 dithering positions. We used the K-continuum band centered on 2.2718 μm and a variety of exposure times and dates (listed in Table 7.3). Because the targets are all extremely bright, we used the high read noise and high flux detector settings to allow for very short co-add exposure times. We reduced the data using the Gemini set of IRAF tasks, which include steps for nonlinearity correction, flat-fielding, sky subtraction, and co-addition of the dither frames.

We measure the flux and position of both stars by fitting a 2D Moffat function (Moffat, 1969) to both stars simultaneously, constraining the shape parameters for both functions to be the same. The ratio of the amplitudes gives the magnitude difference, and the pixel locations along with the detector pixel scale gives the separation and position angle between the stars. We note that the goal of these images was confirmation and we did not observe any reference targets to make a distortion map and correct the image rotation. The uncertainty in position angle and to a lesser degree separation quoted in Table 7.3 is likely underestimated.

7.3 Companion Search

We search for stellar companions to our sample stars using the direct spectral detection technique, described in detail in Gullikson et al. (2016). In short, we unsharp-mask each spectrum using a gaussian filter with width proportional to the primary star $v \sin i$ to remove the broad lines from the primary star. We then cross-correlate each échelle order of each filtered spectrum against a large grid of Phoenix model spectra (Husser et al., 2013) with the following parameters:

- $T_{\rm eff} = 3000 - 12000$ K, in steps of 100 K
- [Fe/H] = -0.5, 0.0, +0.5

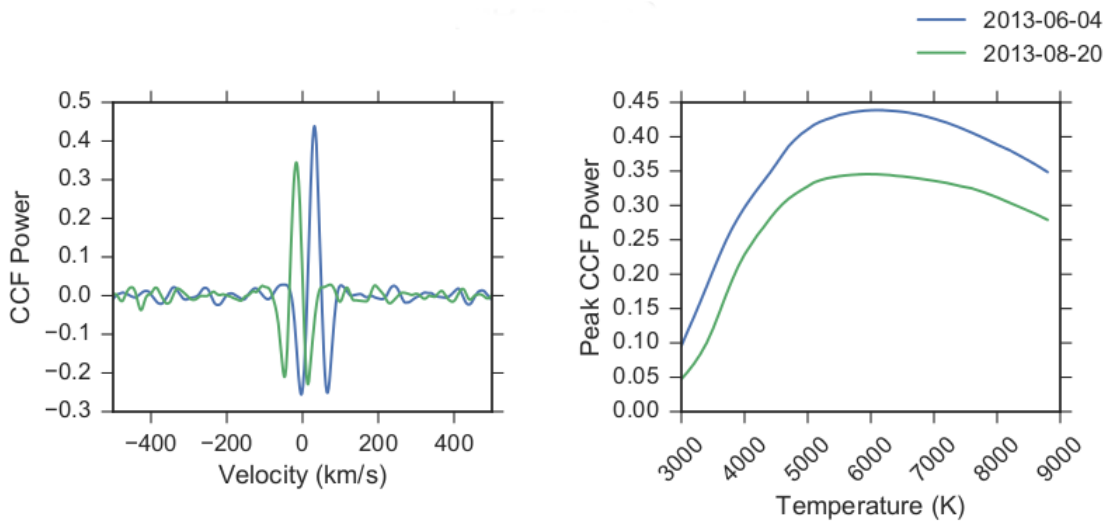

Figure 7.1: *Left*: Cross-correlation function between the observed spectra of HIP 109139 and a 5700 K Phoenix model spectra. The detection at two dates shows significant velocity variation, indicating orbital motion with a short period. *Right*: Peak CCF height as a function of Phoenix model spectra template temperature. The maxima of the curves indicate the temperature of the companion.

- $v \sin i = 1, 5, 10, 20, 30$ km s^{-1}

In order to be sensitive to hot companions, we additionally cross-correlate the spectra against a second grid of Kurucz model spectra (Castelli & Kurucz, 2003). The change in model is necessary because the Phoenix model library does not extend beyond 12000 K. The Kurucz grid is defined as follows:

- $T_{\rm eff} = 9000 - 30000$ K, in steps of 1000 K
- [Fe/H] = -0.5, 0.0, +0.5
- $v \sin i = 1, 5, 10, 20, 30, 40, 50$ km s^{-1}

We combine the cross-correlation functions for all orders using both a simple average and the maximum-likelihood weighting scheme (Zucker, 2003). A companion detection is denoted by a strong peak in the combined cross-correlation function (CCF). While the maximum-likelihood scheme produces detections with much higher

significance, it also magnifies spurious peaks and so has a larger false-positive rate. For this reason, we use the simple average CCFs in all further analysis.

The peak height in the CCF as a function of the stellar model acts in a similar way to the more typical χ^2 map of parameter space. More concretely, as the stellar model template gets closer to the true companion spectrum, the CCF peak gets higher. We can therefore measure the companion temperature and, to a lesser degree its metallicity and $v \sin i$, in a single spectrum. We calculate the measured temperature (T_m) and variance (σ_T^2) as a weighted sum near the grid point with the highest CCF peak value, weighting by the peak CCF height at each temperature (C_i):

$$T_m = \sum_i C_i T_i / \sum_i C_i \tag{7.1}$$

$$\sigma_T^2 = \frac{\sum_i C_i (T_i - T_m)^2}{\sum_i C_i - \sum_i C_i^2 / \sum_i C_i} \tag{7.2}$$

Typical uncertainties are on the order of 200 K. In the case of multiple observations for the same star, we use the variance-weighted mean of the individually measured temperatures.

Imperfect stellar models cause a bias between the true companion temperature and the measured temperature (T_m). This bias is most pronounced at low temperatures, where the difficult-to-model molecular absorption becomes important. We correct for the bias by applying the linear calibrations developed in Gullikson et al. (2016). These calibrations are only valid for companions with $3000 < T_{\rm eff} < 7000K$; for detections at hotter temperatures we assume that the temperature which produces the maximum CCF peak is an *unbiased* estimator of the true companion temperature.

We list the companion detections in Table 7.4, and report the estimate of the companion temperature, $v \sin i$, and metallicity derived from the model parameters which produce the largest CCF peak. The $v \sin i$ and metallicity values do not have uncertainties and should only be taken as a rough estimate of the true value. The mean and standard deviation of the companion metallicities is -0.29 ± 0.30; the marginal bias towards low metallicities is most likely a measurement bias and does not reflect the true companion population (Gullikson et al., 2016). We show the detection CCFs and a plot of peak CCF height as a function of model temperature for HIP 109139 in Figure 7.1. Similar figures for all companions are available in the supplementary files.

We have follow-up spectroscopy for 15/23 of the new companions to confirm their existence. In most cases, there is a clear shift in the radial velocity of the companion, indicating that it is orbiting the target star and is not a foreground or background contaminant (See Figure 7.1). Two of the new detections (companions to HIPs 38593 and 79404) were detected twice but not in a third attempt, most likely because the third spectrum had low signal-to-noise. The companion to HIP 93805, at $\sim$ 4000 K, was detected twice with near-infrared IGRINS but not the optical CHIRON instrument that is less sensitive to cool companions than IGRINS. Two of the companions with only one detection were observed at least twice (HIPs 19949 and HIP 23362); both of the non-detections are from the IGRINS instrument, which is less sensitive to hot companions with rapid rotation speeds because there are far fewer spectral lines of the companion in the near-infrared than there are in the optical.

In addition to the spectroscopic follow-up, we obtained Gemini/NIRI adaptive optics imaging data for 18 of the northern companions, and were able to resolve 7 of them. We show the separation, position angle, and magnitude difference measurements in Table 7.3, and display the images in Figure 7.2. We also derive the projected separation in AU and the companion mass from the images. We calculate the separation from the measured angular separation and the Hipparchos parallax (ESA, 1997). We calculate the companion mass and uncertainties from 1000 samples of the magnitude difference measurement and the primary star mass, temperature, age, and radius (see Section 7.4). For each sample, we use a grid of Kurucz stellar model spectra (Castelli & Kurucz, 2003)and the pysynphot code[3] to determine the companion temperature needed to replicate the observed magnitude difference. We estimate the companion radius by interpolating solar metallicity Dartmouth isochrones (Dotter et al., 2008) from the companion temperature and system age sample. We convert the best temperature to a companion mass using the same isochrone grid. The masses derived from the imaging data have very large uncertainties because the primary star property estimates that they depend on are very uncertain. The imaging masses agree with the spectroscopically-derived masses in Table 7.4, with the exception of HIP 115115 which has a much higher mass from the imaging data than the spectroscopic data. The spectroscopic masses for all stars are more reliable, since they are less model-dependent.

[3]pysynphot is a python package to perform synthetic photometry, and is available at this url: `https://pypi.python.org/pypi/pysynphot`

One star in the imaging sample, HIP 88116, has several nearby sources in the image. We quote the magnitude difference and separation of the brightest source in Table 7.3, but stress that *none* of the visible sources is likely to be the companion we see in the spectroscopic data. The two epochs of spectroscopic data show a radial velocity shift of $\Delta v = 30.7$ km s^{-1} over the course of roughly one year; this orbital motion is much too large to allow for any of the companions visible in the image (all with separations $> 1''$ and projected separations > 300 AU).

7.4 Sample Star Parameters

In order to convert from companion temperature to mass ratio, we first need an estimate of the primary mass. In addition, since the primary stars in our survey have short main-sequence lifetimes, some companions may still be contracting onto the main sequence and so an age estimate for the system is necessary to convert from companion temperature to mass.

About half of our sample stars have robust mass and age estimates from Strömgren uvbyβ photometry (David & Hillenbrand, 2015). For those that do not, we estimate the mass and age of the system from our spectra. We first cross-correlate the data against a grid of solar metallicity Kurucz model spectra (Castelli & Kurucz, 2003) spanning

- $7000\ K < T_{\rm eff} < 30000\ K$ in steps of 500 K for $T < 10000\ K$, and in steps of 1000 K for hotter templates.
- $3.0 < \log g < 4.5$ in steps of 0.5 dex
- $75 < v \sin i < 300$ kms^{-1} in steps of 25 kms^{-1}

For the optical data, we use the blue échelle orders ($\lambda < 5550\mathring{A}$). We ignore the strong hydrogren Balmer lines in the spectrum because they span several échelle orders and make continuum normalization very difficult, potentially biasing the result. There are sufficient metal lines in the optical spectra that the resulting CCF always has a very strong peak at the radial velocity of the primary star. The near-infrared IGRINS spectra have very few strong metal lines; we use the subset from $1.51-1.73\mu m$ that is dominated by hydrogren Brackett lines for these spectra. Similar to the

companion search, we estimate the temperature and surface gravity of the stars from the CCF with the largest peak. We adopt the following errors on the temperature and surface gravity, which are based on the grid step size and are somewhat more pessimistic than typical uncertainties seen in the literature for A- and B-type stars (e.g. Aydi et al., 2014; David & Hillenbrand, 2015):

$$\sigma_T = \begin{cases} 500\ K & T < 10000\ K \\ 1000\ K & T >= 10000\ K \end{cases} \tag{7.3}$$

$$\sigma_{\log g} = 0.25 \tag{7.4}$$

The IGRINS parameters are less reliable because they rely almost solely on the hydrogren Brackett lines that span an entire échelle order, so we double the uncertainty on the IGRINS-derived temperature and surface gravity. Additionally, we throw out the IGRINS parameters if the star was also observed by one of the optical instruments in our survey. For stars observed multiple times, we use the average parameters and reduce the uncertainties accordingly.

Next, we use Padova stellar evolutionary tracks (Bressan et al., 2012) and the isochrones code (Morton, 2015) to estimate the mass and age of the system from the measured temperature and surface gravity. As a consistency check, we also interpolate from a table of stellar properties as a function of spectral type (Pecaut & Mamajek, 2013) to estimate the primary mass from the published spectral types. We show the comparison in Figure 7.3. We estimate uncertainties in the spectral type mass by assuming a spectral type uncertainty of ± 0.5 spectral types and propagating to mass. There is excellent agreement between the masses we measure and the spectral type masses.

We show the temperature, surface gravity, mass, and age estimates for most of our sample stars in Table 7.1. We do not give parameters for the few stars that show strong discrepancies with the spectral-type estimate, most of which are early B-stars that have temperatures higher than the maximum grid temperature of 30000 K.

7.5 Survey Completeness

The detectability of a companion mostly depends on its temperature: cooler companions emit much less light and so are increasingly lost in the Poisson noise from the primary star spectrum. A companion with a high rotation rate is also more difficult to detect because the cross-correlation function gets most of its power from narrow spectral lines.

7.5.1 Injection and Recovery Tests

To quantify the detection rate as a function of companion temperature and $v \sin i$, we performed a series of injection and recovery experiments. We started by creating synthetic binary star observations from each of our observed spectra. We made two distinct grids of companion stars: a low temperature grid spanning

- $3000\ K < T_{\rm eff} < 6500\ K$ in steps of $100\ K$
- $0\ \mathrm{km\ s^{-1}} < v \sin i < 50\ \mathrm{km\ s^{-1}}$ in steps of $10\ \mathrm{km\ s^{-1}}$

and a high temperature grid spanning

- $7000\ K < T_{\rm eff} < 12000\ K$ in steps of $1000\ K$
- $100\ \mathrm{km\ s^{-1}} < v \sin i < 250\ \mathrm{km\ s^{-1}}$ in steps of $50\ \mathrm{km\ s^{-1}}$

For each grid point, we added a solar metallicity Phoenix model spectrum to the observed data after scaling to replicate the expected flux between a main sequence companion of the model temperature and the known target star spectral type. If the target star had known companions within $3''$, we included the expected flux from the companion when computing the flux ratio. We repeated each grid point at different radial velocities spanning $-400\ \mathrm{km\ s^{-1}} < v < 400\ \mathrm{km\ s^{-1}}$ in $50\ \mathrm{km\ s^{-1}}$ steps to sample the noise properties of the spectra and estimate a probability of detection at each point.

Next, we cross correlated all of the synthetic observations against the Phoenix model template that was used to construct them. We counted the companion as detected if the highest point in the resulting CCF was found at the correct radial velocity, and if the peak had a significance of $> 5\sigma$, where σ is the standard deviation

of the CCF for points more than 100 km s^{-1} away from the peak. We combined all of the radial velocity trials for each grid point to estimate a probability of detection at that grid point:

$$P(\text{detection}) = \frac{N_{\text{detected}}}{N_{\text{rv}}} \tag{7.5}$$

where $N_{\text{rv}} = 17$ is the number of radial velocity trial points.

Finally, we interpolated between the grid points using a linear radial basis function interpolator (Figure 7.4). In order to extrapolate from our grids to estimate the detection rate at high temperature and low $v \sin i$ and at low temperature and high $v \sin i$, we made the following assumptions about the shape of the two-dimensional detection rate surface: First, we assumed that if all companions are detected at temperature $T = 6500$ K and rotation speed $v \sin i$, then all companions with the same $v \sin i$ and larger temperature will also be detected (lower right points in Figure 7.4). Likewise, we assume that if no companions are detected at temperature T and rotation speed $v \sin i = 50$ km s^{-1}, then no companions will be detected at the same temperature and faster rotation speeds (upper left points in Figure 7.4). We tested the former assumption with injection and recovery experiments on a small subset of stars, and found that it is valid.

Figure 7.4 shows a clear diagonal dividing line between hot, slow rotators that are always detected and cool, fast rotators that never are. Additionally the figure shows that very fast rotators are never detected, regardless of their temperature, because the signal is completely removed when we unsharp-mask the data (see Section 7.3).

7.5.2 Marginalization

By sampling a suitable distribution of $v \sin i$ values for a star of each temperature, we marginalize over the rotation speed:

$$Q(T) = \sum_k Q(T, v_k) v_k \tag{7.6}$$

where $Q(T, v)$ is the surface plotted in Figure 7.4 and v_k are the samples from the distribution of $v \sin i$. For $T < 6000$ K, we sample $v \sin i$ using the gyrochronology relation given in Barnes (2010):

$$\frac{k_C t}{\tau} = \ln\left(\frac{P}{P_0}\right)\frac{k_I k_C}{2\tau^2}(P^2 - P_0^2) \tag{7.7}$$

In Equation 7.7, k_C and k_I are constants fit to data with known ages and rotation periods, P and P_0 are respectively the current and zero-age main sequence (ZAMS) rotation periods, τ is the convective turnover time scale and t is the current age of the star. We use the same values that Barnes (2010) use for the constants:

- $k_C = 0.646$ day/Myr
- $k_I = 452$ Myr/day

We estimate the convective timescale (τ) by interpolating Table 1 of Barnes & Kim (2010). We then randomly draw a system age t from its probability distribution function (see Section 7.4 and Table 7.1). Young stars have rotation periods in the range of 0.2 to 10 days (Bouvier et al., 2014), so we randomly choose an initial rotation period P_0 from a log-uniform distribution in this range for each age sample. Equation 7.7 then gives a current rotation period for each sample, which we convert to an equatorial velocity with the stellar radius R. We estimate R by interpolating Dartmouth pre main sequence isochrones (Dotter et al., 2008) using the companion temperature and system age. We finally convert to projected velocity $v \sin i$ by randomly sampling a uniform distribution for the inclination $\sin i$.

The gyrochronology relations are invalid for stars with $T \gtrsim 6250\ K$, the canonical limit at which the convective zone is too small to efficiently remove angular momentum to the stellar wind and spin down the star (Pinsonneault et al., 2001). Zorec & Royer (2012) fit maxwellian distributions to the equatorial velocity of A- and B-type stars in several mass bins. For $T > 7000\ K$, we linearly interpolate the fit parameters as a function of mass and sample the resulting maxwellian probability density function.

Typical velocities from the gyrochronology relationships are $10 - 20$km s^{-1}, while the maxwellian velocity distributions have typical velocities ~ 100km s^{-1}. We transition between the two regimes for temperatures in the range $6000\ K < T < 7000\ K$ by first estimating the equatorial velocities from the gyrochronology relationship (Equation 7.7) at $T = 6000\ K$. We then fit the velocities to a maxwellian distribution, and add the result to the tabulated parameters from (Zorec & Royer, 2012). With

the extended table, we treat stars in the transition range the same way we treat hot stars.

We show the marginalized detection rate and mean value of $v \sin i$ as a function of temperature in Figure 7.5. Both the detection rate and the average $v \sin i$ are smoothly varying, and show the expected behaviour with temperature. The detection rate falls with hotter temperatures because the companions are expected to be fast rotators, which are more difficult to detect.

7.5.3 Conversion to Mass Ratio

The result of the previous analysis is a series of estimates for the detection rate as a function of companion temperature for each observation of each star. We convert companion temperature to mass by interpolating Table 5 of Pecaut & Mamajek (2013). Next, we estimate the primary mass for each star as the median of the mass samples developed in Section 7.4. We then convert each detection rate curve to be a function of mass ratio ($Q_j(q)$, where j denotes the jth star in the sample), and linearly interpolate onto a grid in mass ratio from $0 < q_i < 1$. Finally, we combine the detection rate curves for each star *with no companion detection in our data* into an estimate of the survey-wide completeness by taking the average of the detection rate for all stars:

$$Q(q_i) = \frac{1}{N_i} \sum_j Q_j(q_i) \tag{7.8}$$

In the equation above, N_i is the number of sample stars that contain an estimate for $Q(q_i)$ without extrapolating. For $q_i \sim 0.2$, N_i is near the total sample size. However, N_i falls for both low and high q, since a 3000 K/12000 K companion has a mass ratio $q = 0.08/2.0$ for an A9V primary, but $q = 0.007/0.19$ for a B0V primary. Our sensitivity analysis therefore does not sample large mass ratios around the very early-type primary stars in the sample, and does not sample very low mass ratios around late-type primary stars.

Gullikson et al. (2016) used a very similar method to search for known companions to A- and B-type stars, and found that the detection rate is high for G- and K-dwarf companions but very low for hot companions. The search grid used in this work includes much hotter temperatures, and we have several detections of hot companions

(see Table 7.4). We test to determine if the completeness is reasonable at large mass ratios by comparing to known binary systems. We detect 15 of the 25 stars in our sample with a hot ($T > 7000\ K$) companion in either the Washington Double Star Catalog (Mason et al., 2014) or the Ninth Catalog of Spectroscopic Binary Orbits (Pourbaix et al., 2009). The completeness function for hot, roughly equal-mass companions suggests the probability of detection is $\sim 80\%$, which is still incompatible with our low detection rate. The discrepancy may be due to an underestimate of the typical rotation rates for hot stars, which we use when marginalizing out the dependence on $v \sin i$. Additionally, rapidly rotating companions, especially when they have a similar temperature to the primary, are more difficult to detect if they have a small radial velocity offset from the primary star. While the injection and recovery experiments do sample velocity space to account for this, they may be over-sampling companions with very large velocity offsets and producing anomalously high detection rates. We account for the discrepancy by introducing a scaling factor: we multiply the estimated detection rate for all companions with $T > 7000\ K$ by $f = 0.8$.

We show the resulting total survey completeness in Figure 7.6. The completeness falls very rapidly towards low mass ratios, although we are still $\sim 60\%$ complete at $q = 0.1$. The slow fall-off towards large mass ratios is caused by a combination of the scale factor described above and the inherent difficulty of detecting rapidly rotating companions (see Figure 7.5). The detection rate at large mass ratios is now $\sim 0.6 - 0.7$, which is consistent with our 15/25 empirical detection rate.

7.6 Mass-Ratio Distribution

We are now finally in a position to estimate the mass-ratio distribution for our sample. We estimate the mass for each detected companion star by sampling the temperatures given in Table 7.4 as a gaussian, and converting each temperature sample into a mass sample. We do the conversion to mass both by interpolating Table 5 from Pecaut & Mamajek (2013), and by interpolating from temperature and system age (see Section 7.4) to mass with Dartmouth isochrones (Dotter et al., 2008). Both methods give similar results in most cases. Since the isochrone masses are more accurate at young ages, we use them throughout the analysis that follows. We sample the mass ratio of the system by dividing the companion mass samples by samples of the primary

mass (Section 7.4). We denote the nth mass ratio sample for the kth star as $q_k^{(n)}$, and denote the number of these samples as N_k.

We do not use systems with more than one companion, unless the wider companion is separated by $> 10''$ from the primary star. We mark the 50 companions we use in the mass ratio analysis with the fourth column of Table 7.4. Many of the companions we use in the analysis only have one detection in our data; 26/36 of these are previously known companions and so don't need follow-up to confirm. The remaining 10 are new and unconfirmed detections; these all have very strong CCF signals and are likely to be confirmed with follow-up spectroscopy or imaging. Their inclusion does not significantly change the results.

7.6.1 Fitting Methodology

We use the methodology developed in Foreman-Mackey et al. (2014) to perform bayesian inference on the shape and form of the mass-ratio distribution. The log-likelihood function in this formalism is derived from modeling the survey as a draw from the inhomogeneous Poisson process with rate density $\Gamma \equiv KQ(q)P(q)$:

$$\ln \mathcal{L}(\{\vec{x_k}\}|\vec{\theta}) = -K \int_0^1 Q(q)P(q|\vec{\theta})dq + \sum_{k=1}^{K} \ln \frac{K}{N_k} \sum_{n=1}^{N_k} Q(q_k^{(n)})P(q_k^{(n)}|\vec{\theta}) \quad (7.9)$$

In the above equation, $\{\vec{x_k}\}$ denotes the data for star k, and $\vec{\theta}$ denotes the parameters for the model we are fitting. $K = 50$ is the number of stars used in the analysis, $Q(q)$ is the completeness function shown in Figure 7.6, and $P(q|\vec{\theta})$ is the likelihood function for the mass ratio given the model parameters. We fit the data to three distinct distributions: a histogram (P_1), a lognormal distribution (P_2), and a power law (P_3):

$$P_1(q|\vec{\theta}) = \begin{cases} \theta_1 & q \in \Delta_1 \\ \theta_2 & q \in \Delta_2 \\ \dots & \\ \theta_7 & q \in \Delta_7 \end{cases} \tag{7.10}$$

$$P_2(q|\vec{\theta}) = \frac{A}{q\sqrt{2\pi\sigma^2}} e^{-\frac{(\ln q - \mu)^2}{2\sigma^2}} \tag{7.11}$$

$$P_3(q|\vec{\theta}) = (1-\gamma) q^{-\gamma} \tag{7.12}$$

The constant A in the lognormal distribution is a renormalization factor such that the distribution is only defined from $0 < q < 1$:

$$A = \frac{2}{1 - \mathrm{erf}\left(\frac{\mu}{\sigma\sqrt{2}}\right)} \tag{7.13}$$

We fit all distributions via Importance Nested Sampling with the MultiNest code (Feroz et al., 2013). Following Foreman-Mackey et al. (2014), we apply a smoothing prior on the parameters $\vec{\theta}$ for the histogram model:

$$P(\vec{\theta}|\alpha, m, \tau, \epsilon) = \mathcal{N}(\vec{\theta}|m, K(\{\Delta_j\}, \alpha, \tau, \epsilon)) \tag{7.14}$$

$$K_{ij} = \sqrt{\left[\alpha \exp\left(-\frac{(\Delta_i - \Delta_j)^2}{2\tau^2}\right)\right]^2 + \epsilon^2 \delta_{ij}} \tag{7.15}$$

The smoothing prior is an 7-dimensional gaussian with mean m and covariance matrix K_{ij}, and encodes our belief that the mass-ratio distribution is a smoothly varying function while leaving enough flexibility to let the data drive the shape of the function. Since we have introduced three new hyperparameters (a, m, τ, ϵ), we must apply a prior to them and marginalize over them when estimating the bin heights. We choose log-uniform priors for a, τ, and ϵ, and a uniform prior for the mean m. The full posterior probability distribution for the histogram model is:

$$P_1(\vec{\theta}|\{\vec{x_k}\}) \propto \mathcal{L}_1(\{\vec{x_k}\}|\vec{\theta}) P(\vec{\theta}|\alpha, m, \tau, \epsilon) P(\alpha, m, \tau, \epsilon) \tag{7.16}$$

The lognormal distribution only has two parameters (μ, σ), and was chosen because it has a similar shape to the histogram resulting from the first model. We use

uniform priors on both μ and σ, although we note that μ is compared to $\ln q$ and so acts like a log-uniform prior. The power law has only one parameter (γ); we use a uniform prior in the fit.

7.6.2 Malmquist Bias Correction

We are trying to recover the intrinsic distribution from an observed sample, so we must fit the data to the probability distribution function (PDF) for mass ratio, *given that we observed the star*: $P(q|\vec{\theta}, \text{obs})$. In a volume-limited sample, this is equal to $P(q|\vec{\theta})$. However, our sample is magnitude-limited and therefore suffers from Malmquist bias. There is a higher probability for equal-mass binary systems to occur in our survey because they contribute twice the flux and are therefore more likely to fall under the magnitude limit. We can calculate the PDF for mass ratio, given that we observed the system, from Bayes' theorem:

$$P(q|\vec{\theta}, \text{obs}) = \frac{P(\text{obs}|q)P(q|\vec{\theta})}{\int_0^1 P(\text{obs}|q)P(q|\vec{\theta})dq} \tag{7.17}$$

We already know $P(q|\vec{\theta})$ (Equations 7.10 - 7.12). We estimate $P(\text{obs}|q)$ by simulating a very large sample of binary stars via these steps:

1. Draw random primary star masses from the Kroupa IMF (Kroupa, 2002)
2. Draw a random distance for each star from a disk with infinite extent and scale height of 150 pc (the approximate scale height of the Milky Way disk for A-type stars, Binney & Merrifield, 1998).
3. For each q from 0 to 1, in steps of 0.01:
    a) Add a companion star to each primary with the appropriate mass to make a binary system with mass ratio q.
    b) Calculate the combined absolute V-magnitude by interpolating Table 5 of Pecaut & Mamajek (2013).
    c) Calculate apparent magnitude V from the absolute magnitude and distance.
    d) Find fraction of stars ($f(q)$) with apparent $V < 6$

4. Fit the sampled fractions $f(q)$ to a 5th-order polynomial.

With the fitted malmquist-correction polynomial, we then substitute $P(q|\vec{\theta}, \mathrm{obs})$ everywhere $P(q|\vec{\theta})$ appears in Equation 7.9.

We summarize the parameters in Table 7.5, and show the resulting fits in Figure 7.7. The 1σ uncertainties in the bin heights from the histogram model are shown as error bars, and we overplot 300 samples of the lognormal distribution fit to show the spread allowed by the data. The best-fit power law is plotted with a red dot-dashed line. We also estimate the mass-ratio distribution expected from random pairing of the Kroupa Initial Mass Function (IMF), and show the result in yellow. We estimate the distribution by drawing 100000 primary stars from the IMF with masses between $1.5 < M/M_{\odot} < 20$. We then draw companions from the same IMF, with the restriction that the companion has a lower mass than the primary. The result plotted in yellow in Figure 7.7 is a gaussian kernel density estimate of the resulting mass ratios, with a bandwidth of 0.05.

7.7 Discussion

Previous measurements of the mass-ratio distribution find that the data is well fit by a power law. Kouwenhoven et al. (2007) compiled spectroscopic, imaging, and astrometric observations of binary stars with intermediate-mass primaries in the Scorpius OB association, and derived a power law index of -0.45 ± 0.15. More recently De Rosa et al. (2014) performed an adaptive optics and common proper motion search for companions to field A-type stars. They found that the distribution for companions on wide ($a > 125\ AU$) orbits has a very steep power law index of $-2.3^{+1.0}_{-0.9}$, while the distribution for close ($30\ AU < a < 125\ AU$) companions is consistent with flat.

7.7.1 Model Comparison

The most striking feature of the mass-ratio distribution shown in Figure 7.7 is the turnover or flattening at intermediate q. The maximum of the lognormal distribution occurs at $q = 0.30 \pm 0.03$ and is an estimate of the characteristic scale.

Although the power law fit and the Kroupa IMF are visually very poor fits to the data, we formally compare the models to ensure that the different form is not

an artifact of binning or simple noise. We make the comparison using the posterior odds:

$$\text{Odds} = \frac{\int_{\vec{\theta_1}} P_1(q|\vec{\theta_1})P(\vec{\theta_1})}{\int_{\vec{\theta_2}} P_2(q|\vec{\theta_2}P(\vec{\theta_2})} \equiv \frac{Z_1}{Z_2} \tag{7.18}$$

The integrals are estimated as part of the nested sampling algorithm in the MultiNest code. The odds ratio comparing the lognormal distribution to power law fit is $Z_{\text{lognormal}}/Z_{\text{power}} = 5.1 \pm 0.1 \times 10^6$, indicating a very strong preference for the lognormal distribution model. We also compare to the mass-ratio distribution expected for random pairing from the Kroupa IMF and to a uniform distribution (a special case of the power law). In these cases, there are no free parameters so the evidence integral just becomes the likelihood function (Equation 7.9). The corresponding odds ratios are $Z_{\text{lognormal}}/Z_{\text{IMF}} = 6.5 \pm 0.1 \times 10^{22}$ and $Z_{\text{lognormal}}/Z_{\text{uniform}} = 7.0 \pm 0.1 \times 10^6$. Both of these again demonstrate a very strong preference for the lognormal distribution.

The extreme unlikeliness of the Kroupa IMF model also indicates that our sample is not significantly biased by foreground or background contaminants. In fact, the present-day background star mass function is more bottom heavy than the initial mass function because some of the massive stars have evolved to white dwarfs or ended their lives in a supernova. The comparison to a Kroupa IMF therefore *underestimates* the likelihood of background star contamination.

7.7.2 Comparison to Previous Results

Our mass-ratio distribution appears to be in tension with the results of the VAST survey (De Rosa et al., 2014), which finds a nearly flat distribution for close companions. However, their subsample of close companions only includes 18 binaries, so it is possible that the different forms are just a result of small number statistics. To assess the degree of tension, we use the Anderson-Darling test (Anderson & Darling, 1954) to find the probability that both their close companion subsample and our companions are drawn from the same parent distribution. We only use companions from this work with mean $\overline{q} > 0.15$ because the VAST survey subsample makes the same cut. The VAST survey also only included stars with projected separations $a < 125$ AU in their close companion subsample. Since we cannot estimate the separation from our data, we do not make such a cut. We could make a cut using the *maximum*

possible separation, set by the distance and spectrograph slit width, but doing so vastly reduces the number of detections and does not affect the result.

To account for measurement uncertainties in the mass ratios, we draw from both our mass ratio samples ($q_k^{(n)}$, see Section 7.6) and the VAST mass ratio values many times and compute the Anderson-Darling test statistic each time. Since De Rosa et al. (2014) do not quote uncertainties, we assume uncertainties of $\sigma_q = 0.05$ for all of their measurements. The result is $p = 0.10^{+0.07}_{-0.04}$; we cannot reject the hypothesis that both samples come from the same distribution.

7.7.3 Theoretical Implications

The mass-ratio distribution derived in this work has a very different form than the power law found for companions at wide separations. This is likely a result of disk interactions as the two components are accreting. The close companions that we detect may form with similar masses to their counterparts at large separations ($a \gtrsim 1000\ AU$), but preferentially accrete matter from the dense primary star disk. The result would be a depletion of low mass ratio companions as they become intermediate to high mass ratio companions. The characteristic scale of ~ 0.3 that we see in Figure 7.7 would then be related to the disk timescale, since with enough time the preferential accretion would push all companions to $q = 1.0$.

It is also possible that some of the companions found in this work were formed from a gravitationally unstable disk (e.g. Kratter & Matzner, 2006; Stamatellos & Whitworth, 2011). Being a completely different formation mechanism than the way wide companions form, we would expect the initial companion mass function to differ. Additionally, such companions would undergo the same preferential accretion discussed above. This explanation may even be preferable, since it could explain why we see a separation-dependent mass-ratio distribution around intermediate-mass stars but not low-mass stars: more massive stars tend to have more massive disks (Andrews et al., 2013) that are more likely to fragment (Kratter et al., 2010).

Large scale simulations are likely needed to distinguish between the two scenarios and fully interpret the results of this survey. A significant amount of work has already been put towards this end in the form of radiation hydrodynamic simulations of giant molecular clouds (Bate, 2012; Krumholz et al., 2012). However, the present simulations do not generate enough stars more massive than the sun to quantitatively

compare binary and multiple star statistics to observations.

7.8 Summary

In this work, we described a binary survey of 341 bright A- and B-type stars. We used the direct spectral detection method (Gullikson et al., 2016) to find the spectral lines of 64 companions with temperatures ranging from $3600 - 16000\ K$. We used the cross-correlation functions to estimate the temperature and surface gravity of most of our sample stars, and converted to mass and age by interpolating Padova stellar evolutionary tracks (Bressan et al., 2012). Likewise, we convert the companion temperature measurements to mass by using solar metallicity Dartmough evolutionary tracks (Dotter et al., 2008).

We then use the formalism introduced in Foreman-Mackey et al. (2014), which self-consistently accounts for measurement errors, to infer the form of the mass-ratio distribution (shown in Figure 7.7). Unlike most previous work, we find that a power law is a poor descriptor of the data and find that a lognormal distribution performs much better. This result, which only includes close companions since it is a spectroscopic technique, is consistent with the 18 close companions found in the VAST survey (De Rosa et al., 2014). However, this result shows much more detail due to a larger number of companions.

We interpret the mass-ratio distribution in terms of formation mechanism in Section 7.7.3. It is likely that the mass-ratio distribution we find is largely a result of preferential accretion onto the secondary star, which largely stops when the circumprimary or circumbinary disk dissipates.

In the effort of open and reproducible research, we have made several data products freely available to the community. All of the reduced and telluric-corrected spectra used in this study are available at `https://zenodo.org/record/46340`. Samples of the primary and companion mass and system age posterior distributions are available at `https://zenodo.org/record/48073`, as are the posterior distributions for the parameters fit in Section 7.6 and every cross-correlation function generated in our analysis. We additionally provide a series of python libraries and jupyter notebooks with the computer code we used for the analysis on github: `https://github.com/kgullikson88/BinaryInference`.

Acknowledgements

This research has made use of the SIMBAD database, operated at CDS, Strasbourg, France, and of Astropy, a community-developed core Python package for Astronomy (Astropy Collaboration, 2013). It was supported by a start-up grant to Adam Kraus as well as a University of Texas Continuing Fellowship and a Dissertation Writing Fellowship to Kevin Gullikson.

This work used the Immersion Grating Infrared Spectrograph (IGRINS) that was developed under a collaboration between the University of Texas at Austin and the Korea Astronomy and Space Science Institute (KASI) with the financial support of the US National Science Foundation under grant AST-1229522, of the University of Texas at Austin, and of the Korean GMT Project of KASI.

The Hobby-Eberly Telescope (HET) is a joint project of the University of Texas at Austin, the Pennsylvania State University, Stanford University, Ludwig-Maximilians-Universität München, and Georg-August-Universität Göttingen. The HET is named in honor of its principal benefactors, William P. Hobby and Robert E. Eberly.

Based on observations at Cerro Tololo Inter-American Observatory, National Optical Astronomy Observatory (NOAO Prop. IDs: 13A-0139, 13B-0112, 2014A-0260, 14A-0260, 15A-0245; PI: Kevin Gullikson), which is operated by the Association of Universities for Research in Astronomy (AURA) under a cooperative agreement with the National Science Foundation.

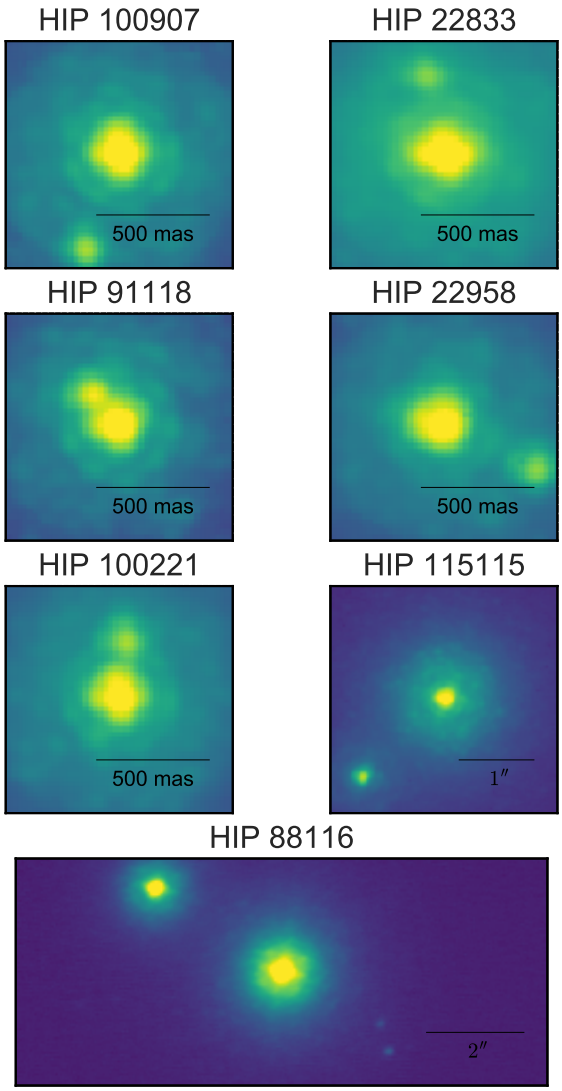

Figure 7.2: Detection images for all stars in which we detect a companion in the follow-up NIRI data. There are several nearby sources for HIP 88116, none of which are the source we detect in the spectroscopic data (see Section 7.3).

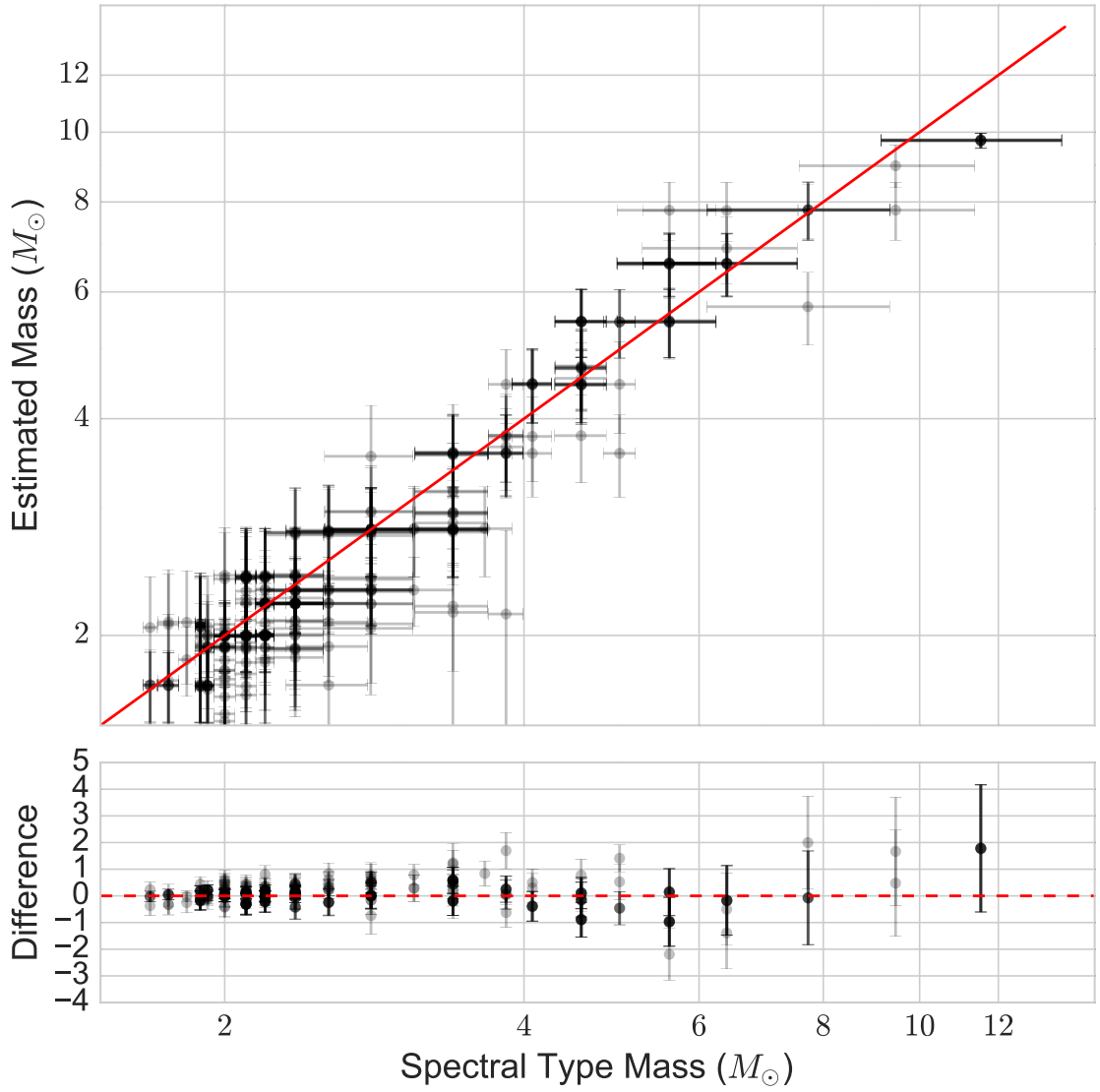

Figure 7.3: Comparison of primary star masses derived from our cross-correlation analysis and Padova isochrones (Bressan et al., 2012) with those expected from the published spectral type. There is excellent agreement between the two measures across the entire range of masses.

.

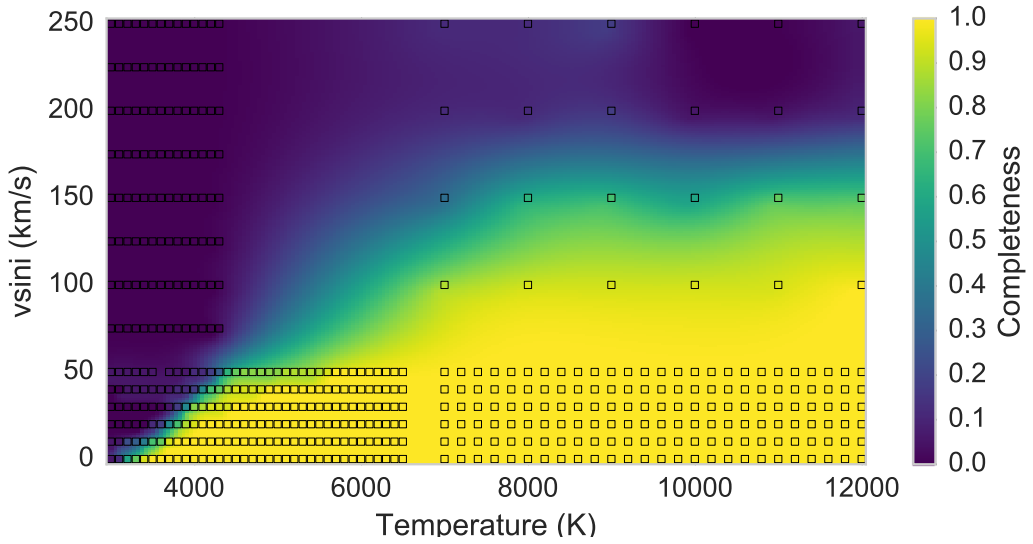

Figure 7.4: Detection rate as a function of companion temperature and $v \sin i$ for HIP 24244. All companions that are shaded yellow are detectable, while companions in the purple region are never detectable. The grids of squares in the lower left and upper right show the low temperature and high temperature grid points we used in the sensitivity analysis. The remaining squares come from assumptions about the shape of the detection rate surface and allow us to fully interpolate (see text for details).

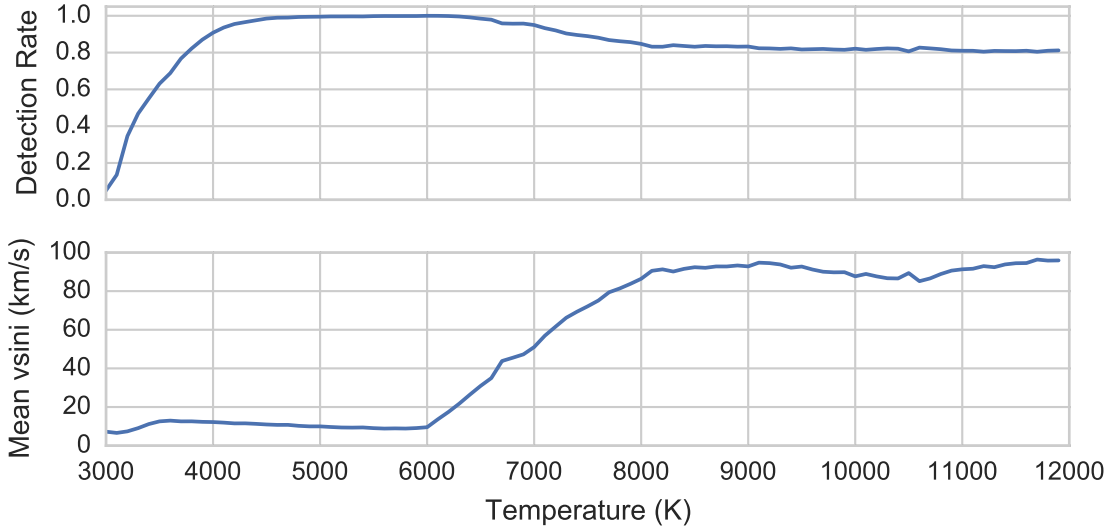

Figure 7.5: Marginalized detection rate for the same star as shown in Figure 7.4. The fall in detection rate towards hotter stars is caused by the increase in typical rotational speeds.

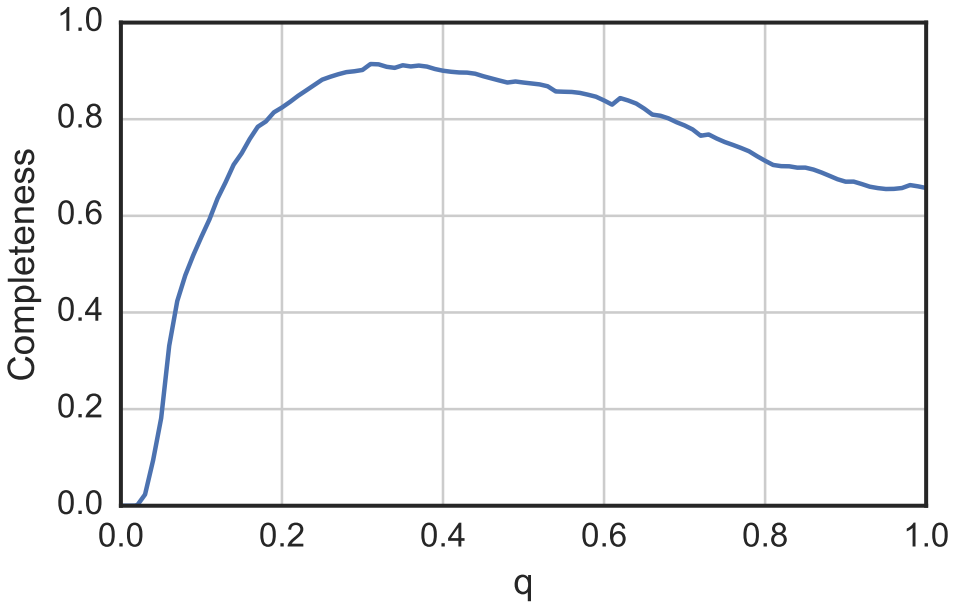

Figure 7.6: Survey completeness as a function of mass ratio (q).

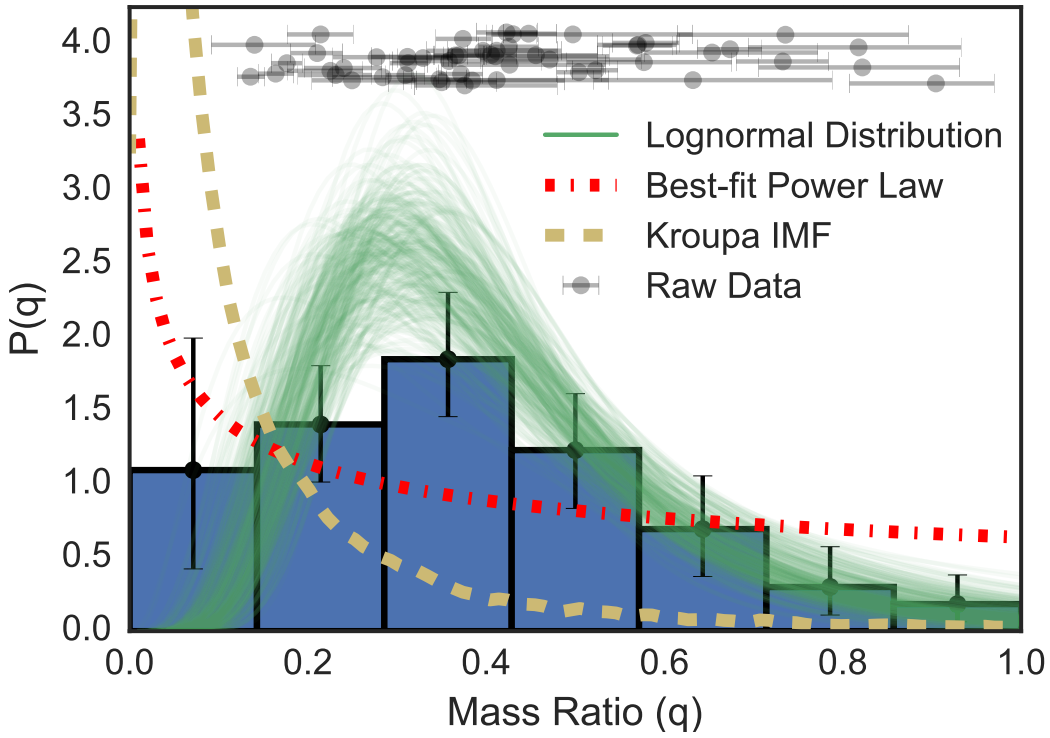

Figure 7.7: mass-ratio distribution for our sample. The data was fit to a histogram, a lognormal distribution, and a power law. The histogram is shown in the solid blue blocks, with 1σ uncertainties marked with error bars. The variance of the lognormal fit is shown with 300 samples from the posterior probability distribution for the parameters in green. We also show the best-fit power law and the mass-ratio distribution resulting from random pairing of the Kroupa initial mass function. Finally, we display the raw mass ratio measurements with associated uncertainties in the cluster of data points near the top of the figure.

Table 7.1: Sample Properties.
The spectral types, coordinates, V-band magnitudes, and parallax measurements are taken from the Simbad database; the spectral type given is that of the brightest star if part of a known multiple system. The "Ref" column denotes the reference for the stellar effective temperature, surface gravity, mass, and age. The references are: [1]: (David & Hillenbrand, 2015); [2]: This study.

Star	SpT	RA	DEC	V	parallax (mas)	$T_{\rm eff}$ (K)	$\log g$ (cgs)	Mass ($M_\odot$)	Age (Myr)	Ref
HIP 813	B9Vn	00:10:02.20	+11:08:44.93	5.537	10.68	12516 ± 426	4.3 ± 0.14	$3.1^{+0.18}_{-0.17}$	85^{+56}_{-52}	1
HIP 1191	B8.5V	00:14:54.52	-09:34:10.45	5.757	9.63	12000 ± 1000	4.5 ± 0.25	$2.8^{+0.41}_{-0.37}$	23^{+63}_{-16}	2
HIP 1366	A2V	00:17:05.50	+38:40:53.89	4.610	10.56	9371 ± 319	4.0 ± 0.14	$2.2^{+0.18}_{-0.16}$	464^{+83}_{-119}	1
HIP 1647	B9V	00:20:39.04	-69:37:29.68	5.498	10.25	11393 ± 387	4.0 ± 0.14	$2.8^{+0.21}_{-0.18}$	206^{+48}_{-79}	1
HIP 2381	A3V	00:30:22.65	-23:47:15.65	5.190	18.83	8364 ± 284	4.0 ± 0.14	$1.9^{+0.16}_{-0.13}$	715^{+135}_{-183}	1
HIP 2505	B8Vn	00:31:46.36	+54:31:20.23	4.732	8.64	12000 ± 1000	4.0 ± 0.25	$2.9^{+0.45}_{-0.40}$	58^{+104}_{-48}	2
HIP 2548	B9.5V	00:32:23.78	+06:57:19.66	5.698	12.35	11864 ± 403	4.4 ± 0.14	$2.8^{+0.16}_{-0.15}$	77^{+69}_{-51}	1
HIP 3300	B2V	00:42:03.90	+50:30:45.09	4.810	2.28	18000 ± 1000	4.0 ± 0.25	$5.7^{+0.67}_{-0.63}$	19^{+19}_{-13}	2
HIP 3478	B5V	00:44:26.19	+47:51:50.34	5.646	5.23	18000 ± 1000	4.5 ± 0.25	$5.4^{+0.60}_{-0.57}$	11^{+14}_{-5}	2
HIP 5131	A1Vn	01:05:40.96	+21:28:23.45	5.317	11.86	11956 ± 406	4.4 ± 0.14	$2.8^{+0.16}_{-0.14}$	69^{+65}_{-45}	1
HIP 5132	A0Vn	01:05:41.71	+21:27:55.60	5.532	11.64	12053 ± 410	4.4 ± 0.14	$2.9^{+0.16}_{-0.14}$	64^{+61}_{-42}	1
HIP 5310	A3V	01:07:57.16	+20:44:20.83	5.569	21.14	8611 ± 293	4.4 ± 0.14	$1.8^{+0.10}_{-0.08}$	307^{+228}_{-196}	1
HIP 5361	B8V	01:08:33.47	+58:15:48.41	5.773	5.41	14000 ± 1000	4.5 ± 0.25	$3.6^{+0.49}_{-0.43}$	18^{+36}_{-11}	2
HIP 5518	A0Vnn	01:10:39.32	+68:46:43.04	5.318	11.78	11894 ± 404	4.1 ± 0.14	$3.0^{+0.21}_{-0.19}$	172^{+40}_{-72}	1
HIP 5626	A3V	01:12:16.82	+79:40:26.27	5.600	12.07	10342 ± 352	4.2 ± 0.14	$2.4^{+0.15}_{-0.14}$	218^{+102}_{-127}	1
HIP 7345	A1V	01:34:37.78	-15:40:34.90	5.619	16.84	10007 ± 340	4.4 ± 0.14	$2.2^{+0.12}_{-0.11}$	156^{+130}_{-100}	1
HIP 8016	B9V	01:42:55.86	+70:37:21.09	5.177	11.75	10000 ± 500	4.0 ± 0.25	$2.3^{+0.25}_{-0.21}$	67^{+188}_{-57}	2
HIP 8704	B1.5V	01:51:59.32	+55:08:50.58	5.520	2.52	22000 ± 1000	4.5 ± 0.25	$7.8^{+0.74}_{-0.70}$	8^{+6}_{-3}	2
HR 545	B9V	01:53:31.77	+19:17:46.27	4.700	···	10000 ± 500	4.5 ± 0.25	$2.2^{+0.21}_{-0.20}$	34^{+106}_{-27}	2
HIP 9312	A0Vn	01:59:38.04	+64:37:17.76	5.283	13.28	11913 ± 405	4.1 ± 0.14	$2.8^{+0.13}_{-0.11}$	77^{+65}_{-50}	1
HIP 9564	A1Vn	02:02:52.48	+64:54:05.27	5.999	11.92	11266 ± 383	4.3 ± 0.14	$2.7^{+0.15}_{-0.12}$	149^{+74}_{-88}	1
HR 604	B8V	02:03:54.72	+42:19:51.41	5.820	···	10000 ± 500	3.5 ± 0.25	$2.8^{+0.46}_{-0.42}$	281^{+82}_{-117}	2
HIP 10320	B9V	02:12:54.47	-30:43:25.77	5.261	10.18	11745 ± 399	3.7 ± 0.14	$3.1^{+0.23}_{-0.19}$	205^{+22}_{-43}	1
HIP 10670	A1Vnn	02:17:18.87	+33:50:49.90	4.000	29.04	10772 ± 366	4.2 ± 0.14	$2.6^{+0.16}_{-0.13}$	230^{+63}_{-109}	1

Table 7.1: - (Continued)

Star	SpT	RA	DEC	V	parallax (mas)	$T_{\rm eff}$ (K)	$\log g$ (cgs)	Mass ($M_\odot$)	Age (Myr)	Ref
HIP 10732	A1Vn	02:18:07.54	+19:54:04.19	5.575	7.29	9500 ± 1000	4.0 ± 0.25	$2.1^{+0.37}_{-0.31}$	107^{+286}_{-93}	2
HIP 11345	A0V	02:25:57.01	-12:17:25.71	4.869	7.15	10000 ± 500	4.0 ± 0.25	$2.3^{+0.25}_{-0.22}$	72^{+206}_{-60}	2
HIP 12332	A7V	02:38:48.99	+21:57:41.06	5.454	9.68	8000 ± 500	3.5 ± 0.25	$2.0^{+0.40}_{-0.33}$	621^{+269}_{-268}	2
HIP 12706	A2Vn	02:43:18.04	+03:14:08.94	3.470	40.97	8551 ± 291	4.3 ± 0.14	$1.9^{+0.15}_{-0.13}$	647^{+104}_{-184}	1
HIP 12719	B3V	02:43:27.11	+27:42:25.72	4.670	9.51	18000 ± 1000	4.5 ± 0.25	$5.4^{+0.62}_{-0.57}$	11^{+14}_{-5}	2
HIP 12803	B9Vn	02:44:32.97	+15:18:42.71	5.776	5.49	12000 ± 1000	4.5 ± 0.25	$2.8^{+0.39}_{-0.36}$	25^{+63}_{-17}	2
HIP 13165	B6V	02:49:17.56	+17:27:51.52	5.314	4.18	16000 ± 1000	4.5 ± 0.25	$4.4^{+0.55}_{-0.51}$	13^{+22}_{-7}	2
HIP 13202	A0V	02:49:54.18	-27:56:31.14	5.389	7.11	9000 ± 500	3.5 ± 0.25	$2.4^{+0.44}_{-0.38}$	401^{+138}_{-170}	2
HIP 13209	B8Vn	02:49:59.03	+27:15:37.83	3.606	19.69	13316 ± 453	4.1 ± 0.14	$3.3^{+0.15}_{-0.13}$	45^{+43}_{-30}	1
HIP 13327	B7V	02:51:29.59	+15:04:55.45	5.514	6.60	14000 ± 1000	4.0 ± 0.25	$3.8^{+0.55}_{-0.46}$	36^{+57}_{-27}	2
HIP 13717	A3V	02:56:37.42	-03:42:44.35	5.160	17.49	8612 ± 293	4.0 ± 0.14	$1.9^{+0.13}_{-0.11}$	571^{+138}_{-255}	1
HIP 13879	A2Vn	02:58:45.67	+39:39:45.81	4.700	10.53	9298 ± 316	3.5 ± 0.14	$2.1^{+0.12}_{-0.09}$	340^{+141}_{-193}	1
HIP 14043	B7V	03:00:52.21	+52:21:06.22	5.253	7.11	14000 ± 1000	4.5 ± 0.25	$3.6^{+0.48}_{-0.45}$	17^{+33}_{-10}	2
HIP 14293	A5V	03:04:16.52	-07:36:03.08	5.300	24.06	8039 ± 273	4.2 ± 0.14	$1.8^{+0.14}_{-0.10}$	782^{+166}_{-291}	1
HIP 14764	B8V	03:10:38.79	+11:52:21.44	5.965	7.33	12000 ± 1000	4.0 ± 0.25	$2.9^{+0.47}_{-0.40}$	54^{+103}_{-44}	2
HIP 14862	A2Vnn	03:11:56.27	+74:23:37.17	4.840	19.72	8875 ± 1000	4.2 ± 0.25	$1.8^{+0.32}_{-0.29}$	71^{+317}_{-60}	2
HIP 15110	A1V	03:14:54.10	+21:02:40.01	4.880	12.44	9902 ± 337	4.0 ± 0.14	$2.4^{+0.18}_{-0.15}$	375^{+52}_{-104}	1
HIP 15338	B8V	03:17:47.35	+44:01:30.08	5.478	4.46	12000 ± 1000	3.5 ± 0.25	$3.5^{+0.65}_{-0.59}$	155^{+68}_{-59}	2
HIP 15404	B3V	03:18:37.74	+50:13:19.83	5.158	5.12	20000 ± 1000	4.5 ± 0.25	$6.5^{+0.68}_{-0.64}$	9^{+9}_{-4}	2
HIP 15444	B5V	03:19:07.64	+50:05:41.88	5.036	5.82	18000 ± 1000	4.5 ± 0.25	$5.5^{+0.60}_{-0.60}$	11^{+14}_{-6}	2
HIP 16210	B6Vn	03:28:52.33	+49:50:54.17	5.578	6.22	...	...	...	...	...
HIP 16244	B3V	03:29:22.05	+49:30:32.21	4.678	6.05	18000 ± 1000	4.5 ± 0.25	$5.4^{+0.61}_{-0.57}$	11^{+14}_{-5}	2
HIP 16285	A5V	03:29:55.15	-42:38:03.32	5.768	15.28	7884 ± 268	3.9 ± 0.14	$1.7^{+0.13}_{-0.09}$	841^{+183}_{-335}	1
HIP 16322	A0Vn	03:30:24.47	+11:20:11.19	5.125	9.03	10000 ± 500	4.0 ± 0.25	$2.3^{+0.26}_{-0.22}$	80^{+200}_{-69}	2
HIP 16340	B8V	03:30:36.95	+48:06:12.95	5.820	3.65	12000 ± 1000	4.0 ± 0.25	$2.9^{+0.48}_{-0.40}$	54^{+107}_{-44}	2
HIP 16599	A3V	03:33:39.06	+54:58:29.49	5.981	13.44	8383 ± 285	4.0 ± 0.14	$2.0^{+0.19}_{-0.15}$	737^{+102}_{-102}	1
HIP 16611	B9V	03:33:47.28	-21:37:58.38	4.300	11.12	12514 ± 425	4.0 ± 0.14	$3.3^{+0.24}_{-0.20}$	157^{+23}_{-45}	1
HIP 17457	B7IV	03:44:30.51	-01:09:47.14	5.250	4.98	14000 ± 1000	4.5 ± 0.25	$3.6^{+0.47}_{-0.44}$	17^{+36}_{-10}	2
HIP 17527	B8V	03:45:09.74	+24:50:21.34	5.640	7.97	14000 ± 1000	4.5 ± 0.25	$3.6^{+0.47}_{-0.44}$	18^{+34}_{-11}	2
HIP 17563	B3V	03:45:40.44	+06:02:59.97	5.332	6.11	18000 ± 1000	4.5 ± 0.25	$5.4^{+0.64}_{-0.57}$	11^{+14}_{-5}	2
HIP 18141	B8V	03:52:41.66	-05:21:40.54	5.476	5.57	14000 ± 1000	4.5 ± 0.25	$3.6^{+0.47}_{-0.43}$	18^{+35}_{-12}	2

Table 7.1: - (Continued)

Star	SpT	RA	DEC	V	parallax (mas)	$T_{\rm eff}$ (K)	$\log g$ (cgs)	Mass ($M_\odot$)	Age (Myr)	Ref
HIP 18396	B6V	03:55:58.17	+47:52:17.12	5.379	4.47	16000 ± 1000	4.5 ± 0.25	$4.5^{+0.54}_{-0.50}$	14^{+21}_{-8}	2
HIP 18788	B5V	04:01:32.05	-01:32:58.78	5.280	7.88	16000 ± 1000	4.5 ± 0.25	$4.5^{+0.51}_{-0.49}$	13^{+22}_{-7}	2
HIP 18805	B5V	04:01:46.14	+09:59:52.84	5.676	5.71	18000 ± 1000	4.5 ± 0.25	$5.4^{+0.60}_{-0.57}$	10^{+14}_{-5}	2
HIP 19799	B9Vn	04:14:36.23	+10:00:41.05	5.208	8.34	10000 ± 500	4.5 ± 0.25	$2.2^{+0.21}_{-0.19}$	34^{+116}_{-26}	2
HIP 19949	A2Vn	04:16:43.09	+53:36:42.47	5.200	9.98	9825 ± 334	3.8 ± 0.14	$2.2^{+0.11}_{-0.10}$	197^{+140}_{-122}	1
HIP 19968	B7V	04:16:53.56	+61:50:59.97	5.700	7.31	16000 ± 1000	4.5 ± 0.25	$4.5^{+0.53}_{-0.51}$	13^{+21}_{-8}	2
HIP 20264	A0V	04:20:39.01	-20:38:22.64	5.380	6.86	10000 ± 500	4.0 ± 0.25	$2.3^{+0.25}_{-0.21}$	77^{+207}_{-65}	2
HIP 20380	A3V	04:21:51.81	+56:30:22.74	5.920	10.31	8738 ± 297	3.9 ± 0.14	$1.9^{+0.10}_{-0.08}$	338^{+206}_{-209}	1
HIP 20430	B9Vnn	04:22:34.94	+25:37:45.54	5.376	11.20	11981 ± 407	4.2 ± 0.14	$3.2^{+0.28}_{-0.23}$	195^{+23}_{-27}	1
HIP 20507	A2V	04:23:40.85	-03:44:43.68	5.171	15.60	8793 ± 299	4.0 ± 0.14	$1.9^{+0.10}_{-0.08}$	340^{+200}_{-210}	1
HIP 20579	B8V	04:24:29.16	+34:07:50.73	5.722	7.28	14000 ± 1000	4.5 ± 0.25	$3.6^{+0.46}_{-0.46}$	17^{+32}_{-10}	2
HIP 20789	B7V	04:27:17.45	+22:59:46.80	5.515	8.63	14000 ± 1000	4.0 ± 0.25	$3.7^{+0.53}_{-0.47}$	38^{+55}_{-28}	2
HIP 21589	A6V	04:38:09.46	+12:30:39.01	4.270	21.24	8591 ± 292	3.9 ± 0.14	$1.8^{+0.09}_{-0.07}$	300^{+231}_{-193}	1
HIP 21683	A5Vn	04:39:16.50	+15:55:04.70	4.675	20.97	8165 ± 278	4.0 ± 0.14	$1.7^{+0.07}_{-0.06}$	318^{+266}_{-211}	1
HIP 21819	A2V	04:41:19.76	+28:36:53.98	5.726	8.55	9000 ± 500	3.5 ± 0.25	$2.4^{+0.41}_{-0.37}$	411^{+135}_{-158}	2
HIP 21928	A1Vn	04:42:54.33	+43:21:54.53	5.301	13.52	10734 ± 365	4.0 ± 0.14	$2.6^{+0.16}_{-0.13}$	242^{+59}_{-108}	1
HIP 22028	A1V	04:44:07.98	-18:39:59.71	5.527	10.66	10118 ± 344	4.0 ± 0.14	$2.3^{+0.14}_{-0.11}$	246^{+105}_{-135}	1
HIP 22509	A1Vn	04:50:36.72	+08:54:00.65	4.350	14.53	9784 ± 333	2.7 ± 0.14	$2.2^{+0.11}_{-0.10}$	205^{+141}_{-129}	1
HIP 22833	A3V	04:54:46.90	+11:25:33.63	5.186	14.29	8278 ± 281	3.9 ± 0.14	$1.8^{+0.12}_{-0.09}$	645^{+165}_{-304}	1
HIP 22840	B5V	04:54:50.71	+00:28:01.81	5.975	4.50	16000 ± 1000	4.0 ± 0.25	$4.7^{+0.61}_{-0.55}$	27^{+32}_{-18}	2
HIP 22913	B9V	04:55:50.15	+15:02:25.00	5.785	8.97	12000 ± 1000	3.5 ± 0.25	$3.5^{+0.67}_{-0.57}$	155^{+68}_{-64}	2
HIP 22958	B6V	04:56:24.19	-05:10:16.87	5.490	4.40	16000 ± 1000	4.5 ± 0.25	$4.5^{+0.52}_{-0.53}$	13^{+20}_{-7}	2
HIP 23362	B9V	05:01:25.58	-20:03:06.91	4.894	16.48	12450 ± 423	4.3 ± 0.14	$3.2^{+0.21}_{-0.16}$	147^{+28}_{-59}	1
HIP 23916	B8V	05:08:20.19	-08:39:55.17	5.780	4.79	...	...	...	...	...
HIP 24244	B7.5Vn	05:12:17.90	-11:52:09.19	4.450	14.07	13781 ± 469	4.2 ± 0.14	$3.9^{+0.29}_{-0.23}$	114^{+11}_{-23}	1
HIP 24327	B7V	05:13:13.88	-12:56:28.65	4.421	4.48	14000 ± 1000	4.5 ± 0.25	$3.6^{+0.47}_{-0.44}$	18^{+35}_{-11}	2
HIP 24505	B9V	05:15:24.37	-26:56:36.63	5.040	11.73	11748 ± 399	4.2 ± 0.14	$2.9^{+0.16}_{-0.14}$	152^{+53}_{-80}	1
HIP 24902	A3V	05:20:14.67	+41:05:10.35	5.468	11.77	8275 ± 281	4.0 ± 0.14	$1.8^{+0.09}_{-0.08}$	457^{+261}_{-281}	1
ADS 3962 AB	B1Vn	05:22:50.30	+03:32:52.00	4.990	...	...	...	...	...	...
HIP 25143	A3V	05:22:50.31	+41:01:45.33	5.545	11.15	8101 ± 275	3.8 ± 0.14	$1.7^{+0.06}_{-0.06}$	231^{+250}_{-156}	1
HIP 25280	A0V	05:24:28.49	-16:58:32.81	5.644	14.65	10398 ± 354	4.4 ± 0.14	$2.4^{+0.13}_{-0.11}$	199^{+101}_{-115}	1

Table 7.1: - (Continued)

Star	SpT	RA	DEC	V	parallax (mas)	$T_{\rm eff}$ (K)	$\log g$ (cgs)	Mass ($M_\odot$)	Age (Myr)	Ref
HIP 25555	B9.5Vn	05:27:45.61	+15:52:26.58	5.512	7.69	10000 ± 500	3.5 ± 0.25	$2.8^{+0.45}_{-0.43}$	283^{+79}_{-104}	2
HIP 25608	A1V	05:28:15.34	-37:13:50.75	5.562	11.39	9960 ± 339	4.1 ± 0.14	$2.3^{+0.15}_{-0.12}$	311^{+83}_{-149}	1
HIP 25695	B9Vn	05:29:16.50	+25:09:00.78	5.480	7.67	12000 ± 1000	4.5 ± 0.25	$2.8^{+0.43}_{-0.37}$	24^{+63}_{-17}	2
HIP 25790	A3Vn	05:30:26.16	+15:21:37.61	5.940	12.89	8397 ± 286	3.9 ± 0.14	$1.8^{+0.08}_{-0.07}$	329^{+250}_{-212}	1
HIP 25813	B5V	05:30:47.05	+05:56:53.29	4.200	10.77	15603 ± 531	4.4 ± 0.14	$4.7^{+0.35}_{-0.28}$	71^{+8}_{-16}	1
HIP 26063	B1V	05:33:31.45	-01:09:21.87	5.340	2.22	...	...	...	...	...
HIP 26093	B3V	05:33:54.28	+14:18:20.08	5.588	7.31	20000 ± 1000	4.5 ± 0.25	$6.6^{+0.66}_{-0.64}$	9^{+9}_{-4}	2
HIP 26126	A2V	05:34:16.77	+03:46:00.82	5.332	11.82	9542 ± 324	3.9 ± 0.14	$2.1^{+0.09}_{-0.07}$	177^{+150}_{-115}	1
HIP 26563	A4Vn	05:38:53.08	-07:12:46.18	4.800	22.42	8416 ± 286	4.1 ± 0.14	$1.8^{+0.08}_{-0.07}$	344^{+256}_{-218}	1
HIP 27100	A7V	05:44:46.38	-65:44:07.90	4.360	21.80	7828 ± 266	3.9 ± 0.14	$1.8^{+0.18}_{-0.15}$	965^{+153}_{-148}	1
HIP 27321	A6V	05:47:17.09	-51:03:59.44	3.860	51.44	8300 ± 282	4.4 ± 0.14	$1.8^{+0.11}_{-0.09}$	528^{+235}_{-300}	1
HIP 27713	A2Vn	05:52:07.73	-09:02:30.84	5.964	10.11	8474 ± 288	3.9 ± 0.14	$1.8^{+0.09}_{-0.07}$	383^{+238}_{-240}	1
HIP 28691	B5V	06:03:27.37	+19:41:26.02	5.135	4.54	14000 ± 1000	4.0 ± 0.25	$3.8^{+0.54}_{-0.48}$	36^{+55}_{-27}	2
HIP 28756	B2.5V	06:04:20.27	-32:10:20.74	5.631	3.24	20000 ± 1000	4.0 ± 0.25	$6.9^{+0.75}_{-0.68}$	14^{+13}_{-8}	2
HIP 28910	A0V	06:06:09.32	-14:56:06.92	4.669	18.88	10453 ± 355	4.1 ± 0.14	$2.4^{+0.16}_{-0.14}$	252^{+80}_{-122}	1
HIP 29150	A0V	06:08:57.87	-22:25:38.68	5.482	13.24	11283 ± 384	4.2 ± 0.14	$2.6^{+0.12}_{-0.11}$	112^{+82}_{-71}	1
HIP 29151	A3Vn	06:08:57.90	+02:29:58.89	5.730	4.98	9000 ± 500	3.5 ± 0.25	$2.4^{+0.43}_{-0.37}$	406^{+141}_{-177}	2
HIP 29735	B9V	06:15:44.89	-13:43:06.29	4.998	8.00	10000 ± 500	3.5 ± 0.25	$2.8^{+0.48}_{-0.41}$	281^{+84}_{-105}	2
HIP 29997	A0Vn	06:18:50.78	+69:19:11.23	4.762	18.64	10834 ± 368	4.2 ± 0.14	$2.5^{+0.12}_{-0.10}$	119^{+95}_{-77}	1
HIP 30069	B9V	06:19:40.96	-34:23:47.73	5.750	8.00	12000 ± 1000	4.5 ± 0.25	$2.8^{+0.42}_{-0.38}$	25^{+62}_{-18}	2
HIP 30073	B2V	06:19:42.7989	-07:49:22.473	5.246	3.74	22000 ± 1000	4.5 ± 0.25	$7.8^{+0.71}_{-0.71}$	8^{+6}_{-3}	2
HIP 30666	A3Vn	06:26:39.59	-01:30:26.41	5.874	13.80	10520 ± 358	4.2 ± 0.14	$2.6^{+0.20}_{-0.16}$	304^{+37}_{-72}	1
HIP 30788	B4V	06:28:10.21	-32:34:48.25	4.480	7.70	18000 ± 1000	4.5 ± 0.25	$5.4^{+0.59}_{-0.57}$	11^{+13}_{-6}	2
HIP 31278	B5Vn	06:33:37.92	-01:13:12.55	5.083	5.89	16000 ± 1000	4.0 ± 0.25	$4.7^{+0.61}_{-0.56}$	26^{+31}_{-18}	2
HIP 31362	B8V	06:34:35.33	-32:42:58.51	5.610	6.20	12000 ± 1000	4.5 ± 0.25	$2.8^{+0.41}_{-0.37}$	24^{+62}_{-17}	2
HIP 31434	A0Vnn	06:35:12.06	+28:01:20.32	5.266	8.82	10000 ± 500	3.5 ± 0.25	$2.7^{+0.46}_{-0.41}$	281^{+83}_{-131}	2
HIP 32474	B9.5V	06:46:39.02	-10:06:26.50	5.653	6.04	10000 ± 500	3.5 ± 0.25	$2.8^{+0.47}_{-0.43}$	281^{+85}_{-117}	2
HIP 32607	A8V	06:48:11.46	-61:56:29.00	3.300	33.78	7770 ± 264	3.8 ± 0.14	$1.6^{+0.07}_{-0.06}$	519^{+344}_{-333}	1
HIP 33372	B8Vn	06:56:25.83	+09:57:23.67	5.905	7.18	14000 ± 1000	4.5 ± 0.25	$3.6^{+0.47}_{-0.46}$	18^{+37}_{-11}	2
HIP 34769	A2V	07:11:51.86	-00:29:33.96	4.150	8.49	9000 ± 500	3.5 ± 0.25	$2.4^{+0.43}_{-0.38}$	405^{+135}_{-207}	2
HIP 35180	A1V	07:16:14.55	-15:35:08.49	5.454	12.12	9562 ± 325	4.1 ± 0.14	$2.1^{+0.12}_{-0.09}$	267^{+139}_{-158}	1

Table 7.1: - (Continued)

Star	SpT	RA	DEC	V	parallax (mas)	$T_{\rm eff}$ (K)	$\log g$ (cgs)	Mass ($M_\odot$)	Age (Myr)	Ref
HIP 35341	A5Vn	07:18:02.22	+40:53:00.22	5.870	11.73	8014 ± 272	3.9 ± 0.14	$1.7^{+0.07}_{-0.06}$	357^{+293}_{-237}	1
HIP 36393	A4V	07:29:20.44	+28:07:05.79	5.072	18.51	9184 ± 312	4.1 ± 0.14	$2.1^{+0.15}_{-0.13}$	431^{+128}_{-200}	1
HIP 36760	A1Vn	07:33:36.48	+15:49:35.98	5.269	7.70	9000 ± 500	3.7 ± 0.25	$2.1^{+0.40}_{-0.26}$	351^{+175}_{-318}	2
HIP 36812	A0Vnn	07:34:15.89	+03:22:18.19	5.830	5.67	9500 ± 1000	4.0 ± 0.25	$2.1^{+0.40}_{-0.31}$	108^{+273}_{-95}	2
HIP 36917	B7V	07:35:22.89	-28:22:09.57	4.630	14.72	13926 ± 473	4.3 ± 0.14	$3.7^{+0.17}_{-0.15}$	62^{+35}_{-37}	1
HIP 37297	B2.5V	07:39:27.34	-38:18:28.88	4.840	5.87	20000 ± 1000	4.5 ± 0.25	$6.6^{+0.67}_{-0.62}$	9^{+9}_{-4}	2
HIP 37322	B5V	07:39:43.81	-38:08:21.44	5.664	5.70	16000 ± 1000	4.5 ± 0.25	$4.5^{+0.50}_{-0.50}$	13^{+22}_{-7}	2
HIP 37450	B5V	07:41:15.81	-38:32:00.72	5.410	5.50	16000 ± 1000	4.5 ± 0.25	$4.4^{+0.53}_{-0.48}$	13^{+22}_{-8}	2
HIP 38538	A3V	07:53:29.81	+26:45:56.82	4.977	14.66	8551 ± 291	4.0 ± 0.14	$1.9^{+0.15}_{-0.12}$	637^{+111}_{-199}	1
HIP 38593	B2V	07:54:11.01	-35:52:38.23	5.462	4.81	22000 ± 1000	4.5 ± 0.25	$7.8^{+0.77}_{-0.68}$	8^{+6}_{-3}	2
HIP 38846	B2.5V	07:56:57.80	-43:30:01.48	5.340	2.08	22000 ± 1000	4.5 ± 0.25	$7.8^{+0.75}_{-0.72}$	8^{+6}_{-3}	2
HIP 39095	A1V	07:59:52.05	-18:23:57.23	4.610	13.52	8872 ± 302	3.4 ± 0.14	$2.1^{+0.18}_{-0.15}$	593^{+74}_{-85}	1
HIP 39236	B9.5Vn	08:01:30.29	+16:27:19.12	5.990	6.04	10000 ± 500	4.5 ± 0.25	$2.2^{+0.21}_{-0.19}$	36^{+119}_{-27}	2
HIP 39567	A1V	08:05:04.49	+13:07:05.58	5.146	15.20	10352 ± 352	4.3 ± 0.14	$2.4^{+0.12}_{-0.10}$	178^{+110}_{-109}	1
HIP 39847	A2V	08:08:27.45	+51:30:24.01	4.802	13.04	10014 ± 340	4.0 ± 0.14	$2.2^{+0.14}_{-0.12}$	190^{+127}_{-116}	1
HIP 39906	B5V	08:09:01.64	-19:14:42.05	4.390	7.01	18000 ± 1000	4.5 ± 0.25	$5.4^{+0.63}_{-0.54}$	11^{+15}_{-5}	2
HIP 40429	A2V	08:15:15.92	-62:54:56.32	5.160	12.90	8725 ± 297	3.9 ± 0.14	$2.1^{+0.20}_{-0.17}$	635^{+88}_{-88}	1
HIP 40706	A8V	08:18:33.31	-36:39:33.44	4.400	34.93	7986 ± 272	4.3 ± 0.14	$1.7^{+0.08}_{-0.06}$	540^{+282}_{-330}	1
HIP 40881	B9.5V	08:20:32.14	+24:01:20.32	5.930	7.13	9500 ± 1000	4.0 ± 0.25	$2.1^{+0.39}_{-0.32}$	105^{+287}_{-93}	2
HIP 41039	B1V	08:22:31.69	-48:29:25.36	4.820	1.90	...	...	...	...	...
HIP 41307	A0Va	08:25:39.63	-03:54:23.12	3.900	26.66	10281 ± 350	4.2 ± 0.14	$2.3^{+0.12}_{-0.10}$	201^{+109}_{-120}	1
HIP 42090	A2Vnn	08:34:43.88	+36:25:10.63	5.755	9.19	9000 ± 1000	4.0 ± 0.25	$1.9^{+0.36}_{-0.31}$	133^{+379}_{-119}	2
HIP 42129	B3V	08:35:15.56	-58:13:29.05	5.241	3.64	18000 ± 1000	4.5 ± 0.25	$5.4^{+0.61}_{-0.56}$	11^{+14}_{-5}	2
HIP 42313	A0Vnn	08:37:39.37	+05:42:13.61	4.137	20.34	11055 ± 376	4.0 ± 0.14	$2.9^{+0.23}_{-0.19}$	260^{+29}_{-44}	1
HIP 42334	A0V	08:37:52.15	-26:15:18.01	5.270	14.07	11614 ± 395	4.3 ± 0.14	$2.7^{+0.12}_{-0.10}$	79^{+71}_{-51}	1
HIP 43142	A3V	08:47:14.99	-01:53:49.31	5.279	8.12	9000 ± 500	4.0 ± 0.25	$2.0^{+0.21}_{-0.18}$	94^{+314}_{-83}	2
HIP 44127	A7V	08:59:12.45	+48:02:30.57	3.140	68.92	8233 ± 280	4.4 ± 0.14	$1.7^{+0.09}_{-0.07}$	474^{+257}_{-294}	1
HIP 44307	A2V	09:01:24.13	+32:15:08.26	5.870	6.99	8500 ± 1000	4.0 ± 0.25	$1.7^{+0.33}_{-0.28}$	162^{+537}_{-148}	2
HIP 45336	B9.5V	09:14:21.86	+02:18:51.34	3.880	28.74	10826 ± 368	4.2 ± 0.14	$2.5^{+0.12}_{-0.10}$	111^{+95}_{-71}	1
HIP 45344	B4V	09:14:24.48	-43:13:38.97	5.250	5.33	18000 ± 1000	4.5 ± 0.25	$5.4^{+0.62}_{-0.57}$	11^{+14}_{-5}	2
HIP 45688	A1V	09:18:50.64	+36:48:09.33	3.820	26.13	8862 ± 301	3.9 ± 0.14	$1.9^{+0.08}_{-0.07}$	255^{+202}_{-160}	1

Table 7.1: - (Continued)

Star	SpT	RA	DEC	V	parallax (mas)	$T_{\rm eff}$ (K)	$\log g$ (cgs)	Mass ($M_\odot$)	Age (Myr)	Ref
HIP 46225	A4V	09:25:27.23	-61:57:01.72	5.781	12.92	8577 ± 292	4.0 ± 0.14	$1.8^{+0.10}_{-0.07}$	418^{+206}_{-252}	1
HIP 46283	B6V	09:26:17.96	-53:22:44.07	5.088	7.60	16000 ± 1000	4.5 ± 0.25	$4.5^{+0.54}_{-0.50}$	13^{+20}_{-8}	2
HIP 46897	B9.5V	09:33:26.05	-22:51:49.99	5.911	12.46	10075 ± 343	4.2 ± 0.14	$2.3^{+0.16}_{-0.13}$	286^{+93}_{-140}	1
HIP 47006	A0Vn	09:34:49.43	+52:03:05.32	4.479	12.44	9757 ± 332	3.9 ± 0.14	$2.1^{+0.10}_{-0.08}$	181^{+138}_{-114}	1
HIP 47175	A7V	09:36:49.54	-49:21:18.09	4.350	30.94	8331 ± 283	4.3 ± 0.14	$1.8^{+0.11}_{-0.09}$	453^{+256}_{-278}	1
HIP 50303	A0Vn	10:16:14.43	+29:18:37.81	5.490	12.51	10377 ± 353	4.1 ± 0.14	$2.4^{+0.13}_{-0.11}$	204^{+103}_{-116}	1
HIP 50860	A6V	10:23:06.33	+33:54:29.31	5.900	13.46	8327 ± 283	4.1 ± 0.14	$1.8^{+0.11}_{-0.09}$	591^{+183}_{-303}	1
HIP 51362	B9.5V	10:29:28.70	-02:44:20.69	5.180	10.13	10899 ± 371	4.0 ± 0.14	$2.6^{+0.14}_{-0.12}$	182^{+81}_{-101}	1
HIP 51685	A2Vn	10:33:30.91	+34:59:19.30	5.580	4.77	9000 ± 500	3.5 ± 0.25	$2.4^{+0.42}_{-0.38}$	406^{+134}_{-172}	2
HIP 52422	A4Vn	10:43:01.88	+26:19:32.09	5.517	20.67	8170 ± 278	4.3 ± 0.14	$1.7^{+0.08}_{-0.06}$	432^{+278}_{-278}	1
HIP 52457	A3Vn	10:43:24.96	+23:11:18.25	5.075	14.23	9902 ± 337	4.0 ± 0.14	$2.2^{+0.12}_{-0.10}$	228^{+126}_{-137}	1
HIP 52638	A1Vn	10:45:51.89	+30:40:56.33	5.349	8.53	10000 ± 500	4.0 ± 0.25	$2.3^{+0.25}_{-0.21}$	69^{+199}_{-59}	2
HIP 52678	B6Vnn	10:46:16.56	-64:30:52.41	5.340	6.85	16000 ± 1000	4.5 ± 0.25	$4.4^{+0.55}_{-0.48}$	13^{+20}_{-7}	2
HIP 52736	B2.5Vn	10:46:51.22	-64:23:00.50	4.850	6.79	20000 ± 1000	4.5 ± 0.25	$6.5^{+0.66}_{-0.62}$	9^{+9}_{-4}	2
HIP 52911	A2V	10:49:15.43	+10:32:42.73	5.314	8.57	9000 ± 500	3.5 ± 0.25	$2.4^{+0.44}_{-0.37}$	406^{+138}_{-172}	2
HR 4259	A1V	10:55:36.80	+24:44:59.00	4.500	...	9000 ± 500	3.5 ± 0.25	$2.4^{+0.44}_{-0.36}$	411^{+137}_{-168}	2
HIP 54849	A0V	11:13:45.55	-00:04:10.20	5.399	6.18	10000 ± 500	4.0 ± 0.25	$2.3^{+0.24}_{-0.21}$	72^{+197}_{-62}	2
HIP 55434	B9.5V	11:21:08.1934	+06:01:45.571	4.044	14.82	10618 ± 361	3.9 ± 0.14	$2.7^{+0.23}_{-0.19}$	304^{+32}_{-38}	1
HIP 56034	A2V	11:29:04.12	+39:20:13.11	5.354	15.33	10000 ± 500	4.5 ± 0.25	$2.2^{+0.21}_{-0.21}$	37^{+118}_{-29}	2
HIP 56633	B9.5V	11:36:40.91	-09:48:08.09	4.682	11.63	11524 ± 392	4.0 ± 0.14	$2.8^{+0.15}_{-0.12}$	145^{+66}_{-82}	1
HIP 57328	A4V	11:45:17.04	+08:15:29.21	4.845	26.73	8298 ± 282	4.3 ± 0.14	$1.9^{+0.17}_{-0.14}$	757^{+105}_{-135}	1
HIP 58590	A5V	12:00:52.39	+06:36:51.56	4.659	8.49	8000 ± 500	3.5 ± 0.25	$2.0^{+0.41}_{-0.35}$	618^{+265}_{-300}	2
HIP 59394	A1V	12:11:03.84	-23:36:08.72	5.470	17.00	9671 ± 329	4.3 ± 0.14	$2.1^{+0.10}_{-0.09}$	203^{+144}_{-128}	1
HIP 59449	B3V	12:11:39.12	-52:22:06.44	3.960	8.61	18000 ± 1000	4.5 ± 0.25	$5.4^{+0.61}_{-0.55}$	11^{+14}_{-5}	2
HIP 59819	A3V	12:16:00.19	+14:53:56.65	5.090	16.42	9528 ± 324	4.0 ± 0.14	$2.2^{+0.16}_{-0.14}$	394^{+95}_{-165}	1
HIP 60009	B2.5V	12:18:26.25	-64:00:11.05	4.050	9.12	20000 ± 1000	4.5 ± 0.25	$6.6^{+0.65}_{-0.66}$	9^{+9}_{-4}	2
HIP 60030	A5Vn	12:18:40.32	-00:47:13.87	5.908	8.73	7750 ± 1000	3.5 ± 0.25	$1.9^{+0.50}_{-0.39}$	778^{+807}_{-403}	2
HIP 60595	A1V	12:25:11.76	-11:36:38.12	5.949	14.18	10396 ± 353	4.4 ± 0.14	$2.4^{+0.12}_{-0.10}$	161^{+111}_{-100}	1
HIP 60710	B3Vn	12:26:31.76	-51:27:02.29	4.805	7.28	20000 ± 1000	4.5 ± 0.25	$6.5^{+0.67}_{-0.63}$	9^{+9}_{-4}	2
HIP 60957	A3V	12:29:43.24	+20:53:45.99	5.680	11.90	9079 ± 309	3.9 ± 0.14	$2.1^{+0.15}_{-0.12}$	480^{+100}_{-192}	1
HIP 61558	A3V	12:36:47.35	-05:49:54.84	5.880	14.49	9600 ± 326	4.2 ± 0.14	$2.3^{+0.19}_{-0.16}$	436^{+57}_{-75}	1

Table 7.1: - (Continued)

Star	SpT	RA	DEC	V	parallax (mas)	$T_{\rm eff}$ (K)	$\log g$ (cgs)	Mass ($M_\odot$)	Age (Myr)	Ref
HIP 61622	A2V	12:37:42.16	-48:32:28.69	3.860	24.85	10533 ± 358	4.0 ± 0.14	$2.3^{+0.25}_{-0.23}$	158^{+137}_{-102}	1
HIP 62541	A1V	12:48:54.21	+14:07:21.31	5.702	8.17	9250 ± 1000	4.0 ± 0.25	$2.0^{+0.36}_{-0.31}$	124^{+326}_{-110}	2
HIP 62576	A2V	12:49:17.45	+27:33:08.57	5.780	10.76	9955 ± 338	4.1 ± 0.14	$2.2^{+0.12}_{-0.11}$	188^{+132}_{-117}	1
HIP 63724	A0V	13:03:33.31	-49:31:38.15	4.830	14.79	10462 ± 356	4.1 ± 0.14	$2.4^{+0.12}_{-0.10}$	154^{+106}_{-96}	1
HIP 63945	B5V	13:06:16.70	-48:27:47.85	4.694	8.36	18000 ± 1000	4.5 ± 0.25	$5.4^{+0.61}_{-0.56}$	11^{+13}_{-6}	2
HIP 65198	A2V	13:21:41.64	+02:05:14.07	5.693	14.77	10291 ± 350	4.2 ± 0.14	$2.3^{+0.11}_{-0.10}$	174^{+111}_{-108}	1
HIP 65477	A5V	13:25:13.54	+54:59:16.65	4.010	39.91	8221 ± 280	4.2 ± 0.14	$1.8^{+0.16}_{-0.13}$	754^{+157}_{-222}	1
HIP 65728	A1Vn	13:28:27.09	+59:56:44.83	5.400	14.01	10388 ± 353	4.2 ± 0.14	$2.7^{+0.24}_{-0.19}$	331^{+39}_{-45}	1
HIP 66249	A2Van	13:34:41.74	-00:35:45.38	3.380	44.03	8542 ± 290	4.1 ± 0.14	$1.9^{+0.15}_{-0.12}$	631^{+113}_{-226}	1
HIP 66798	A2V	13:41:29.89	+64:49:20.68	5.850	14.66	9347 ± 318	4.2 ± 0.14	$2.1^{+0.11}_{-0.09}$	291^{+153}_{-170}	1
HIP 66821	B8.5Vn	13:41:44.77	-54:33:33.93	5.010	12.02	13141 ± 447	4.4 ± 0.14	$3.7^{+0.29}_{-0.24}$	138^{+12}_{-20}	1
HIP 67143	A0V	13:45:36.89	-26:06:57.63	5.805	11.49	10338 ± 351	4.3 ± 0.14	$2.3^{+0.11}_{-0.09}$	143^{+112}_{-93}	1
HIP 67194	A5V	13:46:13.55	+41:05:19.48	5.891	19.03	7953 ± 270	4.3 ± 0.14	$1.7^{+0.10}_{-0.09}$	504^{+325}_{-319}	1
HIP 67782	A8IV	13:53:10.28	+28:38:53.28	5.911	15.21	8051 ± 274	4.1 ± 0.14	$1.8^{+0.16}_{-0.12}$	846^{+121}_{-164}	1
HIP 68092	A8V	13:56:27.88	+01:03:02.09	5.906	11.08	7866 ± 267	3.9 ± 0.14	$1.6^{+0.07}_{-0.07}$	410^{+331}_{-274}	1
HIP 68520	A3V	14:01:38.79	+01:32:40.31	4.244	14.50	8413 ± 286	3.4 ± 0.14	$2.0^{+0.18}_{-0.14}$	722^{+118}_{-129}	1
HIP 70327	A0V	14:23:22.70	+08:26:47.84	5.120	15.17	9678 ± 329	4.0 ± 0.14	$2.2^{+0.12}_{-0.09}$	261^{+133}_{-154}	1
HIP 70384	A3V	14:24:00.88	+08:14:38.30	5.935	7.38	9000 ± 500	4.0 ± 0.25	$2.0^{+0.22}_{-0.18}$	99^{+316}_{-87}	2
HIP 70400	A3V	14:24:11.34	+05:49:12.47	5.103	20.51	8490 ± 289	4.2 ± 0.14	$1.8^{+0.08}_{-0.07}$	336^{+238}_{-215}	1
HIP 70915	B8Vn	14:30:08.63	-45:19:16.88	5.500	6.84	12000 ± 1000	4.5 ± 0.25	$2.8^{+0.42}_{-0.37}$	24^{+65}_{-17}	2
HIP 71865	B3V	14:41:57.59	-37:47:36.59	4.000	9.62	20000 ± 1000	4.5 ± 0.25	$6.6^{+0.66}_{-0.64}$	9^{+9}_{-4}	2
HIP 71974	B9.5V	14:43:13.55	-24:59:51.91	5.730	6.56	10000 ± 500	4.0 ± 0.25	$2.3^{+0.26}_{-0.22}$	65^{+210}_{-55}	2
HIP 72104	A0Vnn	14:44:59.20	-35:11:30.57	4.923	15.22	9618 ± 327	3.8 ± 0.14	$2.1^{+0.12}_{-0.09}$	239^{+143}_{-144}	1
HIP 72154	B9.5V	14:45:30.20	+00:43:02.19	5.673	6.61	10000 ± 500	4.0 ± 0.25	$2.3^{+0.24}_{-0.21}$	75^{+199}_{-65}	2
HIP 72250	A1V	14:46:28.99	-47:26:28.02	5.740	10.67	9784 ± 333	4.1 ± 0.14	$2.4^{+0.21}_{-0.18}$	411^{+49}_{-59}	1
HIP 72378	B9V	14:47:57.56	-26:38:46.16	5.768	7.29	9500 ± 1000	4.0 ± 0.25	$2.0^{+0.39}_{-0.31}$	103^{+291}_{-91}	2
HIP 72552	A4V	14:49:58.40	+28:36:57.00	5.800	10.16	9591 ± 326	3.9 ± 0.14	$2.2^{+0.14}_{-0.11}$	359^{+95}_{-168}	1
HIP 73049	A0V	14:55:44.71	-33:51:20.82	5.318	12.85	10108 ± 344	4.3 ± 0.14	$2.4^{+0.18}_{-0.14}$	337^{+53}_{-113}	1
HR 5605	B5V	15:05:07.18	-47:03:04.00	4.720	···	16000 ± 1000	4.5 ± 0.25	$4.5^{+0.53}_{-0.52}$	14^{+21}_{-8}	2
HIP 74117	B3V	15:08:50.62	-45:16:47.49	4.070	4.20	20000 ± 1000	4.5 ± 0.25	$6.6^{+0.67}_{-0.66}$	9^{+9}_{-4}	2
HIP 74689	A4V	15:15:49.08	+00:22:19.70	5.629	21.67	8255 ± 281	4.4 ± 0.14	$1.9^{+0.17}_{-0.14}$	780^{+102}_{-113}	1

Table 7.1: - (Continued)

Star	SpT	RA	DEC	V	parallax (mas)	$T_{\rm eff}$ (K)	$\log g$ (cgs)	Mass ($M_\odot$)	Age (Myr)	Ref
HIP 75178	B9Vn	15:21:48.58	+32:56:01.30	5.375	12.45	12140 ± 413	4.3 ± 0.14	$3.3^{+0.26}_{-0.21}$	184^{+19}_{-28}	1
HIP 75304	B4V	15:23:09.35	-36:51:30.55	4.540	6.28	18000 ± 1000	4.5 ± 0.25	$5.4^{+0.58}_{-0.55}$	11^{+13}_{-6}	2
HIP 76267	A0V	15:34:41.27	+26:42:52.89	2.240	43.46	10342 ± 352	4.0 ± 0.14	$2.5^{+0.19}_{-0.16}$	313^{+53}_{-100}	1
HIP 76600	B2.5V	15:38:39.37	-29:46:39.89	3.644	8.89	20000 ± 1000	4.5 ± 0.25	$6.6^{+0.63}_{-0.65}$	9^{+9}_{-4}	2
HIP 76852	A1V	15:41:33.05	+19:40:13.44	4.509	17.16	9366 ± 318	4.1 ± 0.14	$2.0^{+0.09}_{-0.08}$	190^{+162}_{-123}	1
HIP 77233	A3V	15:46:11.25	+15:25:18.59	3.670	21.03	8928 ± 304	3.3 ± 0.14	$1.9^{+0.10}_{-0.08}$	332^{+191}_{-201}	1
HIP 77336	A3V	15:47:17.32	+14:06:55.26	5.712	13.04	8917 ± 303	4.0 ± 0.14	$2.9^{+0.23}_{-0.21}$	403^{+70}_{-75}	1
HIP 77516	A0V	15:49:37.21	-03:25:48.73	3.530	19.23	10000 ± 500	4.5 ± 0.25	$2.2^{+0.21}_{-0.19}$	37^{+113}_{-28}	2
HIP 77635	B1.5Vn	15:50:58.74	-25:45:04.66	4.638	6.59	24000 ± 1000	4.5 ± 0.25	$9.0^{+0.60}_{-0.67}$	7^{+4}_{-2}	2
HIP 77858	B5V	15:53:53.92	-24:31:59.37	5.376	7.76	16000 ± 1000	4.5 ± 0.25	$4.4^{+0.56}_{-0.49}$	13^{+21}_{-8}	2
HIP 78105	A3V	15:56:53.50	-33:57:58.01	5.080	23.60	9206 ± 313	4.1 ± 0.14	$2.0^{+0.12}_{-0.10}$	291^{+173}_{-171}	1
HIP 78106	B9V	15:56:54.12	-33:57:51.34	5.550	21.71	9725 ± 331	4.2 ± 0.14	$2.4^{+0.19}_{-0.15}$	412^{+50}_{-83}	1
HIP 78265	B1V	15:58:51.1132	-26:06:50.788	2.910	5.57	...	...	...	...	...
HIP 78554	A3V	16:02:17.69	+22:48:16.03	4.817	18.22	9226 ± 314	4.1 ± 0.14	$2.1^{+0.15}_{-0.13}$	464^{+88}_{-171}	1
HIP 78820	B1V	16:05:26.23	-19:48:19.63	2.620	8.07	...	...	...	...	...
HR 6025	A0Vn	16:06:19.6762	+67:48:36.480	5.439	12.85	9250 ± 1000	4.5 ± 0.25	$1.9^{+0.32}_{-0.31}$	48^{+210}_{-39}	2
HIP 78918	B2.5Vn	16:06:35.55	-36:48:08.26	4.205	7.87	20000 ± 1000	4.5 ± 0.25	$6.6^{+0.68}_{-0.63}$	9^{+9}_{-4}	2
HIP 78933	B1V	16:06:48.4269	-20:40:09.090	3.970	6.92	...	...	...	...	...
HIP 79005	B9V	16:07:36.42	-12:44:43.46	5.757	8.90	10000 ± 500	3.5 ± 0.25	$2.8^{+0.46}_{-0.42}$	281^{+84}_{-111}	2
HIP 79007	A7V	16:07:37.54	+09:53:30.27	5.639	10.10	7893 ± 268	3.9 ± 0.14	$1.6^{+0.08}_{-0.07}$	463^{+324}_{-301}	1
HIP 79199	B8V	16:09:52.59	-33:32:44.90	5.496	8.00	12000 ± 1000	4.5 ± 0.25	$2.8^{+0.40}_{-0.39}$	25^{+65}_{-17}	2
HIP 79387	A4V	16:12:07.32	-08:32:51.28	5.435	12.92	8418 ± 286	4.0 ± 0.14	$1.9^{+0.16}_{-0.12}$	694^{+108}_{-181}	1
HIP 79404	B2V	16:12:18.20	-27:55:34.95	4.567	6.81	22000 ± 1000	4.5 ± 0.25	$7.8^{+0.71}_{-0.68}$	8^{+6}_{-3}	2
HIP 79653	B8V	16:15:15.32	-47:22:19.27	5.124	8.46	14000 ± 1000	4.5 ± 0.25	$3.6^{+0.47}_{-0.44}$	17^{+35}_{-11}	2
HIP 80460	A5V	16:25:24.17	+37:23:38.68	5.540	13.43	7810 ± 266	3.7 ± 0.14	$1.7^{+0.11}_{-0.08}$	783^{+229}_{-412}	1
HIP 80815	B3V	16:30:12.48	-25:06:54.80	4.790	7.89	22000 ± 1000	4.5 ± 0.25	$7.8^{+0.76}_{-0.71}$	8^{+6}_{-3}	2
HIP 80883	A0V	16:30:54.82	+01:59:02.12	3.900	18.84	9000 ± 500	4.0 ± 0.25	$2.0^{+0.22}_{-0.18}$	97^{+294}_{-86}	2
HIP 80991	A2V	16:32:25.68	+60:49:23.96	5.910	8.79	9000 ± 500	3.5 ± 0.25	$2.4^{+0.42}_{-0.39}$	405^{+134}_{-176}	2
HIP 81126	B9V	16:34:06.18	+42:26:13.34	4.196	10.36	...	...	...	...	...
HIP 81641	A1V	16:40:38.69	+04:13:11.23	5.772	11.11	10572 ± 359	4.1 ± 0.14	$2.6^{+0.21}_{-0.17}$	301^{+38}_{-66}	1
HIP 82350	A1V	16:49:34.66	+13:15:40.10	5.910	9.99	9630 ± 327	4.1 ± 0.14	$2.1^{+0.10}_{-0.08}$	207^{+145}_{-130}	1

Table 7.1: - (Continued)

Star	SpT	RA	DEC	V	parallax (mas)	$T_{\rm eff}$ (K)	$\log g$ (cgs)	Mass ($M_\odot$)	Age (Myr)	Ref
HIP 82514	B1.5V	16:51:52.2311	-38:02:50.569	2.980	6.51	26000 ± 1000	4.5 ± 0.25	$9.6^{+0.25}_{-0.43}$	5^{+3}_{-1}	2
HIP 82673	B8V	16:54:00.47	+10:09:55.30	4.380	13.30	12000 ± 1000	3.8 ± 0.25	$3.1^{+0.58}_{-0.45}$	118^{+82}_{-98}	2
HIP 83635	B1V	17:05:32.26	-00:53:31.45	5.610	2.92	...	...	...	...	...
HIP 84606	A2V	17:17:40.25	+37:17:29.40	4.650	18.59	9702 ± 330	4.0 ± 0.14	$2.1^{+0.10}_{-0.09}$	155^{+137}_{-100}	1
HIP 85290	A1Vn	17:25:41.35	+60:02:54.23	5.645	10.32	10989 ± 374	4.0 ± 0.14	$2.5^{+0.12}_{-0.11}$	110^{+88}_{-70}	1
HIP 85379	A4V	17:26:44.24	+48:15:36.23	5.830	8.68	8000 ± 500	3.5 ± 0.25	$2.0^{+0.42}_{-0.32}$	621^{+266}_{-320}	2
HIP 85385	B5V	17:26:49.13	+20:04:51.52	5.510	5.59	...	...	...	...	...
HIP 85537	A8Vp	17:28:49.65	+00:19:50.25	5.424	16.77	7624 ± 259	3.8 ± 0.14	$1.8^{+0.16}_{-0.14}$	1064^{+148}_{-159}	1
HIP 85727	B8Vn	17:31:05.91	-60:41:01.85	3.620	16.48	12740 ± 433	4.0 ± 0.14	$3.2^{+0.15}_{-0.13}$	92^{+48}_{-54}	1
HIP 85922	A5V	17:33:29.85	-05:44:41.29	5.619	20.79	8000 ± 500	4.0 ± 0.25	$1.7^{+0.19}_{-0.16}$	117^{+539}_{-105}	2
HIP 86019	B8Vn	17:34:46.35	-11:14:31.19	5.537	8.11	12000 ± 1000	4.5 ± 0.25	$2.8^{+0.42}_{-0.37}$	25^{+62}_{-17}	2
HIP 86782	A2V	17:43:59.18	+53:48:06.17	5.760	6.12	10000 ± 500	4.0 ± 0.25	$2.3^{+0.25}_{-0.22}$	58^{+207}_{-49}	2
HIP 87108	A0Vn	17:47:53.56	+02:42:26.20	3.750	31.73	10075 ± 343	4.2 ± 0.14	$2.3^{+0.15}_{-0.12}$	258^{+101}_{-138}	1
HIP 88116	A0	17:59:47.56	-23:48:58.09	4.731	7.85	10000 ± 500	4.0 ± 0.25	$2.3^{+0.25}_{-0.20}$	76^{+200}_{-66}	2
HIP 88290	A2Vn	18:01:45.20	+01:18:18.28	4.439	11.15	10010 ± 340	3.8 ± 0.14	$2.3^{+0.12}_{-0.11}$	243^{+112}_{-140}	1
HIP 88818	A3V	18:07:49.45	+26:06:04.13	5.870	20.16	9162 ± 312	4.3 ± 0.14	$2.7^{+0.24}_{-0.23}$	442^{+86}_{-70}	1
HIP 88817	A3V	18:07:49.50	+26:05:50.40	5.900	25.92	9162 ± 312	4.3 ± 0.14	$2.1^{+0.15}_{-0.12}$	481^{+83}_{-173}	1
HIP 89156	A3V	18:11:45.12	+33:26:49.41	5.970	4.21	9000 ± 500	3.5 ± 0.25	$2.4^{+0.42}_{-0.39}$	410^{+135}_{-157}	2
HIP 89935	A7V	18:21:01.02	+28:52:11.83	5.129	12.40	7594 ± 258	3.4 ± 0.14	$2.3^{+0.10}_{-0.13}$	727^{+108}_{-70}	1
HIP 90052	A2V	18:22:35.32	+12:01:46.85	5.980	7.42	9000 ± 500	3.5 ± 0.25	$2.4^{+0.43}_{-0.40}$	404^{+138}_{-175}	2
HIP 90762	A2V	18:31:04.45	+16:55:42.80	5.760	7.49	8750 ± 1000	3.5 ± 0.25	$2.2^{+0.54}_{-0.46}$	482^{+375}_{-247}	2
HIP 90887	A3Vn	18:32:21.33	-39:42:14.40	5.162	14.23	9403 ± 320	4.1 ± 0.14	$2.1^{+0.14}_{-0.12}$	335^{+143}_{-187}	1
HIP 91118	A0Vn	18:35:12.60	+18:12:12.28	5.790	5.04	9500 ± 1000	4.0 ± 0.25	$2.1^{+0.39}_{-0.32}$	111^{+276}_{-98}	2
HIP 91875	A2Vn	18:43:46.94	-38:19:24.39	5.120	15.89	9287 ± 316	4.0 ± 0.14	$2.1^{+0.12}_{-0.10}$	339^{+145}_{-189}	1
HIP 92027	A1V	18:45:28.36	+05:30:00.44	5.830	5.30	9000 ± 500	3.5 ± 0.25	$2.4^{+0.43}_{-0.37}$	406^{+140}_{-167}	2
HIP 92312	A1V	18:48:53.39	+19:19:43.40	5.894	11.41	9923 ± 337	4.2 ± 0.14	$2.2^{+0.10}_{-0.09}$	164^{+128}_{-105}	1
HIP 92728	B2.5V	18:53:43.56	+36:58:18.19	5.569	3.29	20000 ± 1000	4.5 ± 0.25	$6.6^{+0.68}_{-0.61}$	9^{+9}_{-4}	2
HIP 92855	B2V	18:55:15.93	-26:17:48.21	2.058	14.32	19192 ± 653	4.3 ± 0.14	$6.3^{+0.38}_{-0.28}$	29^{+6}_{-12}	1
HIP 92946	A5V	18:56:13.18	+04:12:12.91	4.620	21.09	7968 ± 271	4.1 ± 0.14	$1.6^{+0.19}_{-0.23}$	658^{+683}_{-409}	1
HIP 93225	B4V	18:59:23.80	-12:50:25.86	5.516	6.84	15000 ± 1000	3.8 ± 0.25	$4.4^{+0.71}_{-0.55}$	54^{+34}_{-42}	2
HIP 93393	B5V	19:01:17.36	+26:17:29.08	5.683	5.02	18000 ± 1000	4.5 ± 0.25	$5.4^{+0.60}_{-0.55}$	11^{+13}_{-5}	2

Table 7.1: - (Continued)

Star	SpT	RA	DEC	V	parallax (mas)	$T_{\rm eff}$ (K)	$\log g$ (cgs)	Mass ($M_\odot$)	Age (Myr)	Ref
HIP 93580	A4V	19:03:32.25	+01:49:07.57	5.826	18.22	8224 ± 280	4.3 ± 0.14	$1.8^{+0.12}_{-0.10}$	590^{+236}_{-315}	1
HIP 93713	A0Vn	19:04:55.17	+53:23:47.96	5.380	9.00	9000 ± 1000	4.0 ± 0.25	$1.9^{+0.36}_{-0.31}$	129^{+363}_{-115}	2
HIP 93747	A0Vn	19:05:24.61	+13:51:48.52	2.990	39.28	11409 ± 388	4.2 ± 0.14	$3.3^{+0.29}_{-0.25}$	231^{+23}_{-26}	1
HIP 93805	B9Vn	19:06:14.94	-04:52:57.20	3.430	26.37	11962 ± 407	4.2 ± 0.14	$3.5^{+0.33}_{-0.27}$	194^{+20}_{-22}	1
HIP 94620	A4V	19:15:17.36	+21:13:55.62	5.654	10.89	9190 ± 312	4.0 ± 0.14	$2.0^{+0.09}_{-0.07}$	202^{+169}_{-130}	1
HIP 94720	B9.5V	19:16:26.79	+14:32:40.62	5.630	7.96	10000 ± 500	4.0 ± 0.25	$2.3^{+0.25}_{-0.20}$	69^{+194}_{-58}	2
HIP 95241	B9V	19:22:38.30	-44:27:32.25	4.010	10.40	12000 ± 1000	4.0 ± 0.25	$2.9^{+0.50}_{-0.41}$	53^{+108}_{-43}	2
HIP 95560	A0V	19:26:13.25	+20:05:51.84	5.594	13.72	9250 ± 1000	4.5 ± 0.25	$1.9^{+0.32}_{-0.29}$	45^{+197}_{-37}	2
HIP 95619	B8.5V	19:26:56.48	-29:44:35.62	5.650	14.30	11997 ± 408	4.3 ± 0.14	$2.9^{+0.15}_{-0.12}$	107^{+60}_{-63}	1
HIP 95853	A5V	19:29:42.36	+51:43:47.21	3.769	26.88	8216 ± 279	3.9 ± 0.14	$1.8^{+0.14}_{-0.11}$	693^{+186}_{-300}	1
HIP 96288	A2V	19:34:41.26	+42:24:45.04	5.348	5.66	9000 ± 500	3.5 ± 0.25	$2.4^{+0.43}_{-0.39}$	405^{+137}_{-166}	2
HIP 97376	B8Vn	19:47:27.78	+38:24:27.41	5.826	6.90	11500 ± 2000	4.5 ± 0.25	$2.2^{+0.73}_{-0.70}$	34^{+157}_{-26}	2
HIP 97496	A3V	19:48:58.66	+19:08:31.35	5.000	12.79	8422 ± 286	3.9 ± 0.14	$1.8^{+0.09}_{-0.07}$	435^{+227}_{-265}	1
HIP 97870	B5V	19:53:17.38	+57:31:24.53	5.132	5.15	16000 ± 1000	4.0 ± 0.25	$4.7^{+0.64}_{-0.53}$	26^{+32}_{-19}	2
HIP 97966	B7Vn	19:54:37.65	-08:13:38.24	5.710	6.76	14000 ± 1000	4.2 ± 0.25	$3.6^{+0.47}_{-0.46}$	24^{+45}_{-16}	2
HIP 98055	A4Vn	19:55:37.79	+52:26:20.21	4.920	11.59	9000 ± 500	4.5 ± 0.25	$1.9^{+0.18}_{-0.17}$	47^{+186}_{-38}	2
HIP 98325	B9Vn	19:58:37.98	+30:59:01.19	5.506	7.01	12000 ± 1000	4.5 ± 0.25	$2.8^{+0.41}_{-0.37}$	25^{+65}_{-17}	2
HIP 99080	B3V	20:06:53.41	+23:36:51.93	5.064	6.47	20000 ± 1000	4.5 ± 0.25	$6.6^{+0.68}_{-0.64}$	9^{+9}_{-4}	2
HIP 99742	A1Va	20:14:16.62	+15:11:51.39	4.947	21.75	9645 ± 328	4.3 ± 0.14	$2.3^{+0.17}_{-0.14}$	412^{+59}_{-116}	1
HIP 100069	B0V	20:18:06.99	+40:43:55.50	5.840	1.68	...	...	...	...	...
HIP 100221	B9V	20:19:36.72	+62:15:26.90	5.712	8.63	10000 ± 500	4.0 ± 0.25	$2.3^{+0.25}_{-0.21}$	70^{+205}_{-60}	2
HIP 100907	A3V	20:27:34.26	+38:26:25.19	5.620	12.28	9042 ± 307	4.0 ± 0.14	$2.1^{+0.16}_{-0.13}$	514^{+99}_{-166}	1
HIP 101123	A1V	20:29:53.91	-18:34:59.48	5.906	15.07	10492 ± 357	4.2 ± 0.14	$2.4^{+0.11}_{-0.09}$	143^{+109}_{-91}	1
HIP 101589	A3V	20:35:18.54	+14:40:27.17	4.664	14.82	8639 ± 294	3.8 ± 0.14	$2.0^{+0.15}_{-0.12}$	624^{+98}_{-176}	1
HIP 101716	B8V	20:37:04.67	+26:27:43.01	5.589	10.27	12949 ± 440	4.2 ± 0.14	$3.3^{+0.17}_{-0.14}$	91^{+44}_{-53}	1
HIP 101909	B3V	20:39:04.97	+15:50:17.52	5.980	2.42	...	...	...	...	...
HIP 102487	A1V	20:46:09.99	-21:30:50.52	5.913	12.37	9702 ± 330	4.1 ± 0.14	$2.1^{+0.11}_{-0.09}$	180^{+143}_{-116}	1
HIP 103298	A5V	20:55:38.57	+12:34:06.81	5.540	16.53	9093 ± 309	4.1 ± 0.14	$2.0^{+0.13}_{-0.11}$	400^{+150}_{-215}	1
HIP 104105	B8Vn	21:05:29.27	+78:07:35.02	5.915	8.10	9750 ± 1000	4.0 ± 0.25	$2.1^{+0.39}_{-0.32}$	92^{+255}_{-80}	2
HIP 104139	A1V	21:05:56.83	-17:13:58.30	4.070	20.11	10001 ± 340	4.2 ± 0.14	$2.2^{+0.11}_{-0.09}$	187^{+130}_{-116}	1
HIP 104365	A0V	21:08:33.63	-21:11:37.22	5.280	18.14	10878 ± 370	4.3 ± 0.14	$2.8^{+0.21}_{-0.17}$	272^{+33}_{-53}	1

Table 7.1: - (Continued)

Star	SpT	RA	DEC	V	parallax (mas)	$T_{\rm eff}$ (K)	$\log g$ (cgs)	Mass ($M_\odot$)	Age (Myr)	Ref
HIP 105140	A1V	21:17:56.28	-32:10:21.15	4.721	17.90	9126 ± 310	4.4 ± 0.14	$2.3^{+0.21}_{-0.18}$	538^{+69}_{-70}	1
HIP 105282	B6V	21:19:28.75	+49:30:37.06	5.740	5.98	16000 ± 1000	4.5 ± 0.25	$4.5^{+0.53}_{-0.51}$	13^{+21}_{-7}	2
HIP 105891	B6V	21:26:44.97	+52:53:54.73	5.989	7.28	10500 ± 2000	4.0 ± 0.25	$2.1^{+0.71}_{-0.58}$	102^{+404}_{-89}	2
HIP 105942	B3V	21:27:21.37	+37:07:00.47	5.289	2.50	20000 ± 1000	4.5 ± 0.25	$6.6^{+0.69}_{-0.64}$	9^{+9}_{-4}	2
HIP 105966	A1V	21:27:40.06	+27:36:30.94	5.389	17.14	9622 ± 327	4.3 ± 0.14	$2.1^{+0.12}_{-0.10}$	263^{+138}_{-156}	1
HIP 105972	B7V	21:27:46.14	+66:48:32.74	5.407	4.05	14000 ± 1000	4.0 ± 0.25	$3.8^{+0.53}_{-0.48}$	38^{+54}_{-29}	2
HIP 106711	A3Vn	21:36:56.98	+40:24:48.67	5.052	15.19	7859 ± 267	3.9 ± 0.14	$1.7^{+0.11}_{-0.08}$	767^{+226}_{-387}	1
HIP 106786	A7V	21:37:45.11	-07:51:15.13	4.690	18.26	8140 ± 277	4.0 ± 0.14	$1.7^{+0.10}_{-0.07}$	567^{+239}_{-326}	1
HIP 107517	A1V	21:46:32.10	-11:21:57.44	5.570	11.58	10674 ± 363	4.2 ± 0.14	$2.5^{+0.14}_{-0.11}$	191^{+89}_{-108}	1
HIP 107608	A2V	21:47:44.15	-30:53:53.90	5.016	10.16	9716 ± 330	4.0 ± 0.14	$2.2^{+0.15}_{-0.12}$	342^{+93}_{-161}	1
HIP 108294	A2Vn	21:56:22.77	-37:15:13.16	5.457	9.71	9000 ± 500	4.0 ± 0.25	$2.0^{+0.22}_{-0.18}$	93^{+318}_{-81}	2
HIP 108339	A2Vnn	21:56:56.37	+12:04:35.37	5.544	8.14	9250 ± 1000	4.0 ± 0.25	$2.0^{+0.35}_{-0.31}$	121^{+316}_{-109}	2
HIP 109056	B9Vn	22:05:34.67	+28:57:50.32	5.700	9.40	9800 ± 1200	4.4 ± 0.25	$2.0^{+0.41}_{-0.36}$	51^{+200}_{-42}	2
HIP 109139	B8V	22:06:26.23	-13:52:10.86	4.270	18.62	12641 ± 430	4.3 ± 0.14	$3.2^{+0.20}_{-0.16}$	124^{+37}_{-62}	1
HIP 109521	A5V	22:11:09.89	+50:49:24.26	5.386	17.81	8420 ± 286	4.2 ± 0.14	$2.0^{+0.19}_{-0.16}$	728^{+107}_{-106}	1
HIP 109831	A2Vnn	22:14:44.37	+42:57:14.07	5.720	12.14	10932 ± 372	4.2 ± 0.14	$2.5^{+0.13}_{-0.12}$	123^{+92}_{-79}	1
HIP 110838	B9Vn	22:27:19.97	-64:57:58.88	4.495	13.00	11271 ± 383	4.1 ± 0.14	$3.0^{+0.24}_{-0.20}$	243^{+24}_{-33}	1
HIP 110935	A4V	22:28:37.67	-67:29:20.62	5.570	23.19	8026 ± 273	4.3 ± 0.14	$1.7^{+0.08}_{-0.07}$	447^{+301}_{-291}	1
HIP 111056	A3V	22:29:52.98	+78:49:27.43	5.460	13.31	8750 ± 1000	4.2 ± 0.25	$1.8^{+0.33}_{-0.30}$	85^{+347}_{-74}	2
HIP 111068	B9.5V	22:30:01.81	+32:34:21.50	5.650	9.05	10000 ± 500	3.5 ± 0.25	$2.8^{+0.47}_{-0.42}$	280^{+85}_{-112}	2
HIP 111169	A1V	22:31:17.50	+50:16:56.97	3.770	31.79	10071 ± 342	4.3 ± 0.14	$2.3^{+0.12}_{-0.10}$	202^{+123}_{-123}	1
HIP 112029	B8V	22:41:27.73	+10:49:52.64	3.410	···	11913 ± 405	3.8 ± 0.14	$2.9^{+0.17}_{-0.14}$	135^{+57}_{-76}	1
HIP 113788	A1V	23:02:36.38	+42:45:28.06	···	7.74	9000 ± 500	4.0 ± 0.25	$2.0^{+0.22}_{-0.18}$	100^{+309}_{-88}	2
HIP 114520	A5Vn	23:11:44.19	+08:43:12.40	5.157	13.46	8220 ± 279	3.8 ± 0.14	$1.7^{+0.10}_{-0.08}$	437^{+277}_{-270}	1
HIP 114822	A2V	23:15:34.26	-03:29:46.96	5.550	14.04	9678 ± 329	4.1 ± 0.14	$2.2^{+0.12}_{-0.10}$	255^{+136}_{-153}	1
HIP 115115	A0V	23:18:57.68	-09:36:38.70	5.001	12.47	10671 ± 363	4.2 ± 0.14	$2.6^{+0.20}_{-0.16}$	284^{+38}_{-79}	1
HIP 116247	A0V	23:33:16.62	-20:54:52.21	4.709	11.11	10267 ± 349	3.9 ± 0.14	$2.5^{+0.20}_{-0.16}$	334^{+46}_{-78}	1
HIP 116582	B8V	23:37:32.04	+44:25:44.37	5.817	4.04	12000 ± 1000	4.0 ± 0.25	$2.9^{+0.46}_{-0.43}$	54^{+104}_{-44}	2
HIP 116611	A0Vn	23:37:56.80	+18:24:02.40	5.482	14.01	11060 ± 376	4.1 ± 0.14	$2.7^{+0.19}_{-0.15}$	228^{+46}_{-92}	1
HIP 116631	B8V	23:38:08.20	+43:16:05.06	4.290	6.53	12000 ± 1000	3.8 ± 0.25	$3.1^{+0.55}_{-0.48}$	116^{+82}_{-96}	2
HIP 116805	A0V	23:40:24.51	+44:20:02.16	4.140	19.37	11903 ± 405	4.3 ± 0.14	$2.9^{+0.17}_{-0.14}$	145^{+51}_{-74}	1

Table 7.1: - (Continued)

Star	SpT	RA	DEC	V	parallax (mas)	$T_{\rm eff}$ (K)	$\log g$ (cgs)	Mass ($M_\odot$)	Age (Myr)	Ref
HIP 116971	B9V	23:42:43.34	-14:32:41.65	4.483	21.96	11108 ± 378	4.3 ± 0.14	$2.6^{+0.15}_{-0.14}$	109^{+90}_{-70}	1
HIP 117089	B9V	23:44:12.08	-18:16:36.97	5.235	8.61	12000 ± 1000	4.5 ± 0.25	$2.8^{+0.40}_{-0.37}$	24^{+63}_{-17}	2
HIP 117371	A1Vn	23:47:54.77	+67:48:24.51	5.048	10.76	10308 ± 350	3.9 ± 0.14	$2.5^{+0.19}_{-0.17}$	323^{+53}_{-92}	1
HIP 117452	A0Vn	23:48:55.55	-28:07:48.97	4.570	23.73	11417 ± 388	4.3 ± 0.14	$3.0^{+0.26}_{-0.22}$	233^{+32}_{-37}	1
HIP 118121	A1V	23:57:35.08	-64:17:53.63	5.002	21.08	9979 ± 339	4.3 ± 0.14	$2.3^{+0.16}_{-0.13}$	335^{+70}_{-134}	1
HIP 118243	B1V	23:59:00.54	+55:45:17.74	4.997	0.72	...	...	...	...	...

Table 7.2: Spectroscopic Observation Log.
See Section 7.2.1 for details of the signal-to-noise ratio calculation (the snr column)

Star	MJD (JD-2450000)	Instrument	exptime (sec)	snr
HIP 813	6618.58	TS23	557	1810
HIP 1191	6552.60	CHIRON	1200	320
HIP 1366	6585.73	TS23	274	1790
HIP 1647	6510.74	CHIRON	1105	630
HIP 2381	6874.71	CHIRON	505	580
HIP 2505	6586.71	TS23	235	1700
HIP 2505	6962.71	TS23	804	1960
HIP 2505	6945.71	IGRINS	224	210
HIP 2548	7240.93	IGRINS	360	100
HIP 2548	6516.84	HRS	412	1070
HIP 3300	6299.55	TS23	689	1010
HIP 3478	6963.63	TS23	1200	1020
HIP 3478	7288.82	IGRINS	540	30
HIP 3478	6669.53	TS23	743	1870
HIP 3478	6945.72	IGRINS	224	150
HIP 5131	6587.70	TS23	655	1780
HIP 5131	7083.57	IGRINS	930	70
HIP 5131	6847.89	IGRINS	1600	110
HIP 5132	6587.77	TS23	535	1550
HIP 5132	6847.89	IGRINS	480	110
HIP 5310	6945.75	IGRINS	224	200
HIP 5361	6523.84	HRS	1000	810
HIP 5518	7238.94	IGRINS	540	80
HIP 5518	6945.77	IGRINS	224	160
HIP 5626	6945.88	IGRINS	224	160
HIP 7345	6888.76	CHIRON	1080	480
HIP 7345	6887.76	CHIRON	706	540
HIP 8016	6522.96	HRS	328	580
HIP 8704	6506.90	HRS	365	420
HIP 8704	7084.57	IGRINS	960	30
HIP 8704	7237.93	IGRINS	720	90
HR 545	6668.56	TS23	597	1920
HR 545	6586.75	TS23	265	1710
HR 545	6945.81	IGRINS	224	230
HIP 9312	6586.78	TS23	419	1750
HIP 9564	6945.78	IGRINS	224	140
HR 604	6585.86	TS23	349	1650
HIP 10320	6532.80	CHIRON	1020	550
HIP 10670	6618.68	TS23	141	1810
HIP 10732	6945.82	IGRINS	224	180
HIP 10732	7083.56	IGRINS	240	110
HIP 11345	6894.90	CHIRON	540	520

Table 7.2: - (Continued)

Star	MJD (JD-2450000)	Instrument	exptime (sec)	snr
HIP 12332	6677.54	TS23	1107	1530
HIP 12332	6947.79	IGRINS	224	170
HIP 12706	6584.86	TS23	362	990
HIP 12706	6946.84	IGRINS	224	150
HIP 12719	6583.87	TS23	264	1720
HIP 12803	6676.53	TS23	452	1410
HIP 12803	6947.80	IGRINS	224	140
HIP 12803	7240.95	IGRINS	780	120
HIP 13165	6518.91	HRS	275	850
HIP 13202	6910.83	CHIRON	580	570
HIP 13209	6618.66	TS23	143	1880
HIP 13327	6670.54	TS23	1200	1800
HIP 13717	6917.83	CHIRON	644	550
HIP 13717	6970.75	CHIRON	703	550
HIP 13879	6945.79	IGRINS	224	260
HIP 13879	6681.68	TS23	930	230
HIP 13879	6618.70	TS23	265	1490
HIP 14043	6523.92	HRS	400	620
HIP 14293	6919.89	CHIRON	800	240
HIP 14764	6679.53	TS23	532	1370
HIP 14764	6946.80	IGRINS	360	150
HIP 14862	6945.86	IGRINS	224	180
HIP 14862	7084.60	IGRINS	1200	120
HIP 15110	6946.83	IGRINS	224	120
HIP 15338	6523.90	HRS	570	690
HIP 15404	6517.92	HRS	205	620
HIP 15444	6582.94	TS23	340	1790
HIP 16210	6676.58	TS23	406	1440
HIP 16210	6945.84	IGRINS	224	160
HIP 16244	6583.84	TS23	311	1750
HIP 16244	6945.83	IGRINS	224	230
HIP 16285	6933.84	CHIRON	767	570
HIP 16322	6944.72	CHIRON	680	410
HIP 16322	6946.82	IGRINS	224	170
HIP 16340	6678.54	TS23	570	1410
HIP 16599	6945.85	IGRINS	224	170
HIP 16611	6946.85	IGRINS	224	210
HIP 16611	6522.88	CHIRON	255	580
HIP 17457	6531.82	CHIRON	1005	520
HIP 17527	6947.82	IGRINS	224	120
HIP 17527	6517.93	HRS	429	670
HIP 17527	6963.91	TS23	818	470
HIP 17563	6538.82	CHIRON	1088	400
HIP 18141	6678.59	TS23	605	1430
HIP 18396	6516.94	HRS	259	510

Table 7.2: - (Continued)

Star	MJD (JD-2450000)	Instrument	exptime (sec)	snr
HIP 18788	6535.81	CHIRON	1039	180
HIP 18805	6585.78	TS23	631	1760
HIP 19799	6668.63	TS23	1200	1900
HIP 19949	6945.90	IGRINS	224	220
HIP 19949	7084.62	IGRINS	960	30
HIP 19968	6676.62	TS23	524	1390
HIP 20264	6718.53	CHIRON	860	410
HIP 20380	6945.89	IGRINS	224	180
HIP 20380	7084.67	IGRINS	1200	30
HIP 20430	6520.95	HRS	360	710
HIP 20507	6719.50	CHIRON	715	470
HIP 20579	6517.96	HRS	490	830
HIP 20789	6946.86	IGRINS	224	150
HIP 20789	6586.83	TS23	524	1610
HIP 21589	6962.94	TS23	220	1020
HIP 21589	7065.63	CHIRON	754	290
HIP 21589	6948.96	IGRINS	112	140
HIP 21683	6948.98	IGRINS	230	110
HIP 21683	6962.97	TS23	335	1040
HIP 21819	6679.64	TS23	466	1480
HIP 21928	6677.63	TS23	1124	1470
HIP 22028	6947.90	IGRINS	240	140
HIP 22509	6667.62	TS23	1200	1100
HIP 22509	7126.51	CHIRON	2612	440
HIP 22833	6679.60	TS23	521	1520
HIP 22833	6946.87	IGRINS	224	140
HIP 22840	6678.64	TS23	528	1380
HIP 22913	6585.74	CHIRON	1200	230
HIP 22958	6551.79	CHIRON	1200	340
HIP 22958	6943.77	CHIRON	650	320
HIP 23362	6548.87	CHIRON	725	520
HIP 23362	6946.93	IGRINS	240	180
HIP 23916	6555.82	CHIRON	1200	40
HIP 23916	6946.95	IGRINS	280	140
HIP 24244	6949.84	CHIRON	370	560
HIP 24244	6554.91	CHIRON	488	330
HIP 24327	6529.88	CHIRON	277	560
HIP 24505	7036.69	CHIRON	2045	480
HIP 24902	6946.88	IGRINS	224	180
ADS 3962 AB	6946.92	IGRINS	280	170
HIP 25143	7084.65	IGRINS	960	80
HIP 25143	6946.89	IGRINS	224	180
HIP 25280	6950.75	CHIRON	597	540
HIP 25280	6947.91	IGRINS	240	130
HIP 25555	6670.63	TS23	600	1950

Table 7.2: - (Continued)

Star	MJD (JD-2450000)	Instrument	exptime (sec)	snr
HIP 25608	6718.62	CHIRON	1030	360
HIP 25695	6669.65	TS23	1200	1860
HIP 25790	6946.90	IGRINS	224	160
HIP 25813	7083.58	IGRINS	1020	200
HIP 25813	6544.88	CHIRON	384	260
HIP 26063	6582.80	CHIRON	1139	250
HIP 26093	6946.91	IGRINS	280	150
HIP 26093	6676.66	TS23	525	1380
HIP 26093	7084.72	IGRINS	1800	90
HIP 26126	6946.96	IGRINS	240	170
HIP 26126	6721.50	CHIRON	507	450
HIP 26126	6948.81	CHIRON	550	360
HIP 26563	6677.68	TS23	502	1550
HIP 27100	6692.59	CHIRON	294	680
HIP 27100	6727.54	CHIRON	177	560
HIP 27321	6696.62	CHIRON	178	640
HIP 27713	6946.97	IGRINS	240	150
HIP 28691	6298.78	TS23	646	1300
HIP 28756	6571.74	CHIRON	1200	320
HIP 28910	6693.61	CHIRON	343	560
HIP 29150	6697.63	CHIRON	950	380
HIP 29151	6946.99	IGRINS	264	170
HIP 29151	6953.82	CHIRON	617	540
HIP 29735	6559.80	CHIRON	803	380
HIP 29735	6946.98	IGRINS	240	170
HIP 29997	6679.70	TS23	415	1460
HIP 30069	6573.75	CHIRON	1200	250
HIP 30073	6581.82	CHIRON	1011	280
HIP 30666	6947.00	IGRINS	280	160
HIP 30788	6574.75	CHIRON	488	340
HIP 31278	7084.69	IGRINS	960	90
HIP 31278	6668.71	TS23	797	1920
HIP 31278	6947.01	IGRINS	280	170
HIP 31362	6598.72	CHIRON	1200	250
HIP 31434	6676.71	TS23	611	1480
HIP 32474	6592.74	CHIRON	1200	340
HIP 32607	7037.75	CHIRON	56	210
HIP 32607	7039.62	CHIRON	49	210
HIP 32607	6724.56	CHIRON	67	560
HIP 33372	6948.00	IGRINS	320	110
HIP 33372	6678.72	TS23	720	1380
HIP 34769	6677.75	TS23	279	1520
HIP 35180	6696.76	CHIRON	925	290
HIP 35341	6680.75	TS23	833	1070
HIP 36393	6676.76	TS23	616	1550

Table 7.2: - (Continued)

Star	MJD (JD-2450000)	Instrument	exptime (sec)	snr
HIP 36393	6670.76	TS23	494	1400
HIP 36760	7084.74	IGRINS	720	150
HIP 36760	7037.76	CHIRON	4284	370
HIP 36760	7039.68	CHIRON	3127	480
HIP 36760	6668.79	TS23	836	700
HIP 36812	6947.99	IGRINS	280	110
HIP 36917	6583.81	CHIRON	571	420
HIP 36917	6971.83	CHIRON	435	690
HIP 37297	6698.74	CHIRON	370	480
HIP 37297	6574.82	CHIRON	686	340
HIP 37297	6729.53	CHIRON	231	460
HIP 37322	6975.79	CHIRON	817	540
HIP 37450	6600.74	CHIRON	1171	450
HIP 38538	6669.78	TS23	474	1990
HIP 38593	7039.70	CHIRON	331	170
HIP 38593	6599.82	CHIRON	1200	410
HIP 38593	6592.87	CHIRON	1200	300
HIP 38846	6601.76	CHIRON	1098	400
HIP 39095	6765.53	CHIRON	430	450
HIP 39095	6757.56	CHIRON	238	490
HIP 39095	6711.62	CHIRON	288	500
HIP 39236	6679.73	TS23	730	1420
HIP 39567	6668.80	TS23	613	1940
HIP 39847	7084.68	IGRINS	480	160
HIP 39847	6676.80	TS23	402	1500
HIP 39906	6580.86	CHIRON	457	270
HIP 40429	6691.72	CHIRON	710	560
HIP 40706	6327.64	CHIRON	277	630
HIP 40881	6947.97	IGRINS	240	100
HIP 41039	7039.73	CHIRON	1728	530
HIP 41039	6330.77	CHIRON	404	400
HIP 41307	6667.82	TS23	700	1220
HIP 42090	7124.62	IGRINS	630	120
HIP 42129	6603.80	CHIRON	1001	370
HIP 42313	6681.81	TS23	489	1020
HIP 42334	6712.64	CHIRON	381	480
HIP 43142	6670.79	TS23	647	1980
HIP 44127	6677.88	TS23	239	1600
HIP 44307	6947.98	IGRINS	280	80
HIP 45336	6328.70	CHIRON	171	290
HIP 45336	7122.66	IGRINS	270	130
HIP 45336	7084.75	IGRINS	240	140
HIP 45344	6612.79	CHIRON	1001	320
HIP 45688	6299.93	TS23	600	880
HIP 46225	6679.84	TS23	933	1300

Table 7.2: - (Continued)

Star	MJD (JD-2450000)	Instrument	exptime (sec)	snr
HIP 46283	6732.56	CHIRON	357	490
HIP 46283	6619.80	CHIRON	872	430
HIP 46283	6712.70	CHIRON	352	450
HIP 46897	7084.78	IGRINS	1200	20
HIP 46897	7139.59	IGRINS	720	120
HIP 47006	6677.03	TS23	373	1590
HIP 47175	6424.56	CHIRON	264	660
HIP 50303	6677.78	TS23	1200	1350
HIP 50860	6678.81	TS23	1151	1470
HIP 51362	7043.79	CHIRON	1298	340
HIP 51362	6625.81	CHIRON	947	200
HIP 51362	6673.75	CHIRON	606	510
HIP 51362	7084.76	IGRINS	720	100
HIP 51685	6677.90	TS23	1046	1460
HIP 52422	6676.87	TS23	522	1540
HIP 52457	6676.83	TS23	647	1500
HIP 52638	6669.83	TS23	711	1900
HIP 52678	6748.56	CHIRON	375	500
HIP 52678	6690.70	CHIRON	618	610
HIP 52736	6748.52	CHIRON	530	540
HIP 52736	6713.70	CHIRON	263	490
HIP 52911	6670.86	TS23	758	1950
HR 4259	6335.70	CHIRON	304	330
HIP 54849	6670.94	TS23	797	2080
HIP 55434	6332.77	CHIRON	199	410
HIP 56034	6676.91	TS23	502	1460
HIP 56633	6669.91	TS23	447	1990
HIP 56633	6335.75	CHIRON	358	470
HIP 57328	6338.68	CHIRON	419	490
HIP 57328	6370.62	CHIRON	419	450
HIP 58590	6338.72	CHIRON	352	520
HIP 59394	6754.57	CHIRON	815	500
HIP 59394	6690.78	CHIRON	940	370
HIP 59449	6711.88	CHIRON	186	440
HIP 59449	6641.76	CHIRON	305	150
HIP 59819	6669.96	TS23	465	1940
HIP 60009	6370.66	CHIRON	200	520
HIP 60009	7009.78	CHIRON	206	510
HIP 60030	7084.81	IGRINS	2400	80
HIP 60595	6676.94	TS23	746	1540
HIP 60710	7062.77	CHIRON	1515	470
HIP 60957	6678.92	TS23	904	1500
HIP 61558	7139.67	IGRINS	1440	180
HIP 61558	7084.84	IGRINS	1200	70
HIP 61622	6378.69	CHIRON	167	620

Table 7.2: - (Continued)

Star	MJD (JD-2450000)	Instrument	exptime (sec)	snr
HIP 62541	7124.80	IGRINS	480	120
HIP 62541	7084.86	IGRINS	1500	80
HIP 62576	7122.83	IGRINS	546	130
HIP 63724	6338.76	CHIRON	412	560
HIP 63724	6371.72	CHIRON	412	630
HIP 63945	6371.68	CHIRON	362	560
HIP 65198	7044.85	CHIRON	3352	430
HIP 65477	6670.01	TS23	207	2520
HIP 65728	6677.98	TS23	1200	1710
HIP 66249	6378.71	CHIRON	110	520
HIP 66798	6377.82	HRS	362	610
HIP 66821	6718.75	CHIRON	610	540
HIP 67143	7139.77	IGRINS	480	120
HIP 67194	6389.70	HRS	368	740
HIP 67782	6394.92	HRS	359	680
HIP 68092	7139.80	IGRINS	840	200
HIP 68520	6403.59	CHIRON	239	470
HIP 70327	7123.90	IGRINS	420	90
HIP 70327	6681.98	TS23	1152	230
HIP 70327	6719.80	CHIRON	368	460
HIP 70384	6403.73	HRS	420	560
HIP 70400	6669.00	TS23	602	2000
HIP 70915	7136.63	CHIRON	3281	480
HIP 70915	7090.71	CHIRON	2985	460
HIP 71865	6383.71	CHIRON	190	460
HIP 71865	7060.80	CHIRON	1205	500
HIP 71974	7078.80	CHIRON	3786	470
HIP 72104	6720.86	CHIRON	492	490
HIP 72154	6403.75	HRS	300	470
HIP 72250	7070.72	CHIRON	4025	490
HIP 72378	7139.82	IGRINS	720	140
HIP 72552	7124.81	IGRINS	600	110
HIP 73049	6715.73	CHIRON	749	530
HR 5605	6383.74	CHIRON	330	530
HIP 74117	6383.77	CHIRON	204	370
HIP 74689	6872.52	CHIRON	693	550
HIP 75178	6678.99	TS23	815	1620
HIP 75304	6427.78	CHIRON	309	340
HIP 76267	6380.88	CHIRON	36	290
HIP 76600	6380.91	CHIRON	137	500
HIP 76852	6426.65	CHIRON	306	370
HIP 77233	6426.69	CHIRON	140	320
HIP 77336	6396.79	HRS	264	610
HIP 77336	7122.91	IGRINS	480	120
HIP 77516	6380.89	CHIRON	126	450

Table 7.2: - (Continued)

Star	MJD (JD-2450000)	Instrument	exptime (sec)	snr
HIP 77635	6725.72	CHIRON	288	420
HIP 77858	6733.75	CHIRON	628	490
HIP 78105	6870.54	CHIRON	655	590
HIP 78106	6736.70	CHIRON	584	500
HIP 78265	6766.77	CHIRON	22	250
HIP 78554	6427.74	CHIRON	408	270
HIP 78820	6380.93	CHIRON	53	490
HIP 78820	7139.83	IGRINS	120	190
HIP 78820	7060.85	CHIRON	263	360
HIP 78820	7156.63	CHIRON	164	390
HR 6025	6847.83	IGRINS	600	100
HIP 78918	6718.86	CHIRON	300	610
HIP 78933	6737.76	CHIRON	77	250
HIP 79005	7090.77	CHIRON	4646	430
HIP 79007	6874.48	CHIRON	659	550
HIP 79199	6734.71	CHIRON	451	470
HIP 79387	6746.75	CHIRON	573	500
HIP 79404	6415.77	CHIRON	324	470
HIP 79404	7076.81	CHIRON	1307	430
HIP 79404	7090.88	CHIRON	1135	450
HIP 79653	6740.79	CHIRON	469	490
HIP 80460	7122.93	IGRINS	720	110
HIP 80815	6378.86	CHIRON	393	530
HIP 80883	6378.84	CHIRON	174	550
HIP 80991	6389.86	HRS	404	720
HIP 81126	7122.95	IGRINS	720	150
HIP 81641	6404.83	HRS	320	540
HIP 82350	6391.84	HRS	404	660
HIP 82514	6726.81	CHIRON	34	250
HIP 82673	6871.58	CHIRON	250	310
HIP 82673	6410.86	CHIRON	272	180
HIP 83635	6407.86	HRS	316	480
HIP 84606	6945.54	IGRINS	224	150
HIP 85290	6946.56	IGRINS	224	120
HIP 85379	6398.85	HRS	330	740
HIP 85385	6848.83	IGRINS	480	80
HIP 85537	7096.88	CHIRON	4227	570
HIP 85537	6792.73	CHIRON	900	600
HIP 85537	6848.73	IGRINS	240	60
HIP 85727	6771.85	CHIRON	175	570
HIP 85922	6847.82	IGRINS	480	120
HIP 85922	7139.95	IGRINS	240	170
HIP 85922	6886.56	CHIRON	791	590
HIP 85922	7103.85	CHIRON	2543	370
HIP 85922	7104.82	CHIRON	7386	360

Table 7.2: - (Continued)

Star	MJD (JD-2450000)	Instrument	exptime (sec)	snr
HIP 86019	6747.85	CHIRON	228	510
HIP 86782	6404.85	HRS	310	500
HIP 87108	6847.87	IGRINS	120	120
HIP 87108	6445.79	CHIRON	152	300
HIP 88116	6488.71	CHIRON	373	590
HIP 88116	6876.54	CHIRON	320	380
HIP 88290	6873.59	CHIRON	365	540
HIP 88818	7122.98	IGRINS	960	90
HIP 88818	7230.66	IGRINS	600	110
HIP 88818	6397.85	HRS	355	510
HIP 88817	7123.00	IGRINS	960	100
HIP 88817	6405.84	HRS	400	720
HIP 89156	6405.82	HRS	470	610
HIP 89935	6848.85	IGRINS	240	100
HIP 89935	6945.56	IGRINS	224	250
HIP 90052	6405.88	HRS	500	760
HIP 90762	6848.85	IGRINS	480	80
HIP 90762	6945.57	IGRINS	480	200
HIP 90887	6748.80	CHIRON	710	560
HIP 91118	6945.58	IGRINS	360	190
HIP 91875	6745.81	CHIRON	680	580
HIP 92027	6405.91	HRS	360	570
HIP 92312	6408.88	HRS	390	650
HIP 92728	6405.86	HRS	280	560
HIP 92855	6880.57	CHIRON	30	550
HIP 92855	6415.80	CHIRON	32	400
HIP 92946	6475.79	CHIRON	339	500
HIP 93225	6946.54	IGRINS	224	80
HIP 93225	6516.69	CHIRON	1200	540
HIP 93225	6962.56	TS23	562	1430
HIP 93393	6404.88	HRS	320	540
HIP 93580	7116.84	CHIRON	5594	520
HIP 93580	6848.84	IGRINS	480	100
HIP 93713	6848.87	IGRINS	600	90
HIP 93747	6587.54	TS23	85	1880
HIP 93805	6852.82	IGRINS	2640	60
HIP 93805	7139.96	IGRINS	120	210
HIP 93805	6775.78	CHIRON	150	520
HIP 94620	6848.88	IGRINS	480	100
HIP 94720	6517.78	HRS	400	880
HIP 95241	6869.63	CHIRON	325	120
HIP 95241	6508.80	CHIRON	294	600
HIP 95241	6459.89	CHIRON	183	360
HIP 95560	6848.89	IGRINS	480	110
HIP 95619	7139.97	IGRINS	480	120

Table 7.2: - (Continued)

Star	MJD (JD-2450000)	Instrument	exptime (sec)	snr
HIP 95619	7118.79	CHIRON	3451	320
HIP 95619	6523.61	CHIRON	768	670
HIP 95853	6585.54	TS23	129	2010
HIP 96288	6585.56	TS23	489	1860
HIP 96840	6408.92	HRS	552	940
HIP 97376	6848.90	IGRINS	1680	70
HIP 97496	6584.54	TS23	342	1820
HIP 97870	6517.81	HRS	185	830
HIP 97966	6925.51	CHIRON	655	380
HIP 97966	6881.70	CHIRON	1158	660
HIP 98055	6586.54	TS23	320	1820
HIP 98325	6587.56	TS23	543	1750
HIP 99080	6583.63	TS23	358	1740
HIP 99742	6945.59	IGRINS	224	210
HIP 100069	6409.91	HRS	451	560
HIP 100221	7230.72	IGRINS	1100	80
HIP 100221	6523.79	HRS	874	830
HIP 100907	6946.57	IGRINS	224	120
HIP 100907	7230.67	IGRINS	600	120
HIP 101123	6945.70	IGRINS	224	160
HIP 101589	6448.83	CHIRON	352	420
HIP 101716	6582.60	TS23	549	1260
HIP 101909	6945.60	IGRINS	360	140
HIP 101909	7230.69	IGRINS	720	90
HIP 102487	6847.80	IGRINS	480	80
HIP 103298	6946.58	IGRINS	224	100
HIP 103298	7230.70	IGRINS	600	80
HIP 103298	7155.93	CHIRON	1141	290
HIP 104105	6945.69	IGRINS	280	140
HIP 104139	6448.90	CHIRON	204	490
HIP 104365	6847.81	IGRINS	480	100
HIP 104365	7237.82	IGRINS	720	50
HIP 105140	6485.90	CHIRON	372	420
HIP 105282	6522.65	HRS	1006	850
HIP 105891	6946.59	IGRINS	224	90
HIP 105942	6523.87	HRS	480	760
HIP 105966	6585.64	TS23	530	1800
HIP 105972	6507.82	HRS	267	690
HIP 106711	6584.60	TS23	689	700
HIP 106711	6618.53	TS23	557	2010
HIP 106786	6945.64	IGRINS	224	230
HIP 106786	6962.59	TS23	284	1620
HIP 106786	6794.81	CHIRON	232	470
HIP 107517	6873.74	CHIRON	1025	490
HIP 107608	6788.84	CHIRON	620	470

Table 7.2: - (Continued)

Star	MJD (JD-2450000)	Instrument	exptime (sec)	snr
HIP 108294	6790.81	CHIRON	470	510
HIP 108339	6945.65	IGRINS	224	160
HIP 109056	6945.66	IGRINS	240	150
HIP 109056	6948.56	IGRINS	1156	160
HIP 109056	6946.65	IGRINS	784	230
HIP 109056	6947.57	IGRINS	1746	170
HIP 109139	6524.67	CHIRON	207	590
HIP 109139	6447.91	CHIRON	248	470
HIP 109521	6586.58	TS23	511	1860
HIP 109521	6962.60	TS23	587	1500
HIP 109521	6945.68	IGRINS	224	200
HIP 109831	6945.67	IGRINS	224	160
HIP 109831	7237.77	IGRINS	1440	100
HIP 109831	7288.73	IGRINS	900	30
HIP 110838	6543.82	CHIRON	506	550
HIP 110838	6880.76	CHIRON	354	780
HIP 110935	6896.67	CHIRON	696	630
HIP 111056	7288.80	IGRINS	180	30
HIP 111056	6945.76	IGRINS	224	120
HIP 111068	6512.74	HRS	362	500
HIP 111169	6585.62	TS23	121	1900
HIP 112029	6487.85	CHIRON	109	460
HIP 112029	6892.74	CHIRON	95	250
HIP 113788	6586.63	TS23	367	1830
HIP 114520	6587.64	TS23	541	1880
HIP 114822	6886.68	CHIRON	715	550
HIP 114822	6884.68	CHIRON	530	530
HIP 115115	7163.90	CHIRON	600	190
HIP 115115	7230.95	IGRINS	500	40
HIP 115115	6797.87	CHIRON	610	330
HIP 116247	6463.89	CHIRON	368	560
HIP 116247	7237.94	IGRINS	240	100
HIP 116582	6510.77	HRS	534	670
HIP 116611	6946.61	IGRINS	224	140
HIP 116631	6962.63	TS23	249	1980
HIP 116631	6946.78	IGRINS	224	160
HIP 116631	6583.71	TS23	162	1740
HIP 116631	7288.80	IGRINS	180	30
HIP 116805	6528.84	TS23	158	1680
HIP 116971	6527.85	TS23	407	1650
HIP 116971	6487.88	CHIRON	298	540
HIP 116971	6555.56	CHIRON	497	430
HIP 116971	6869.76	CHIRON	380	110
HIP 116971	6936.73	CHIRON	344	600
HIP 117089	7288.81	IGRINS	180	20

Table 7.2: - (Continued)

Star	MJD (JD-2450000)	Instrument	exptime (sec)	snr
HIP 117089	7237.95	IGRINS	720	60
HIP 117089	6513.86	CHIRON	853	600
HIP 117371	6586.67	TS23	349	1760
HIP 117452	6469.90	CHIRON	327	540
HIP 118121	6795.86	CHIRON	233	500
HIP 118243	6945.73	IGRINS	224	170
HIP 118243	6583.74	TS23	351	1760

Table 7.3: NIRI Observation log.

Star	K	date	Exposure	ρ	θ	ΔK_c	$M_2(M_\odot)$	a (AU)
HIP 22833	4.83	2015-03-29	50x0.3	$0.352 +/- 0.003$	14.1 ± 0.7	3.04 ± 0.06	$0.9^{+0.16}_{-0.17}$	25.1 ± 0.24
HIP 22958	5.79	2015-10-19	52x0.4	$0.445 +/- 0.003$	65.0 ± 0.3	2.57 ± 0.05	$1.5^{+0.35}_{-0.28}$	124.1 ± 0.81
HIP 26093	5.96	2015-03-23	33x0.6	...	...	...	...	...
HIP 26126	5.07	2015-03-29	40x0.4	...	...	...	...	...
HIP 29735	5.10	2015-03-22	83x0.2	...	...	...	...	...
HIP 31278	5.46	2015-03-28	29x0.6	...	...	...	...	...
HIP 38538	4.66	2015-10-19	75x0.2	...	...	...	...	...
HIP 39847	4.66	2015-03-27	50x0.3	...	...	...	...	...
HIP 75178	5.49	2015-03-24	29x0.6	...	...	...	...	...
HIP 88116	4.47	2015-03-22	50x0.3	$3.671 +/- 0.001$	242.99 ± 0.02	3.9 ± 0.4	$1.2^{+0.28}_{-0.24}$	467.7 ± 0.18
HIP 91118	5.67	2015-10-16	43x0.4	$0.1667 +/- 0.0007$	41.7 ± 0.2	1.77 ± 0.01	$1.5^{+0.39}_{-0.25}$	36.4 ± 0.16
HIP 100221	5.70	2015-10-18	26x0.7	$0.250 +/- 0.002$	346.8 ± 0.92	2.28 ± 0.04	$0.9^{+0.2}_{-0.23}$	28.5 ± 0.24
HIP 100907	5.41	2015-10-16	43x0.4	$0.463 +/- 0.002$	335.4 ± 0.30	2.91 ± 0.04	$0.7^{+0.14}_{-0.10}$	37.7 ± 0.16
HIP 101909	$6.47^{\dagger}$	2015-10-16	39x0.5	...	...	...	...	...
HIP 109139	4.40	2015-04-26	50x0.3	...	...	...	...	...
HIP 109521	4.96	2015-04-25	40x0.4	...	...	...	...	...
HIP 115115	4.96	2015-10-18	40x0.4	$1.497 +/- 0.002$	313.14 ± 0.08	2.54 ± 0.04	$1.3^{+0.28}_{-0.19}$	120.0 ± 0.17

†: There is no K-magnitude tabulated in the Simbad Database. The value quoted here is estimated from the spectral type of the star and its V-band magnitude.

Table 7.4: Companion Detections.

Star	Component	$N_{\rm obs}$	Used in Analysis	$T_{\rm eff}$ (K)	$v \sin i$ (km s^{-1})	[Fe/H] (dex)	Mass ($M_\odot$) Isochrone	Mass ($M_\odot$) Spectral Type
HIP 2548	Aa,Ab	2	yes	5732 ± 112	30	-0.5	$1.0^{+0.06}_{-0.04}$	$1.0^{+0.04}_{-0.03}$
HIP 5348	AB	1	no	12000 ± 1000	75	0.0	$2.9^{+0.40}_{-0.36}$	$3.3^{+0.23}_{-0.29}$
HR 545	Aa,Ab†	3	yes	4312 ± 87	5	-0.5	$0.8^{+0.11}_{-0.10}$	$0.7^{+0.01}_{-0.02}$
HR 604	AB	1	no	4736 ± 150	5	0.5	$0.9^{+0.17}_{-0.12}$	$0.8^{+0.02}_{-0.02}$
HIP 10732	AB†	2	yes	5578 ± 109	5	0.0	$1.0^{+0.29}_{-0.04}$	$1.0^{+0.02}_{-0.04}$
HIP 12332	AB†	2	yes	5551 ± 107	10	0.0	$1.0^{+0.03}_{-0.03}$	$1.0^{+0.01}_{-0.04}$
HIP 12706	AB	2	yes	6051 ± 107	10	0.0	$1.1^{+0.03}_{-0.03}$	$1.1^{+0.04}_{-0.05}$
HIP 13165	Aa,Ab	1	no	5773 ± 163	5	-0.5	$1.1^{+0.31}_{-0.08}$	$1.0^{+0.10}_{-0.03}$
HIP 13327	AB†	1	yes	5524 ± 150	5	-0.5	$1.2^{+0.20}_{-0.21}$	$1.0^{+0.03}_{-0.04}$
HIP 14043	Aa,Ab†	1	yes	11500 ± 500	20	0.5	$2.6^{+0.36}_{-0.29}$	$3.3^{+0.15}_{-0.67}$
HIP 14764	AB†	2	yes	5623 ± 150	5	-0.5	$1.0^{+0.32}_{-0.07}$	$1.0^{+0.03}_{-0.04}$
HIP 16147	AB	1	yes	13000 ± 1000	1	0.0	$3.1^{+0.38}_{-0.36}$	$3.6^{+0.34}_{-0.23}$
HIP 16244	AB	2	yes	5592 ± 107	5	-0.5	$1.2^{+0.20}_{-0.22}$	$1.0^{+0.03}_{-0.03}$
HIP 16340	AB†	1	yes	6214 ± 150	5	-0.5	$1.2^{+0.29}_{-0.07}$	$1.2^{+0.06}_{-0.05}$
HIP 16611	AB	1	yes	11500 ± 1000	75	0.0	$2.7^{+0.47}_{-0.37}$	$3.3^{+0.15}_{-0.66}$
HIP 19949	AB†	1	yes	6492 ± 155	20	-0.5	$1.3^{+0.06}_{-0.05}$	$1.3^{+0.06}_{-0.06}$
HIP 20380	AB†	2	yes	6492 ± 109	20	-0.5	$1.3^{+0.04}_{-0.04}$	$1.3^{+0.03}_{-0.05}$
HIP 21589	Aa,Ab	1	yes	4562 ± 154	5	0.0	$0.7^{+0.04}_{-0.03}$	$0.8^{+0.02}_{-0.03}$
HIP 22833	AB	2	yes	4745 ± 107	10	0.0	$0.8^{+0.02}_{-0.02}$	$0.8^{+0.02}_{-0.01}$
HIP 22958	Aa,Ab	2	yes	5762 ± 158	30	-0.5	$1.3^{+0.19}_{-0.23}$	$1.0^{+0.09}_{-0.03}$
HIP 23362	AB†	1	yes	6283 ± 158	5	-0.5	$1.2^{+0.06}_{-0.05}$	$1.2^{+0.07}_{-0.05}$
HIP 24902	AB	1	yes	5679 ± 154	30	0.0	$1.0^{+0.05}_{-0.04}$	$1.0^{+0.04}_{-0.03}$
HIP 26126	AB?	3	yes	5841 ± 91	5	-0.5	$1.0^{+0.03}_{-0.03}$	$1.0^{+0.05}_{-0.04}$
HIP 28691	AB	1	no	15000 ± 1000	1	0.5	$4.0^{+0.45}_{-0.43}$	$4.2^{+0.43}_{-0.34}$
HIP 28691	AC	1	no	12000 ± 1000	1	0.5	$2.8^{+0.40}_{-0.34}$	$3.3^{+0.23}_{-0.30}$
HIP 32607	AB†	3	yes	5068 ± 91	5	-0.5	$0.8^{+0.02}_{-0.02}$	$0.9^{+0.01}_{-0.01}$
HIP 37322	AB	1	yes	8157 ± 147	30	-0.5	$1.8^{+0.30}_{-0.07}$	$1.9^{+0.01}_{-0.07}$
HIP 37450	AB†	1	yes	16000 ± 1000	30	0.0	$4.3^{+0.36}_{-0.43}$	$4.7^{+0.71}_{-0.39}$
HIP 38538	AB	1	no	6576 ± 150	30	-0.5	$1.3^{+0.05}_{-0.05}$	$1.3^{+0.09}_{-0.05}$
HIP 38593	AB†	2	yes	5398 ± 112	5	-0.5	$1.3^{+0.08}_{-0.13}$	$0.9^{+0.03}_{-0.03}$
HIP 38846	AB†	1	yes	6595 ± 158	10	0.0	$1.7^{+0.12}_{-0.21}$	$1.3^{+0.09}_{-0.05}$
HIP 39847	Aa,Ab†	2	no	5750 ± 107	10	-0.5	$1.0^{+0.04}_{-0.03}$	$1.0^{+0.05}_{-0.03}$
HIP 40881	AB†	1	yes	4562 ± 154	10	-0.5	$0.8^{+0.18}_{-0.05}$	$0.8^{+0.02}_{-0.03}$
HIP 42129	AB	1	yes	5241 ± 158	10	-0.5	$1.2^{+0.12}_{-0.18}$	$0.9^{+0.04}_{-0.02}$
HIP 46283	AB?	3	yes	9268 ± 85	10	0.5	$2.0^{+0.04}_{-0.02}$	$2.2^{+0.02}_{-0.02}$
HIP 52678	AB†	2	yes	5033 ± 112	10	-0.5	$1.0^{+0.15}_{-0.19}$	$0.8^{+0.01}_{-0.02}$
HIP 63945	AC	1	no	7038 ± 162	10	-0.5	$1.6^{+0.26}_{-0.16}$	$1.5^{+0.08}_{-0.06}$
HIP 72154	AB†	1	yes	4918 ± 162	30	-0.5	$0.9^{+0.22}_{-0.09}$	$0.8^{+0.03}_{-0.03}$
HR 5605	AB	1	no	16000 ± 1000	10	0.0	$4.3^{+0.37}_{-0.42}$	$4.7^{+0.76}_{-0.40}$
HR 5605	AC	1	no	14000 ± 1000	10	0.0	$3.5^{+0.42}_{-0.38}$	$3.9^{+0.35}_{-0.34}$
HIP 74117	AB	1	no	14000 ± 1000	10	0.0	$3.5^{+0.42}_{-0.38}$	$3.9^{+0.34}_{-0.34}$
HIP 76267	AB	1	yes	5449 ± 158	5	-0.5	$0.9^{+0.04}_{-0.04}$	$0.9^{+0.04}_{-0.03}$
HIP 77336	AB†	2	yes	6407 ± 112	20	0.0	$1.2^{+0.04}_{-0.04}$	$1.3^{+0.04}_{-0.05}$
HIP 77516	AB	1	yes	6825 ± 141	5	0.5	$1.4^{+0.21}_{-0.06}$	$1.4^{+0.03}_{-0.04}$

Table 7.4: - (Continued)

Star	Component	$N_{\rm obs}$	Used in Analysis	$T_{\rm eff}$ (K)	$v \sin i$ (km s^{-1})	[Fe/H] (dex)	Mass ($M_\odot$) Isochrone	Mass ($M_\odot$) Spectral Type
HIP 78820	AB	1	no	5658 ± 158	5	0	$1.3^{+0.11}_{-0.13}$	$1.0^{+0.04}_{-0.04}$
HIP 78918	AB	1	yes	9000 ± 500	120	-0.5	$2.0^{+0.22}_{-0.17}$	$2.1^{+0.13}_{-0.17}$
HIP 79199	AB	1	no	4616 ± 158	5	-0.5	$0.9^{+0.14}_{-0.14}$	$0.8^{+0.02}_{-0.03}$
HIP 79404	AB†	2	yes	4773 ± 112	10	-0.5	$1.1^{+0.07}_{-0.08}$	$0.8^{+0.02}_{-0.01}$
HIP 80460	AB	1	yes	6391 ± 155	10	0.0	$1.2^{+0.06}_{-0.05}$	$1.3^{+0.06}_{-0.06}$
HIP 82673	AB†	2	yes	4668 ± 112	5	0.5	$0.8^{+0.03}_{-0.03}$	$0.8^{+0.01}_{-0.02}$
HIP 84606	AB	1	yes	5476 ± 154	10	-0.5	$0.9^{+0.05}_{-0.04}$	$0.9^{+0.04}_{-0.03}$
HIP 88116	AB†	2	yes	5293 ± 112	5	0.0	$0.9^{+0.03}_{-0.03}$	$0.9^{+0.02}_{-0.03}$
HIP 88817	Ba,Bb†	1	yes	3647 ± 154	20	0.0	$0.5^{+0.07}_{-0.10}$	$0.5^{+0.03}_{-0.05}$
HIP 88818	Aa,Ab	3	yes	5296 ± 91	20	-0.5	$0.9^{+0.02}_{-0.02}$	$0.9^{+0.02}_{-0.03}$
HIP 91118	AB	1	yes	6492 ± 155	10	-0.5	$1.3^{+0.26}_{-0.07}$	$1.3^{+0.06}_{-0.06}$
HIP 93225	AB	2	yes	14000 ± 700	10	0.5	$3.6^{+0.34}_{-0.30}$	$3.9^{+0.18}_{-0.23}$
HIP 93805	Aa,Ab†	2	yes	4054 ± 109	5	-0.5	$0.6^{+0.03}_{-0.03}$	$0.6^{+0.04}_{-0.02}$
HIP 96840	AB	1	yes	9942 ± 152	10	0.0	$2.2^{+0.06}_{-0.05}$	$2.3^{+0.03}_{-0.01}$
HIP 100221	AB	1	yes	5273 ± 154	20	-0.5	$0.9^{+0.29}_{-0.07}$	$0.9^{+0.04}_{-0.03}$
HIP 100907	AB†	2	yes	5222 ± 109	10	0.0	$0.9^{+0.03}_{-0.03}$	$0.9^{+0.04}_{-0.02}$
HIP 103298	Aa,Ab	3	yes	4615 ± 90	5	-0.5	$0.7^{+0.02}_{-0.02}$	$0.8^{+0.01}_{-0.02}$
HIP 109139	AB	2	yes	5710 ± 112	20	-0.5	$1.0^{+0.04}_{-0.03}$	$1.0^{+0.03}_{-0.03}$
HIP 109521	Aa,Ab†	3	yes	4412 ± 87	10	0.0	$0.7^{+0.02}_{-0.02}$	$0.7^{+0.01}_{-0.01}$
HIP 115115	AB	3	yes	4943 ± 91	5	-0.5	$0.8^{+0.02}_{-0.02}$	$0.8^{+0.02}_{-0.02}$

†: Newly discovered companions.

Table 7.5: Mass-Ratio Distribution Parameters.

			1σ credible interval	
Model	Parameter	Median Value	Lower	Upper
Histogram	θ_1	0.50	0.18	1.00
	θ_2	1.53	1.14	1.89
	θ_3	2.17	1.80	2.65
	θ_4	1.42	0.98	1.81
	θ_5	0.74	0.40	1.12
	θ_6	0.29	0.10	0.55
	θ_7	0.16	0.06	0.33
Lognormal	μ	-0.99	-1.06	-0.92
	σ	0.46	0.40	0.54
	maximum†	0.30	0.27	0.33
Power Law	γ	0.29	0.15	0.42

Chapter Eight: Summary & Conclusions

8.1 Summary of Key Results

In this thesis, we developed and characterized a spectral search method to find companions to stars with a variety of temperatures. The method can be summarized as a two step process: first, prepare the spectrum by attempting to remove the signal from the primary star spectrum. The second step is to cross-correlate the prepared spectra against a grid of model spectra spanning a large parameter space. The cross correlation function (CCF) attempts to match the model spectrum template against the prepared data; if it finds a match for the template in the data then the CCF will have a strong peak at the radial velocity of the companion.

We present two different ways to prepare the spectrum. In Chapter 2, we discuss the method we use for our main survey program (Chapters 6 and 7), which takes advantage of the fact that the primary star spectrum is very simple compared to the expected companion spectrum. In this case, we prepare the spectra for a companion search by simply subtracting a low-pass filtered version of the original spectrum, a process known as unsharp masking. We extensively characterize the direct spectral detection method for this type of primary star, estimating the companion sensitivity as well as the accuracy of the companion parameters we derive. We find that our method is capable of detecting late-K to early-M spectral type companions to A0V primary stars, and can detect them *independent of the orbital separation*. As the primary star increases in mass and temperature, the coolest detectable companion gets hotter; however, the lowest detectable mass ratio decreases.

We search for a bias in the derived parameters of the companion star by simulating binary star observations with real data, and find that the estimated temperature tends to be larger than the true temperature. The bias is usually largest at the coolest temperatures where the model spectra are least accurate due to the difficulty of modeling complex molecular absorption features. We calibrate the bias for four different spectrographs using a linear fit, which we use to convert from measured to actual temperature.

The second way for preparing the spectrum is by using orbital information and

a large degree of orbital phase coverage to remove the signal from the primary star spectrum. We describe this method in Chapters 4 and 5. The basic idea is to take advantage of the fact that the spectral lines from the primary and secondary move in different directions. Therefore if you align several spectra from different epochs such that the primary star lines are in a constant position, the companion spectral lines will be washed out. The result is an empirical estimate of the primary star spectrum that is only minimally contaminated by the companion spectrum. We remove the primary star contamination from each individual spectrum by subtracting the empirical estimate, leaving only a spectrum of the companion star. Unlike the method we describe above and in Chapter 2, this method requires several observations of the system that span a large fraction of the orbit; it is therefore not independent of separation. The great advantage of this method is that it can detect cool companions even when the primary star spectrum is complicated, and can detect much more extreme flux-ratio companions. In Chapter 5, we show that the method is even capable of detecting planet-mass companions, which entails a contrast ratio of $\sim 10^4$ in the K-band.

8.2 The Separation-Variant Companion Mass-Ratio Distribution

The bulk of the work in this thesis was motivated by the following question: is the companion mass-ratio distribution for binary systems with close ($a \lesssim 100AU$) orbits significantly different from companions on wide ($a \gtrsim 100AU$) orbits? Since we care about a quantity that changes with separation, we want a method that detects companions in such a way that the completeness does not depend on separation. Additionally, we want a method that can detect and characterize the binary system quickly. The direct spectral detection method described in Chapter 2 is just such a method, and we apply it to a binary survey in Chapter 7 after performing a pilot survey with archived data in Chapter 6.

We find that the companions we detect, which are necessarily all close companions because the light from both components must fall on the spectrograph slit, show a preference for companions with $q \sim 0.3$. The mass-ratio distribution for wide companions is well-fit by a power law with slope ~ -2.3 (De Rosa et al., 2014),

indicating a very strong preference for low-mass companions. In contrast, our result is poorly fit by a power law, and is much better fit by a lognormal distribution. Our result is consistent with the inner mass-ratio distribution found by the VAST survey (De Rosa et al., 2014), an adaptive optics imaging survey. However, our distribution contains far more companions since it is specifically optimized for finding close, low-mass companions. We are therefore able to determine that not only does the slope of the mass-ratio distribution change with separation, the *shape* of the distribution changes.

8.3 Theoretical Implications

The mass-ratio distribution derived in this work has a very different form than the power law found for companions at wide separations. This is likely a result of the companion's accretion history. If it started at a wide separation, it may have migrated in by accreting a significant fraction of its final mass from core material, a process that can change the separation by 1-2 orders of magnitude (Bate, 2000). Thus if the companion formed with a small mass ratio at large separations, its final configuration will be a close companion with large mass ratio. Companions that migrated to inside of $\sim$ 100 AU will likely have large mass ratios due to this process.

Likewise, if the companion formed within a few tens to hundred AU from its primary it will preferentially accrete matter from the dense primary star disk as well as the infalling core material (Bate et al., 2002). The result would be a depletion of low mass-ratio companions as they become intermediate to high mass-ratio companions. The characteristic scale of $\sim$ 0.3 that we see in Figure 7.7 would then be related to the disk timescale and the time at which the fragments form, since with enough time the preferential accretion would push all companions to $q = 1.0$.

It is also possible that some of the companions found in this work were formed from a gravitationally unstable disk (e.g. Kratter & Matzner, 2006; Stamatellos & Whitworth, 2011). Being a completely different formation mechanism than the way wide companions form, we would expect the initial companion mass function to differ. Such companions would undergo the same preferential accretion discussed above. This explanation may even be preferable, since it could explain why we see a separation-dependent mass-ratio distribution around intermediate-mass stars but not low-mass

stars: more massive stars tend to have more massive disks (Andrews et al., 2013) that are more likely to fragment (Kratter et al., 2010). It is not clear whether the scaling of disk mass with stellar mass holds at very early times, when disk fragmentation is likely to be strongest and generate the largest companions. Observations of the dust mass with large submillimeter interferometers such as the Atacama Large Millimeter Array (ALMA) could help determine how big a role disk fragmentation is likely to play in binary star formation.

8.4 Future Work Needed

Large scale simulations are likely needed to distinguish between the two formation scenarios and fully interpret the results of this survey. A significant amount of work has already been put towards this end in the form of radiation hydrodynamic simulations of giant molecular clouds (Bate, 2012; Krumholz et al., 2012). However, the present simulations do not generate enough stars more massive than the sun to quantitatively compare binary and multiple star statistics to observations. Additionally, there is a strong need for high resolution simulations to follow the full accretion and migration history of both core and disk fragments in order to compare the final mass ratios generated to observational studies such as the one presented here.

There is also a need for further observational efforts. Many of the companions we present in Chapter 7 are unconfirmed, and so need at minimum follow-up spectroscopy. Follow-up imaging of more of the detections with an adaptive optics system would be useful as well, both for confirmation and validation of the companion temperature and to provide an estimate of the orbital separation. Alternatively or in addition to the imaging, the detections could be observed with spectroscopic measurements over several years to map out the full double-lined spectroscopic orbit and provide a dynamical mass ratio and separation measurement. Not only would this help to fully characterize the binary systems, but it would allow for an independent test on stellar evolutionary models at young ages.

This thesis represents 6 years of hard work, over 100 long nights at the observatory, and countless hours writing and debugging analysis code. The result is something I am truly proud of. I planned, ran, and analyzed a full survey program that hinged on a rarely-studied and poorly-characterized method, and came out the end with a new

and interesting result. As I go on in my career, I will surely look back at this time as so much more than just school. The lessons learned cannot be taught, and the importance of the friendships made cannot be understated. More than coding, long nights, and hard work this thesis represents countless hours learning new things, over 100 nights of paid stargazing, and 6 of the best years yet. Thank you to everyone who made it so.

Bibliography

Abt, H. A. 1965, ApJS, 11, 429 38

Abt, H. A., Gomez, A. E., & Levy, S. G. 1990, ApJS, 74, 551 38

Abt, H. A., & Levy, S. G. 1978, ApJS, 36, 241 38

Agol, E., Cowan, N. B., Knutson, H. A., et al. 2010, ApJ, 721, 1861 69

Aldoretta, E. J., Caballero-Nieves, S. M., Gies, D. R., et al. 2015, AJ, 149, 26 4, 8

Alonso, A., Arribas, S., & Martinez-Roger, C. 1996, A&AS, 117, 227 34

Anderson, T. W., & Darling, D. A. 1954, Journal of the American Statistical Association, 49, 765 137

Andrews, S. M., Rosenfeld, K. A., Kraus, A. L., & Wilner, D. J. 2013, ApJ, 771, 129 138, 177

Asplund, M., Grevesse, N., & Sauval, A. J. 2005, in Astronomical Society of the Pacific Conference Series, Vol. 336, Cosmic Abundances as Records of Stellar Evolution and Nucleosynthesis, ed. T. G. Barnes, III & F. N. Bash, 25 71

Astropy Collaboration, Robitaille, T. P., Tollerud, E. J., et al. 2013, A&A, 558, A33 49

Aydi, E., Gebran, M., Monier, R., et al. 2014, in SF2A-2014: Proceedings of the Annual meeting of the French Society of Astronomy and Astrophysics, ed. J. Ballet, F. Martins, F. Bournaud, R. Monier, & C. Reylé, 451–455 127

Barman, T. S. 2008, ApJ, 676, L61 71

Barman, T. S., Hauschildt, P. H., & Allard, F. 2001, ApJ, 556, 885 71

Barman, T. S., Hauschildt, P. H., Schweitzer, A., et al. 2002, ApJ, 569, L51 71

Barman, T. S., Macintosh, B., Konopacky, Q. M., & Marois, C. 2011, ApJ, 733, 65 71

Barnes, S. A. 2003, ApJ, 586, 464 18

—. 2010, ApJ, 722, 222 18, 19, 129, 130

Barnes, S. A., & Kim, Y.-C. 2010, ApJ, 721, 675 18, 19, 130

Bate, M. R. 2000, MNRAS, 314, 33 87, 176

—. 2012, MNRAS, 419, 3115 89, 138, 177

Bate, M. R., & Bonnell, I. A. 1997, MNRAS, 285, 33 2, 117, 118

Bate, M. R., Bonnell, I. A., & Bromm, V. 2002, MNRAS, 336, 705 2, 87, 118, 176

Bate, M. R., Bonnell, I. A., & Price, N. M. 1995, MNRAS, 277, 362 1, 87, 117

Becker, J. C., Johnson, J. A., Vanderburg, A., & Morton, T. D. 2015, ApJS, 217, 29 4

Beer. 1852, Annalen der Physik, 162, 78 41, 47

Benedict, G. F., McArthur, B. E., Gatewood, G., et al. 2006, AJ, 132, 2206 68

Bergmann, C., Endl, M., Hearnshaw, J. B., Wittenmyer, R. A., & Wright, D. J. 2015, International Journal of Astrobiology, 14, 173 3, 55

Bertaux, J. L., Lallement, R., Ferron, S., Boonne, C., & Bodichon, R. 2014, A&A, 564, A46 41

Binney, J., & Merrifield, M. 1998, Galactic Astronomy 135

Bonnell, I. A., & Bate, M. R. 2005, MNRAS, 362, 915 87, 89

Boss, A. P. 1986, ApJS, 62, 519 1, 87, 117

—. 2006, ApJ, 643, 501 89

—. 2011, ApJ, 731, 74 89

Boss, A. P., & Bodenheimer, P. 1979, ApJ, 234, 289 1, 87, 117

Bouvier, J., Matt, S. P., Mohanty, S., et al. 2014, Protostars and Planets VI, 433 130

Boyajian, T. S., von Braun, K., van Belle, G., et al. 2012, ApJ, 757, 112 34

—. 2013, ApJ, 771, 40 34

Bressan, A., Marigo, P., Girardi, L., et al. 2012, MNRAS, 427, 127 xv, 23, 127, 139, 142

Brogi, M., Snellen, I. A. G., de Kok, R. J., et al. 2012, Nature, 486, 502 9, 69, 74, 75, 78

—. 2013, ApJ, 767, 27 69, 74, 75, 78

Burgasser, A. J. 2007, AJ, 134, 1330 8

Butler, R. P., Marcy, G. W., Williams, E., et al. 1996, PASP, 108, 500 56

Carroll, B. W., & Ostlie, D. A. 2006, An introduction to modern astrophysics and cosmology 99

Casagrande, L., Flynn, C., & Bessell, M. 2008, MNRAS, 389, 585 34

Casagrande, L., Ramírez, I., Meléndez, J., Bessell, M., & Asplund, M. 2010, A&A, 512, A54 34

Casagrande, L., Schönrich, R., Asplund, M., et al. 2011, A&A, 530, A138 34

Castelli, F., & Kurucz, R. L. 2003, in IAU Symposium, Vol. 210, Modelling of Stellar Atmospheres, ed. N. Piskunov, W. W. Weiss, & D. F. Gray, 20P 12, 123, 125, 126

Chacón, A., Cuevas, O., Pozo, D., et al. 2010, in Society of Photo-Optical Instrumentation Engineers (SPIE) Conference Series, Vol. 7733, Society of Photo-Optical Instrumentation Engineers (SPIE) Conference Series 95

Charbonneau, D., Knutson, H. A., Barman, T., et al. 2008, ApJ, 686, 1341 69, 71

Clarke, C. J. 2009, MNRAS, 396, 1066 88, 105

Clough, S., Shephard, M., Mlawer, E., et al. 2005, Journal of Quantitative Spectroscopy and Radiative Transfer, 91, 233 41, 71, 95

Collier Cameron, A., Horne, K., Penny, A., & Leigh, C. 2002, MNRAS, 330, 187 69

Cotton, D. V., Bailey, J., & Kedziora-Chudczer, L. 2014, MNRAS, 439, 387 41

Cowan, N. B., Machalek, P., Croll, B., et al. 2012, ApJ, 747, 82 72

Crepp, J., Serabyn, E., Carson, J., Ge, J., & Kravchenko, I. 2010, ApJ, 715, 1533 3

Crossfield, I. J. M., Barman, T., Hansen, B. M. S., Tanaka, I., & Kodama, T. 2012, ApJ, 760, 140 76

Cubillos, P., Harrington, J., Stevenson, K., & Madhusudhan, N. 2010, in Bulletin of the American Astronomical Society, Vol. 42, AAS/Division for Planetary Sciences Meeting Abstracts #42, 1071 69

David, T. J., & Hillenbrand, L. A. 2015, ArXiv e-prints, arXiv:1501.03154 18, 21, 23, 126, 127, 146

de Kok, R. J., Brogi, M., Snellen, I. A. G., et al. 2013, A&A, 554, A82 9, 69, 74, 75, 78

De Rosa, R. J., Patience, J., Vigan, A., et al. 2012, MNRAS, 422, 2765 39

De Rosa, R. J., Patience, J., Wilson, P. A., et al. 2014, MNRAS, 437, 1216 4, 6, 8, 118, 136, 137, 138, 139, 175, 176

Delfosse, X., Beuzit, J.-L., Marchal, L., et al. 2004, in Astronomical Society of the Pacific Conference Series, Vol. 318, Spectroscopically and Spatially Resolving the Components of the Close Binary Stars, ed. R. W. Hilditch, H. Hensberge, & K. Pavlovski, 166–174 118

Demory, B.-O., Gillon, M., Seager, S., et al. 2012, ApJ, 751, L28 69

Dodson-Robinson, S. E., Veras, D., Ford, E. B., & Beichman, C. A. 2009, ApJ, 707, 79 89

Dotter, A., Chaboyer, B., Jevremović, D., et al. 2008, ApJS, 178, 89 64, 125, 130, 132, 139

Drummond, J. D. 2014, AJ, 147, 65 39

Duchêne, G., & Kraus, A. 2013, ARA&A, 51, 269 1, 117, 118

Duerbeck, H. W. 1975, A&AS, 22, 19 38

Duquennoy, A., & Mayor, M. 1991, A&A, 248, 485 118

Endl, M., Kürster, M., & Els, S. 2000, A&A, 362, 585 56, 57

Endl, M., Brugamyer, E. J., Cochran, W. D., et al. 2016, ApJ, 818, 34 56, 57, 64, 66

ESA. 1997, VizieR Online Data Catalog, 1239, 0 39, 125

Evans, C. J., Bastian, N., Beletsky, Y., et al. 2010, in IAU Symposium, Vol. 266, IAU Symposium, ed. R. de Grijs & J. R. D. Lépine, 35–40 89

Evans, N. R., DeGioia-Eastwood, K., Gagné, M., et al. 2011, ApJS, 194, 13 xv, 90, 103, 105, 112

Fabian, A. C., Pringle, J. E., & Rees, M. J. 1975, MNRAS, 172, 15p 1

Fabrycky, D. C. 2010, Non-Keplerian Dynamics of Exoplanets, ed. S. Seager, 217–238 71

Fekel, Jr., F. C., & Tomkin, J. 1982, ApJ, 263, 289 38

Feroz, F., Hobson, M. P., Cameron, E., & Pettitt, A. N. 2013, ArXiv e-prints, arXiv:1306.2144 134

Fischer, D., Driscoll, P., Isaacson, H., et al. 2009, ApJ, 703, 1545 4, 55

Fischer, D. A., & Marcy, G. W. 1992, ApJ, 396, 178 5, 118

Foreman-Mackey, D., Hogg, D. W., Lang, D., & Goodman, J. 2013, PASP, 125, 306 16, 63

Foreman-Mackey, D., Hogg, D. W., & Morton, T. D. 2014, ApJ, 795, 64 133, 134, 139

Gagne, M., Caillault, J.-P., Stauffer, J. R., & Linsky, J. L. 1997, ApJ, 478, L87 90

Gibson, N. P., Aigrain, S., Pont, F., et al. 2012, MNRAS, 422, 753 76

Grillmair, C. J., Charbonneau, D., Burrows, A., et al. 2007, ApJ, 658, L115 69

Gullikson, K., & Dodson-Robinson, S. 2013, AJ, 145, 3 55, 86

Gullikson, K., Dodson-Robinson, S., & Kraus, A. 2014, AJ, 148, 53 10, 41, 57, 121

Gullikson, K., & Endl, M. 2013, PASP, 125, 924 9, 41, 49, 55, 57, 68

Gullikson, K., Endl, M., Cochran, W. D., & MacQueen, P. J. 2015, ApJ, 815, 62 55

Gullikson, K., Kraus, A., Dodson-Robinson, S., et al. 2016, AJ, 151, 3 8, 119, 122, 124, 131, 139

Harrington, J., Hansen, B. M., Luszcz, S. H., et al. 2006, Science, 314, 623 71

Harris, R. J., Andrews, S. M., Wilner, D. J., & Kraus, A. L. 2012, ApJ, 751, 115 3, 55

Hauschildt, P. H., Allard, F., & Baron, E. 1999, ApJ, 512, 377 43, 97, 101

Hill, G., Barnes, J. V., Hutchings, J. B., & Pearce, J. A. 1971, ApJ, 168, 443 38

Horch, E., Ninkov, Z., & Franz, O. G. 2001, AJ, 121, 1583 39

Horch, E. P., Falta, D., Anderson, L. M., et al. 2010, AJ, 139, 205 39

Horch, E. P., van Altena, W. F., Cyr, Jr., W. M., et al. 2008, AJ, 136, 312 39

Horne, K. 1986, PASP, 98, 609 13, 121

Hube, D. P. 1973, JRASC, 67, 161 38

Huélamo, N., Neuhäuser, R., Stelzer, B., & Zinnecker, H. 2000, Ap&SS, 272, 311 90

Husser, T.-O., & Ulbrich, K. 2013, ArXiv e-prints, arXiv:1312.2450 41, 57

Husser, T.-O., Wende-von Berg, S., Dreizler, S., et al. 2013, A&A, 553, A6 10, 122

Ireland, M. J., Kraus, A., Martinache, F., Lloyd, J. P., & Tuthill, P. G. 2008, ApJ, 678, 463 4

Johnson, J. A., Clanton, C., Howard, A. W., et al. 2011, ApJS, 197, 26 2

Kelson, D. D. 2003, PASP, 115, 688 43

Kerber, F., Querel, R., Hanuschik, R., et al. 2010, The Messenger, 141, 9 95

Kiminki, D. C., & Kobulnicky, H. A. 2012, ApJ, 751, 4 6

Klahr, H., & Brandner, W. 2006, Planet Formation, ed. Klahr, H. & Brandner, W. 88

Knutson, H. A., Charbonneau, D., Allen, L. E., Burrows, A., & Megeath, S. T. 2008, ApJ, 673, 526 71

Knutson, H. A., Charbonneau, D., Noyes, R. W., Brown, T. M., & Gilliland, R. L. 2007a, ApJ, 655, 564 69

Knutson, H. A., Charbonneau, D., Allen, L. E., et al. 2007b, Nature, 447, 183 69, 71

Kolbl, R., Marcy, G. W., Isaacson, H., & Howard, A. W. 2015, AJ, 149, 18 9, 10, 20, 55

Kouwenhoven, M. B. N., Brown, A. G. A., Portegies Zwart, S. F., & Kaper, L. 2007, A&A, 474, 77 6, 136

Kratter, K. M., & Matzner, C. D. 2006, MNRAS, 373, 1563 1, 2, 87, 88, 89, 105, 117, 138, 176

Kratter, K. M., Matzner, C. D., & Krumholz, M. R. 2008, ApJ, 681, 375 88

Kratter, K. M., Matzner, C. D., Krumholz, M. R., & Klein, R. I. 2010, ApJ, 708, 1585 138, 177

Kraus, A. L., Ireland, M. J., Hillenbrand, L. A., & Martinache, F. 2012, ApJ, 745, 19 3, 55

Kraus, A. L., Shkolnik, E. L., Allers, K. N., & Liu, M. C. 2014, AJ, 147, 146 43

Kroupa, P. 2002, Science, 295, 82 135

Krumholz, M. R., Klein, R. I., & McKee, C. F. 2007, ApJ, 656, 959 88, 89

—. 2012, ApJ, 754, 71 89, 138, 177

Krumholz, M. R., Klein, R. I., McKee, C. F., Offner, S. S. R., & Cunningham, A. J. 2009, Science, 323, 754 88, 105

Lafrenière, D., Marois, C., Doyon, R., Nadeau, D., & Artigau, É. 2007, ApJ, 660, 770 4

Lagrange, A.-M., Bonnefoy, M., Chauvin, G., et al. 2010, Science, 329, 57 2

Landin, N. R., Mendes, L. T. S., & Vaz, L. P. R. 2008, VizieR Online Data Catalog, 349, 40209 92, 98, 100, 101

Langford, S. V., Wyithe, J. S. B., Turner, E. L., et al. 2011, MNRAS, 415, 673 69

Lebovitz, N. R. 1974, ApJ, 190, 121 1, 86

—. 1984, ApJ, 284, 364 1, 86

Lee, J.-J. 2015, plp: Version 2.0, doi:10.5281/zenodo.18579 14, 121

Leone, F., & Catanzaro, G. 1999, A&A, 343, 273 38

Levato, H., Malaroda, S., Morrell, N., & Solivella, G. 1987, ApJS, 64, 487 38

Lloyd, C. 1981, MNRAS, 195, 805 38

Lucy, L. B., & Sweeney, M. A. 1971, AJ, 76, 544 38

Lyttleton, R. A. 1953, The stability of rotating liquid masses : [bibliog.] (Univ. Press, Camb. :) 1, 86

Machida, M. N., Tomisaka, K., Matsumoto, T., & Inutsuka, S.-i. 2008, ApJ, 677, 327 2

Madhusudhan, N., & Seager, S. 2009, ApJ, 707, 24 76

Maíz Apellániz, J. 2010, A&A, 518, A1 89

Mamajek, E. E., Kenworthy, M. A., Hinz, P. M., & Meyer, M. R. 2010, AJ, 139, 919 39

Mann, A. W., Feiden, G. A., Gaidos, E., Boyajian, T., & von Braun, K. 2015, ArXiv e-prints, arXiv:1501.01635 34

Marley, M. S., Fortney, J. J., Hubickyj, O., Bodenheimer, P., & Lissauer, J. J. 2007, ApJ, 655, 541 3

Marois, C., Lafrenière, D., Doyon, R., Macintosh, B., & Nadeau, D. 2006, ApJ, 641, 556 4

Marois, C., Macintosh, B., Barman, T., et al. 2008, Science, 322, 1348 2

Marquardt, D. 1963, Journal of the Society for Industrial and Applied Mathematics, 11, 431 44

Martins, J. H. C., Figueira, P., Santos, N. C., & Lovis, C. 2013, MNRAS, 436, 1215 55, 57

Mason, B. D., Hartkopf, W. I., Gies, D. R., Henry, T. J., & Helsel, J. W. 2009, AJ, 137, 3358 86, 103

Mason, B. D., Wycoff, G. L., Hartkopf, W. I., Douglass, G. G., & Worley, C. E. 2014, VizieR Online Data Catalog, 1, 2026 12, 39, 56, 132

Mazeh, T., & Zucker, S. 1994, Ap&SS, 212, 349 10

McAlister, H. A., Hartkopf, W. I., Hutter, D. J., Shara, M. M., & Franz, O. G. 1987, AJ, 93, 183 39

McAlister, H. A., Hartkopf, W. I., Sowell, J. R., Dombrowski, E. G., & Franz, O. G. 1989, AJ, 97, 510 39

Mishenina, T. V., Soubiran, C., Kovtyukh, V. V., Katsova, M. M., & Livshits, M. A. 2012, A&A, 547, A106 34

Moffat, A. F. J. 1969, A&A, 3, 455 122

Montet, B. T., Morton, T. D., Foreman-Mackey, D., et al. 2015, ArXiv e-prints, arXiv:1503.07866 64

Morrell, N., & Abt, H. A. 1992, ApJ, 393, 666 38

Morton, T. D. 2015, isochrones: Stellar model grid package, Astrophysics Source Code Library, ascl:1503.010 127

Neves, V., Bonfils, X., Santos, N. C., et al. 2014, A&A, 568, A121 34

Oliphant, T. E. 2007, Computing in Science & Engineering, 9, 10 49

Park, C., Jaffe, D. T., Yuk, I.-S., et al. 2014, in Society of Photo-Optical Instrumentation Engineers (SPIE) Conference Series, Vol. 9147, Society of Photo-Optical Instrumentation Engineers (SPIE) Conference Series, 1 13, 70, 72, 121

Parker, R. J., & Reggiani, M. M. 2013, MNRAS, 432, 2378 1, 117

Pearce, J. A. 1936, PASP, 48, 214 38

Pecaut, M. J., & Mamajek, E. E. 2013, ApJS, 208, 9 12, 15, 21, 34, 127, 131, 132, 135

Pepe, F., Lovis, C., Ségransan, D., et al. 2011, A&A, 534, A58 4, 55

Peter, D., Feldt, M., Henning, T., & Hormuth, F. 2012, A&A, 538, A74 6

Pinsonneault, M. H., DePoy, D. L., & Coffee, M. 2001, ApJ, 556, L59 19, 130

Pogo, A. 1928, ApJ, 68, 309 38

Porter, J. M., & Rivinius, T. 2003, PASP, 115, 1153 94

Pourbaix, D., Tokovinin, A. A., Batten, A. H., et al. 2004, A&A, 424, 727 38

—. 2009, VizieR Online Data Catalog, 1, 2020 12, 132

Prato, L., Simon, M., Mazeh, T., et al. 2002, ApJ, 569, 863 9

Raghavan, D., McAlister, H. A., Henry, T. J., et al. 2010, ApJS, 190, 1 1, 5, 117, 118

Ramírez, I., & Meléndez, J. 2005, ApJ, 626, 446 34

Reggiani, M., & Meyer, M. R. 2013, A&A, 553, A124 5, 118

Reggiani, M. M., & Meyer, M. R. 2011, ApJ, 738, 60 5, 118

Richardson, E. H., & McKellar, A. 1957, Publications of the Dominion Astrophysical Observatory Victoria, 10, 407 38

Roberts, Jr., L. C., Turner, N. H., & ten Brummelaar, T. A. 2007, AJ, 133, 545 39

Rodler, F., Kürster, M., & Henning, T. 2008, A&A, 485, 859 69

—. 2010, A&A, 514, A23 69

Rodler, F., Lopez-Morales, M., & Ribas, I. 2012, ApJ, 753, L25 69, 72, 74, 75, 78

Rothman, L., Gordon, I., Barbe, A., et al. 2009, Journal of Quantitative Spectroscopy and Radiative Transfer, 110, 533 , ¡ce:title¿HITRAN¡/ce:title¿ 71, 96

Rucinski, S. 1999, in Astronomical Society of the Pacific Conference Series, Vol. 185, IAU Colloq. 170: Precise Stellar Radial Velocities, ed. J. B. Hearnshaw & C. D. Scarfe, 82 45

Rucinski, S. M., Pych, W., Ogłoza, W., et al. 2005, AJ, 130, 767 38

Sana, H., & Evans, C. J. 2011, in IAU Symposium, Vol. 272, IAU Symposium, ed. C. Neiner, G. Wade, G. Meynet, & G. Peters, 474–485 86

Sana, H., Gosset, E., & Evans, C. J. 2009, MNRAS, 400, 1479 89

Sana, H., de Mink, S. E., de Koter, A., et al. 2012, Science, 337, 444 xv, 6, 103, 105, 112

Sana, H., de Koter, A., de Mink, S. E., et al. 2013, A&A, 550, A107 5

Savitzky, A., & Golay, M. J. E. 1964, Analytical Chemistry, 36, 1627 43

Scarfe, C. D., Barlow, D. J., & Fekel, F. C. 2000, AJ, 119, 2415 38

Schmitt, J. H. M. M. 1997, A&A, 318, 215 90

Seifahrt, A., Käufl, H. U., Zängl, G., et al. 2010, A&A, 524, A11 41, 49, 95

Shatsky, N., & Tokovinin, A. 2002, A&A, 382, 92 6, 21, 39

Slesnick, C. L., Carpenter, J. M., & Hillenbrand, L. A. 2006, AJ, 131, 3016 48

Snellen, I. A. G., de Kok, R. J., de Mooij, E. J. W., & Albrecht, S. 2010, Nature, 465, 1049 9, 10, 55

Sousa, S. G., Santos, N. C., Mayor, M., et al. 2008, A&A, 487, 373 34

Sozzetti, A., Casertano, S., Lattanzi, M. G., & Spagna, A. 2001, A&A, 373, L21 68

Stamatellos, D., & Whitworth, A. 2011, Research, Science and Technology of Brown Dwarfs and Exoplanets: Proceedings of an International Conference held in Shangai on Occasion of a Total Eclipse of the Sun, Shangai, China, Edited by E.L. Martin; J. Ge; W. Lin; EPJ Web of Conferences, Volume 16, id.05001, 16, 5001 1, 2, 87, 88, 105, 117, 138, 176

Swain, M. R., Bouwman, J., Akeson, R. L., Lawler, S., & Beichman, C. A. 2008, ApJ, 674, 482 69

Swift, D. C., Eggert, J. H., Hicks, D. G., et al. 2012, ApJ, 744, 59 77

Tetzlaff, N., Neuhaeuser, R., & Hohle, M. M. 2010, VizieR Online Data Catalog, 741, 190 92, 94, 99, 100, 101

Thalmann, C., Desidera, S., Bonavita, M., et al. 2014, A&A, 572, A91 3

Tohline, J. E. 2002, ARA&A, 40, 349 1, 2, 87

Tohline, J. E., & Durisen, R. H. 2001, in IAU Symposium, Vol. 200, The Formation of Binary Stars, ed. H. Zinnecker & R. Mathieu, 40 1, 87

Tokovinin, A., Fischer, D. A., Bonati, M., et al. 2013, PASP, 125, 1336 13, 120

Tokovinin, A., Mason, B. D., & Hartkopf, W. I. 2010, AJ, 139, 743 39

Tokovinin, A., Mason, B. D., Hartkopf, W. I., Mendez, R. A., & Horch, E. P. 2015, AJ, 150, 50 23

Tokovinin, A. A., & Smekhov, M. G. 2002, A&A, 382, 118 56

Tomkin, J., & Popper, D. M. 1986, AJ, 91, 1428 38

Torres, G., Winn, J. N., & Holman, M. J. 2008, ApJ, 677, 1324 80

Toyota, E., Itoh, Y., Ishiguma, S., et al. 2009, PASJ, 61, 19 56

Tull, R. G. 1998, in Society of Photo-Optical Instrumentation Engineers (SPIE) Conference Series, Vol. 3355, Optical Astronomical Instrumentation, ed. S. D'Odorico, 387–398 13, 121

Tull, R. G., MacQueen, P. J., Sneden, C., & Lambert, D. L. 1995, PASP, 107, 251 13, 56, 121

Tuthill, P. G., Monnier, J. D., & Danchi, W. C. 2000, in Proc. SPIE, Vol. 4006, Interferometry in Optical Astronomy, ed. P. Léna & A. Quirrenbach, 491–498 4

Valenti, J. A., & Fischer, D. A. 2005, ApJS, 159, 141 34

Vuissoz, C., & Debernardi, Y. 2004, in Astronomical Society of the Pacific Conference Series, Vol. 318, Spectroscopically and Spatially Resolving the Components of the Close Binary Stars, ed. R. W. Hilditch, H. Hensberge, & K. Pavlovski, 320–322 6, 119

Wenger, M., Ochsenbein, F., Egret, D., et al. 2000, A&AS, 143, 9 12, 15, 29, 37, 120

Westin, T. N. G. 1985, A&AS, 60, 99 94

Wittenmyer, R. A., Endl, M., Cochran, W. D., et al. 2006, AJ, 132, 177 4, 55

Woolf, V. M., & Wallerstein, G. 2005, MNRAS, 356, 963 34

Wright, J. T., Fakhouri, O., Marcy, G. W., et al. 2011, PASP, 123, 412 68, 77

Zboril, M., & Byrne, P. B. 1998, MNRAS, 299, 753 34

Zhao, B., & Li, Z.-Y. 2013, ApJ, 763, 7 2, 118

Zhao, M., Milburn, J., Barman, T., et al. 2012, ApJ, 748, L8 69

Zinnecker, H., & Yorke, H. W. 2007, ARA&A, 45, 481 1, 89, 117

Zorec, J., & Royer, F. 2012, A&A, 537, A120 21, 130

Zucker, S. 2003, MNRAS, 342, 1291 123